

1 **The Sensitivity to Oscillation Parameters**
2 **from a Simultaneous Beam and**
3 **Atmospheric Neutrino Analysis that**
4 **combines the T2K and SK Experiments**



6 Daniel Robert Clement Barrow
7 Magdalen College
8 University of Oxford

9 A thesis submitted for the degree of
10 *Doctor of Philosophy*
11 Michaelmas 2022

Abstract

12

13 Lorem ipsum dolor sit amet, consectetur adipiscing elit. Pellentesque sit amet
14 nibh volutpat, scelerisque nibh a, vehicula neque. Integer placerat nulla massa,
15 et vestibulum velit dignissim id. Ut eget nisi elementum, consectetur nibh in,
16 condimentum velit. Quisque sodales dui ut tempus mattis. Duis malesuada arcu
17 at ligula egestas egestas. Phasellus interdum odio at sapien fringilla scelerisque.
18 Mauris sagittis eleifend sapien, sit amet laoreet felis mollis quis. Pellentesque
19 dui ante, finibus eget blandit sit amet, tincidunt eu neque. Vivamus rutrum
20 dapibus ligula, ut imperdiet lectus tincidunt ac. Pellentesque ac lorem sed
21 diam egestas lobortis.

22 Suspendisse leo purus, efficitur mattis urna a, maximus molestie nisl. Aenean
23 porta semper tortor a vestibulum. Suspendisse viverra facilisis lorem, non
24 pretium erat lacinia a. Vestibulum tempus, quam vitae placerat porta, magna
25 risus euismod purus, in viverra lorem dui at metus. Sed ac sollicitudin nunc.
26 In maximus ipsum nunc, placerat maximus tortor gravida varius. Suspendisse
27 pretium, lorem at porttitor rhoncus, nulla urna condimentum tortor, sed suscipit
28 nisi metus ac risus.

29 Aenean sit amet enim quis lorem tristique commodo vitae ut lorem. Duis
30 vel tincidunt lacus. Sed massa velit, lacinia sed posuere vitae, malesuada vel
31 ante. Praesent a rhoncus leo. Etiam sed rutrum enim. Pellentesque lobortis
32 elementum augue, at suscipit justo malesuada at. Lorem ipsum dolor sit amet,
33 consectetur adipiscing elit. Praesent rhoncus convallis ex. Etiam commodo nunc
34 ex, non consequat diam consectetur ut. Pellentesque vitae est nec enim interdum
35 dapibus. Donec dapibus purus ipsum, eget tincidunt ex gravida eget. Donec
36 luctus nisi eu fringilla mollis. Donec eget lobortis diam.

37 Suspendisse finibus placerat dolor. Etiam ornare elementum ex ut vehicula.
38 Donec accumsan mattis erat. Quisque cursus fringilla diam, eget placerat neque
39 bibendum eu. Ut faucibus dui vitae dolor porta, at elementum ipsum semper.
40 Sed ultrices dui non arcu pellentesque placerat. Etiam posuere malesuada turpis,
41 nec malesuada tellus malesuada.

Acknowledgements

⁴³ Personal

⁴⁴ This is where you thank your advisor, colleagues, and family and friends.

⁴⁵ Lorem ipsum dolor sit amet, consectetur adipiscing elit. Vestibulum feugiat
⁴⁶ et est at accumsan. Praesent sed elit mattis, congue mi sed, porta ipsum. In
⁴⁷ non ullamcorper lacus. Quisque volutpat tempus ligula ac ultricies. Nam sed
⁴⁸ erat feugiat, elementum dolor sed, elementum neque. Aliquam eu iaculis est,
⁴⁹ a sollicitudin augue. Cras id lorem vel purus posuere tempor. Proin tincidunt,
⁵⁰ sapien non dictum aliquam, ex odio ornare mauris, ultrices viverra nisi magna
⁵¹ in lacus. Fusce aliquet molestie massa, ut fringilla purus rutrum consectetur.
⁵² Nam non nunc tincidunt, rutrum dui sit amet, ornare nunc. Donec cursus
⁵³ tortor vel odio molestie dignissim. Vivamus id mi erat. Duis porttitor diam
⁵⁴ tempor rutrum porttitor. Lorem ipsum dolor sit amet, consectetur adipiscing
⁵⁵ elit. Sed condimentum venenatis consectetur. Lorem ipsum dolor sit amet,
⁵⁶ consectetur adipiscing elit.

⁵⁷ Aenean sit amet lectus nec tellus viverra ultrices vitae commodo nunc. Mauris
⁵⁸ at maximus arcu. Aliquam varius congue orci et ultrices. In non ipsum vel
⁵⁹ est scelerisque efficitur in at augue. Nullam rhoncus orci velit. Duis ultricies
⁶⁰ accumsan feugiat. Etiam consectetur ornare velit et eleifend.

⁶¹ Suspendisse sed enim lacinia, pharetra neque ac, ultricies urna. Phasellus sit
⁶² amet cursus purus. Quisque non odio libero. Etiam iaculis odio a ex volutpat, eget
⁶³ pulvinar augue mollis. Mauris nibh lorem, mollis quis semper quis, consequat
⁶⁴ nec metus. Etiam dolor mi, cursus a ipsum aliquam, eleifend venenatis ipsum.
⁶⁵ Maecenas tempus, nibh eget scelerisque feugiat, leo nibh lobortis diam, id laoreet
⁶⁶ purus dolor eu mauris. Pellentesque habitant morbi tristique senectus et netus
⁶⁷ et malesuada fames ac turpis egestas. Nulla eget tortor eu arcu sagittis euismod
⁶⁸ fermentum id neque. In sit amet justo ligula. Donec rutrum ex a aliquet egestas.

⁶⁹ Institutional

⁷⁰ If you want to separate out your thanks for funding and institutional support,
⁷¹ I don't think there's any rule against it. Of course, you could also just remove
⁷² the subsections and do one big traditional acknowledgement section.

⁷³ Lorem ipsum dolor sit amet, consectetur adipiscing elit. Ut luctus tempor ex at
⁷⁴ pretium. Sed varius, mauris at dapibus lobortis, elit purus tempor neque, facilisis
⁷⁵ sollicitudin felis nunc a urna. Morbi mattis ante non augue blandit pulvinar.
⁷⁶ Quisque nec euismod mauris. Nulla et tellus eu nibh auctor malesuada quis
⁷⁷ imperdiet quam. Sed eget tincidunt velit. Cras molestie sem ipsum, at faucibus
⁷⁸ quam mattis vel. Quisque vel placerat orci, id tempor urna. Vivamus mollis,
⁷⁹ neque in aliquam consequat, dui sem volutpat lorem, sit amet tempor ipsum felis
⁸⁰ eget ante. Integer lacinia nulla vitae felis vulputate, at tincidunt ligula maximus.
⁸¹ Aenean venenatis dolor ante, euismod ultrices nibh mollis ac. Ut malesuada
⁸² aliquam urna, ac interdum magna malesuada posuere.

Contents

83

84	1 Introduction	1
85	2 Neutrino Oscillation Physics	2
86	2.1 Discovery of Neutrinos	3
87	2.2 Theory of Neutrino Oscillation	4
88	2.3 Neutrino Oscillation Measurements	8
89	2.4 Summary Of Oscillation Parameter Measurements	18
90	3 T2K and SK Experiment Overview	20
91	3.1 The Super-Kamiokande Experiment	20
92	3.2 The Tokai to Kamioka Experiment	31
93	4 Bayesian Statistics and Markov Chain Monte Carlo Techniques	46
94	4.1 Bayesian Statistics	47
95	4.2 Monte Carlo Simulation	48
96	4.3 Understanding the MCMC Results	57
97	5 Simulation, Reconstruction, and Event Reduction	62
98	5.1 Simulation	62
99	5.2 Event Reconstruction at SK	67
100	5.3 Event Reduction at SK	76
101	6 Sample Selections and Systematics	83
102	6.1 Atmospheric Samples	85
103	6.2 Near Detector Beam Samples	91
104	6.3 Far Detector Beam Samples	94
105	6.4 Systematic Uncertainties	98
106	7 Oscillation Probability Calculation	119
107	7.1 Overview	120
108	7.2 Treatment of Fast Oscillations	128
109	7.3 Calculation Engine	134
110	7.4 Matter Density Profile	138
111	7.5 Production Height Averaging	143

112	8 Oscillation Analysis	146
113	8.1 Monte Carlo Prediction	147
114	8.2 Likelihood Calculation	148
115	8.3 Sensitivities	163
116	9 Conclusions and Outlook	212
117	Appendices	
118	A Atmospheric Sample Spectra	214
119	A.1 Binning	214
120	A.2 Fully Contained Sub-GeV Samples	214
121	A.3 Fully Contained Multi-GeV Samples	218
122	A.4 Fully Contained Multi-Ring Samples	219
123	A.5 Partially Contained Samples	220
124	A.6 Upward-Going Muon Samples	221

1

125

126

Introduction

2

¹²⁷

¹²⁸

Neutrino Oscillation Physics

¹²⁹ When first proposed, neutrinos were expected to be approximately massless
¹³⁰ fermions that only interact through weak and gravitational forces. This meant
¹³¹ they were very difficult to detect as they can pass through significant amounts
¹³² of matter without interacting. Despite this, experimental neutrino physics has
¹³³ developed with many different detection techniques and neutrino sources being
¹³⁴ used today. In direct tension with Standard Model physics, neutrinos have
¹³⁵ been determined to oscillate between different lepton flavours, requiring them
¹³⁶ to have mass.

¹³⁷ The observation techniques which led to the discovery of the neutrino are doc-
¹³⁸ umented in section 2.1. The theory underpinning neutrino oscillation is described
¹³⁹ in section 2.2 and includes the approximations which can be made to simplify
¹⁴⁰ the understanding of neutrino oscillation in the two-flavour approximation. Past,
¹⁴¹ current, and future neutrino experiments are detailed in section 2.3, including the
¹⁴² reactor, atmospheric, and long-baseline accelerator neutrino sources that have
¹⁴³ been used to successfully constrain oscillation parameters. Finally, the current
¹⁴⁴ state of oscillation parameter measurements are summarised in section 2.4.

2.1 Discovery of Neutrinos

At the start of the 20th century, the electrons emitted from the β -decay of the nucleus were found to have a continuous energy spectrum [1, 2]. This observation seemingly broke the energy conservation invoked within that period's nuclear models. Postulated in 1930 by Pauli as the solution to this problem, the neutrino (originally termed "neutron") was theorized to be an electrically neutral spin-1/2 fermion with a mass of the same order of magnitude as the electron [3]. This neutrino was to be emitted with the electron in β -decay to alleviate the apparent breaking of energy conservation. As a predecessor of today's weak interaction model, Fermi's theory of β -decay developed the understanding by coupling the four constituent particles: electron, proton, neutron, and neutrino, into a quantitative model [4].

Whilst Pauli was not convinced of the ability to detect neutrinos, the first observations of the particle were made in the mid-1950s when neutrinos from a reactor were observed via the inverse β -decay (IBD) process, $\bar{\nu}_e + p \rightarrow n + e^+$ [5, 6]. The detector consisted of two parts: a neutrino interaction medium and a liquid scintillator. The interaction medium was built from two water tanks. These were loaded with cadmium chloride to allow increased efficiency for the detection of neutron capture. The positron emitted from IBD annihilates, $e^+ + e^- \rightarrow 2\gamma$, generating a prompt signal and the neutron is captured on the cadmium via $n + ^{108}Cd \rightarrow ^{109*}Cd \rightarrow ^{109}Cd + \gamma$, producing a delayed signal. An increase in the coincidence rate was observed when the reactor was operating which was interpreted as interactions from neutrinos generated in the reactor.

After the discovery of the ν_e , the question of how many flavours of neutrino exist was asked. In 1962, a measurement of the ν_μ was conducted at the Brookhaven National Laboratory [7]. A proton beam was directed at a beryllium target, generating pions which then decayed via $\pi^\pm \rightarrow \mu^\pm + (\nu_\mu, \bar{\nu}_\mu)$, and the subsequent interactions of the ν_μ were observed. As the subsequent interaction of the neutrino generates muons rather than electrons, it was determined the ν_μ

174 was fundamentally different from ν_e . The final observation to be made was
175 that of the ν_τ from the DONUT experiment [8]. Three neutrinos seem the
176 obvious solution as it mirrors the known number of charged lepton (as they form
177 weak isospin doublets) but there could be evidence of more. Several neutrino
178 experiments have found anomalous results [9, 10] which could be attributed
179 to “sterile” neutrinos. These hypothesised particles are not affected by gauge
180 interactions in the Standard Model so their presence can only be inferred through
181 the observation of non-standard oscillation modes. However, cosmological
182 observations indicate the number of neutrino species $N_{eff} = 2.99 \pm 0.17$ [11], as
183 measured from the cosmic microwave background power spectrum. LEP also
184 measured the number of active neutrino flavours to be $N_\nu = 2.9840 \pm 0.0082$ [12]
185 from measurements of the Z-decay width, but this does not strongly constrain
186 the number of sterile neutrinos.

187 2.2 Theory of Neutrino Oscillation

188 A neutrino generated with lepton flavour α can change into a different lepton
189 flavour β after propagating some distance. This phenomenon is called neutrino
190 oscillation and requires that neutrinos must have a non-zero mass. This behaviour
191 has been characterised by the Pontecorvo-Maki-Nakagawa-Sakata (PMNS) [13–
192 15] mixing matrix which describes how the flavour and mass of neutrinos are
193 associated. This is analogous to the Cabibbo-Kobayashi-Maskawa (CKM) [16]
194 matrix measured in quark physics.

195 2.2.1 Three Flavour Oscillations

196 The PMNS parameterisation defines three flavour eigenstates, ν_e , ν_μ and ν_τ
197 (indexed ν_α), which are eigenstates of the weak interaction and three mass
198 eigenstates, ν_1 , ν_2 and ν_3 (indexed ν_i). Each mass eigenstate is the superposition

¹⁹⁹ of all three flavour states,

$$|\nu_i\rangle = \sum_{\alpha} U_{\alpha i} |\nu_{\alpha}\rangle. \quad (2.1)$$

²⁰⁰ Where U is the 3×3 PMNS matrix which is unitary and connects the mass
²⁰¹ and flavour eigenstates.

²⁰² The weak interaction, when interacting via a W^{\pm} boson, couples to flavour
²⁰³ eigenstates so neutrinos interact with leptons of the same flavour. The prop-
²⁰⁴ agation of a neutrino flavour eigenstate, in a vacuum, can be re-written as a
²⁰⁵ plane-wave solution to the time-dependent Schrödinger equation,

$$|\nu_{\alpha}(t)\rangle = \sum_i U_{\alpha i}^{*} |\nu_i\rangle e^{-i\phi_i}. \quad (2.2)$$

²⁰⁶ The probability of observing a neutrino of flavour eigenstate β from one
²⁰⁷ which originated as flavour α can be calculated as,

$$P(\nu_{\alpha} \rightarrow \nu_{\beta}) = |\langle \nu_{\beta} | \nu_{\alpha}(t) \rangle|^2 = \sum_{i,j} U_{\alpha i}^{*} U_{\beta i} U_{\alpha j} U_{\beta j}^{*} e^{-i(\phi_j - \phi_i)} \quad (2.3)$$

²⁰⁸ The ϕ_i term can be expressed in terms of the energy, E_i , and magnitude of
²⁰⁹ the three momenta, p_i , of the neutrino, $\phi_i = E_i t - p_i x$ (t and x being time and
²¹⁰ position coordinates). Therefore,

$$\phi_j - \phi_i = E_j t - E_i t - p_j x + p_i x. \quad (2.4)$$

²¹¹ For a relativistic particle, $E_i \gg m_i$,

$$p_i = \sqrt{E_i^2 - m_i^2} \approx E_i - \frac{m_i^2}{2E_i}. \quad (2.5)$$

²¹² Making the approximations that neutrinos are relativistic, the mass eigenstates
²¹³ were created with the same energy and that $x = L$, where L is the distance
²¹⁴ traveled by the neutrino, Equation 2.4 then becomes

$$\phi_j - \phi_i = \frac{\Delta m_{ij}^2 L}{2E}, \quad (2.6)$$

where $\Delta m_{ij}^2 = m_i^2 - m_j^2$. This, combined with further use of unitarity relations results in Equation 2.3 becoming

$$\begin{aligned} P(\nu_\alpha \rightarrow \nu_\beta) &= \delta_{\alpha\beta} - 4 \sum_{i>j} \Re \left(U_{\alpha i}^* U_{\beta i} U_{\alpha j} U_{\beta j}^* \right) \sin^2 \left(\frac{\Delta m_{ij}^2 L}{4E} \right) \\ &\quad + (-) 2 \sum_{i>j} \Im \left(U_{\alpha i}^* U_{\beta i} U_{\alpha j} U_{\beta j}^* \right) \sin \left(\frac{\Delta m_{ij}^2 L}{2E} \right) \end{aligned} \quad (2.7)$$

Where $\delta_{\alpha\beta}$ is the Kronecker delta function and the negative sign on the last term is included for the oscillation probability of antineutrinos. As an important point to note, the observation of oscillation probability requires a non-zero value of Δm_{ij}^2 , which in turn requires that neutrinos have differing masses.

Typically, the PMNS matrix is parameterised into three mixing angles, a charge parity (CP) violating phase δ_{CP} , and two Majorana phases $\alpha_{1,2}$,

$$U = \underbrace{\begin{pmatrix} 1 & 0 & 0 \\ 0 & c_{23} & s_{23} \\ 0 & -s_{23} & c_{23} \end{pmatrix}}_{\text{Atmospheric, Accelerator}} \underbrace{\begin{pmatrix} c_{13} & 0 & s_{13} e^{-i\delta_{CP}} \\ 0 & 1 & 0 \\ -s_{13} e^{-i\delta_{CP}} & 0 & c_{13} \end{pmatrix}}_{\text{Reactor, Accelerator}} \times \underbrace{\begin{pmatrix} c_{12} & s_{12} & 0 \\ -s_{12} & c_{12} & 0 \\ 0 & 0 & 1 \end{pmatrix}}_{\text{Reactor, Solar}} \underbrace{\begin{pmatrix} e^{i\alpha_1/2} & 0 & 0 \\ 0 & e^{i\alpha_2/2} & 0 \\ 0 & 0 & 1 \end{pmatrix}}_{\text{Majorana}}. \quad (2.8)$$

Where $s_{ij} = \sin(\theta_{ij})$ and $c_{ij} = \cos(\theta_{ij})$. The oscillation parameters are often grouped: (1,2) as “solar”, (2,3) as “atmospheric” and (1,3) as “reactor”. Many neutrino experiments aim to measure the PMNS parameters from a wide array of origins, as is the purpose of this thesis.

The Majorana phase, $\alpha_{1,2}$, included within the fourth matrix in Equation 2.8 is only included for completeness. For an oscillation analysis experiment, any terms containing this phase disappear due to taking the expectation value of the PMNS matrix. Measurements of these phases can be performed by experiments searching for neutrino-less double β -decay [17].

232 A two flavour approximation can be obtained when one assumes the third
233 mass eigenstate is degenerate with another. As discussed in section 2.3, it is
234 found that $\Delta m_{21}^2 \ll |\Delta m_{31}^2|$. This results in the two flavour approximation being
235 reasonable for understanding the features of the oscillation. In this two flavour
236 case, the mixing matrix becomes,

$$U_{\text{2 Flav.}} = \begin{pmatrix} \cos(\theta) & \sin(\theta) \\ -\sin(\theta) & \cos(\theta) \end{pmatrix}. \quad (2.9)$$

237 This culminates in the oscillation probability,

$$\begin{aligned} P(\nu_\alpha \rightarrow \nu_\alpha) &= 1 - \sin^2(2\theta) \sin^2\left(\frac{\Delta m^2 L}{4E}\right), \\ P(\nu_\alpha \rightarrow \nu_\beta) &= \sin^2(2\theta) \sin^2\left(\frac{\Delta m^2 L}{4E}\right). \end{aligned} \quad (2.10)$$

238 Where $\alpha \neq \beta$. For a fixed neutrino energy, the oscillation probability is
239 a sinusoidal function depending upon the distance over which the neutrino
240 propagates. The frequency and amplitude of oscillation are dependent upon
241 $\Delta m^2 / 4E$ and $\sin^2 2\theta$, respectively. The oscillation probabilities presented thus far
242 assume $c = 1$, where c is the speed of light in vacuum. In more familiar units, the
243 maximum oscillation probability for a fixed value of θ is given at $L[\text{km}] / E[\text{GeV}] \sim$
244 $1.27 / \Delta m^2$. It is this calculation that determines the best L/E value for a given
245 experiment to be designed around for measurements of a specific value of Δm^2 .

246 2.2.2 The MSW Effect

247 The theory of neutrino oscillation in a vacuum has been described in subsec-
248 tion 2.2.1. However, the beam neutrinos and atmospheric neutrinos originating
249 from below the horizon propagate through matter in the Earth. The coherent
250 scattering of neutrinos from a material target modifies the Hamiltonian of the
251 system which results in a change of the oscillation probability. This modification
252 is termed the Mikheyev-Smirnov-Wolfenstein (MSW) effect [18–20]. This occurs
253 because charged current scattering ($\nu_e + e^- \rightarrow \nu_e + e^-$, propagated by a W boson)

- 254 only affects electron neutrinos whereas the neutral current scattering ($\nu_l + l^- \rightarrow$
 255 $\nu_l + l^-$, propagated by a Z^0 boson) interacts through all neutrino flavours equally.
 256 In the two-flavour approximation, the effective mixing parameter becomes

$$\sin^2(2\theta) \rightarrow \sin^2(2\theta_m) = \frac{\sin^2(2\theta)}{(A/\Delta m^2 - \cos(2\theta))^2 + \sin^2(2\theta)}, \quad (2.11)$$

257 where $A = 2\sqrt{2}G_F N_e E$, N_e is the electron density of the medium and G_F is
 258 Fermi's constant. It is clear to see that there exists a value of $A = \Delta m^2 \cos(2\theta)$ for
 259 $\Delta m^2 > 0$ which results in a divergent mixing parameter, colloquially called the
 260 matter resonance. This resonance regenerates the electron neutrino component of
 261 the neutrino flux [18–20]. The density at which the resonance occurs is given by

$$N_e = \frac{\Delta m^2 \cos(2\theta)}{2\sqrt{2}G_F E}. \quad (2.12)$$

262 At densities lower than this critical value, the oscillation probability will
 263 be much closer to that of vacuum oscillation. For antineutrinos, $N_e \rightarrow -N_e$
 264 [21]. The resonance occurring from the MSW effect depends on the sign of Δm^2 .
 265 Therefore, any neutrino oscillation experiment which observes neutrinos and
 266 antineutrinos which have propagated through matter can have some sensitivity
 267 to the ordering of the neutrino mass eigenstates.

268 2.3 Neutrino Oscillation Measurements

269 As evidence of beyond Standard Model physics, the 2015 Nobel Prize in Physics
 270 was awarded to the Super-Kamiokande (SK) [22] and Sudbury Neutrino Ob-
 271 servatory (SNO) [23] collaborations for the first definitive observation of solar
 272 and atmospheric neutrino oscillation [24]. Since then, the field has seen a wide
 273 array of oscillation measurements from a variety of neutrino sources. As seen
 274 in subsection 2.2.1, the neutrino oscillation probability is dependent on the ratio
 275 of the propagation baseline, L , to the neutrino energy, E . It is this ratio that
 276 determines the type of neutrino oscillation a particular experiment is sensitive to.

277 As illustrated in Figure 2.1, there are many neutrino sources that span a wide
 278 range of energies. The least energetic neutrinos are from diffuse supernovae and
 279 terrestrial neutrinos at $O(1)$ MeV whereas the most energetic neutrinos originate
 280 from atmospheric and galactic neutrinos of $> O(1)$ TeV.

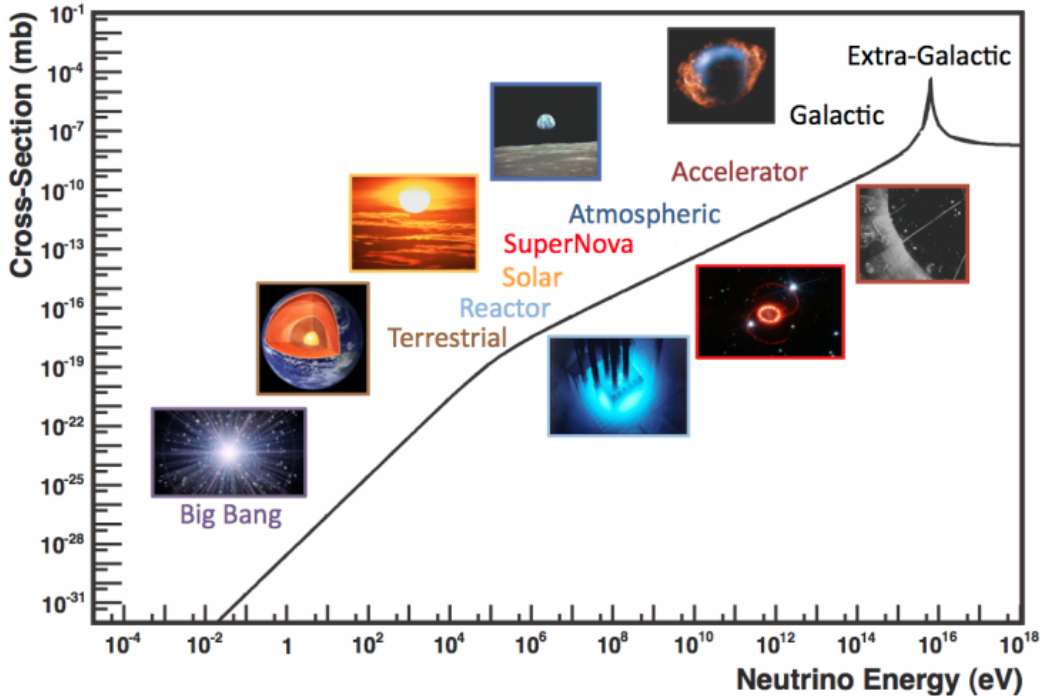


Figure 2.1: The electro-weak cross-section for $\bar{\nu}_e + e^- \rightarrow \bar{\nu}_e + e^-$ scattering on free electrons from various natural and man-made neutrino sources, as a function of neutrino energy. Taken from [25]

281 2.3.1 Solar Neutrinos

282 Solar neutrinos are emitted from fusion reaction chains at the center of the Sun.
 283 The solar neutrino flux, given as a function of neutrino energy for different
 284 fusion and decay chains, is illustrated in Figure 2.2. Whilst proton-proton
 285 fusion generates the largest flux of neutrinos, the neutrinos are of low energy
 286 and are difficult to reconstruct due to the IBD interaction threshold of 1.8MeV.
 287 Consequently, most experiments focus on the neutrinos from the decay of 8B
 288 (via $^8B \rightarrow ^8Be^* + e^+ + \nu_e$), which are higher energy.

289 The first measurements of solar neutrinos observed a significant reduction in
 290 the event rate compared to predictions from the Standard Solar Model [27, 28]. A

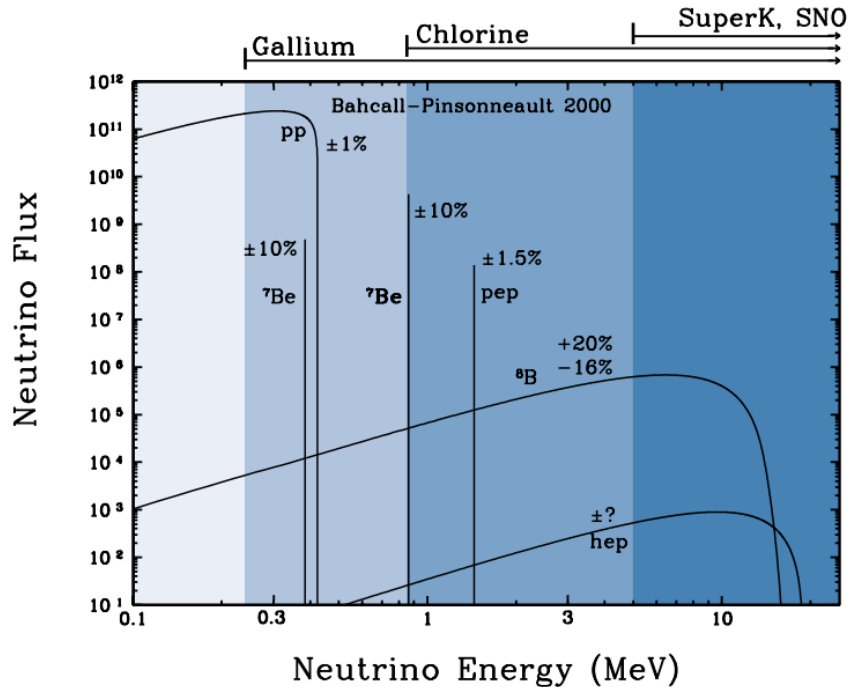
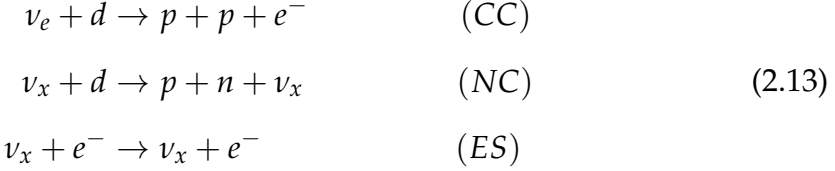


Figure 2.2: The solar neutrino flux as a function of neutrino energy for various fusion reactions and decay chains as predicted by the Standard Solar Model. Taken from [26].

proposed solution to this “solar neutrino problem” was $\nu_e \leftrightarrow \nu_\mu$ oscillations in a precursory version of the PMNS model [29]. The Kamiokande [30], Gallex [31] and Sage [32] experiments confirmed the ~ 0.5 factor deficit of solar neutrinos.

The conclusive solution to this problem was determined by the SNO collaboration [33]. Using a deuterium water target to observe 8B neutrinos, the event rate of charged current (CC), neutral current (NC), and elastic scattering (ES) interactions (Given in Equation 2.13) was simultaneously measured. CC events can only occur for electron neutrinos, whereas the NC channel is agnostic to neutrino flavour, and the ES reaction has a small excess sensitivity for detection of electron neutrino interactions. This meant that there were direct measurements of the ν_e and ν_x neutrino flux. It was concluded that the CC and ES interaction rates were consistent with the deficit previously observed. Most importantly, the NC reaction rate was only consistent with the others under the hypothesis

304 of flavour transformation.



305 Many experiments have since measured the neutrino flux of different interaction chains within the sun [34–36]. The most recent measurement was that of CNO 306 neutrinos which were recently observed with 5σ significance by the Borexino 307 collaboration. Future neutrino experiments aim to further these spectroscopic 308 measurements of different fusion chains within the Sun [37–39]. 309

310 2.3.2 Accelerator Neutrinos

311 The concept of using a man-made “neutrino beam” was first realised in 1962 [40]. 312 Since then, many experiments have followed which all use the same fundamental 313 concepts. Typically, a proton beam is aimed at a target producing charged mesons 314 that decay to neutrinos. The mesons can be sign-selected by the use of magnetic 315 focusing horns to generate a neutrino or antineutrino beam. Pions are the primary 316 mesons that decay and depending on the orientation of the magnetic field, a 317 muon (anti-)neutrino beam is generated via $\pi^+ \rightarrow \mu^+ + \nu_\mu$ or $\pi^- \rightarrow \mu^- + \bar{\nu}_\mu$. The 318 decay of muons and kaons does result in an irreducible intrinsic electron neutrino 319 background. In T2K, this background contamination is $O(< 1\%)$ [41]. There is 320 also an approximately $\sim 5\%$ “wrong-sign” neutrino background of $\bar{\nu}_\mu$ generated 321 via the same decays. As the beam is generated by proton interactions (rather 322 than anti-proton interactions), the wrong-sign component in the antineutrino 323 beam is larger when operating in neutrino mode.

324 Tuning the proton energy in the beam and using beam focusing techniques 325 allows the neutrino energy to be set to a value that maximises the disappearance 326 oscillation probability in the L/E term in Equation 2.10. This means that 327 accelerator experiments are typically more sensitive to the mixing parameters as 328 compared to a natural neutrino source. However, the disadvantage compared

329 to atmospheric neutrino experiments is the cost of building a facility to provide
 330 high-energy neutrinos, with a high flux, which is required for longer baselines.
 331 Consequently, there is typically less sensitivity to matter effects and the ordering
 332 of the neutrino mass eigenstates.

333 A neutrino experiment measures

$$R(\vec{x}) = \Phi(E_\nu) \times \sigma(E_\nu) \times \epsilon(\vec{x}) \times P(\nu_\alpha \rightarrow \nu_\beta), \quad (2.14)$$

334 where $R(\vec{x})$ is the event rate of neutrinos at position \vec{x} , $\Phi(E_\nu)$ is the flux of
 335 neutrinos with energy E_ν , $\sigma(E_\nu)$ is the cross-section of the neutrino interaction and
 336 $\epsilon(\vec{x})$ is the efficiency and resolution of the detector. In order to leverage the most
 337 out of an accelerator neutrino experiment, the flux and cross-section systematics
 338 need to be constrained. This is typically done via the use of a “near detector”,
 339 situated at a baseline of $O(1)$ km. This detector observes the unoscillated neutrino
 340 flux and constrains the parameters used within the flux and cross-section model.

341 The first accelerator experiments to precisely measure oscillation parameters
 342 were MINOS [42] and K2K [43]. These experiments confirmed the ν_μ disappear-
 343 ance seen in atmospheric neutrino experiments by finding consistent parameter
 344 values for $\sin^2(\theta_{23})$ and Δm_{23}^2 . The current generation of accelerator neutrino
 345 experiments, T2K and NO ν A extended this field by observing $\bar{\nu}_\mu \rightarrow \bar{\nu}_e$ and lead
 346 the sensitivity to atmospheric mixing parameters as seen in Figure 2.6 [44]. The
 347 two experiments differ in their peak neutrino energy, baseline, and detection tech-
 348 nique. The NO ν A experiment is situated at a baseline of 810km from the NuMI
 349 beamline which delivers 2GeV neutrinos. The T2K neutrino beam is peaked
 350 around 0.6GeV and propagates 295km. Additionally, the NO ν A experiment
 351 uses functionally identical detectors (near and far) whereas T2K uses a plastic
 352 scintillator technique at the near detector and a water Cherenkov far detector.
 353 The future generation experiments DUNE [45] and Hyper-Kamiokande [46]
 354 will succeed these experiments as the high-precision era of neutrino oscillation
 355 parameter measurements develops.

Several anomalous results have been observed in the LSND [9] and Mini-BooNE [10] detectors which were designed with purposefully short baselines. Parts of the neutrino community attributed these results to oscillations induced by a fourth “sterile” neutrino [47] but several searches in other experiments, MicroBooNE [48] and KARMEN [49], found no hints of additional neutrino species. The solution to the anomalous results is still being determined.

2.3.3 Atmospheric Neutrinos

The interactions of primary cosmic ray protons in Earth’s upper atmosphere generate showers of energetic hadrons. These are mostly pions and kaons which, when they decay, produce a natural source of neutrinos spanning energies of MeV to TeV [50]. The main decay is via

$$\begin{aligned} \pi^\pm &\rightarrow \mu^\pm + (\nu_\mu, \bar{\nu}_\mu) \\ \mu^\pm &\rightarrow e^\pm + (\nu_e, \bar{\nu}_e) \end{aligned} \tag{2.15}$$

such that for a single pion decay, three neutrinos can be produced. The atmospheric neutrino flux energy spectra as predicted by the Bartol [51], Honda [52–54], and FLUKA [55] models are illustrated in Figure 2.3. The flux distribution peaks at an energy of $O(10)$ GeV. The uncertainties associated with these models are dominated by the hadronic production of kaon and pions as well as the primary cosmic flux.

Unlike long-baseline experiments which have a fixed baseline, the distance atmospheric neutrinos propagate is dependent upon the zenith angle at which they interact. This is illustrated in Figure 2.4. Neutrinos that are generated directly above the detector ($\cos(\theta) = 1.0$) have a baseline equivalent to the height of the atmosphere whereas neutrinos that interact directly below the detector ($\cos(\theta) = -1.0$) have to travel a length equal to the diameter of the Earth. This means atmospheric neutrinos have a baseline that varies from $O(20)$ km to $O(6 \times 10^3)$ km. Any neutrino generated at or below the horizon will be subject to matter effects as they propagate through the Earth.

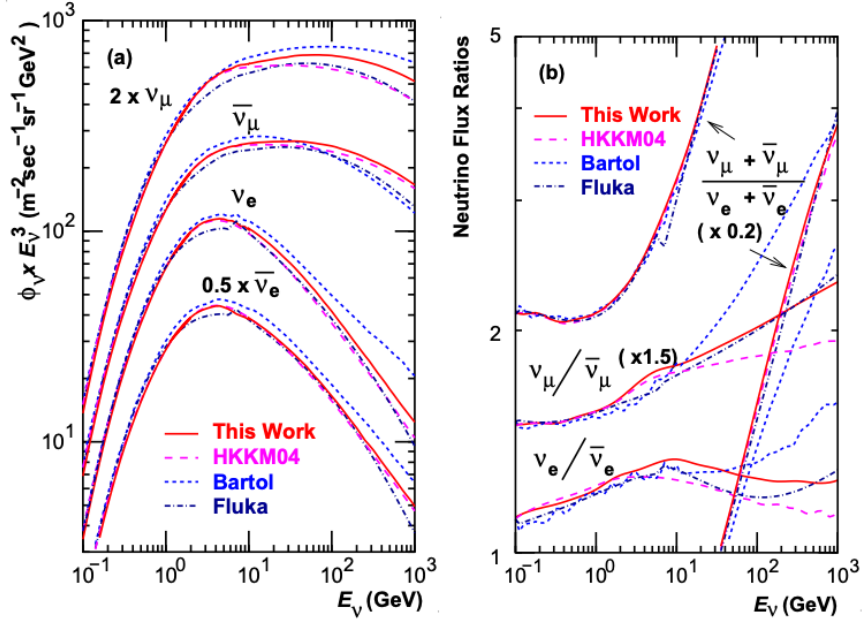


Figure 2.3: Left panel: The atmospheric neutrino flux for different neutrino flavours as a function of neutrino energy as predicted by the 2007 Honda model (“This work”) [52], the 2004 Honda model (“HKKM04”)[53], the Bartol model [51] and the FLUKA model [55]. Right panel: The ratio of the muon to electron neutrino flux as predicted by all the quoted models. Both figures taken from [52].



Figure 2.4: A diagram illustrating the definition of zenith angle as used in the Super Kamiokande experiment [56].

382 Figure 2.5 highlights the neutrino flux as a function of the zenith angle for
 383 different slices of neutrino energy. For medium to high-energy neutrinos (and to
 384 a lesser degree for low-energy neutrinos), the flux is approximately symmetric
 385 around $\cos(\theta) = 0$. To the accuracy of this approximation, the systematic

386 uncertainties associated with atmospheric flux for comparing upward-going
 387 and down-going neutrino cancels. This allows the down-going events, which are
 388 mostly insensitive to oscillation probabilities, to act as an unoscillated prediction
 389 (similar to a near detector in an accelerator neutrino experiment).

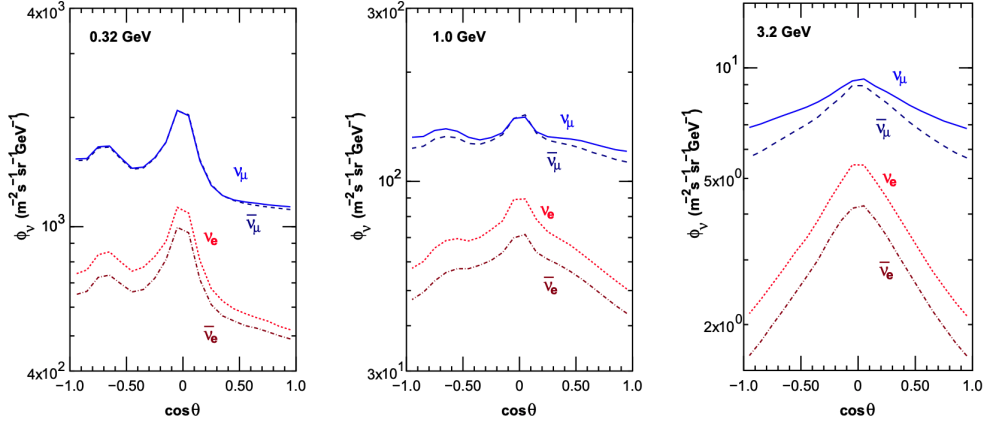


Figure 2.5: Prediction of $\nu_e, \bar{\nu}_e, \nu_\mu, \bar{\nu}_\mu$ fluxes as a function of zenith angle as calculated by the HKKM model [54]. The left, middle and right panels represent three values of neutrino energy, 0.32GeV, 1.0GeV and 3.2GeV respectively. Predictions for other models including Bartol [51], Honda [52] and FLUKA [55] are given in [56].

390 Precursory hints of atmospheric neutrinos were observed in the mid-1960s
 391 searching for $\nu_\mu + X \xrightarrow{(-)} X^* + \mu^\pm$ [57]. This was succeeded by the IMB-3 [58]
 392 and Kamiokande [59] experiments which measured the double ratio of muon
 393 to electron neutrinos in data to Monte Carlo, $R(\nu_\mu/\nu_e) = (\mu/e)_{Data}/(\mu/e)_{MC}$.
 394 Both experiments were found to have a consistent deficit of muon neutrinos,
 395 with $R(\nu_\mu/\nu_e) = 0.67 \pm 0.17$ and $R(\nu_\mu/\nu_e) = 0.658 \pm 0.016 \pm 0.035$, respectively.
 396 Super-Kamiokande (SK) [56] extended this analysis by fitting oscillation pa-
 397 rameters in $P(\nu_\mu \rightarrow \nu_\tau)$ which found best fit parameters $\sin^2(2\theta) > 0.92$ and
 398 $1.5 \times 10^{-3} < \Delta m^2 < 3.4 \times 10^{-3} \text{ eV}^2$.

399 Since then, atmospheric neutrino experiments have been making precision
 400 measurements of the $\sin^2(\theta_{23})$ and Δm^2_{32} oscillation parameters. Atmospheric
 401 neutrino oscillation is dominated by $P(\nu_\mu \rightarrow \nu_\tau)$, where SK observed a 4.6σ
 402 discovery of ν_τ appearance [60]. Figure 2.6 illustrates the current estimates
 403 on the atmospheric mixing parameters from a wide range of atmospheric and
 404 accelerator neutrino observatories.

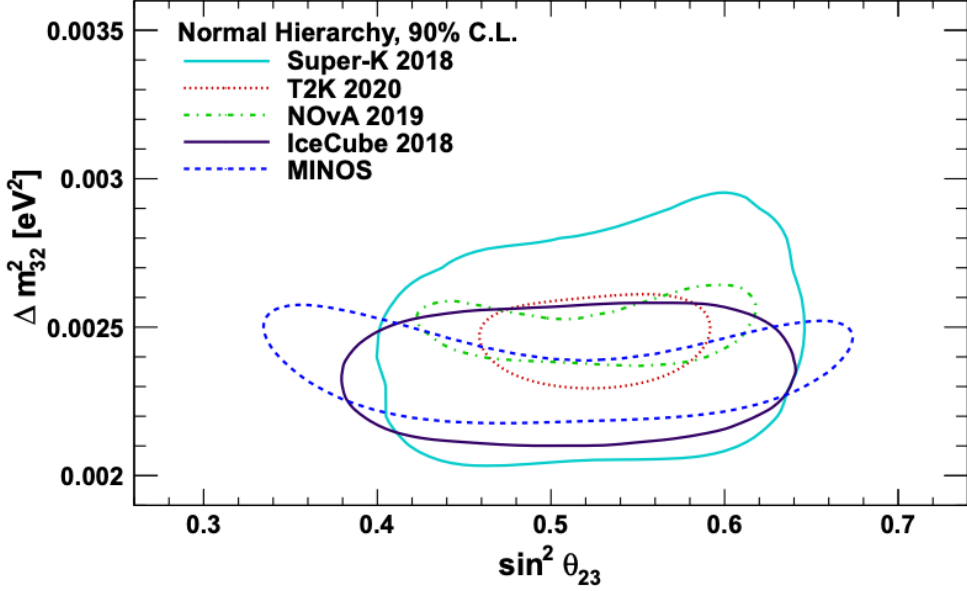


Figure 2.6: Constraints on the atmospheric oscillation parameters, $\sin^2(\theta_{23})$ and Δm_{32}^2 , from atmospheric and long baseline experiments: SK [61], T2K [62], NOvA [63], IceCube [64] and MINOS [65]. Figure taken from [66].

2.3.4 Reactor Neutrinos

As illustrated in the first discovery of neutrinos (section 2.1), nuclear reactors are a very useful man-made source of electron antineutrinos. For reactors that use low-enriched uranium ^{235}U as fuel, the antineutrino flux is dominated by the β -decay fission of ^{235}U , ^{238}U , ^{239}Pu and ^{241}Pu [67] as illustrated in Figure 2.7.

Due to their low energy, reactor electron antineutrinos predominantly interact via the inverse β -decay (IBD) interaction. The typical signature contains two signals delayed by $O(200)\mu\text{s}$; firstly the prompt photons from positron annihilation, and secondly the photons emitted ($E_{tot}^\gamma = 2.2\text{MeV}$) from de-excitation after neutron capture on hydrogen. Searching for both signals improves the detector's ability to distinguish between background and signal events [69].

There are many short baseline experiments ($L \sim O(1)\text{km}$) that have measured the $\sin^2(\theta_{13})$ and Δm_{23}^2 oscillation parameters. Daya Bay [70], RENO [71] and Double Chooz [72] have all provided precise measurements, with the first discovery of a non-zero θ_{13} made by Daya Bay and RENO (and complemented by T2K [72]). The constraints on $\sin^2(\theta_{13})$ by the reactor experiments lead the field and



Figure 2.7: Reactor electron antineutrino fluxes for ^{235}U (Black), ^{238}U (Green), ^{239}Pu (Purple), and ^{241}Pu (Orange) isotopes. The inverse β -decay cross-section (Blue) and corresponding measurable neutrino spectrum (Red) are also given. Top panel: Schematic of Inverse β -decay interaction including the eventual capture of the emitted neutron. This capture emits a γ -ray which provides a second signal of the event. Taken from [68].

are often used as external inputs to accelerator neutrino experiments to improve their sensitivity to δ_{CP} and mass hierarchy determination. JUNO-TAO [73], a small collaboration within the larger JUNO experiment, is a next-generation reactor experiment that aims to precisely measure the isotopic antineutrino yields from the different fission chains.

Kamland [74] is the only experiment to have observed reactor neutrinos using a long baseline (flux weighted averaged baseline of $L \sim 180\text{km}$) which allows it to have sensitivity to Δm_{12}^2 . Combined with the SK solar neutrino experiment, the combined analysis puts the most stringent constraint on Δm_{12}^2 [75].

2.4 Summary Of Oscillation Parameter Measurements

Since the first evidence of neutrino oscillations, numerous measurements of the mixing parameters have been made. Many experiments use neutrinos as a tool for discovery of new physics (diffuse supernova background, neutrinoless double beta decay and others) so the PMNS parameters are summarised in the Particle Data Group (PDG) review tables. The analysis presented in this thesis focuses on the 2020 T2K oscillation analysis presented in [76] where the 2020 PDG constraints [77] were used. These constraints are outlined in Table 2.1.

Parameter	2020 Constraint
$\sin^2(\theta_{12})$	0.307 ± 0.013
Δm_{21}^2	$(7.53 \pm 0.18) \times 10^{-5} \text{ eV}^2$
$\sin^2(\theta_{13})$	$(2.18 \pm 0.07) \times 10^{-2}$
$\sin^2(\theta_{23})$ (I.H.)	0.547 ± 0.021
$\sin^2(\theta_{23})$ (N.H.)	0.545 ± 0.021
Δm_{32}^2 (I.H.)	$(-2.546^{+0.034}_{-0.040}) \times 10^{-3} \text{ eV}^2$
Δm_{32}^2 (N.H.)	$(2.453 \pm 0.034) \times 10^{-3} \text{ eV}^2$

Table 2.1: The 2020 Particle Data Group constraints of the oscillation parameters taken from [77]. The value of Δm_{23}^2 is given for both normal hierarchy (N.H.) and inverted hierarchy (I.H.) and $\sin^2(\theta_{23})$ is broken down by whether its value is below (Q1) or above (Q2) 0.5.

The $\sin^2(\theta_{13})$ measurement stems from the electron antineutrino disappearance, $P(\bar{\nu}_e \rightarrow \bar{\nu}_e)$, and is take as the average best-fit from the combination of Daya Bay, Reno and Double Chooz. It is often used as a prior uncertainty within other neutrino oscillation experiments, typically termed the reactor constraint. The $\sin^2(\theta_{12})$ parameter is predominantly measured through electron neutrino disappearance, $P(\nu_e \rightarrow \nu_{\mu,\tau})$, in solar neutrino experiments. The long-baseline reactor neutrino experiment Kamland also has sensitivity to this parameter and is used in a joint fit to solar data from SNO and SK, using the reactor constraint. Measurements of $\sin^2(\theta_{23})$ are made by long-baseline and atmospheric neutrino experiments. The PDG value is a joint fit of T2K, NO ν A , MINOS and IceCube DeepCore experiments. The latest T2K-only measurement, provided at Neutrino2020 and is the basis of this thesis, is given as $\sin^2(\theta_{23}) = 0.546^{+0.024}_{-0.046}$ [76].

The PDG constraint on Δm_{12}^2 is provided by the KamLAND experiment using solar and geoneutrino data. This measurement utilised a $\sin^2(\theta_{13})$ constraint from accelerator (T2K, MINOS) and reactor neutrino (Daya Bay, RENO, Double Chooz) experiments. Accelerator measurements make some of the most stringent constraints on Δm_{23}^2 although atmospheric experiments have more sensitivity to the mass hierarchy determination. The PDG performs a joint fit of accelerator and atmospheric data, in both normal and inverted hierarchy separately. The latest T2K-only result is $\Delta m_{32}^2 = 2.49^{+0.058}_{-0.082} \times 10^{-3} \text{ eV}^2$ favouring normal hierarchy [76]. The value of δ_{CP} is largely undetermined. CP-conserving values of 0 and π were rejected with $\sim 2\sigma$ intervals, as published in Nature, although more recent analysis have reduced the credible intervals to 90%. Since the 2020 PDG publication, there has been a new measurement of $\sin^2(\theta_{13}) = (2.20 \pm 0.07) \times 10^{-2}$ [78], alongside updated Δm_{23}^2 and $\sin^2(\theta_{23})$ measurements.

Throughout this thesis, several sample spectra predictions and contours are presented which require oscillation parameters to be assumed. Table 2.2 defines two sets of oscillation parameters, with “Asimov A” set being close to the preferred values from a previous T2K-only fit [79] and “Asimov B” being CP-conserving and further from maximal θ_{23} mixing.

Parameter	Asimov A	Asimov B
Δm_{12}^2	$7.53 \times 10^{-5} \text{ eV}^2$	
Δm_{32}^2	$2.509 \times 10^{-3} \text{ eV}^2$	
$\sin^2(\theta_{12})$	0.304	
$\sin^2(\theta_{13})$	0.0219	
$\sin^2(\theta_{23})$	0.528	0.45
δ_{CP}	-1.601	0.0

Table 2.2: Reference values of the neutrino oscillation parameters for two different oscillation parameter sets.

3

468

469

T2K and SK Experiment Overview

470 As the successor of the Kamiokande experiment, the Super-Kamiokande (SK)
471 collaboration has been leading atmospheric neutrino oscillation analyses for
472 over two decades. The detector has provided some of the strongest constraints
473 on proton decay and the first precise measurements of the Δm_{23}^2 and $\sin^2(\theta_{23})$
474 neutrino oscillation parameters. The history, detection technique, and operation
475 of the SK detector is described in section 3.1.

476 The Tokai-to-Kamioka (T2K) experiment was one of the first long-baseline
477 experiments to use both neutrino and antineutrino beams to precisely measure
478 the charge parity violation within the neutrino sector. The T2K experiment
479 observed the first hints of a non-zero $\sin^2(\theta_{13})$ measurement and continues to
480 lead the field with the constraints it provides on $\sin^2(\theta_{13})$, $\sin^2(\theta_{23})$, Δm_{23}^2 and
481 δ_{CP} . In section 3.2, the techniques that T2K use to generate the neutrino beam and
482 constrain systematic parameter through near detector constraints are described.

483 3.1 The Super-Kamiokande Experiment

484 The SK experiment began taking data in 1996 [80] and has had many modifi-
485 cations throughout its operation. There have been seven defined periods of
486 data taking as noted in Table 3.1. Data taking began in SK-I which ran for five

487 years. Between the SK-I and SK-II periods, approximately 55% of the PMTs were
 488 damaged during maintenance [81]. Those that survived were equally distributed
 489 throughout the detector in the SK-II era, which resulted in a reduced 19% photo-
 490 coverage. From SK-III onwards, repairs to the detector meant the full suite of
 491 PMTs was operational recovering the 40% photocoverage. Before the start of
 492 SK-IV, the data acquisition and electronic systems were upgraded. Between
 493 SK-IV and SK-V, a significant effort was placed into tank open maintenance
 494 and repair/replacement of defective PMTs, a task for which the author of this
 495 thesis was required. Consequently, the detector conditions were significantly
 496 different between the two operational periods. SK-VI marked the start of the
 497 SK-Gd era, with the detector being doped with gadolinium at a concentration
 498 of 0.01%. SK-VII, which started during the writing of this thesis, has increased
 499 the gadolinium concentration to 0.03% for continued operation [82].

500 The oscillation analysis presented within this thesis focuses on the SK-IV
 501 period of running and the data taking within it. This follows from the recent
 502 SK analysis presented in [83]. Therefore, the information presented within this
 503 section focuses on that period.

Period	Start Date	End Date	Live-time (days)
I	April 1996	July 2001	1489.19
II	October 2002	October 2005	798.59
III	July 2006	September 2008	518.08
IV	September 2008	May 2018	3244.4
V	January 2019	July 2020	461.02
VI	July 2020	May 2022	583.3
VII	May 2022	Ongoing	N/A

Table 3.1: The various SK periods and respective live-time. The SK-VI live-time is calculated until 1st April 2022. SK-VII started during the writing of this thesis.

504 3.1.1 The SK Detector

505 The basic structure of the Super-Kamiokande (SK) detector is a cylindrical tank
 506 with a diameter 39.3m and height 41.1m filled with ultrapure water [81]. A
 507 diagram of the significant components of the SK detector is given in Figure 3.1.

508 The SK detector is situated in the Kamioka mine in Gifu, Japan. The mine
 509 is underground with roughly 1km rock overburden (2.7km water equivalent
 510 overburden) [84]. At this depth, the rate of cosmic ray muons is significantly
 511 decreased to a value of $\sim 2\text{Hz}$. The top of the tank is covered with stainless
 512 steel which is designed as a working platform for maintenance, calibration, and
 513 location for high voltage and data acquisition electronics.



Figure 3.1: A schematic diagram of the Super-Kamiokande Detector. Taken from [85].

514 A smaller cylindrical structure (36.2m diameter, 33.8m height) is situated
 515 inside the tank, with an approximate 2m gap between this structure and the outer
 516 tank wall. The purpose of this structure is to support the photomultiplier tubes
 517 (PMTs). The volume inside and outside the support structure is referred to as the
 518 inner detector (ID) and outer detector (OD), respectively. In the SK-IV era, the
 519 ID and OD are instrumented by 11,129 50cm and 1,885 20cm PMTs respectively
 520 [81]. The ID contains a 32kton mass of water. Many analyses performed at SK
 521 use a “fiducial volume” defined by the volume of water inside the ID excluding
 522 some distance to the ID wall. This reduces the volume of the detector which is
 523 sensitive to neutrino events but reduces radioactive backgrounds and allows for

524 better reconstruction performance. The nominal fiducial volume is defined as the
525 area contained inside 2m from the ID wall for a total of 22.5kton water [86].

526 The two regions of the detector (ID and OD) are optically separated with
527 opaque black plastic hung from the support structure. The purpose of this is
528 to determine whether an event entered or exited the ID. This allows cosmic ray
529 muons and partially contained events to be tagged and separated from neutrino
530 events entirely contained within the ID. This black plastic is also used to cover
531 the area between the ID PMTs to reduce photon reflection from the ID walls.
532 Opposite to this, the OD is lined with a reflective material to allow photons to
533 reflect around inside the OD until collected by one of the PMTs. Furthermore,
534 each OD PMT is optically coupled with $50 \times 50\text{cm}$ plates of wavelength shifting
535 acrylic which increases the efficiency of light collection [84].

536 In the SK-IV data-taking period, the photocathode coverage of the detector, or
537 the fraction of the ID wall instrumented with PMTs, is $\sim 40\%$ [84]. The PMTs have
538 a quantum efficiency (the ratio of detected electrons to incident photons) of $\sim 21\%$
539 for photons with wavelengths of $360\text{nm} < \lambda < 390\text{nm}$ [87]. The proportion of
540 photoelectrons that produce a signal in the dynode of a PMT, termed the collection
541 efficiency, is $> 70\%$ [84]. The PMTs used within SK are most sensitive to photons
542 with wavelength $300\text{nm} \leq \lambda \leq 600\text{nm}$ [84]. One disadvantage of using PMTs as
543 the detection media is that the Earth's geomagnetic field can modify its response.
544 Therefore, a set of compensation coils is built around the inner surface of the
545 detector to mitigate this effect [88].

546 As mentioned, the SK detector is filled with ultrapure water, which in a perfect
547 world would contain no impurities. However, bacteria and organic compounds
548 can significantly degrade the water quality. This decreases the attenuation length,
549 which reduces the total number of photons that hit a PMT. To combat this, a
550 sophisticated water treatment system has been developed [84, 89]. UV lights,
551 mechanical filters, and membrane degasifiers are used to reduce the bacteria,
552 suspended particulates, and radioactive materials from the water. The flow of
553 water within the tank is also critical as it can remove stagnant bacterial growth

554 or build-up of dust on the surfaces within the tank. Gravity drifts impurities in
555 the water towards the bottom of the tank which, if left uncontrolled, can create
556 asymmetric water conditions between the top and bottom of the tank. Typically,
557 the water entering the tank is cooled below the ambient temperature of the tank
558 to control convection and inhibit bacteria growth. Furthermore, the rate of dark
559 noise hits within PMTs is sensitive to the PMT temperature [90] so controlling
560 the temperature gradients within the tank is beneficial for stable measurements.

561 SK-VI is the first phase of the SK experiment to use gadolinium dopants
562 within the ultrapure water [82]. As such, the SK water system had to be replaced
563 to avoid removing the gadolinium concentrate from the ultrapure water [91]. For
564 an inverse β -decay (IBD) interaction in a water target, the emitted neutron is
565 thermally captured on hydrogen. This process releases 2.2MeV γ ray which are
566 difficult to detect as the resulting Compton scattered electrons are very close to the
567 Cherenkov threshold, limiting detection capability. Thermal capture of neutrons
568 on gadolinium generates γ rays with higher energy (8MeV [69]) meaning they
569 are more easily detected and reconstructed. SK-VI has 0.01% Gd loading (0.02%
570 gadolinium sulphate by mass) which causes \approx 50% of neutrons emitted by IBD to
571 be captured on gadolinium[92, 93] . Whilst predominantly useful for low energy
572 analyses, Gd loading allows better $\nu/\bar{\nu}$ separation for atmospheric neutrino
573 event selections [94]. Efforts are currently in place to increase the gadolinium
574 concentrate to 0.03% for \approx 75% neutron capture efficiency on gadolinium [95].
575 The final stage of loading targets 0.1% concentrate targeting \approx 90% neutron
576 capture efficiency on gadolinium.

577 3.1.2 Calibration

578 The calibration of the SK detector is documented in [81] and summarised below.
579 The analysis presented within this thesis is dependent upon ‘high energy events’
580 (Charged particles with $O(> 100)$ MeV momenta). These are events that are
581 expected to generate a larger number of photons such that each PMT will
582 be hit with multiple photons. The reconstruction of these events depends

upon the charge deposited within each PMT and the timing response of each individual PMT. Therefore, the most relevant calibration techniques to this thesis are outlined.

Before installation, 420 PMTs were calibrated to have identical charge responses and then distributed throughout the tank in a cross-shape pattern (As illustrated by Figure 3.2). These are used as a standardised measure for the rest of the PMTs installed at similar geometric positions within SK to be calibrated against. To perform this calibration, a xenon lamp is located at the centre of the SK tank which flashes uniform light at 1Hz. This allows for geometrical effects, water quality variation, and timing effects to be measured in-situ throughout normal data-taking periods.



Figure 3.2: The location of “standard PMTs” (red) inside the SK detector. Taken from [81].

When specifically performing calibration of the detector (in out-of-data taking mode), the water in the tank was circulated to avoid top/bottom asymmetric water quality. Any non-uniformity within the tank significantly affects the PMT hit probability through scattering or absorption. This becomes a dominant effect for the very low-intensity light sources discussed later which are designed such that only one photon is incident upon a given PMT.

600 The “gain” of a PMT is defined as the ratio of the total charge of the signal
 601 produced compared to the charge of photoelectrons emitted by the photocathodes
 602 within the PMT. To calibrate the signal of each PMT, the “relative” and “absolute”
 603 gain values are measured. The relative gain is the variation of gain among each
 604 of the PMTs whereas the absolute gain is the average gain of all PMTs.

605 The relative gain is calibrated as follows. A laser is used to generate two
 606 measurements: a high-intensity flash that illuminates every PMT with a sufficient
 607 number of photons, and a low-intensity flash in which only a small number
 608 of PMTs collect light. The first measurement creates an average charge, $Q_{obs}(i)$
 609 on PMT i , whereas the second measurement ensures that each hit PMT only
 610 generates a single photoelectron. For the low-intensity measurement, the number
 611 of times each PMT records a charge larger than 1/4 photoelectrons, $N_{obs}(i)$, is
 612 counted. The values measured can be expressed as

$$\begin{aligned} Q_{obs}(i) &\propto I_H \times f(i) \times \epsilon(i) \times G(i), \\ N_{obs}(i) &\propto I_L \times f(i) \times \epsilon(i), \end{aligned} \tag{3.1}$$

613 Where I_H and I_L is the intensity of the high and low flashes, $f(i)$ is the
 614 acceptance efficiency of the i^{th} PMT, $\epsilon(i)$ is the product of the quantum and
 615 collection efficiency of the i^{th} PMT and $G(i)$ is the gain of the i^{th} PMT. The
 616 relative gain for each PMT can determined by taking the ratio of these quantities.

617 The absolute gain calibration is performed by observing fixed energy γ -rays
 618 of $E_\gamma \sim 9\text{MeV}$ emitted isotropically from neutron capture on a NiCf source
 619 situated at the centre of the detector. This generates a photon yield of about 0.004
 620 photoelectrons/PMT/event, meaning that $> 99\%$ of PMT signals are generated
 621 from single photoelectrons. A charge distribution is generated by performing
 622 this calibration over all PMTs, and the average value of this distribution is taken
 623 to be the absolute gain value.

624 As mentioned in subsection 3.1.1, the average quantum and collection effi-
 625 ciency for the SK detector PMTs is $\sim 21\%$ and $> 70\%$ respectively. However,
 626 these values do differ between each PMT and need to be calibrated accordingly.

627 Consequently, the NiCf source is also used to calibrate the “quantum \times collection”
628 efficiency (denoted “QE”) value of each PMT. The NiCf low-intensity source is
629 used as the PMT hit probability is proportional to the QE ($N_{obs}(i) \propto \epsilon(i)$ in
630 Equation 3.1). A Monte Carlo prediction which includes photon absorption,
631 scattering, and reflection is made to estimate the number of photons incident on
632 each PMT and the ratio of the number of predicted to observed hits is calculated.
633 The difference is attributed to the QE efficiency of that PMT. This technique is
634 extended to calculate the relative QE efficiency by normalizing the average of
635 all PMTs which removes the dependence on the light intensity.

636 Due to differing cable lengths and readout electronics, the timing response
637 between a photon hitting the PMT and the signal being captured by the data
638 acquisition can be different between each PMT. Due to threshold triggers (De-
639 scribed in subsection 3.1.3), the time at which a pulse reaches a threshold is
640 dependent upon the size of the pulse. This is known as the ‘time-walk’ effect
641 and also needs to be accounted for in each PMT. To calibrate the timing response,
642 a pulse of light with width 0.2ns is emitted into the detector through a diffuser.
643 Two-dimensional distributions of time and pulse height (or charge) are made
644 for each PMT and are used to calibrate the timing response. This is performed
645 in-situ during data taking with the light source pulsing at 0.03Hz.

646 The top/bottom water quality asymmetry is measured using the NiCf calibra-
647 tion data and cross-referencing these results to the “standard PMTs”. The water
648 attenuation length is continuously measured by the rate of vertically-downgoing
649 cosmic-ray muons which enter via the top of the tank.

650 Dark noise is where a PMT registers a pulse that is consistent with a single
651 photoelectron emitted from photon detection despite the PMT being in complete
652 darkness. This is predominately caused by two processes. Firstly there is
653 intrinsic dark noise which is where photoelectrons gain enough thermal energy
654 to be emitted from the photocathode, and secondly, the radioactive decay of
655 contaminants inside the structure of the PMT. Typical dark noise rate for PMTs
656 used within SK are $O(3)$ kHz [84]. This is lower than the expected number of

657 photons generated for a ‘high energy event’ (As described in subsection 3.1.4)
658 but instability in this value can cause biases in reconstruction. Dark noise is
659 related to the gain of a PMT and is calibrated using hits inside a time window
660 recorded before an event trigger [96].

661 3.1.3 Data Acquisition and Triggering

662 As the analysis presented in this thesis only uses the SK-IV period of the SK
663 experiment so this subsection focuses on the relevant points of the data acqui-
664 sition and triggering systems to that SK period. The earlier data acquisition and
665 triggering systems are documented in [97, 98].

666 Before the SK-IV period started, the existing front-end electronics were re-
667 placed with “QTC-Based Electrons with Ethernet, QBEE” systems [99]. When the
668 QBEE observes a signal above a 1/4 photoelectron threshold, the charge-to-time
669 (QTC) converter generates a rectangular pulse. The start of the rectangular pulse
670 indicates the time at which the analog photoelectron signal was received and the
671 width of the pulse indicates the total charge integrated throughout the signal.
672 This is then digitized by time-to-digital converters and sent to the “front-end”
673 PCs. The digitized signal from every QBEE is then chronologically ordered and
674 sent to the “merger” PCs. It is the merger PCs that apply the software trigger.
675 Any triggered events are passed to the “organizer” PC. This sorts the data stream
676 of multiple merger PCs into chronologically ordered events which are then saved
677 to disk. The schematic of data flow from PMTs to disk is illustrated in Figure 3.3.

678 The software trigger (described in [101]) operates by determining the number
679 of PMT hits within a 200ns sliding window, N_{200} . This window coincides with
680 the maximum time that a Cherenkov photon would take to traverse the length
681 of the SK tank [98]. For lower energy events that generate fewer photons, this
682 technique is useful for eliminating background processes like dark noise and
683 radioactive decay which would be expected to separate in time. When the value
684 of N_{200} exceeds some threshold, a software trigger is issued. There are several
685 trigger thresholds used within the SK-IV period which are detailed in Table 3.2.

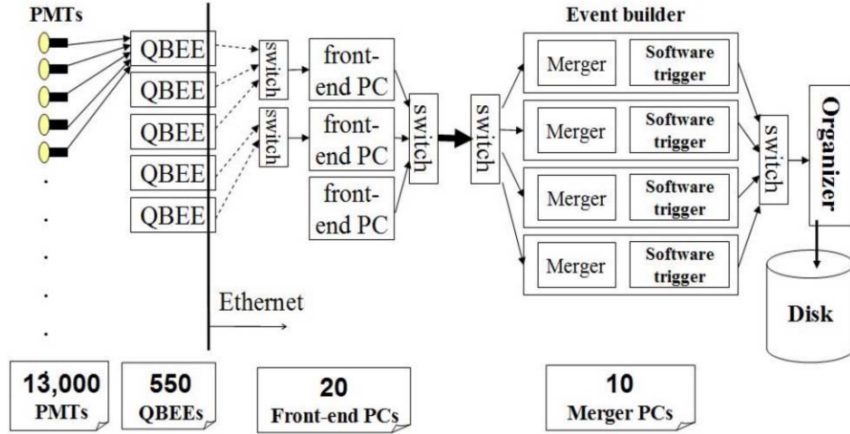


Figure 3.3: Schematic view of the data flow through the data acquisition and online system. Taken from [100].

686 If one of these thresholds is met, the PMT hits within an extended time window
 687 are also read out and saved to disk. In the special case of an event that exceeds
 688 the SHE trigger but does not exceed the OD trigger, the AFT trigger looks for
 689 delayed coincidences of 2.2MeV gamma rays emitted from neutron capture in
 690 a $535\mu\text{s}$ window after the SHE trigger. A similar but more complex “Wideband
 691 Intelligent Trigger (WIT)” has been deployed and is described in [102].

Trigger	Acronym	Condition	Extended time window (μs)
Super Low Energy	SLE	>34/31 hits	1.3
Low Energy	LE	>47 hits	40
High Energy	HE	>50 hits	40
Super High Energy	SHE	>70/58 hits	40
Outer Detector	OD	>22 hits in OD	N/A

Table 3.2: The trigger thresholds and extended time windows saved around an event which were utilised throughout the SK-IV period. The exact thresholds can change and the values listed here represent the thresholds at the start and end of the SK-IV period.

3.1.4 Cherenkov Radiation

693 Cherenkov light is emitted from any highly energetic charged particle traveling
 694 with relativistic velocity, β , greater than the local speed of light in a medium [103].

695 Cherenkov light is formed at the surface of a cone with characteristic pitch angle,

$$\cos(\theta) = \frac{1}{\beta n}. \quad (3.2)$$

696 where n is the refractive index of the medium. Consequently, the Cherenkov
 697 momentum threshold, P_{thres} , is dependent upon the mass, m , of the charged
 698 particle moving through the medium,

$$P_{thres} = \frac{m}{\sqrt{n^2 - 1}} \quad (3.3)$$

699 For water, where $n = 1.33$, the Cherenkov threshold momentum and energy
 700 for various particles are given in Table 3.3. In contrast, γ -rays are detected
 701 indirectly via the combination of photons generated by Compton scattering
 702 and pair production. The threshold for detection in the SK detector is typically
 703 higher than the threshold for photon production. This is due to the fact that the
 704 attenuation of photons in the water means that typically $\sim 75\%$ of Cherenkov
 705 photons reach the ID PMTs. Then the collection and quantum efficiencies
 706 described in subsection 3.1.1 result in the number of detected photons being
 707 lower than the number of photons which reach the PMTs.

Particle	Threshold Momentum (MeV)	Threshold Energy (MeV)
Electron	0.5828	0.7751
Muon	120.5	160.3
Pion	159.2	211.7
Proton	1070.0	1423.1

Table 3.3: The threshold momentum and energy for a particle to generate Cherenkov light in ultrapure water, as calculated in Equation 3.2 in ultrapure water which has refractive index $n = 1.33$.

708 The Frank-Tamm equation [104] describes the relationship between the num-
 709 ber of Cherenkov photons generated per unit length, dN/dx , the wavelength of
 710 the photons generated, λ , and the relativistic velocity of the charged particle,

$$\frac{d^2N}{dxd\lambda} = 2\pi\alpha \left(1 - \frac{1}{n^2\beta^2}\right) \frac{1}{\lambda^2}. \quad (3.4)$$

711 where α is the fine structure constant. For a 100MeV momentum electron,
 712 approximately 330 photons will be produced per centimeter in the $300\text{nm} \leq \lambda \leq$
 713 700nm region which the ID PMTs are most sensitive to [84].

714 3.2 The Tokai to Kamioka Experiment

715 The Tokai to Kamioka (T2K) experiment is a long-baseline neutrino oscillation
 716 experiment located in Japan. Proposed in the early 2000s [105, 106] to replace
 717 K2K [107], T2K was designed to observe electron neutrino appearance whilst
 718 precisely measuring the oscillation parameters associated with muon neutrino
 719 disappearance [108]. The experiment consists of a neutrino beam generated
 720 at the Japan Proton Accelerator Research Complex (J-PARC), a suite of near
 721 detectors situated 280m from the beam target, and the Super Kamiokande far
 722 detector positioned at a 295km baseline. The cross-section view of the T2K
 723 experiment is drawn in Figure 3.4.

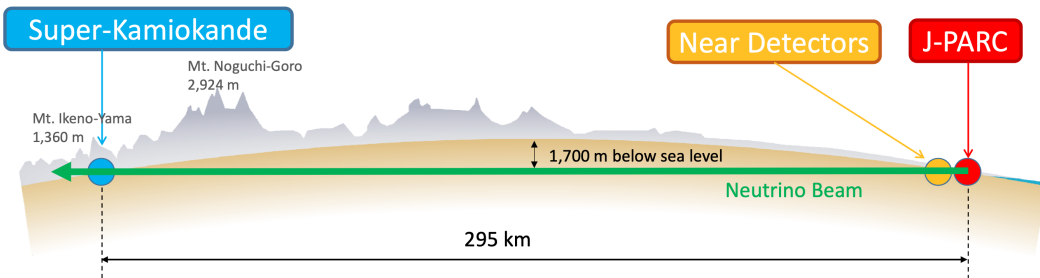


Figure 3.4: The cross-section view of the Tokai to Kamioka experiment illustrating the beam generation facility at J-PARC, the near detector situated at a baseline of 280m and the Super Kamiokande far detector situated 295km from the beam target.

724 The T2K collaboration makes world-leading measurements of the $\sin^2(\theta_{23})$
 725 , Δm_{23}^2 , and δ_{CP} oscillation parameters. Improvements in the precision and
 726 accuracy of parameter estimates are still being made by including new data
 727 samples and developing the models which describe the neutrino interactions
 728 and detector responses [109]. Electron neutrino appearance was first observed
 729 at T2K in 2014 [110] with 7.3σ significance.

730 The near detectors provide constraints on the beam flux and cross-section
 731 model parameters used within the oscillation analysis by observing the unoscil-
 732 lated neutrino beam. There are a host of detectors situated in the near detector hall
 733 (As illustrated in Figure 3.5): ND280 (subsection 3.2.2), INGRID (subsection 3.2.3),
 734 NINJA [111], WAGASCI [112], and Baby-MIND [113]. The latter three are not
 735 currently used within the oscillation analysis presented within this thesis.

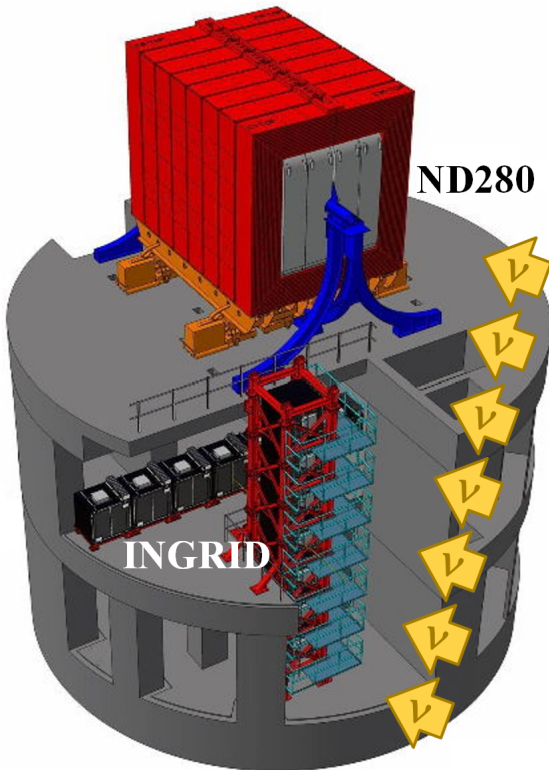


Figure 3.5: The near detector suite for the T2K experiment showing the ND280 and INGRID detectors. The distance between the detectors and the beam target is 280m.

736 Whilst this thesis presents the ND280 in terms of its purpose for the oscillation
 737 analysis, the detector can also make many cross-section measurements at neutrino
 738 energies of $O(1)$ GeV for the different targets within the detector [114, 115]. These
 739 measurements are of equal importance as they can lead the way in determining
 740 the model parameters used in the interaction models for the future high-precision
 741 era of neutrino physics.

742 There are two independent fitters, MaCh3 and BANFF, which perform the near
 743 detector fit. MaCh3 is the basis of this analysis and uses a bayesian Markov

744 Chain Monte Carlo fitting technique, whereas BANFF uses a frequentist gradient
745 descent technique. The output of each fitter is converted into a covariance
746 matrix to describe the error and correlations between all the flux and cross-
747 section parameters. This is then propagated to the far-detector oscillation analysis
748 group for use in the P-Theta and VALOR fitting framework. As MaCh3 can handle
749 both near and far detector samples, it does not use this covariance matrix and
750 instead opts for a simultaneous fit of the two detector measurements. This is an
751 analysis choice which removes the assumption of Gaussian posterior distributions
752 required when building the post-fit covariance matrix.

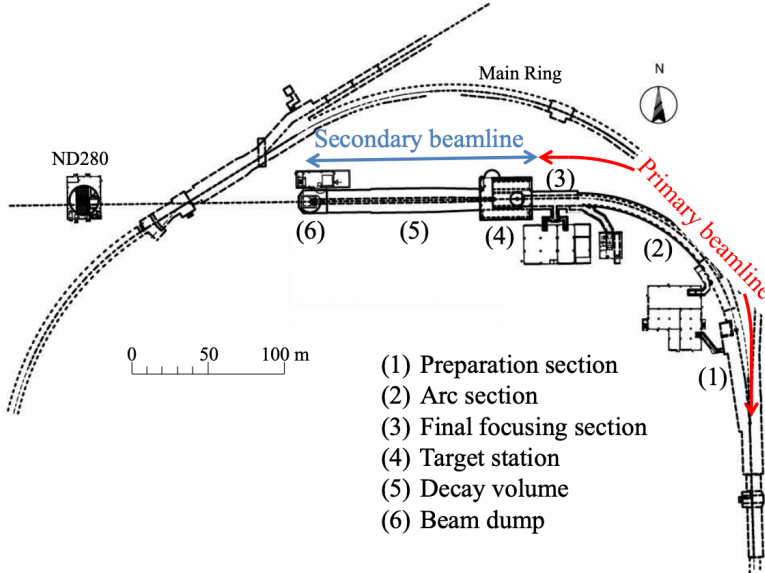
753 DB: MaCh3 vs PTheta and Valor

754 There are three particular tunes of the T2K flux and low energy cross section
755 model typically considered. Firstly, the “generated” tune which is the set of
756 dial values with which the Monte Carlo was generated. Secondly, the set of dial
757 values which are taken from external data measurements and used as inputs.
758 These are the “pre-fit” dial values. The reason these two sets of dial values are
759 different is that the external data measurements are continually updated but it
760 is very computationally intensive to regenerate a Monte Carlo prediction after
761 each update. The final tune is the “post-fit”, “post-ND fit” or “post-BANFF” dial
762 values. These are the values taken from the fit to the beam near detector data.

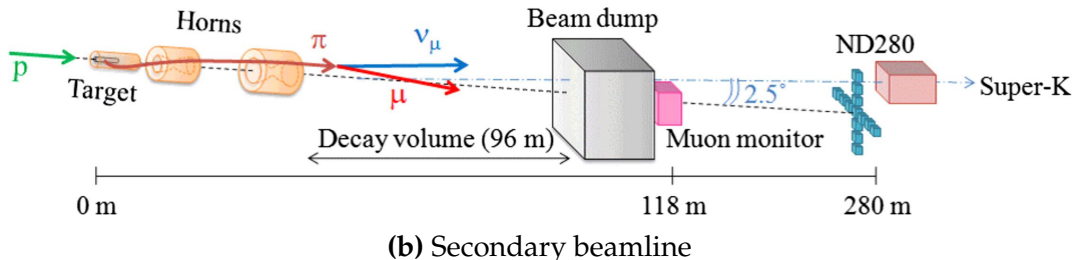
763 3.2.1 The Neutrino Beam

764 The neutrino beam used within the T2K experiment is described in [41, 116]
765 and summarised below. The accelerating facility at J-PARC is composed of two
766 sections; the primary and secondary beamlines. Figure 3.6 illustrates a schematic
767 of the beamline, focusing mostly on the components of the secondary beamline.
768 The primary beamline has three accelerators that progressively accelerate pro-
769 tons; a linear accelerator, a rapid-cycling synchrotron, and the main-ring (MR)
770 synchrotron. Once fully accelerated by the MR, the protons have a kinetic energy
771 of 30GeV. Eight bunches of these protons, separated by 500ns, are extracted
772 per “spill” from the MR and directed towards a graphite target (a rod of length

⁷⁷³ 91.4cm and diameter 2.6cm). Spills are extracted at 0.5Hz with $\sim 3 \times 10^{14}$
⁷⁷⁴ protons contained per spill.



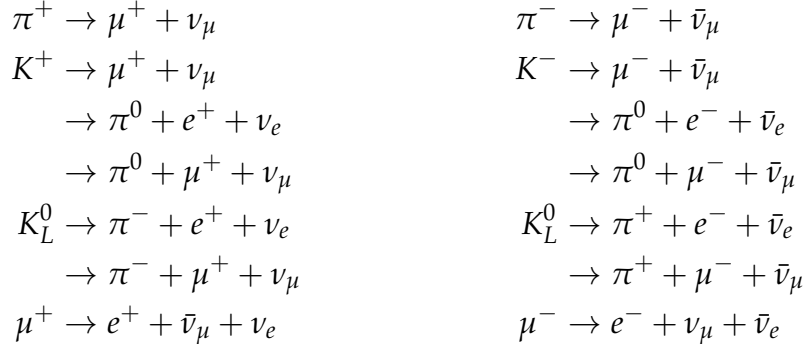
(a) Primary and secondary beamline



(b) Secondary beamline

Figure 3.6: Top panel: Bird's eye view of the most relevant part of primary and secondary beamline used within the T2K experiment. The primary beamline is the main-ring proton synchrotron, kicker magnet, and graphite target. The secondary beamline consists of the three focusing horns, decay volume, and beam dump. Figure taken from [116]. Bottom panel: The side-view of the secondary beamline including the focusing horns, beam dump and neutrino detectors. Figure taken from [117].

⁷⁷⁵ The secondary beamline consists of three main components: the target station,
⁷⁷⁶ the decay volume, and the beam dump. The target station is comprised of the
⁷⁷⁷ target, beam monitors, and three magnetic focusing horns. The proton beam
⁷⁷⁸ interacts with the graphite target to form a secondary beam of mostly pions
⁷⁷⁹ and kaons. The secondary beam travels through a 96m long decay volume,
⁷⁸⁰ generating neutrinos through the following decays [41],



781 The electrically charged component of the secondary beam is focused towards
 782 the far detector by the three magnetic horns. These horns direct charged particles
 783 of a particular polarity towards SK whilst defocusing the oppositely charged
 784 particles. This allows a mostly neutrino or mostly antineutrino beam to be used
 785 within the experiment, denoted as “forward horn current (FHC)” or “reverse
 786 horn current (RHC)” respectively.

788 Figure 3.7 illustrates the different contributions to the FHC and RHC neutrino
 789 flux. The low energy flux is dominated by the decay of pions whereas kaon
 790 decay becomes the dominant source of neutrinos for $E_\nu > 3\text{GeV}$. The “wrong-
 791 sign” component, which is the $\bar{\nu}_\mu$ background in a ν_μ beam, and the intrinsic
 792 irreducible ν_e background, are predominantly due to muon decay for $E_\nu <$
 793 2GeV . As the antineutrino production cross-section is smaller than the neutrino
 794 cross-section, the wrong-sign component is more dominant in the RHC beam
 795 as compared to that in the FHC beam.

796 The beam dump, situated at the end of the decay volume, stops all charged
 797 particles other than highly energetic muons ($p_\mu > 5\text{GeV}$). The MuMon detector
 798 monitors the penetrating muons to determine the beam direction and inten-
 799 sity which is used to constrain some of the beam flux systematics within the
 800 analysis [117, 119].

801 The T2K experiment uses an off-axis beam to narrow the neutrino energy
 802 distribution. This was the first implementation of this technique in a long-
 803 baseline neutrino oscillation experiment after its original proposal [120]. Pion
 804 decay, $\pi \rightarrow \mu + \nu_\mu$, is a two-body decay. Consequently, the neutrino energy,

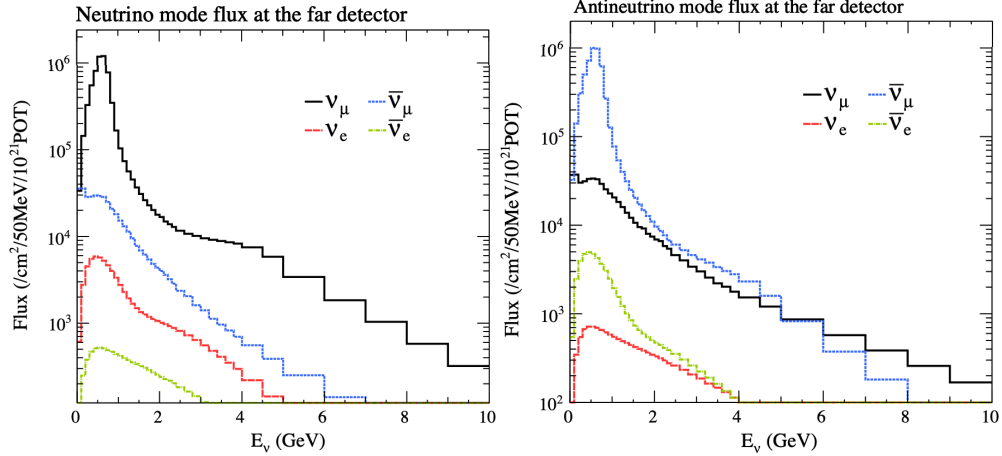


Figure 3.7: The Monte Carlo prediction of the energy spectrum for each flavour of neutrino (ν_e , $\bar{\nu}_e$, ν_μ and $\bar{\nu}_\mu$) in the neutrino dominated beam FHC mode (Left) and antineutrino dominated beam RHC mode (Right) expected at SK. Taken from [118].

805 E_ν , can be determined based on the pion energy, E_π , and the angle at which
 806 the neutrino is emitted, θ ,

$$E_\nu = \frac{m_\pi^2 - m_\mu^2}{2(E_\pi - p_\pi \cos(\theta))}, \quad (3.5)$$

807 where m_π and m_μ are the mass of the pion and muon respectively. For a fixed
 808 energy pion, the neutrino energy distribution is dependent upon the angle at
 809 which the neutrinos are observed from the initial pion beam direction. For the
 810 295km baseline at T2K, $E_\nu = 0.6\text{GeV}$ maximises the electron neutrino appearance
 811 probability, $P(\nu_\mu \rightarrow \nu_e)$, whilst minimising the muon disappearance probability,
 812 $P(\nu_\mu \rightarrow \nu_\mu)$. Figure 3.8 illustrates the neutrino energy distribution for a range of
 813 off-axis angles, as well as the oscillation probabilities most relevant to T2K.

814 3.2.2 The Near Detector at 280m

815 Whilst all the near detectors are situated in the same “pit” located at 280m from
 816 the beamline, the “ND280” detector is the off-axis detector which is situated at
 817 the same off-axis angle as the Super-Kamiokande far detector. It has two primary
 818 functions; firstly it measures the neutrino flux and secondly it counts the event
 819 rates of different types of neutrino interactions. Both of these constrain the flux



Figure 3.8: Top panel: T2K muon neutrino disappearance probability as a function of neutrino energy. Middle panel: T2K electron neutrino appearance probability as a function of neutrino energy. Bottom panel: The neutrino flux distribution for three different off-axis angles (Arbitrary units) as a function of neutrino energy.

and cross-section systematics invoked within the model for a more accurate prediction of the expected event rate at the far detector.

As illustrated in Figure 3.9, the ND280 detector consists of several sub-detectors. The most important part of the detector for this analysis is the tracker region. This is comprised of two time projection chambers (TPCs) sandwiched between three fine grain detectors (FGDs). The FGDs contain both hydrocarbon plastics and water targets for neutrino interactions and provide track reconstruction near the interaction vertex. The emitted charged particles can then propagate into the TPCs which provide particle identification and momentum reconstruction. The FGDs and TPCs are further described in subsubsection 3.2.2.1 and subsubsection 3.2.2.2 respectively. The electromagnetic calorimeter (ECAL)

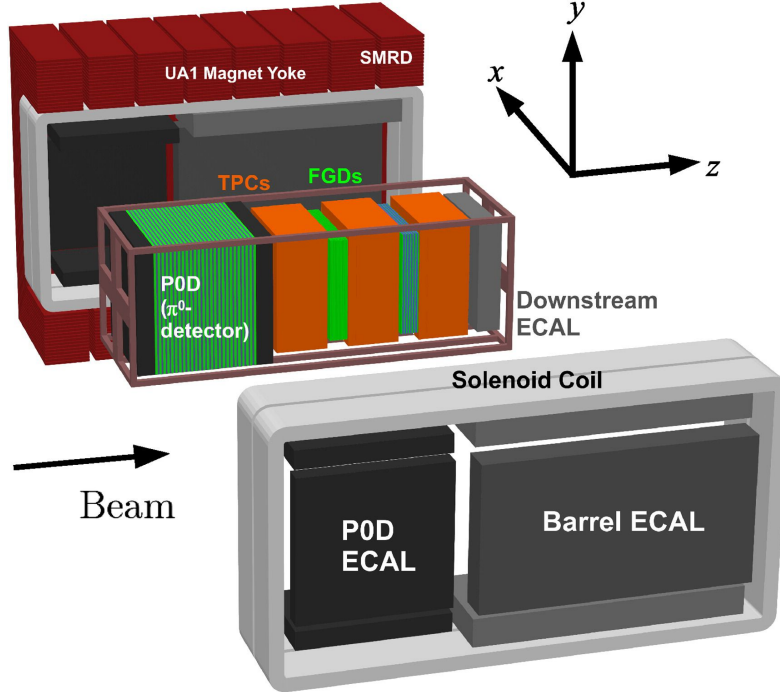


Figure 3.9: The components of the ND280 detector. The neutrino beam travels from left to right. Taken from [116].

831 encapsulates the tracker region alongside the π^0 detector (P0D). The ECAL
 832 measures the deposited energy from photons emitted from interactions within the
 833 FGD. The P0D constrains the cross-section of neutral current interactions which
 834 generate neutral pions, which is one of the largest backgrounds in the electron
 835 neutrino appearance oscillation channel. The P0D and ECAL detectors are
 836 detailed in subsubsection 3.2.2.3 and subsubsection 3.2.2.4 respectively. The entire
 837 detector is located within a large yoke magnet which produces a 0.2T magnetic
 838 field. This design of the magnet also includes a scintillating detector called the
 839 side muon range detector (SMRD) which is used to track high-angle muons as
 840 well as acting as a cosmic veto. The SMRD is described in subsubsection 3.2.2.5.

841 3.2.2.1 Fine Grained Detectors

842 The T2K tracker region is comprised of two fine grained detectors (FGD) and
 843 three Time Projection Chambers (TPC). A detailed description of the FGD design,
 844 construction, and assembly is found in [121] and summarised below. The FGDs
 845 are the primary target for neutrino interactions with a mass of 1.1 tonnes per FGD.

846 Alongside this, the FGDs are designed to be able to track short-range particles
847 which do not exit the FGD. Typically, short-range particles are low momentum
848 and are observed as tracks that deposit a large amount of energy per unit length.
849 This means the FGD needs good granularity to resolve these particles. The
850 FGDs have the best timing resolution ($\sim 3\text{ns}$) of any of the sub-detectors of the
851 ND280 detector. As such, the FGDs are used for time of flight measurements
852 to distinguish forward going positively charged particles from backward going
853 negatively charged particles. Finally, any tracks which pass through multiple
854 sub-detectors are required to be track matched to the FGD.

855 Both FGDs are made from square scintillator planes of side length 186cm and
856 width 2.02cm. Each plane consists of two layers of 192 scintillator bars in an
857 X or Y orientation. A wavelength shifting fiber is threaded through the centre
858 of each bar and is read out by a multi-pixel photon counter (MPPC). FGD1 is
859 the most upstream of the two FGDs and contains 15 planes of carbon plastic
860 scintillator which is a common target in external neutrino scattering data. As
861 the far detector is a pure water target, 7 of the 15 scintillator planes in FGD2
862 have been replaced with a hybrid water-scintillator target. Due to the complexity
863 of the nucleus, nuclear effects can not be extrapolated between different nuclei.
864 Therefore having the ability to take data on one target which is the same as
865 external data and another target which is the same as the far detector target is
866 beneficial for reliable model parameter estimates.

867 The integrated deposited energy is used for particle identification. The FGD
868 can distinguish protons from other charged particles by comparing the integrated
869 deposited energy from data to Monte Carlo prediction as seen in Figure 3.10.

870 3.2.2.2 Time Projection Chambers

871 The majority of particle identification and momentum measurements within
872 ND280 are provided by three Time Projection Chambers (TPCs) [122]. The
873 TPCs are located on either side of the FGDs. They are located inside of the

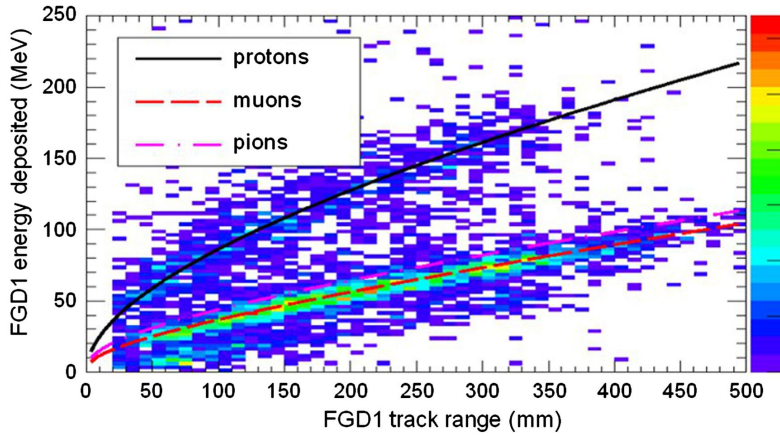


Figure 3.10: Comparison of data to Monte Carlo prediction of integrated deposited energy as a function of track length for particles that stopped in FGD1. Taken from [121].

874 magnetic field meaning the momentum of a charged particle can be determined
875 from the bending of the track.

876 Each TPC module consists of two gas-tight boxes, as shown in Figure 3.11,
877 which are made of non-magnetic material. The outer box is filled with CO₂ which
878 acts as an electrical insulator between the inner box and the ground. The inner box
879 forms the field cage which produces a uniform electric drift field of $\sim 275\text{V/cm}$
880 and is filled with an argon gas mixture. Charged particles moving through this
881 gas mixture ionize the gas and the ionised charge is drifted towards micromegas
882 detectors which measure the ionization charge. The time and position information
883 in the readout allows a three-dimensional image of the neutrino interaction.

884 The particle identification of tracks that pass through the TPCs is performed
885 using dE/dx measurements. Figure 3.12 illustrates the data to Monte Carlo
886 distributions of the energy lost by a charged particle passing through the TPC as
887 a function of the reconstructed particle momentum. The resolution is $7.8 \pm 0.2\%$
888 meaning that electrons and muons can be distinguished. This allows reliable
889 measurements of the intrinsic ν_e component of the beam.

890 3.2.2.3 π^0 Detector

891 If one of the γ -rays from a $\pi^0 \rightarrow 2\gamma$ decay is missed at the far detector, the
892 reconstruction will determine that event to be a charge current ν_e -like event.



Figure 3.11: Schematic design of a Time Projection Chamber detector. Taken from [122].

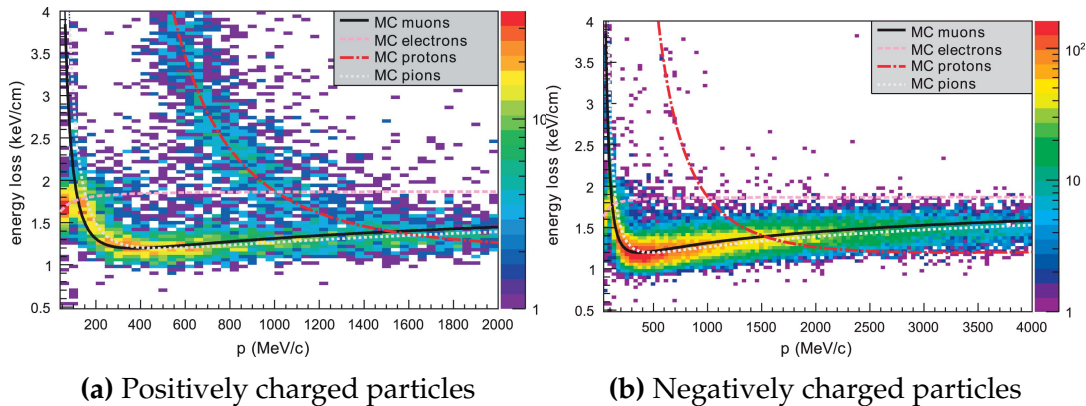


Figure 3.12: The distribution of energy loss as a function of reconstructed momentum for charged particles passing through the TPC, comparing data to Monte Carlo prediction. Taken from [122].

893 This is one of the main backgrounds hindering the electron neutrino appearance
 894 searches. The π^0 detector (P0D) measures the cross-section of the neutral current
 895 induced neutral pion production on a water target to constrain this background.

896 The P0D is a cube of approximately 2.5m length consisting of layers of scin-
 897 tillating bars, brass and lead sheets, and water bags as illustrated in Figure 3.13.
 898 Two electromagnetic calorimeters are positioned at the most upstream and most
 899 downstream position in the sub-detector and the water target is situated in
 900 between them. The scintillator layers are built from two triangular bars orientated
 901 in opposite directions to form a rectangular layer. Each triangular scintillator bar
 902 is threaded with optical fiber which is read out by MPPCs. The high-Z brass and

903 lead regions produce electron showers from the photons emitted in π^0 decay.

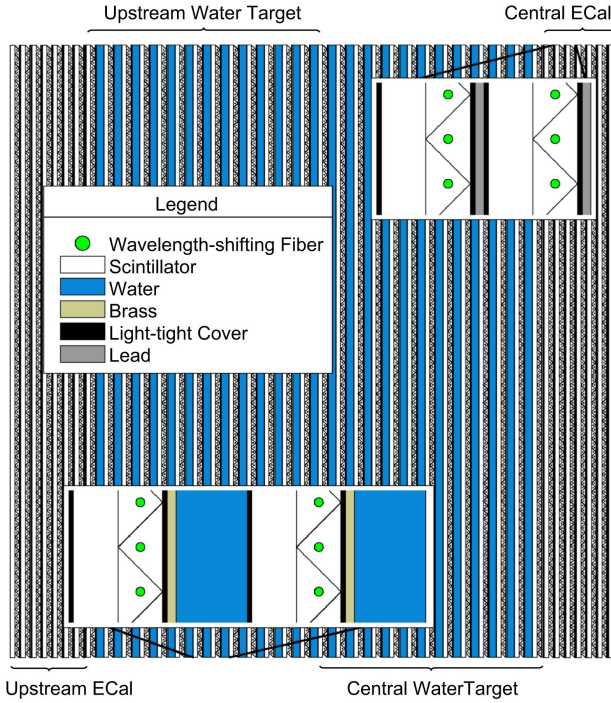


Figure 3.13: A schematic of the P0D side-view. Taken from [123].

904 The sub-detector can generate measurements of NC1 π^0 cross-sections on a
 905 water target by measuring the event rate both with and without the water target,
 906 with the cross-section on a water target being determined as the difference. The to-
 907 tal active mass is 16.1 tonnes when filled with water and 13.3 tonnes when empty.

908 3.2.2.4 Electromagnetic Calorimeter

909 The electromagnetic calorimeter [124] (ECal) encapsulates the P0D and tracking
 910 sub-detectors. Its primary purpose is to aid π^0 reconstruction from any interac-
 911 tion in the tracker. To do this, it measures the energy and direction of photon
 912 showers from $\pi^0 \rightarrow 2\gamma$ decay. It can also distinguish pion and muon tracks
 913 depending on the shape of the photon shower deposited.

914 The ECal is comprised of three sections; the P0D ECal which surrounds the
 915 P0D, the barrel ECal which encompasses the tracking region, and the downstream
 916 ECal which is situated downstream of the tracker region. The barrel and down-
 917 stream ECals are tracking calorimeters that focus on electromagnetic showers

from high-angle particles emitted from the tracking sub-detectors. Particularly in the TPC, high-angle tracks (those which travel perpendicularly to the beam-axis) can travel along a single scintillator bar resulting in very few hits. The width of the barrel and downstream ECal corresponds to ~ 11 electron radiation lengths to ensure a significant amount of the π^0 energy is contained. As the P0D has its own calorimetry which reconstructs showers, the P0D ECal determines the energy which escapes the P0D.

Each ECal is constructed of multiple layers of scintillating bars sandwiched between lead sheets. The scintillating bars are threaded with optical fiber and read out by MPPCs. Each sequential layer of the scintillator is orientated perpendicular to the previous which allows a three dimensional event reconstruction. The target mass of the P0D ECal, barrel ECal, and downstream ECal are 1.50, 4.80 and 6.62 tonnes respectively.

3.2.2.5 Side Muon Range Detector

As illustrated in Figure 3.9, the ECal, FGDs, P0D, and TPCs are enclosed within the UA1 magnet. Originally designed for the NOMAD [125] experiment and reconditioned for use in the T2K experiment [126], the UA1 magnet provides a uniform horizontal magnetic field of 0.2T with an uncertainty of 2×10^{-4} T.

Built into the UA1 magnet, the side muon range detector (SMRD)[127] monitors high-energy muons which leave the tracking region and permeate through the ECal. It additionally acts as a cosmic muon veto and trigger.

3.2.3 The Interactive Neutrino GRID

The Interactive Neutrino GRID (INGRID) detector is situated within the same “pit” as the other near detectors. It is aligned with the beam in the “on-axis” position and measures the beam direction, spread, and intensity. The detector was originally designed with 16 identical modules [116] (two modules have since been decommissioned) and a “proton” module. The design of the detector is cross-shaped with length and height 10m \times 10m as illustrated in Figure 3.14.

946 Each module is composed of iron sheets interlaced with eleven tracking
 947 scintillator planes for a total target mass of 7.1 tonnes per module. The scintillator
 948 design is an X-Y pattern of 24 bars in both orientations, where each bar contains
 949 wave-length shifting fibers which are connected to multi-pixel photon counters
 950 (MPPCs). Each module is encapsulated inside veto planes to aid the rejection
 951 of charged particles entering the module.

952 The proton module is different from the other modules in that it consists
 953 of entirely scintillator planes with no iron target. The scintillator bars are also
 954 smaller than those used in the other modules to increase the granularity of
 955 the detector and improve tracking capabilities. The module sits in the centre
 956 of the beamline and is designed to give precise measurements of quasi-elastic
 957 charged current interactions to evaluate the performance of the Monte Carlo
 958 simulation of the beamline.

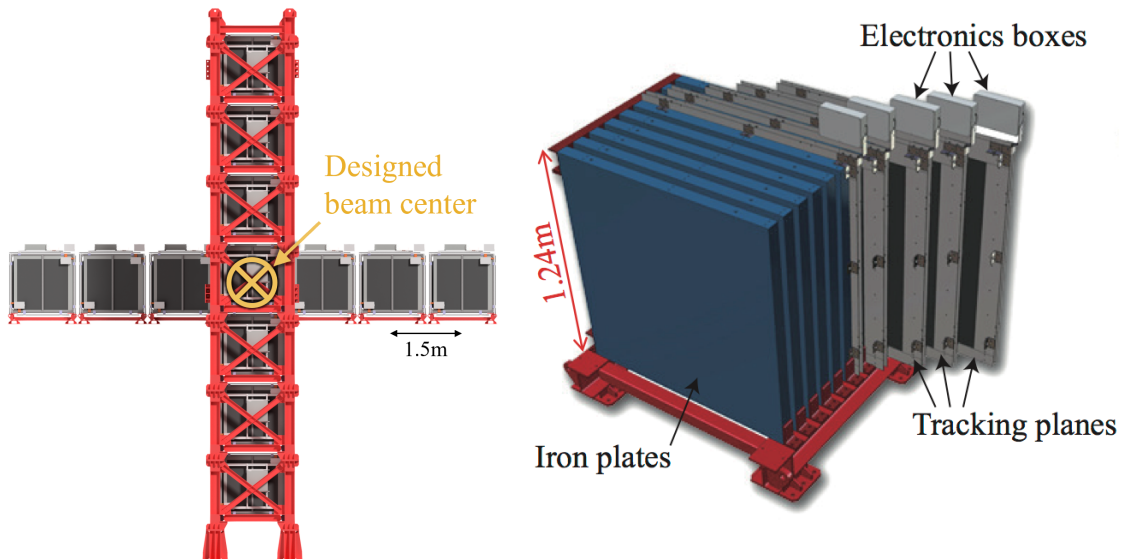


Figure 3.14: Left panel: The Interactive Neutrino GRID on-axis Detector. 14 modules are arranged in a cross-shape configuration, with the centre modules being directly aligned with the on-axis beam. Right panel: The layout of a single module of the INGRID detector. Both figures are recreated from [116].

959 The INGRID detector can measure the beam direction to an uncertainty of
 960 0.4mrad and the beam centre within a resolution of 10cm [116]. The beam
 961 direction in both the vertical and horizontal directions is discussed in [128]

⁹⁶² and it is found to be in good agreement with the MUMON monitor described
⁹⁶³ in subsection 3.2.1.

4

964

965

966

Bayesian Statistics and Markov Chain Monte Carlo Techniques

967 This thesis presents a Bayesian oscillation analysis. To extract the oscillation
968 parameters, a Markov Chain Monte Carlo (MCMC) method is used. This chapter
969 explains the theory of how parameter estimates can be determined using this
970 technique and condenses the material found in the literature [129–132].

971 The oscillation parameter determination presented within this thesis is built
972 upon a simultaneous fit to neutrino beam data in the near detector, beam data at
973 SK and atmospheric data at SK. In total, there are four oscillation parameters of in-
974 terest ($\sin^2(\theta_{23})$, $\sin^2(\theta_{13})$, Δm_{23}^2 , and δ_{CP}), two oscillation parameters to which
975 this study will not be sensitive ($\sin^2(\theta_{12})$, Δm_{12}^2) and many nuisance parameters
976 that control the systematic uncertainty models invoked within this study.

977 The MCMC technique generates a multi-dimensional probability distribution
978 across all of the model parameters used in the fit. To determine the parameter
979 estimate of a single parameter, this multi-dimensional object is integrated over all
980 other parameters. This process is called Marginalisation and is further described
981 in subsection 4.3.1. Monte Carlo techniques approximate the probability distribu-
982 tion of each parameter within the limit of generating infinite samples. As ever,
983 generating a large number of samples is time and resource-dependent. Therefore,

984 an MCMC technique is utilised within this analysis to reduce the required number
 985 of steps to sufficiently sample the parameter space. This technique is described
 986 in further detail in subsection 4.2.1.

987 **4.1 Bayesian Statistics**

988 Bayesian inference treats observable data, D , and model parameters, $\vec{\theta}$, on equal
 989 footing such that a probability model of both data and parameters is required.
 990 This is the joint probability distribution $P(D, \vec{\theta})$ and can be described by the
 991 prior distribution for model parameters $P(\vec{\theta})$ and the likelihood of the data given
 992 the model parameters $P(D|\vec{\theta})$,

$$P(D, \vec{\theta}) = P(D|\vec{\theta})P(\vec{\theta}). \quad (4.1)$$

993 The prior distribution, $P(\vec{\theta})$, describes all previous knowledge about the
 994 parameters within the model. For example, if the risk of developing health
 995 problems is known to increase with age, the prior distribution would describe the
 996 increase. For the purpose of this analysis, the prior distribution is typically
 997 the best-fit values taken from external data measurements with a Gaussian
 998 uncertainty. The prior distribution can also contain correlations between model
 999 parameters. In an analysis using Monte Carlo techniques, the likelihood of
 1000 measuring some data assuming some set of model parameters is calculated
 1001 by comparing the Monte Carlo prediction generated at that particular set of
 1002 model parameters to the data.

1003 It is parameter estimation that is important for this analysis and as such, we
 1004 apply Bayes' theorem [133] to calculate the probability for each parameter to have
 1005 a certain value given the observed data, $P(\vec{\theta}|D)$, which is known as the posterior
 1006 distribution (often termed the posterior). This can be expressed as

$$P(\vec{\theta}|D) = \frac{P(D|\vec{\theta})P(\vec{\theta})}{\int P(D|\vec{\theta})P(\vec{\theta})d\vec{\theta}}. \quad (4.2)$$

1007 The denominator in Equation 4.2 is the integral of the joint probability dis-
 1008 tribution over all values of all parameters used within the fit. For brevity, we
 1009 say that the posterior distribution is

$$P(\vec{\theta}|D) \propto P(D|\vec{\theta})P(\vec{\theta}). \quad (4.3)$$

1010 In subsection 4.3.1, we see that for the cases used within this analysis, it is
 1011 reasonable to know the posterior to some normalisation constant.

1012 4.1.1 Application of Prior Knowledge

1013 The posterior distribution is proportional to the prior uncertainty applied on
 1014 each parameter, as illustrated by Equation 4.3. This means that it is possible
 1015 to change the prior after the posterior distribution has been determined. The
 1016 prior uncertainty of a particular parameter can be ‘divided’ out of the posterior
 1017 distribution and the resulting distribution can be reweighted using the new
 1018 prior uncertainty that is to be applied. The methodology and implementation
 1019 of changing the prior follows that described in [134].

1020 An example implementation that is useful for this analysis is the application
 1021 of the “reactor constraint”. As discussed in section 2.4, an external constraint
 1022 on $\sin^2(\theta_{13})$ is determined from measurements taken from reactor experiments.
 1023 However, the sensitivities from just using the T2K and SK samples is equally
 1024 as important. Without this technique, two fits would have to be run, doubling
 1025 the required resources. Therefore, the key benefit for this analysis is the fact that
 1026 only a single ‘fit’ has to be performed and can be used to build the two posterior
 1027 distributions of the with and without reactor constraint applied.

1028 4.2 Monte Carlo Simulation

1029 Monte Carlo techniques are used to numerically solve a complex problem that
 1030 does not necessarily have an analytical solution. These techniques rely on

1031 building a large ensemble of samples from an unknown distribution and then
1032 using the ensemble to approximate the properties of the distribution.

1033 An example that uses Monte Carlo techniques is to calculate the area under-
1034 neath a curve. For example, take the problem of calculating the area under a
1035 straight line with gradient $M = 0.4$ and intercept $C = 1.0$. Analytically, one can
1036 calculate the area under the line is equal to 30 units for $0 \leq x \leq 10$. Using Monte
1037 Carlo techniques, one can calculate the area under this line by throwing many
1038 random values for the x and y components of each sample and then calculating
1039 whether that point falls below the line. The area can then be calculated by the
1040 ratio of points below the line to the total number of samples thrown multiplied by
1041 the total area in which samples were scattered. The study is shown in Figure 4.1
1042 highlights this technique and finds the area under the curve to be 29.9 compared
1043 to an analytical solution of 30.0. The deviation of the numerical to analytical
1044 solution can be attributed to the number of samples used in the study. The
1045 accuracy of the approximation in which the properties of the Monte Carlo samples
1046 replicate those of the desired distribution is dependent on the number of samples
1047 used. Replicating this study with a differing number of Monte Carlo samples
1048 used in each study (As shown in Figure 4.2) highlights how the Monte Carlo
1049 techniques are only accurate within the limit of a high number of samples.

1050 Whilst the above example has an analytical solution, these techniques are just
1051 as applicable to complex solutions. Clearly, any numerical solution is only as
1052 useful as its efficiency. As discussed, the accuracy of the Monte Carlo technique is
1053 dependent upon the number of samples generated to approximate the properties
1054 of the distribution. Furthermore, if the positions at which the samples are
1055 evaluated are not ‘cleverly’ picked, the efficiency of the Monte Carlo technique
1056 significantly drops. Given the example in Figure 4.1, if the region in which the
1057 samples are scattered significantly extends passed the region of interest, many
1058 calculations will be calculated but do not add to the ability of the Monte Carlo
1059 technique to achieve the correct result. For instance, any sample evaluated at
1060 a $y \geq 5$ could be removed without affecting the final result. This does bring in

- 1061 an aspect of the ‘chicken and egg’ problem in that to achieve efficient sampling,
1062 one needs to know the distribution beforehand.

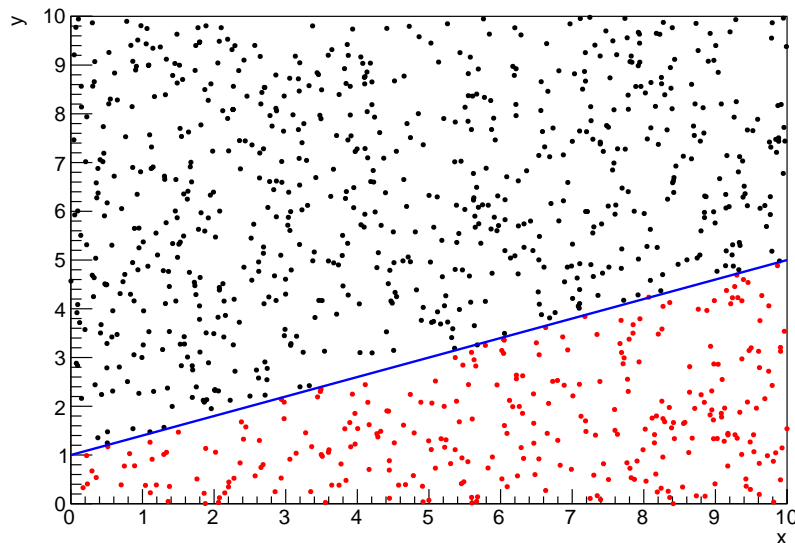


Figure 4.1: Example of using Monte Carlo techniques to find the area under the blue line. The gradient and intercept of the line are 0.4 and 1.0 respectively. The area found to be under the curve using one thousand samples is 29.9 units.

4.2.1 Markov Chain Monte Carlo

- 1063 **4.2.1 Markov Chain Monte Carlo**
- 1064 This analysis utilises a multi-dimensional probability distribution, with some
1065 dimensions being significantly more constrained than others. This could be
1066 from prior knowledge of parameter distributions from external data or un-
1067 physical regions in which parameters can not exist. Consequently, the Monte
1068 Carlo techniques used need to be as efficient as possible. For this analysis, the
1069 Markov Chain Monte Carlo (MCMC) technique is chosen. An MCMC technique
1070 is a Monte Carlo technique that uses a Markov chain to select which points at
1071 which to sample the parameter distribution. This technique performs a semi-
1072 random stochastic walk through the allowable parameter space. This builds a
1073 posterior distribution which has the property that the density of sampled points
1074 is proportional to the probability density of that parameter. This does mean that



Figure 4.2: The area under a line of gradient 0.4 and intercept 1.0 for the range $0 \leq x \leq 10$ as calculated using Monte Carlo techniques as a function of the number of samples used in each repetition. The analytical solution to the area is 30 units as given by the red line.

1075 the samples produced by this technique are not statistically independent but
 1076 they will cover the space of the distribution.

1077 A Markov chain functions by selecting the position of step \vec{x}_{i+1} based on the
 1078 position of \vec{x}_i . The space in which the Markov chain selects samples is dependent
 1079 upon the total number of parameters utilised within the fit, where a discrete point
 1080 in this space is described by the N-dimensional space \vec{x} . In a perfectly operating
 1081 Markov chain, the position of the next step depends solely on the previous step
 1082 and not on the further history of the chain (\vec{x}_0 , \vec{x}_1 , etc.). However, in solving
 1083 the multi-dimensionality of the fit used within this analysis, each step becomes
 1084 correlated with several of the steps preceding itself. This behaviour is further
 1085 explained in subsection 4.2.3. Providing the MCMC chain is well optimised, it will
 1086 begin to converge towards a unique stationary distribution. The period between
 1087 the chain's initial starting point and the convergence to the unique stationary
 1088 distribution is colloquially known as the burn-in period. This is discussed further
 1089 in subsection 4.2.3. Once the chain reaches the stationary distribution, all points
 1090 sampled after that point will look like samples from that distribution.

1091 Further details of the theories underpinning MCMC techniques are discussed
1092 in [130] but can be summarised by the requirement that the chain satisfies the
1093 three ‘regularity conditions’:

- 1094 • Irreducibility: From every position in the parameter space \vec{x} , there must
1095 exist a non-zero probability for every other position in the parameter space
1096 to be reached.
- 1097 • Recurrence: Once the chain arrives at the stationary distribution, every step
1098 following from that position must be samples from the same stationary
1099 distribution.
- 1100 • Aperiodicity: The chain must not repeat the same sequence of steps at any
1101 point throughout the sampling period.

1102 The output of the chain after burn-in (ie. the sampled points after the chain
1103 has reached the stationary distribution) can be used to approximate the posterior
1104 distribution and model parameters $\vec{\theta}$. To achieve the requirement that the unique
1105 stationary distribution found by the chain be the posterior distribution, one
1106 can use the Metropolis-Hastings algorithm. This guides the stochastic process
1107 depending on the likelihood of the current proposed step compared to that
1108 of the previous step. Implementation and other details of this technique are
1109 discussed in subsection 4.2.2.

1110 **4.2.2 Metropolis-Hastings Algorithm**

1111 As a requirement for MCMCs, the Markov chain implemented in this technique
1112 must have a unique stationary distribution that is equivalent to the posterior
1113 distribution. To ensure this requirement and that the regularity conditions are
1114 met, this analysis utilises the Metropolis-Hastings (MH) algorithm [135, 136].
1115 For the i^{th} step in the chain, the MH algorithm determines the position in the
1116 parameter space to which the chain moves to based on the current step, \vec{x}_i , and
1117 the proposed step, \vec{y}_{i+1} . The proposed step is randomly selected from some

1118 proposal function $f(\vec{x}_{i+1}|\vec{x}_i)$, which depends solely on the current step (ie. not
1119 the further history of the chain). The next step in the chain \vec{x}_{i+1} can be either the
1120 current step or the proposed step determined by whether the proposed step is
1121 accepted or rejected. To decide if the proposed step is selected, the acceptance
1122 probability, $\alpha(\vec{x}_i, \vec{y}_i)$, is calculated as

$$\alpha(\vec{x}_i, \vec{y}_{i+1}) = \min\left(1, \frac{P(\vec{y}_{i+1}|D)f(\vec{x}_i|\vec{y}_{i+1})}{P(\vec{x}_i|D)f(\vec{y}_{i+1}|\vec{x}_i)}\right). \quad (4.4)$$

1123 Where $P(\vec{y}_{i+1}|D)$ is the posterior distribution as introduced in section 4.1. To
1124 simplify this calculation, the proposal function is required to be symmetric such
1125 that $f(\vec{x}_i|\vec{y}_{i+1}) = f(\vec{y}_{i+1}|\vec{x}_i)$. In practice, a multi-variate Gaussian distribution is
1126 used to throw parameter proposals from. This reduces Equation 4.4 to

$$\alpha(\vec{x}_i, \vec{y}_{i+1}) = \min\left(1, \frac{P(\vec{y}_{i+1}|D)}{P(\vec{x}_i|D)}\right). \quad (4.5)$$

1127 After calculating this quantity, a random number, β , is generated uniformly
1128 between 0 and 1. If $\beta \leq \alpha(\vec{x}_i, \vec{y}_{i+1})$, the proposed step is accepted. Otherwise, the
1129 chain sets the next step equal to the current step and this procedure is repeated.
1130 This can be interpreted as if the posterior probability of the proposed step is
1131 greater than that of the current step, ($P(\vec{y}_{i+1}|D) \geq P(\vec{x}_i|D)$), the proposed
1132 step will always be accepted. If the opposite is true, ($P(\vec{y}_{i+1}|D) \leq P(\vec{x}_i|D)$),
1133 the proposed step will be accepted with probability $P(\vec{x}_i|D)/P(\vec{y}_{i+1}|D)$. This
1134 ensures that the Markov chain does not get trapped in any local minima in the
1135 potentially non-Gaussian posterior distribution. The outcome of this technique
1136 is that the density of steps taken in a discrete region is directly proportional to
1137 the probability density in that region.

1138 4.2.3 MCMC Optimisation

1139 As discussed in subsection 4.2.2, the proposal function invoked within the MH
1140 algorithm can take any form and the chain will still converge to the stationary
1141 distribution. At each set of proposed parameter values, a prediction of the same
1142 spectra has to be generated which requires significant computational resources.

1143 Therefore, the number of steps taken before the unique stationary distribution
1144 is found should be minimised as only steps after convergence add information
1145 to the oscillation analysis. Furthermore, the chain should entirely cover the
1146 allowable parameter space to ensure that all values have been considered. Tuning
1147 the distance that the proposal function jumps between steps on a parameter-by-
1148 parameter basis can both minimise the length of the burn-in period and ensure
1149 that the correlation between step \vec{x}_i and \vec{x}_j is sufficiently small.

1150 The effect of changing the width of the proposal function is highlighted in
1151 Figure 4.3. Three scenarios, each with the same underlying stationary distribution
1152 (A Gaussian of width 1.0 and mean 0.), are presented. The only difference between
1153 the three scenarios is the width of the proposal function, colloquially known as
1154 the ‘step size σ ’. Each scenario starts at an initial parameter value of 10.0 which
1155 would be considered an extreme variation. For the case where $\sigma = 0.1$, it is
1156 clear to see that the chain takes a long time to reach the expected region of the
1157 parameter. This indicates that this chain would have a large burn-in period and
1158 does not converge to the stationary distribution until step ~ 500 . Furthermore,
1159 whilst the chain does move towards the expected region, each step is significantly
1160 correlated with the previous. Considering the case where $\sigma = 5.0$, the chain
1161 approaches the expected parameter region almost instantly meaning that the
1162 burn-in period is not significant. However, there are clearly large regions of steps
1163 where the chain does not move. This is likely due to the chain proposing steps
1164 in the tails of the distribution which have a low probability of being accepted.
1165 Consequently, this chain would take a significant number of steps to fully span
1166 the allowable parameter region. For the final scenario, where $\sigma = 0.5$, you can
1167 see a relatively small burn-in period of approximately 100 steps. Once the chain
1168 reaches the stationary distribution, it moves throughout the expected region of
1169 parameter values many times, sufficiently sampling the full parameter region.
1170 This example is a single parameter varying across a continuous distribution and
1171 does not fully reflect the difficulties in the many-hundred multi-variate parameter

1172 distribution used within this analysis. However, it does give a conceptual idea of
1173 the importance of selecting the proposal function and associated step size.

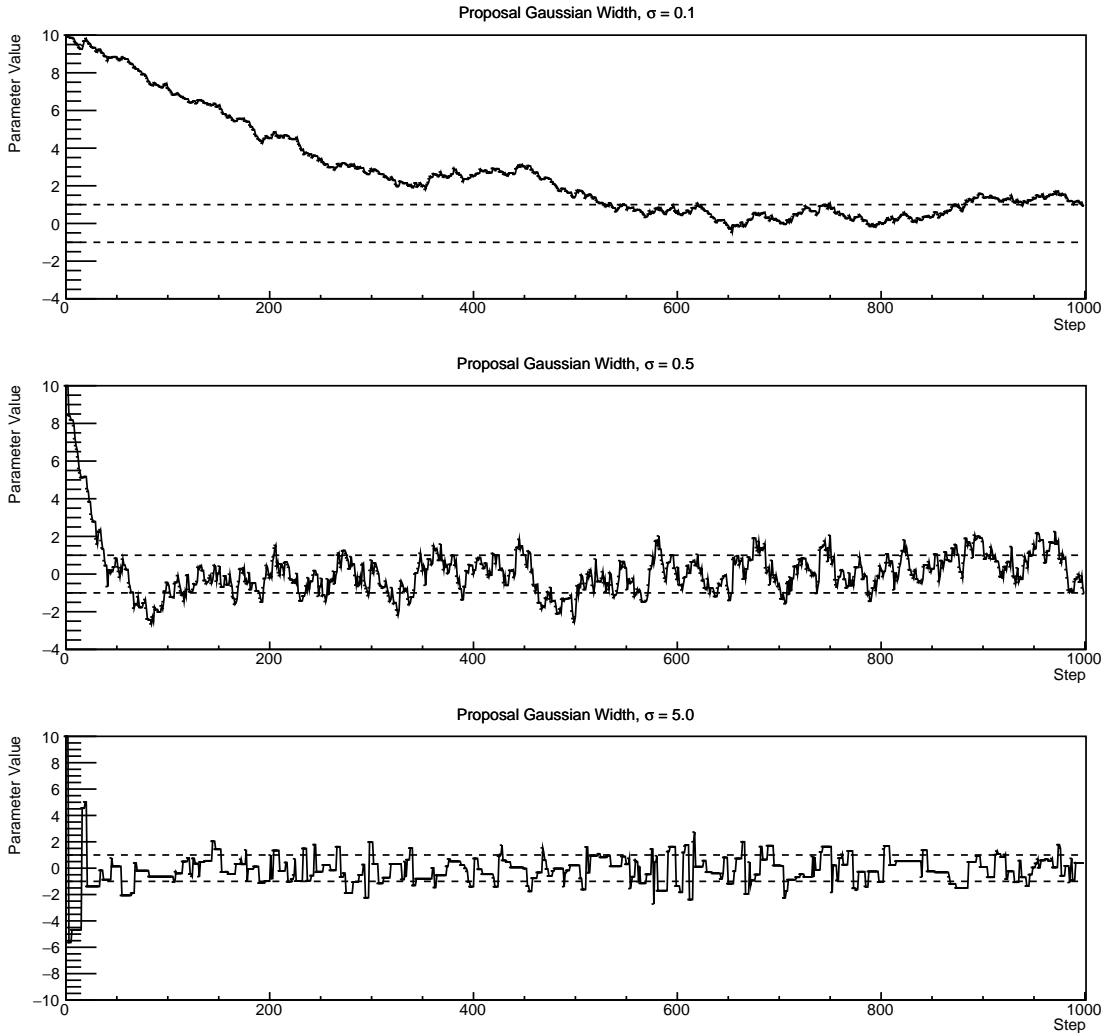


Figure 4.3: Three MCMC chains, each with a stationary distribution equal to a Gaussian centered at 0 and width 1 (As indicated by the black dotted lines). All of the chains use a Gaussian proposal function but have different widths (or ‘step size σ ’). The top panel has $\sigma = 0.1$, middle panel has $\sigma = 0.5$ and the bottom panel has $\sigma = 5.0$.

1174 As discussed, step size tuning directly correlates to the average step accep-
1175 tance rate. If the step size is too small, many steps will be accepted but the
1176 chain moves slowly. If the opposite is true, many steps will be rejected as the
1177 chain proposes steps in the tails of the distribution. Discussion in [137] suggests
1178 that the ‘ideal’ acceptance rate of a high dimension MCMC chain should be

¹¹⁷⁹ approximately $\sim 25\%$. An “ideal” step size [137] of

$$\sigma = \frac{2.4}{N_p}, \quad (4.6)$$

¹¹⁸⁰ where N_p is the number of parameters included in the MCMC fit. However,
¹¹⁸¹ the complex correlations between systematics mean that some parameters have
¹¹⁸² to be hand tuned and many efforts have been taken to select a set of parameter-
¹¹⁸³ by-parameter step sizes to approximately reach the ideal acceptance rate.

¹¹⁸⁴ Figure 4.3 highlights the likelihood as calculated by the fit in DB: [Link to](#)
¹¹⁸⁵ [AsimovA Sensitivity Section](#) as a function of the number of steps in each chain. In
¹¹⁸⁶ practice, many independent MCMC chains are run simultaneously to parallelise
¹¹⁸⁷ the task of performing the fit. This figure overlays the distribution found in each
¹¹⁸⁸ chain. As seen, the likelihood decreases from its initial value and converges
¹¹⁸⁹ towards a stationary distribution after $\sim 1 \times 10^5$ steps.

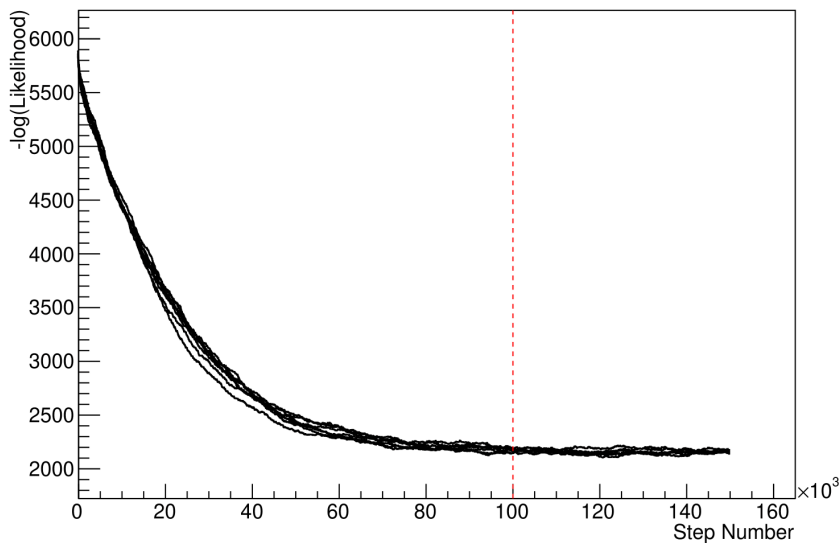


Figure 4.4: The log-likelihood from the fit detailed in DB: [Link to AsimovA Sensitivity Section](#) as a function of the number of steps accumulated in each fit. Many independent MCMC chains were run in parallel and overlaid on this plot. The red line indicates the 1×10^5 step burn-in period after which the log-likelihood becomes stable.

¹¹⁹⁰ Multiple configurations of this analysis have been performed throughout this
¹¹⁹¹ thesis where different samples or systematics have been used. For all of these con-
¹¹⁹² figurations, it was found that a burnin period of 1×10^5 was sufficient in all cases.

1193 4.3 Understanding the MCMC Results

1194 The previous sections have described how to generate the posterior probability
1195 distribution using Bayesian MCMC techniques. However, this analysis focuses
1196 on oscillation parameter determination. The posterior distribution output from
1197 the chain is a high dimension object, with as many dimensions as there are
1198 parameters included in the oscillation analysis. However, this multi-dimensional
1199 object is difficult to conceptualize so parameter estimations are often presented
1200 in one or two-dimensional projections of this probability distribution. To do this,
1201 we invoke the marginalisation technique highlighted in subsection 4.3.1.

1202 4.3.1 Marginalisation

1203 The output of the MCMC chain is a highly dimensional probability distribution
1204 which is very difficult to interpret. From the standpoint of an oscillation analysis
1205 experiment, the one or two-dimensional ‘projections’ of the oscillation parameters
1206 of interest are most relevant. Despite this, the best fit values and uncertainties on
1207 the oscillation parameters of interest should correctly encapsulate the correlations
1208 to the other systematic uncertainties (colloquially called ‘nuisance’ parameters).
1209 For this joint beam and atmospheric analysis, the oscillation parameters of interest
1210 are $\sin^2(\theta_{23})$, $\sin^2(\theta_{13})$, Δm_{23}^2 , and δ_{CP} . All other parameters (Including the
1211 oscillation parameter this fit is insensitive to) are deemed nuisance parameters.
1212 To generate these projections, we rely upon integrating the posterior distribution
1213 over all nuisance parameters. This is called marginalisation. A simple example
1214 of this technique is to imagine the scenario where two coins are flipped. To
1215 determine the probability that the first coin returned a ‘head’, the exact result of
1216 the second coin flip is disregarded and simply integrated over. For the parameters
1217 of interest, $\vec{\theta}_i$, we can calculate the marginalised posterior by integrating over
1218 the nuisance parameters, $\vec{\theta}_n$. In this case, Equation 4.2 becomes

$$P(\vec{\theta}_i|D) = \frac{\int P(D|\vec{\theta}_i, \vec{\theta}_n)P(\vec{\theta}_i, \vec{\theta}_n)d\vec{\theta}_n}{\int P(D|\vec{\theta})P(\vec{\theta})d\vec{\theta}} \quad (4.7)$$

1219 Where $P(\vec{\theta}_i, \vec{\theta}_n)$ encodes the prior knowledge about the uncertainty and
 1220 correlations between the parameters of interest and the nuisance parameters.
 1221 In practice, this is simply taking the one or two-dimensional projection of the
 1222 multi-dimensional probability distribution.

1223 Whilst in principle an easy solution to a complex problem, correlations
 1224 between the interesting and nuisance parameters can bias the marginalised
 1225 results. A similar effect is found when the parameters being marginalised over
 1226 have non-Gaussian probability distributions. For example, Figure 4.5 highlights
 1227 the marginalisation bias in the probability distribution found for a parameter
 1228 when requiring a correlated parameter to have a positive parameter value. Due
 1229 to the complex nature of this oscillation parameter fit presented in this thesis,
 1230 there are correlations occurring between the oscillation parameters of interest
 1231 and the other nuisance parameters included in the fit.

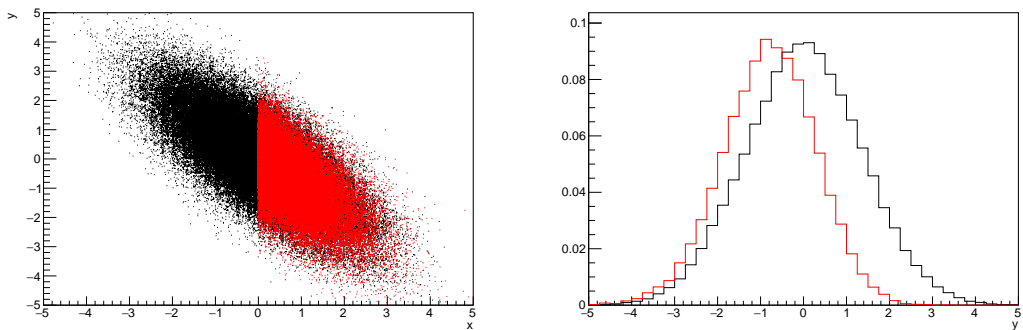


Figure 4.5: Left: The two dimensional probability distribution for two correlated parameters x and y . The red distribution shows the two dimensional probability distribution when $0 \leq x \leq 5$. Right: The marginalised probability distribution for the y parameter found when requiring the x to be bound between $-5 \leq x \leq 5$ and $0 \leq x \leq 5$ for the black and red distribution, respectively.

1232 4.3.2 Parameter Estimation and Credible Intervals

1233 The purpose of this analysis is to determine the best fit values for the oscillation
 1234 parameters that the beam and atmospheric samples are sensitive to: $\sin^2(\theta_{23})$
 1235 , $\sin^2(\theta_{13})$, Δm_{23}^2 , and δ_{CP} . Typically, the results presented take the form of
 1236 one or two-dimension marginalised probability distributions for the appearance

1237 ($\sin^2(\theta_{13})$ and δ_{CP}) and disappearance ($\sin^2(\theta_{23})$ and Δm_{23}^2) parameters. The
1238 posterior probability density taken from the output MCMC chain is binned in
1239 these parameters. The parameter best-fit point is then taken to be the value
1240 that has the highest posterior probability. This is performed in both one and
1241 two-dimensional projections.

1242 However, the single best-fit point in a given parameter is not of much use on
1243 its own. We would also like to determine the uncertainty, or credible interval,
1244 on that best-fit point. The definition of the 1σ credible interval is that we have
1245 68% belief that the parameter is within those bounds. For a more generalised
1246 definition, the credible interval is the region, R , of the posterior distribution that
1247 contains a specific fraction of the total probability, such that

$$\int_R P(\theta|D) d\theta = \alpha \quad (4.8)$$

1248 Where θ is the parameter on which we calculate the credible interval. This
1249 technique then calculates the $\alpha \times 100\%$ credible interval.

1250 In practice, this analysis uses the highest posterior density (HPD) credible in-
1251 tervals which are calculated through the following method. First, the probability
1252 distribution is area-normalised such that it has an integrated area equal to 1.0.
1253 The bins of probability are then summed from the highest to lowest until the sum
1254 exceeds the 1σ level (0.68 in this example). This process is repeated for a range of
1255 credible intervals, notably the 1σ , 2σ and 3σ along with other levels where the
1256 critical values for each level can be found in [77]. This process can be repeated
1257 for the two-dimensional probability distributions by creating two-dimensional
1258 contours of credible intervals rather than a one-dimensional result.

1259 4.3.3 Bayesian Model Comparisons

1260 Due to the matter resonance, this analysis has some sensitivity to the mass
1261 hierarchy of neutrino states (whether Δm_{23}^2 is positive or negative) and the
1262 octant of $\sin^2(\theta_{23})$. The Bayesian approach utilised within this analysis gives an
1263 intuitive method of model comparison by determining which hypothesis is most

₁₂₆₄ favourable. Taking the ratio of Equation 4.3 for the two hypotheses of normal
₁₂₆₅ hierarchy, NH , and inverted hierarchy, IH , gives

$$\frac{P(\vec{\theta}_{NH}|D)}{P(\vec{\theta}_{IH}|D)} = \frac{P(D|\vec{\theta}_{NH})}{P(D|\vec{\theta}_{IH})} \times \frac{P(\vec{\theta}_{NH})}{P(\vec{\theta}_{IH})}. \quad (4.9)$$

₁₂₆₆ The middle term defines the Bayes factor which is a data-driven interpretation
₁₂₆₇ of how strong the data prefers one hierarchy to the other. For this analysis, equal
₁₂₆₈ priors on both mass hierarchy hypotheses are chosen ($P(\vec{\theta}_{NH}) = P(\vec{\theta}_{IH}) = 0.5$).
₁₂₆₉ In practice, the MCMC chain proposes a value of $|\Delta m_{23}^2|$ and then applies a
₁₂₇₀ 50% probability that the value is sign flipped. Consequently, the Bayes factor
₁₂₇₁ can be calculated from the ratio of the probability density in either hypothesis.
₁₂₇₂ This equates to counting the number of steps taken in the normal and inverted
₁₂₇₃ hierarchies and taking the ratio. The same approach can be taken to compare the
₁₂₇₄ upper octant (UO) compared to the lower octant (LO) hypothesis of $\sin^2(\theta_{23})$.

₁₂₇₅ Whilst the value of the Bayes factor should always be shown, the Jeffreys scale
₁₂₇₆ [138] (highlighted in Table 4.1) gives an indication of the strength of preference
₁₂₇₇ for one model compared to the other. Other interpretations of the strength of
₁₂₇₈ preference of a model exist, e.g. the Kass and Raferty Scale [139].

$\log_{10}(B_{AB})$	B_{AB}	Strength of Preference
< 0.0	< 1	No preference for hypothesis A (Supports hypothesis B)
0.0 – 0.5	1.0 – 3.16	Preference for hypothesis A is weak
0.5 – 1.0	3.16 – 10.0	Preference for hypothesis A is substantial
1.0 – 1.5	10.0 – 31.6	Preference for hypothesis A is strong
1.5 – 2.0	31.6 – 100.0	Preference for hypothesis A is very strong
> 2.0	> 100.0	Decisive preference for hypothesis A

Table 4.1: Jeffreys scale for strength of preference for two models A and B as a function of the calculated Bayes factor ($B_{AB} = B(A/B)$) between the two models [138]. The original scale is given in terms of $\log_{10}(B(A/B))$ but converted to linear scale for easy comparison throughout this thesis.

₁₂₇₉ 4.3.4 Comparison of MCMC Output to Expectation

₁₂₈₀ To ensure the fit is performing well, a best-fit spectrum is produced using the
₁₂₈₁ posterior probability distribution and compared with the data, allowing easy

1282 by-eye comparisons to be made. A simple method of doing this is to perform a
1283 comparison in the fitting parameters (For instance, the reconstructed neutrino
1284 energy and lepton direction for T2K far detector beam samples) of the spectra
1285 generated by the MCMC chain to ‘data’. This ‘data’ could be true data or some
1286 variation of Monte Carlo prediction. This allows easy comparison of the MCMC
1287 probability distribution to the data. To perform this, N steps from the post burn-in
1288 MCMC chain are randomly selected (Where for all plots of this style in this thesis,
1289 $N = 3000$). From these, the Monte Carlo prediction at each step is generated by
1290 reweighting the model parameters to the values specified at that step. Due to the
1291 probability density being directly correlated with the density of steps in a certain
1292 region, parameter values close to the best fit value are most likely to be selected.

1293 In practice, for each bin of the fitting parameters has a probability distribution
1294 of event rates, with one entry per sampled MCMC step. This distribution is
1295 binned where the bin with the highest probability is selected as the mean and an
1296 error on the width of this probability distribution is calculated using the approach
1297 highlighted in subsection 4.3.2. Consequently, the best fit distribution in the fit
1298 parameter is not necessarily that which would be attained by reweighting the
1299 Monte Carlo prediction to the most probable parameter values.

1300 A similar study can be performed to illustrate the freedom of the model
1301 parameter space prior to the fit. This can be done by throwing parameter values
1302 from the prior uncertainty of each parameter. This becomes troublesome for
1303 parameters with no prior uncertainty as the range is technically infinite. Where
1304 applicable solutions to remove these have been addressed.

5

1305

1306

1307

Simulation, Reconstruction, and Event Reduction

1308 As a crucial part of the oscillation analysis, an accurate prediction of the expected
1309 neutrino spectrum at the far detector is required. This includes modeling the
1310 flux generation, neutrino interactions, and detector effects. All of the simulation
1311 packages required to do this are briefly described in section 5.1. The reconstruc-
1312 tion of neutrino events inside the far detector, including the `fitQun` algorithm,
1313 is documented in section 5.2. This also includes data quality checks of the SK-
1314 V data which the author performed for the T2K oscillation analysis presented
1315 at Neutrino 2020 [76]. Finally, section 5.3 describes the steps taken in the SK
1316 detector to trigger on events of interest whilst removing the comparatively large
1317 rate of cosmic ray muon events.

1318 5.1 Simulation

1319 In order to generate a Monte Carlo prediction of the expected event rate at the far
1320 detector, all the processes in the beam and atmospheric flux, neutrino interaction,
1321 and detector need to be modeled. Each of these parts is individually modeled
1322 and each of them is detailed below.

1323 The beamline simulation consists of three distinct parts: the initial hadron
1324 interaction modeled by FLUKA [140], the target station geometry and particle
1325 tracking performed by JNUBEAM, [141, 142] and any hadronic re-interactions
1326 simulated by GCALOR [143]. The primary hadronic interactions are $O(10)\text{GeV}$,
1327 where FLUKA matches external cross-section data better than GCALOR [144].
1328 However, FLUKA is not very adaptable so a small simulation is built to model
1329 the interactions in the target and the output is then passed to JNUBEAM and
1330 GCALOR for propagation. The hadronic interactions are tuned to data from the
1331 NA61/SHINE [145–147] and HARP [148] experiments. The tuning is done by
1332 reweighting the FLUKA and GCALOR predictions to match the external data
1333 multiplicity and cross-section measurements, based on final state particle kine-
1334 matics [144]. The culmination of this simulation package generates the predicted
1335 flux for neutrino and antineutrino beam modes which are illustrated in Figure 3.7.

1336 The atmospheric neutrino flux is simulated by the HKKM model [52, 54]. The
1337 primary cosmic ray flux is tuned to AMS [149] and BESS [150] data assuming
1338 the US-standard atmosphere '76 [151] density profile and includes geomagnetic
1339 field effects. The primary cosmic rays interact to generate pions and muons.
1340 The interaction of these secondary particles to generate neutrinos is handled by
1341 DPMJET-III [152] for energies above 32GeV and JAM [54, 153] for energies below
1342 that value **DB: Question for Giles: Why different generators for above/below**
1343 **32GeV?**. These hadronic interactions are tuned to BESS and L3 data [154, 155]
1344 using the same methodology as the tuning of the beamline simulation. The
1345 energy and cosine zenith predictions of $\nu_e, \bar{\nu}_e, \nu_\mu, \bar{\nu}_\mu$ flux are given in Figure 2.3
1346 and Figure 2.5, respectively. The flux is approximately symmetrical and peaked
1347 around the horizon ($\cos(\theta_Z) = 0.0$). This is because horizontally-going pions
1348 and kaons can travel further than their vertically-going counterparts resulting
1349 in a larger probability of decaying to neutrinos. The symmetry is broken in
1350 lower-energy neutrinos due to geomagnetic effects, which modify the track of the
1351 primary cosmic rays. Updates to the HKKM model are currently ongoing [156].

Once a flux prediction has been made for all three detectors, NEUT 5.4.0 [157, 158] models the interactions of the neutrinos in the detectors. For the purposes of this analysis, quasi-elastic (QE), meson exchange (MEC), single meson production (PROD), coherent pion production (COH), and deep inelastic scattering (DIS) interactions are simulated. These interaction categories can be further broken down by whether they were propagated via a W^\pm boson in Charged Current (CC) interactions or via a Z^0 boson in Neutral Current (NC) interactions. CC interactions have a charged lepton in the final state, which can be flavour-tagged in reconstruction to determine the flavour of the neutrino. In contrast, NC interactions have a neutrino in the final state so no flavour information can be determined from the observables left in the detector after an interaction. This is the reason why neutrinos which interact through NC modes are assumed to not oscillate within this analysis. Both CC and NC interactions are modeled for all the above interaction categories, other than MEC interactions which are only modeled for CC events.

As illustrated in Figure 5.1, CCQE interactions dominate the cross-section of neutrino interactions around $E_\nu \sim 0.5\text{GeV}$. The NEUT implementation adopts the Llewellyn Smith [159] model for neutrino-nucleus interactions, where the nuclear ground state of any bound nucleons (neutrino-oxygen interactions) is approximated by a spectral-function [160] model that simulates the effects of Fermi momentum and Pauli blocking. The cross-section of QE interactions is controlled by vector and axial-vector form factors parameterised by the BBBA05 [161] model and a dipole form factor with $M_A^{QE} = 1.21\text{GeV}$ fit to external data [162], respectively. NEUT implements the Valencia [163] model to simulate MEC events, where two nucleons and two holes in the nuclear target are produced (Often called 2p2h interactions).

For neutrinos of energy $O(1)\text{GeV}$, PROD interactions become dominant. These predominantly produce charged and neutral pions although γ , kaon, and η production is also considered. To simulate these interactions, the Berger-Sehgal [164] model is implemented within NEUT. It simulates the excitation of a



Figure 5.1: The NEUT prediction of the ν_μ -H₂O cross-section overlaid on the T2K ν_μ flux. The charged current (black, solid) and neutral current (black, dashed) inclusive, charged current quasi-elastic (blue, solid), charged current 2p2h (blue, dashed), charged current single pion production (pink), and charged current multi- π and DIS (Purple) cross-sections are illustrated. Figure taken from [157].

nucleon from a neutrino interaction, production of an intermediate baryon, and the subsequent decay to a single meson or γ . Pions can also be produced through COH interactions, which occur when the incoming neutrino interacts with the entire oxygen nucleus leaving a single pion outside of the nucleus. NEUT utilises the Berger-Sehgal [165] model to simulate these COH interactions.

DIS and multi- π producing interactions become the most dominant for energies $> O(5)\text{GeV}$. PYTHIA [166] is used to simulate any interaction with invariant mass $W > 2\text{GeV}/c^2$, which produces at least one meson. For any interaction which produces at least two mesons but has $W < 2\text{GeV}/c^2$, the Bronner model is used [167]. Both of these models use parton distribution functions based on the Bodek-Yang model [168–170].

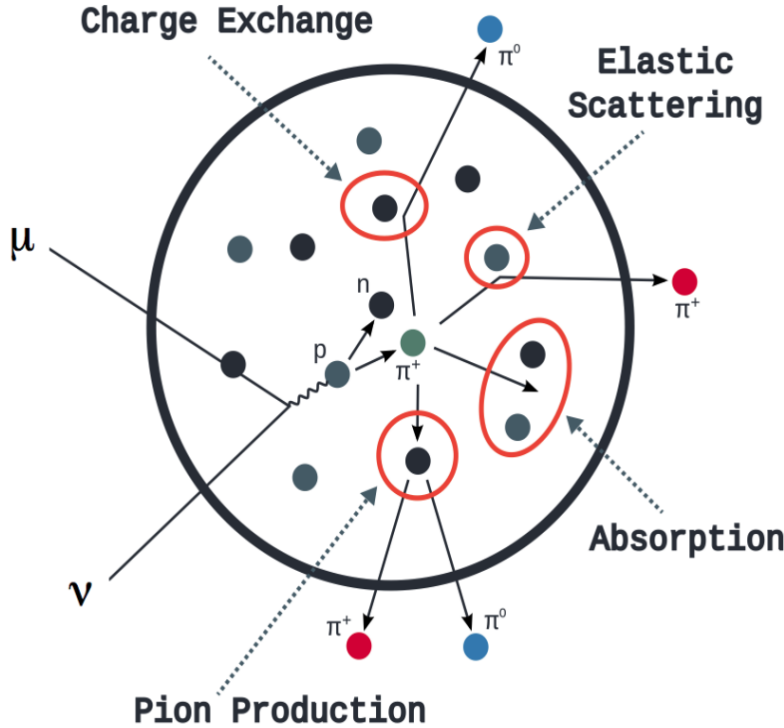


Figure 5.2: Illustration of the various processes which a pion can undergo before exiting the nucleus. Taken from [171].

1393 Any pion which is produced within the nucleus can re-interact through
 1394 final state interactions before it exits, as illustrated by the scattering, absorption,
 1395 production, and exchange interactions in Figure 5.2. These re-interactions alter
 1396 the observable particles within the detector. For instance, if the charged pion
 1397 from a CC PROD interaction is absorbed, the observables would mimic a CC QE
 1398 interaction. To simulate these effects, NEUT uses a semi-classical intranuclear
 1399 cascade model [157]. This cascade functions by stepping the pion through the
 1400 nucleus in fixed-length steps equivalent to $dx = R_N/100$, where R_N is the radius
 1401 of the nucleus. At each step, the simulation allows the pion to interact through
 1402 scattering, charged exchange, absorption, or production with an interaction-
 1403 dependent probability calculated from a fit to external data [172]. This cascade
 1404 continues until the pion is absorbed or exits the nucleus.

1405 Once the final state particle kinematics have been determined by NEUT,
 1406 they are passed into the detector simulation. The near detectors, ND280 and

1407 INGRID, are simulated using a GEANT4 package [116, 173] to simulate the detector
1408 geometry, particle tracking, and energy deposition. The response of the detectors
1409 is simulated using the elecSim package [116]. The far detector simulation is based
1410 upon the original Kamiokande experiment software which uses the GEANT3-based
1411 SKDETSIM [116, 174] package. This simulates the interactions of particles in
1412 the water as well as Cherenkov light production. The water quality and PMT
1413 calibration measurements detailed in subsection 3.1.2 are also used within this
1414 simulation to make accurate predictions of the detector response.

1415 5.2 Event Reconstruction at SK

1416 Any event which generates optical photons that occurs in SK will be observed by
1417 the PMT array, where each PMT records the time and accumulated charge. This
1418 recorded information is shown in event displays similar to those illustrated in
1419 Figure 5.3. To be useful for physics analyses, this series of PMT hit information
1420 needs to be reconstructed to determine the particle’s identity and kinematics (or
1421 track parameters): four-vertex, direction, and momenta. The reconstruction
1422 uses the fact that the charge and timing distribution of photons generated
1423 by a particular particle in an event is dependent upon its initial kinematics.
1424 Electron and muon rings are distinguished by their “fuzziness”. Muons are
1425 heavier and less affected by scattering or showering meaning they typically
1426 produce “crisp” rings. Electrons are more likely to interact via electromagnetic
1427 showering or scattering which results in larger variations of their direction from
1428 the initial direction. Consequently, electrons typically produce “fuzzier” rings
1429 compared to muons.

1430 For the purposes of this analysis, the `fiTQun` reconstruction algorithm is
1431 utilised. Its core function is to compare a prediction of the accumulated charged
1432 and timing distribution from each PMT, generated for a particular particle identity
1433 and track parameters, to that observed in the neutrino event. It determines the
1434 preferred values by minimising a likelihood function which includes information
1435 from PMTs which were hit and those that were not hit. `fiTQun` performs a

1436 simultaneous fit of particle kinematics and identity, improving both the accuracy
 1437 of the fit parameters and the rejection of neutral current π^0 events [175, 176]. The
 1438 `fitQun` algorithm is based on the key concepts of the MiniBooNE reconstruction
 1439 algorithm [177] and is described in [178] which is summarised below. The
 1440 `fitQun` algorithm improves upon the `APFit` reconstruction algorithm which has
 1441 been used for many previous SK analyses. `APFit` fits the vertex from timing
 1442 information and then fits the momentum and direction of the particle from PMT
 1443 hits within a 43 deg Cherenkov cone (which assumes an ultra-relativistic particle).
 1444 It then fits the particle identity once the track parameters have been fit.

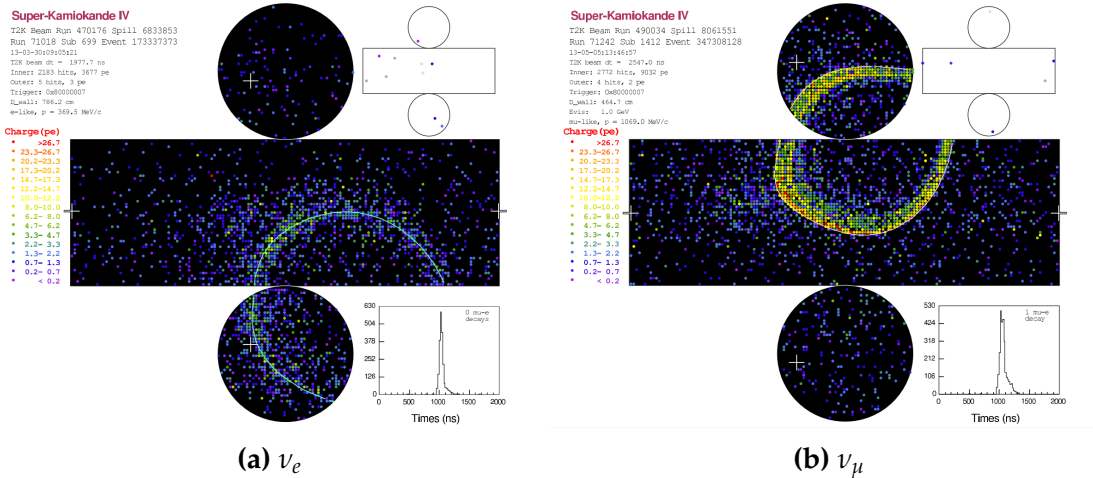


Figure 5.3: Event displays from Super Kamiokande illustrating the “crisp” ring from a muon and the typically “fuzzy” electron ring. Each pixel represents a PMT and the color scheme denotes the accumulated charge deposited on that PMT. Figures taken from [179].

1445 The `fitQun` reconstruction algorithm proceeds by:

- 1446 • **Vertex pre-fitting:** An estimate of the vertex is made using a goodness-of-fit
 1447 metric
- 1448 • **Peak finding:** The initial time of the event is determined by clustering
 1449 events by time residuals
- 1450 • **Single-ring fits:** Given the pre-fit vertex and estimated time of interaction,
 1451 a maximum likelihood technique searches for a single particle generating
 1452 light

- 1453 • **Multi-ring fits:** Seeded from the single-ring fits, hypotheses with multiple
 1454 light-producing particles are considered using the same maximum likeli-
 1455 hood technique

1456 An event in SK can consist of a primary and decay particles. For example,
 1457 a charged current muon neutrino interaction can generate two particles that
 1458 have the potential of generating Cherenkov photons: the primary muon, and
 1459 the secondary decay-electron from the muon. To ensure the particles are recon-
 1460 structed separately, each event is divided into time clusters which are called
 1461 “subevents”. Subevents after the primary subevent are considered to be decay
 1462 electrons. To find all the subevents in an event, a vertex goodness metric is
 1463 calculated for some vertex position \vec{x} and time t ,

$$G(\vec{x}, t) = \sum_i^{\text{hit PMTs}} \exp \left(-\frac{1}{2} \left(\frac{T_{Res}^i(\vec{x}, t)}{\sigma} \right)^2 \right) \quad (5.1)$$

1464 where

$$T_{Res}^i(\vec{x}, t) = t^i - t - |R_{PMT}^i - \vec{x}| / c_n \quad (5.2)$$

1465 is the residual hit time. It is the difference in time between the PMT hit time,
 1466 t^i , of the i^{th} PMT and the expected time of the PMT hit if the photon was emitted
 1467 at the start of the vertex. R_{PMT}^i is the position of the i^{th} PMT, c_n is the speed of
 1468 light in water and $\sigma = 4\text{ns}$ which is comparable to the time resolution of the
 1469 PMT. When the proposed fit values of time and vertex are close to the true values,
 1470 $T_{Res}^i(\vec{x}, t)$ tends to zero resulting in subevents appearing as spikes in the goodness
 1471 metric. The proposed fit vertex and time are grid-scanned, and the values which
 1472 maximise the goodness metric are selected as the “pre-fit vertex”. Whilst this
 1473 predicts a vertex for use in the clustering algorithm, the final vertex is fit using
 1474 the higher-precision maximum likelihood method described below.

1475 Once the pre-fit vertex has been determined, the goodness metric is scanned as
 1476 a function of t to determine the number of subevents. A peak-finding algorithm
 1477 is then used on the goodness metric, requiring the goodness metric to exceed

some threshold and drop below a reduced threshold before any subsequent additional peaks are considered. The thresholds are set such that the rate of false peak finding is minimised while still attaining good data to Monte Carlo agreement. To improve performance, the pre-fit vertex for each delayed subevent is re-calculated after PMT hits from the previous subevent are masked. This improves the decay-electron tagging performance. Once all subevents have been determined, the time window around each subevent is then defined by the earliest and latest time which satisfies $-180 < T_{Res}^i < 800\text{ns}$. The subevents and associated time windows are then used as seeds for further reconstruction.

For a given subevent, the `fitQun` algorithm constructs a likelihood based on the accumulated charge q_i and time information t_i from the i^{th} PMT,

$$L(\Gamma, \vec{\theta}) = \prod_j^{\text{unhit}} P_j(\text{unhit}|\Gamma, \vec{\theta}) \prod_i^{\text{hit}} \{1 - P_i(\text{unhit}|\Gamma, \vec{\theta})\} f_q(q_i|\Gamma, \vec{\theta}) f_t(t_i|\Gamma, \vec{\theta}), \quad (5.3)$$

where $\vec{\theta}$ defines the track parameters; vertex position, direction vector and momenta, and Γ represents the particle hypothesis. $P_i(\text{unhit}|\Gamma, \vec{\theta})$ is the probability of the i^{th} tube to not register a hit given the track parameters and particle hypothesis. The charge likelihood, $f_q(q_i|\Gamma, \vec{\theta})$, and time likelihood, $f_t(t_i|\Gamma, \vec{\theta})$, represents the probability density function of observing charge q_i and time t_i on the i^{th} PMT given the specified track parameters and particle hypothesis.

The predicted charge is calculated based on contributions from both the direct light and the scattered light. The direct light contribution is determined based on the integration of the Cherenkov photon profile along the track. PMT angular acceptance, water quality, and calibration measurements discussed in subsection 3.1.2 are included to accurately predict the charge probability density at each PMT. The scattered light is calculated in a similar way, although it includes a scattering function that depends on the vertex of the particle and the position of the PMT. The charge likelihood is calculated by comparing the prediction to the observed charge in the PMT.

1504 The time likelihood is approximated to depend on the vertex \vec{x} , direction \vec{d} ,
 1505 and time t of the track as well as the particle hypothesis. The expected time
 1506 for PMT hits is calculated by assuming unscattered photons being emitted from
 1507 the midpoint of the track, S_{mid} ,

$$t_{exp}^i = t + S_{mid}/c + |R_{PMT}^i - \vec{x} - S_{mid}\vec{d}|/c_n, \quad (5.4)$$

1508 where c is the speed of light in a vacuum. The time likelihood is then expressed
 1509 in terms of the residual difference between the PMT hit time and the expected
 1510 hit time, $t_{Res}^i = t^i - t_{exp}^i$. The particle hypothesis and momentum also affect the
 1511 Cherenkov photon distribution. These parameters modify the shape of the time
 1512 likelihood density since in reality not all photons are emitted at the midpoint of
 1513 the track. As with the charge likelihood, the contributions from both the direct
 1514 and scattered light to the time likelihood density are calculated separately, which
 1515 are both calculated from particle gun studies.

1516 The track parameters and particle identity which maximise $L(\Gamma, \vec{\theta})$ are defined
 1517 as the best-fit parameters. In practice MINUIT [180] is used to minimise the value
 1518 of $-\ln L(\Gamma, \vec{\theta})$. The `fiTQun` algorithm considers an electron-like, muon-like, and
 1519 charged pion-like hypothesis for events with a single final state particle, denoted
 1520 “single-ring events”. The particle’s identity is determined by taking the ratio of
 1521 the likelihood of each of the hypotheses. For instance, electrons and muons are
 1522 distinguished by considering the value of $\ln(L(e, \vec{\theta}_e)/L(\mu, \vec{\theta}_\mu))$ in comparison
 1523 to the reconstructed momentum of the electron hypothesis, as illustrated by
 1524 Figure 5.4. The coefficients of the discriminator between electron-like and muon-
 1525 like events are determined from Monte Carlo studies [178]. Similar distributions
 1526 exist for distinguishing electron-like events from π^0 -like events, and muon-like
 1527 events from pion-like events. The cuts are defined as,

$$\text{Electron/Muon} : \ln(L_e/L_\mu) > 0.2 \times p_e^{rec} [\text{MeV}],$$

$$\text{Electron}/\pi^0 : \ln(L_e/L_{\pi^0}) < 175 - 0.875 \times m_{\gamma\gamma} [\text{MeV}], \quad (5.5)$$

$$\text{Muon/Pion} : \ln(L_\mu/L_{\pi^\pm}) < 0.15 \times p_\mu^{rec} [\text{MeV}],$$

as taken from [181], where p_e^{rec} and p_μ^{rec} are the reconstructed momentum of the single-ring electron and muon fits, respectively. $m_{\gamma\gamma}$ represents the reconstructed invariant mass of the two photons emitted from π^0 decay. Typically, the distance between a particular entry in these two-dimensional distributions and the cut-line is termed the PID parameter and is illustrated in Figure 5.5.

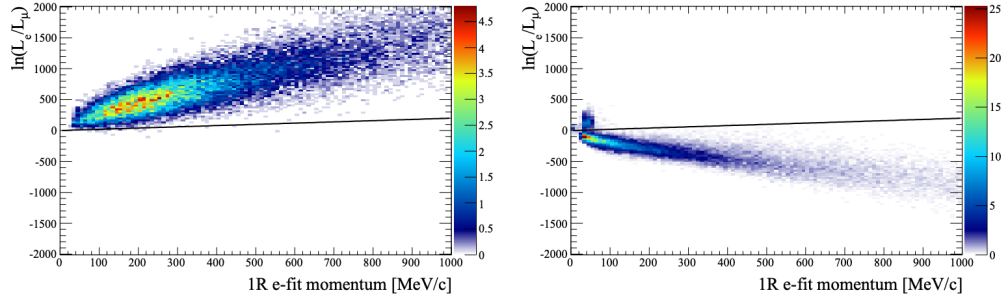


Figure 5.4: The difference of the electron-like and muon-like log-likelihood compared to the reconstructed single-ring fit momentum for atmospheric ν_e (left) and ν_μ (right) samples. The black line represents the cut used to discriminate electron-like and muon-like events, which coefficients obtained from Monte Carlo studies. Figures taken from [178].

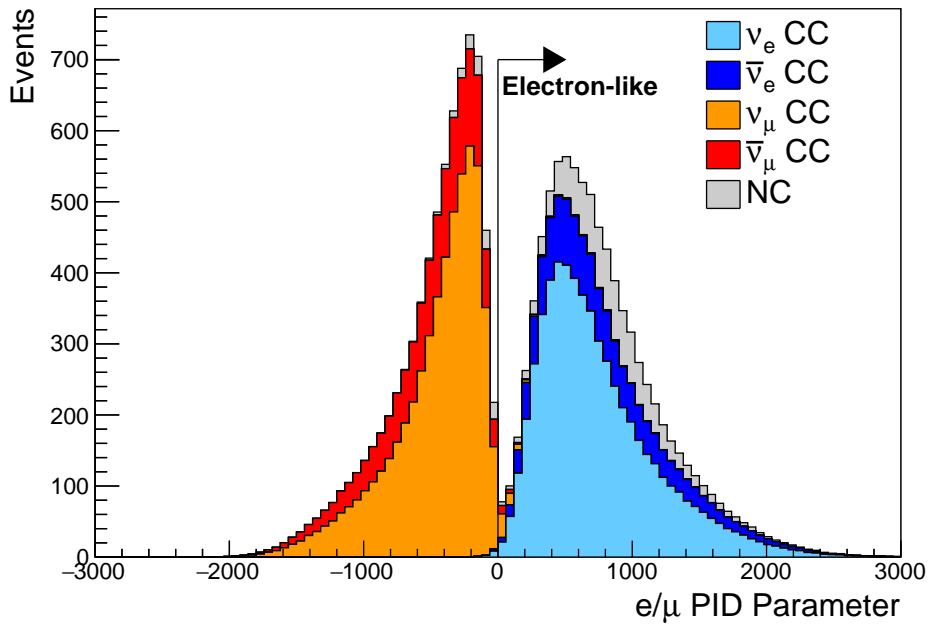


Figure 5.5: The electron/muon PID separation parameter for all sub-GeV single-ring events in SK-IV. The charged current (CC) component is broken down in four flavours of neutrino (ν_μ , $\bar{\nu}_\mu$, ν_e and $\bar{\nu}_e$). Events with positive values of the parameter are determined to be electron-like.

1533 The `fitQun` algorithm also considers a π^0 hypothesis. To do this, it performs
1534 a fit looking for two standard electron-hypothesis tracks which point to the
1535 same four-vertex. This assumes the electron tracks are generated from photon-
1536 conversion so the electron tracks actually appear offset from the proposed π^0
1537 vertex. For these fits, the conversion length, direction, and momentum of each
1538 photon are also considered as track parameters which are then fit in the same
1539 methodology as the standard single-ring hypotheses.

1540 Whilst lower energy events are predominantly single-ring events, higher
1541 energy neutrino events can generate final states with multiple particles which
1542 generate Cherenkov photons. These “multi-ring” hypotheses are also considered
1543 in the `fitQun` algorithm. When calculating the charge likelihood density, the
1544 predicted charge associated with each ring is calculated separately and then
1545 summed to calculate the total accumulated charge on each PMT. Similarly,
1546 the time likelihood for the multi-ring hypothesis is calculated assuming each
1547 ring is independent. Each track is time-ordered based on the time of flight
1548 from the center of the track to the PMT and the direct light from any ring
1549 incident on the PMT is assumed to arrive before any scattered light. To reduce
1550 computational resource usage, the multi-ring fits only consider electron-like
1551 and charged pion-like rings as the pion fit can be used as a proxy for a muon
1552 fit due to their similar mass.

1553 Multi-ring fits proceed by proposing another ring to the previous fit and
1554 then fitting the parameters in the method described above. Typically, multi-ring
1555 fits have the largest likelihood because of the additional degrees of freedom
1556 introduced. A likelihood value is calculated for the n -ring and $(n + 1)$ -ring
1557 hypotheses, where the additional ring is only included if the likelihood value
1558 is above 9.35, based on Monte Carlo studies in [182].

1559 5.2.1 Validation of Reconstruction in SK-V

1560 As an example of how the reconstruction depends on the detector conditions, the
1561 author of this thesis assessed the quality of event reconstruction for SK-V data.

1562 The detector systematics used in the T2K-only oscillation analysis are determined
1563 using data-to-Monte Carlo comparisons of the SK-IV data [183]. Due to tank-open
1564 maintenance occurring between SK-IV and SK-V, the dark rate of each PMT was
1565 observed to increase in SK-V due to light exposure for a significant time during
1566 the repairs. This increase can be seen in Figure 5.6. Run-10 of the T2K experiment
1567 was conducted in the SK-V period, so the consistency of SK-IV and SK-V data
1568 needs to be studied to determine whether the SK-IV-defined systematics can
1569 be applied to the run-10 data. This comparison study was performed using
1570 the stopping muon data set for both the SK-IV and SK-V periods. This data
1571 sample is used due to the high rate of interactions ($O(200)$ events per hour) as
1572 well as having similar energies to muons from CCQE ν_μ interactions from beam
1573 interactions. The rate of cosmic muons does depend on the solar activity cycle
1574 [184] but has been neglected in this comparison study. This is because the shape
1575 of the distributions is most important for the purposes of being compared to the
1576 detector systematics. The SK-IV and SK-V data samples consist of 2398.42 and
1577 626.719 hours of data which equates to 686k and 192k events respectively.

1578 The predicted charge calculated in the `fitQun` algorithm includes a contribu-
1579 tion from the photoelectron emission due to dark noise. Therefore, the increase
1580 in the SK-V dark rate needs to be accounted for. In practice, the average dark rate
1581 in each SK period is calculated and used as an input in the reconstruction. This is
1582 calculated by averaging the dark rate per run for each period separately, using
1583 the calibration measurements detailed in subsection 3.1.2. The average dark rate
1584 from SK-IV and SK-V were found to be 4.57kHz and 6.30kHz, respectively. The
1585 charges associated with the muon and decay electron subevents are illustrated in
1586 Figure 5.7. The photoelectron emission from dark noise is more significant for
1587 events that have lower energy. This is because this contribution becomes more
1588 comparable to the number of photoelectrons emitted from incident photons in
1589 lower-energy events. This behaviour is observed in the data, where the charge
1590 deposited by the muon subevent is mostly unaffected by the increase in dark rate,
1591 whilst the charge associated with the decay-electron is clearly affected.

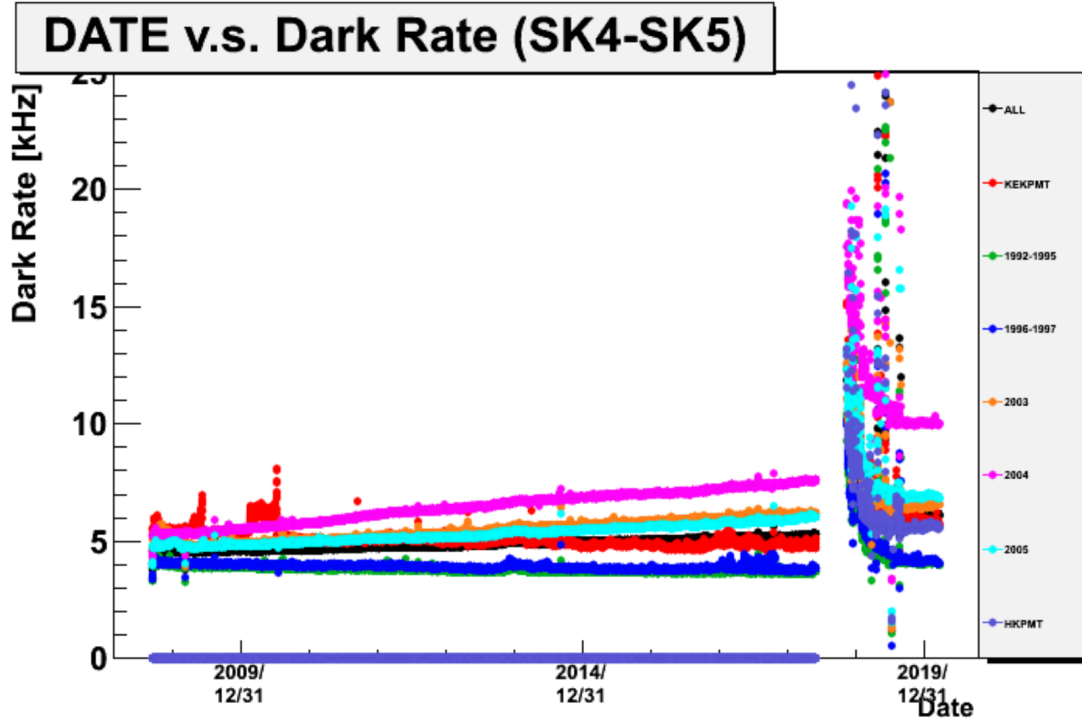


Figure 5.6: The variation of the measured dark rate as a function of date, broken down by PMT type. The SK-IV and SK-V periods span September 2008 to May 2018 and January 2019 to July 2020, respectively. The break in measurement in 2018 corresponds to the period of tank repair and refurbishment. Figure adapted from [183].

1592 The energy scale systematic is estimated from data-to-Monte Carlo differences
 1593 in the stopping muon sample in [185] and found to be 2.1%. To determine the
 1594 consistency of SK-IV and SK-V with respect to the energy scale systematic, the
 1595 muon momentum distribution is compared between the two SK periods. As
 1596 the total number of Cherenkov photons is integrated across the track length,
 1597 the reconstructed momentum divided by track length (or range) is compared
 1598 between SK-IV and SK-V as illustrated in Figure 5.8.

1599 The consistency between these distributions has been computed in two ways.
 1600 Firstly, a Gaussian is fit to the peak of each distribution separately, whose mean
 1601 is found to be $(2.272 \pm 0.003)\text{MeV/cm}$ and $(2.267 \pm 0.006)\text{MeV/cm}$ for SK-IV
 1602 and SK-V respectively. The ratio of these is equal to 1.002 ± 0.003 . The means of
 1603 the Gaussian fits are consistent with the expected stopping power of a minimum
 1604 ionising muon for a target material (water) with $Z/A \sim 0.5$ [186]. The second

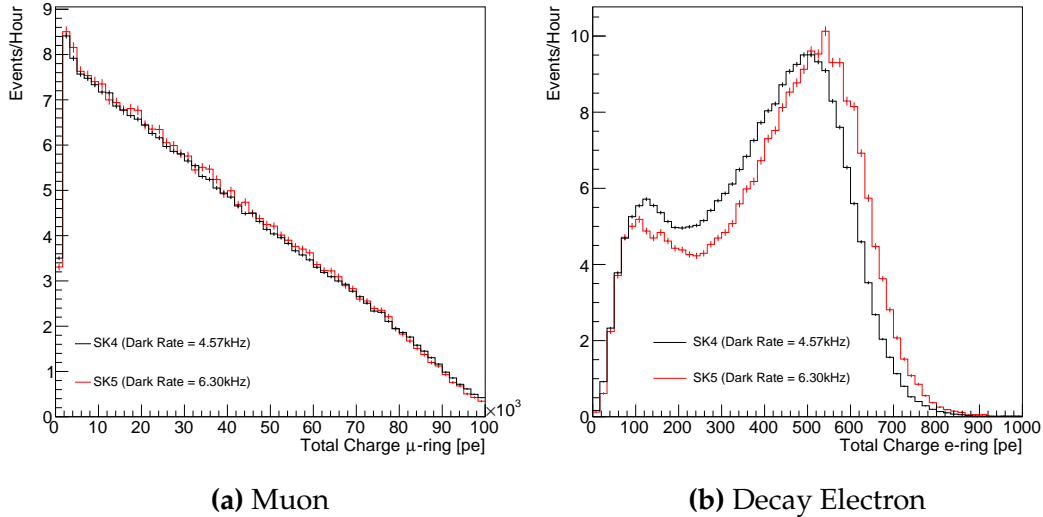


Figure 5.7: Comparison of the measured raw charge deposited per event from the stopping muon data samples between SK-IV (Blue) and SK-V (Red), split by the primary muon subevent and the associated decay electron subevent.

1605 consistency check is performed by introducing a nuisance parameter, α , which
 1606 modifies the SK-V distribution. The value of α which minimises the χ^2 value
 1607 between the SK-IV and SK-V is determined by scanning across a range of values.
 1608 This is repeated by applying the nuisance parameter as both a multiplicative
 1609 factor and an additive shift. The χ^2 distributions for different values of α is
 1610 illustrated in Figure 5.9. The values which minimise the χ^2 are found to be 0.0052
 1611 and 1.0024 for the additive and multiplicative implementations, respectively. No
 1612 evidence of shifts larger than the 2.1% uncertainty on the energy scale systematic
 1613 has been found in the reconstructed momentum distribution of SK-IV and SK-V.

1614 5.3 Event Reduction at SK

1615 Atmospheric neutrino events observed in the SK detector are categorised into
 1616 three different types of samples: fully contained (FC), partially contained (PC)
 1617 and up-going muon (Up- μ), using PMT hit signatures in the inner and outer
 1618 detector (ID and OD, respectively). To identify FC neutrino events, it is re-
 1619 quired that the neutrino interacts inside the fiducial volume of the ID and that
 1620 no significant OD activity is observed. For this analysis, an event is defined

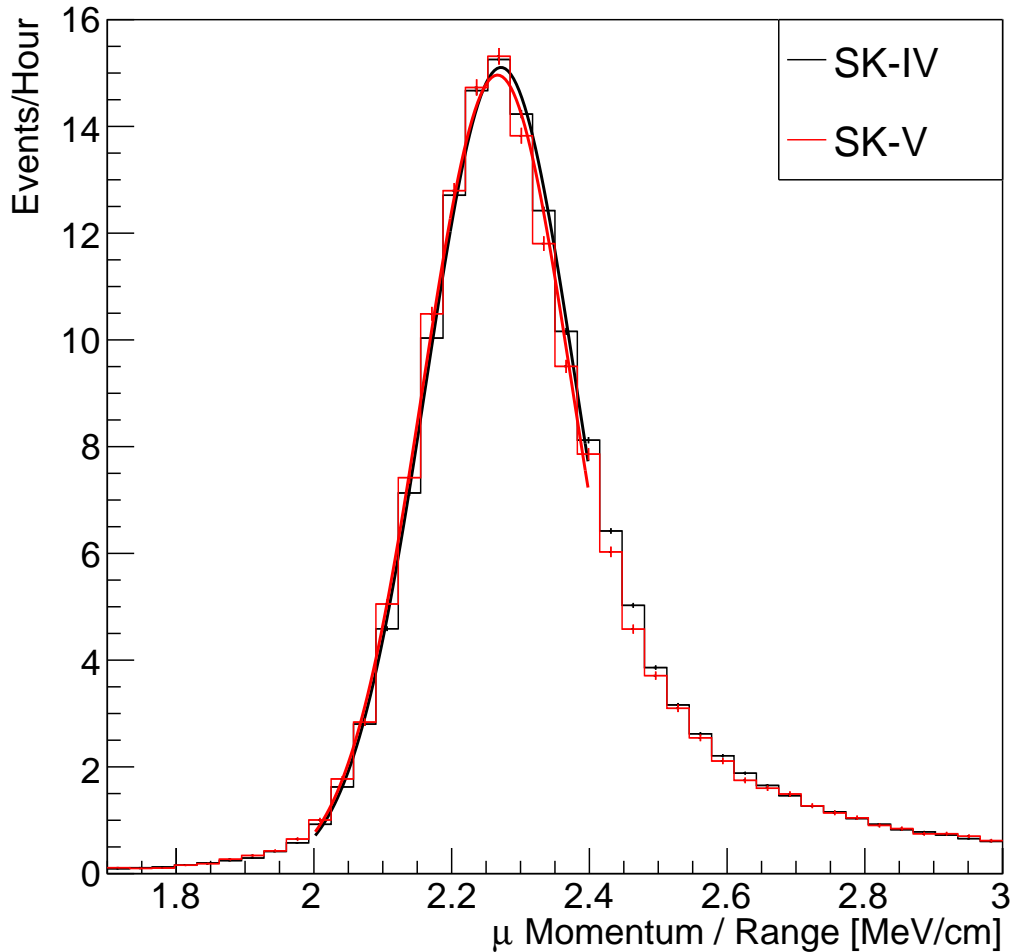


Figure 5.8: The distribution of the reconstructed momentum from the muon ring divided by the distance between the reconstructed muon and decay electron vertices as found in the stopping muon data sets of SK-IV (Black) and SK-IV (Red). Only events with one tagged decay electron are considered. A Gaussian fit is considered in the range [2.0, 2.4] MeV/cm and illustrated as the solid curve.

1621 to be in the fiducial volume provided the event vertex is at least 0.5m away
 1622 from the ID walls. PC events have the same ID requirements but can have a
 1623 larger signal present inside the OD. Typically, only high energy muons from
 1624 ν_μ interactions can penetrate the ID wall. The Up- μ sample contains events where
 1625 muons are created from neutrino interactions in the OD water or rock below the
 1626 tank. They then propagate upwards through the detector. Downward-going
 1627 muons generated from neutrino interactions above the tank are neglected is

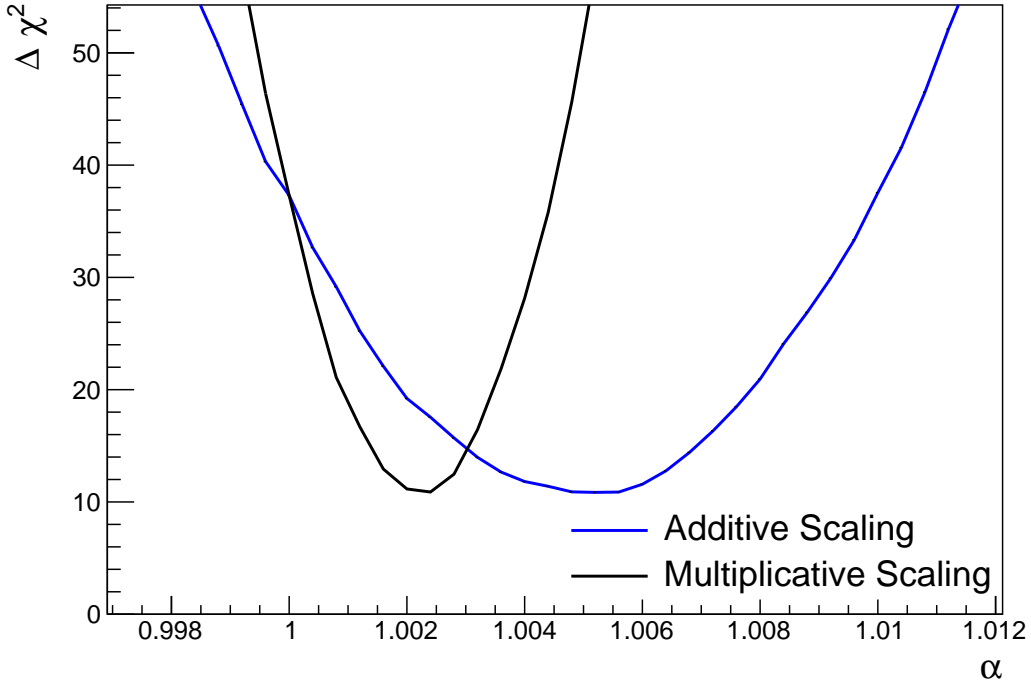


Figure 5.9: The χ^2 difference between the SK-IV and SK-V reconstructed muon momentum divided by range when the SK-V is modified by the scaling parameter α . Both additive (Blue) and multiplicative (Black) scaling factors have been considered. In practice, the additive scaling factor actually uses the value of $(\alpha - 1.0)$ but is illustrated like this so the results can be shown on the same axis range.

¹⁶²⁸ because of the difficulty in separating their signature from the cosmic muon
¹⁶²⁹ shower background. The sample categories are visually depicted in Figure 5.10.

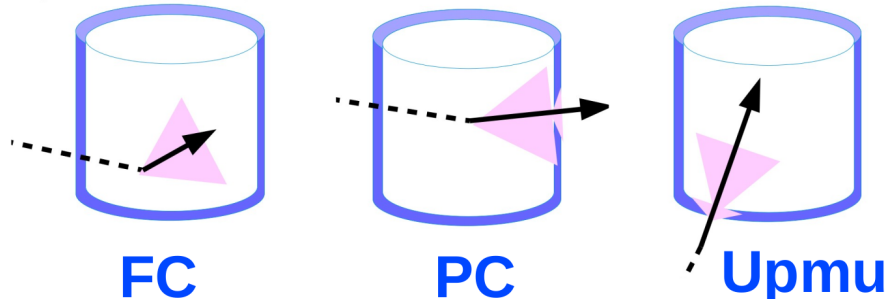


Figure 5.10: A depiction of the topology patterns for fully-contained (FC), partially-contained (PC) and up-going muon ($Up-\mu$) samples included in this analysis.

¹⁶³⁰ Based on the event characteristics, as defined by the `fitQun` event reconstruction software, the FC events are categorised by
¹⁶³¹

- **Visible Energy:** equal to the sum of the reconstructed kinetic energy of particles above the Cerenkov threshold for all rings present in the event. The purpose is to separate events into sub-GeV and multi-GeV categories.
- **Number of observed Cerenkov rings.** The purpose is to separate single-ring and multi-ring events, where single-ring events predominantly consist of quasi-elastic interactions and multi-ring events are typically resonant pion production or deep inelastic scattering events.
- **Particle identification parameter of the most energetic ring:** A value determined from the maximum likelihood value based on `fitQun`'s electron, muon, or pion hypothesis. The purpose is to separate electron-like and muon-like events.
- **Number of decay electrons:** The purpose is to separate quasi-elastic events (which have one decay electron emitted from the muon decay) and resonant pion production events (which have two decay electrons emitted from the muon and pion).

The PC and Up- μ categories are broken down into “through-going” and “stopping” samples depending on whether the muon leaves the detector. This is because the PC stopping events deposit the entire energy of the interaction into the detector, resulting in better reconstruction. The energy of events that exit the detector has to be estimated, with typically worse resolution, which introduces much larger systematic uncertainties. Through-going Up- μ samples are further broken down by whether any hadronic showering was observed in the event which typically indicates DIS interactions. The expected neutrino energy for the different categories is given in Figure 5.11. FC sub-GeV and multi-GeV events peak around 0.7GeV and 3GeV respectively, with slightly different peak energies for ν_e and $n\nu_\mu$ oscillation channels. PC and Up- μ are almost entirely comprised of ν_μ events and peak around 7GeV and 100GeV, respectively.

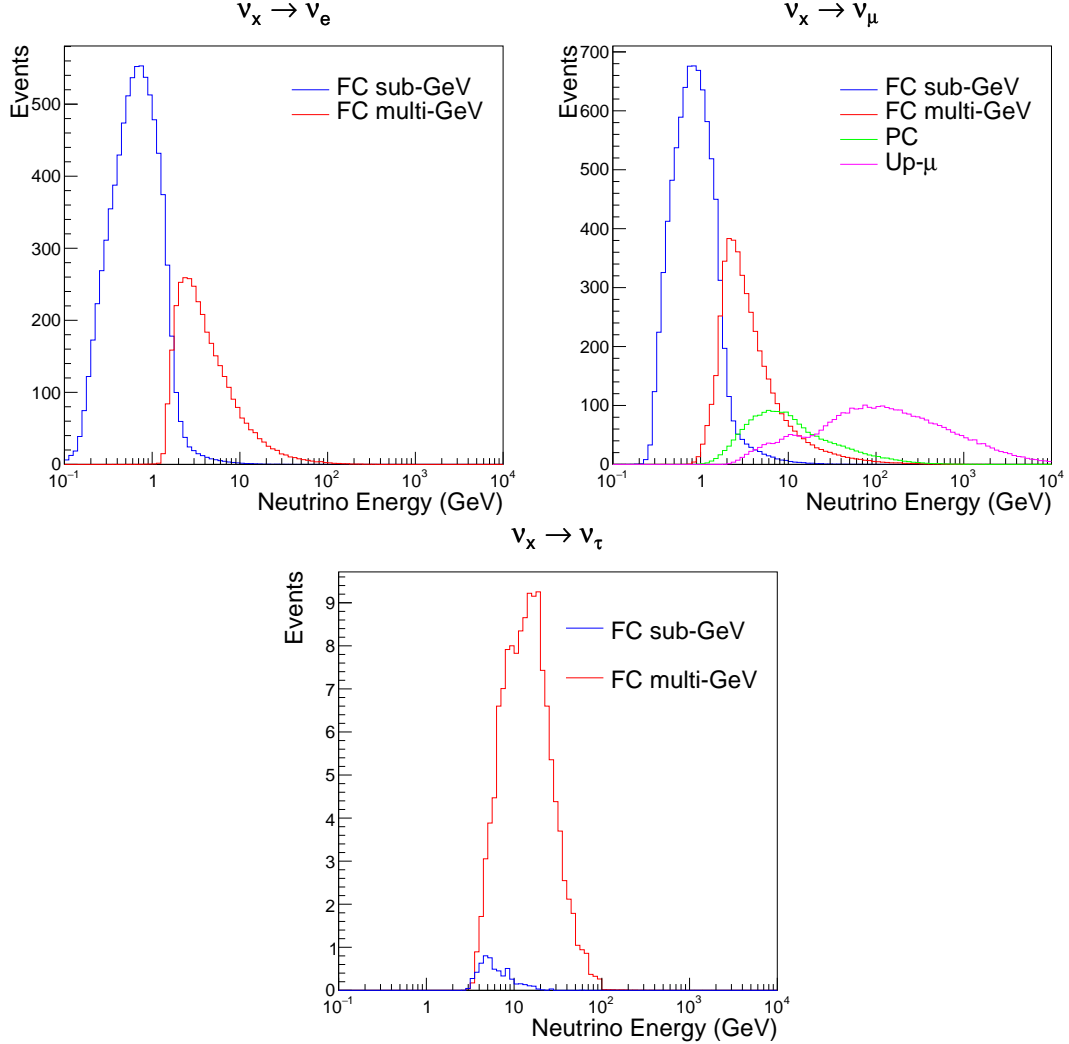


Figure 5.11: The predicted neutrino flux of the fully contained (FC) sub-GeV and multi-GeV, partially contained (PC), and upward-going muon (Up- μ) events. The prediction is broken down by the $\nu_x \rightarrow \nu_e$ prediction (top left), $\nu_x \rightarrow \nu_\mu$ prediction (top right) and $\nu_x \rightarrow \nu_\tau$ prediction (bottom). Asimov A oscillation parameters are assumed (given in Table 2.2).

In normal data-taking operations, the SK detector observes many background events alongside the beam and atmospheric neutrino signal events of physics interest for this thesis. Cosmic ray muons and flasher events, which are the spontaneous discharge of a given PMT, contribute the largest amount of background events in the energy range relevant to this thesis. Lower energy analyses like DSNB searches are also subject to radioactive backgrounds [187]. Therefore the data recorded is reduced with the aim of removing these background events. The reduction process is detailed in [56, 86] and briefly summarised below.

1667 The first two steps in the FC reconstruction remove the majority of cosmic
1668 ray muons by requiring a significant amount of ID activity compared to that
1669 measured in the OD. Events that pass this cut are typically very high momentum
1670 muons or events that leave very little activity in the OD. Consequently, a third
1671 reduction step is then applied to select cosmic-ray muons that pass the initial
1672 reduction step. A purpose-built cosmic muon fitter is used to determine the
1673 entrance (or exit) position of the muon and a cut is applied to OD activity
1674 contained within 8m of this position. Flasher events are removed in the fourth
1675 reduction step which is based on the close proximity of PMT hits surrounding
1676 the PMT producing the flash. Events that pass all these reduction steps are
1677 reconstructed with the APFit algorithm. The fifth step of the reduction uses
1678 information from the more precise fitter to repeat the previous two steps with
1679 tighter cuts. Muons below the Cherenkov threshold can not generate optical
1680 photons in the ID but the associated decay electron can due to its lower mass.
1681 These are the types of events targeted in the fifth reduction step. The final
1682 cuts require the event vertex to be within the fiducial volume (0.5m from the
1683 wall although the nominal distance is 2.0m), visible energy $E_{vis} > 30\text{MeV}$ and
1684 fewer than 16 hits within the higher energy OD cluster. The culmination of
1685 the fully contained reduction results in 8.09 events/day in the nominal fiducial
1686 volume [83]. The uncertainty in the reconstruction is calculated by comparing
1687 Monte Carlo prediction to data. The largest discrepancy is found to be 1.3%
1688 in the fourth reduction step.

1689 The PC and Up- μ events are processed through their own reduction processes
1690 detailed in [56]. Both of these samples are reconstructed with the APFit algorithm
1691 rather than `fiTQun`. This is because the efficiency of reconstructing events that
1692 leave the detector has not been sufficiently studied for reliable systematic uncer-
1693 tainties wth `fiTQun`. The PC and Up- μ samples acquire events at approximately
1694 0.66 and 1.44 events/day.

1695 Events due to beam neutrinos undergo the same reduction steps as FC events
1696 and are then subject to further cuts [188]. The GPS system which links the timing

1697 between the beam facility and SK needs to be operating correctly and there should
1698 be no activity within the detector in the previous $100\mu\text{s}$ before the trigger. The
1699 events then need to triggered between $-2\mu\text{s}$ and $10\mu\text{s}$ of the expected spill timing.

1700 The beam neutrino samples are not split by visible energy since their energy
1701 range is smaller than the atmospheric neutrino events. Following the T2K
1702 analysis in [76], only single-ring beam neutrino events are considered. Similar to
1703 atmospheric event selection, the number of decay electrons is used as a proxy for
1704 distinguishing CCQE and CCRES events. The expected neutrino energy, broken
1705 down by number of decay electrons, is given in Figure 5.12.

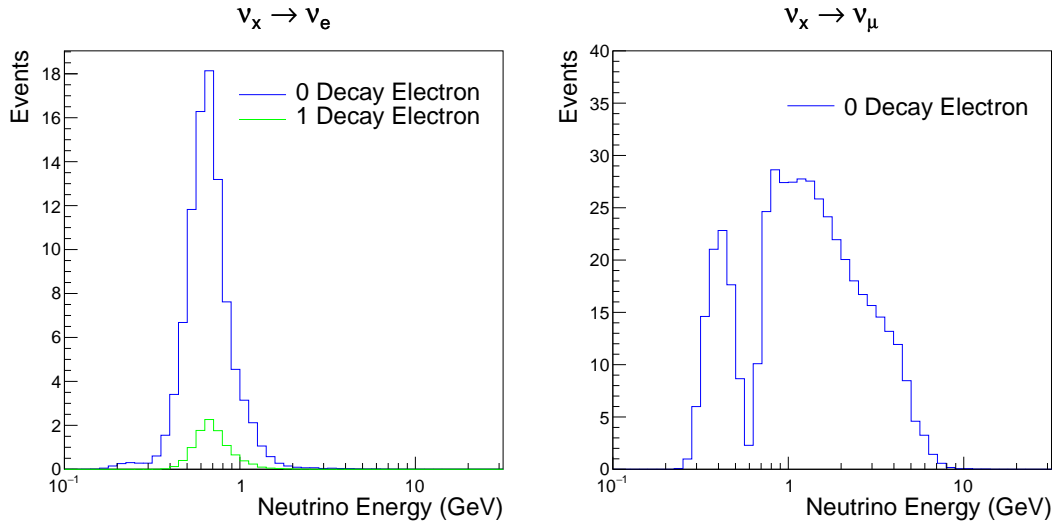


Figure 5.12: The predicted flux of beam neutrinos, as a function of neutrino energy. The predictions are broken down by the number of decay electrons associated with the particular events. Asimov A oscillation parameters are assumed (given in Table 2.2).

6

1706

1707

Sample Selections and Systematics

1708 The oscillation analysis presented within this thesis is built upon a simultaneous
1709 fit to atmospheric data at SK, neutrino beam data in the near detector, and
1710 beam data measured at SK. The definitions of these samples are documented
1711 in section 6.1, section 6.2, and section 6.3, respectively. The data collected and
1712 used within this analysis is detailed in Table 6.1. The near and far detector data
1713 corresponds to T2K runs 2-9 and runs 1-10, respectively. The accumulated POT
1714 and beam power for runs 1 – 10 are illustrated in Figure 6.1.

Data Type	Total
Near Detector FHC	1.15×10^{21} POT
Near Detector RHC	8.34×10^{20} POT
Far Detector FHC	1.97×10^{21} POT
Far Detector RHC	1.63×10^{21} POT
Atmospheric SK-IV	3244.4 days

Table 6.1: The amount of data collected in each detector used within this analysis. The data collected at the near and far detector, for both neutrino beam (FHC) and antineutrino beam (RHC), is measured as the number of protons on target (POT).

1715 The difference in POT recorded at the near and far detector is due to the
1716 difference in downtime. The SK detector is very stable with almost 100% of
1717 data recorded during beam operation. Due to various technical and operational

¹⁷¹⁸ issues, the downtime of the near detector is significantly higher due to its more
¹⁷¹⁹ complex design and operating requirements.

¹⁷²⁰ The systematic parameters invoked within the flux, detector, and interaction
¹⁷²¹ models used within this analysis are documented in section 6.4. The standard
¹⁷²² configuration of the joint beam and atmospheric data fit utilises far detector sys-
¹⁷²³ tematics provided in the official inputs from the two experiments. Additionally,
¹⁷²⁴ a correlated detector model which fits the parameters used in sample selections
¹⁷²⁵ to data has been developed and documented in subsection 6.4.5.

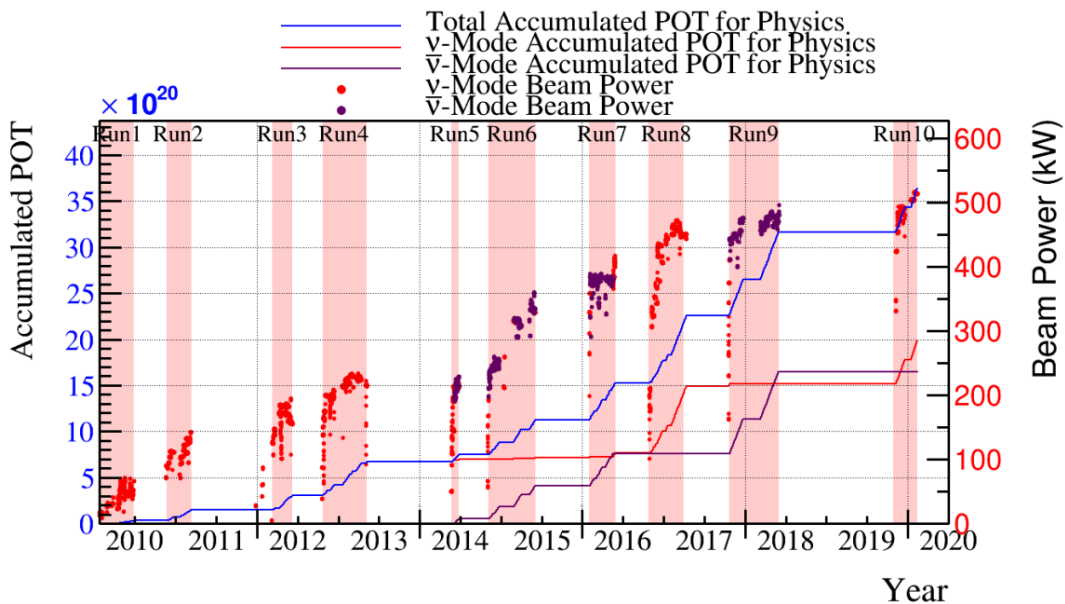


Figure 6.1: The accumulated beam data, measured as the number of protons on target (POT). The total data (blue) is given which comprises of the neutrino beam (red) and antineutrino (purple) components. The beam power for neutrino and antineutrino beams is given as the markers using the same colour scheme. The timescale runs from Run 1 which started in January 2010 until Run 10 which ended in February 2020. The ratio of accumulated data in neutrino and antineutrino beam is 54.7% : 45.3%.

1726 6.1 Atmospheric Samples

1727 The atmospheric event selection follows the official SK-IV analysis presented
1728 in [86] and is documented below. The Monte Carlo prediction used within this
1729 analysis corresponds to 500 years worth of neutrino events, which is scaled down
1730 to match the SK-IV livetime of 3244.4 days.

1731 The fully contained (FC), partially contained (PC), and upward going muon
1732 events ($\text{up-}\mu$) which pass the reduction cuts discussed in section 5.3 are further
1733 broken down into different samples based on reconstruction information. This
1734 section details the samples used within this oscillation analysis, alongside the
1735 chosen binning.

1736 FC events are first separated by the visible energy deposited within the
1737 detector. This is calculated as the sum of the reconstructed kinetic energy
1738 above the Cherenkov threshold for all rings present in the event. Events are
1739 separated by whether they were above or below $E_{\text{vis}} = 1.33\text{GeV}$. This separates
1740 “subGeV” and “multiGeV” events. Typically, lower energy events consist of
1741 charged current quasi-elastic (CCQE) interactions which are better understood
1742 and simpler to reconstruct resulting in smaller systematic uncertainties. Events
1743 are further separated by the number of rings associated with the event due to
1744 similar reasoning. As the oscillation probability is dependent upon the flavour
1745 of neutrino, electron and muon events are separated using a similar likelihood
1746 method to that discussed in section 5.2. To reduce computational resources
1747 required for the reconstruction, only electron and pion hypotheses are considered
1748 so this separation cut depends on the ratio of the electron to pion likelihoods,
1749 $\log(L_e/L_\pi)$. Finally, the number of decay electrons is used to classify events.
1750 Charged current resonant pion production (CCRES) interactions generate a final-
1751 state pion. This can decay, mostly likely through a muon, into a decay electron.
1752 Therefore any electron-like event with one decay electron or muon-like event
1753 with two decay electrons was most likely produced by a CCRES interaction.
1754 Consequently, the number of decay electrons can be used to distinguish CCQE

¹⁷⁵⁵ and CCRES interaction modes. Ultimately, FC subGeV events are separated
¹⁷⁵⁶ into the samples listed in Table 6.2.

Sample Name	Description
SubGeV- <i>e</i> like-0dcy	Single ring <i>e</i> -like events with zero decay electrons
SubGeV- <i>e</i> like-1dcy	Single ring <i>e</i> -like events with one or more decay electrons
SubGeV- <i>μ</i> like-0dcy	Single ring <i>μ</i> -like events with zero decay electrons
SubGeV- <i>μ</i> like-1dcy	Single ring <i>μ</i> -like events with one decay electrons
SubGeV- <i>μ</i> like-2dcy	Single ring <i>μ</i> -like events with two or more decay electrons
SubGeV- <i>π</i> 0like	Two <i>e</i> -like ring events with zero decay electrons and reconstructed π^0 mass $85 \leq m_{\pi^0} < 215$ MeV

Table 6.2: The fully contained subGeV samples, defined as events with visible energy $E_{vis} < 1.33$ GeV, used within this oscillation analysis.

¹⁷⁵⁷ In addition to the cuts discussed above, multiGeV samples also have addi-
¹⁷⁵⁸ tional cuts to separate samples which target neutrino and antineutrino events.
¹⁷⁵⁹ As discussed in section 7.1, the matter resonance only occurs for neutrinos in
¹⁷⁶⁰ normal hierarchy and antineutrinos in an inverted mass hierarchy. Therefore,
¹⁷⁶¹ having flavour-enriched samples aids in the determination of the mass hierarchy.
¹⁷⁶² For a CCRES interaction,

$$\begin{aligned}
 \bar{\nu}_e + N &\rightarrow e^+ + N' + \pi^-, \\
 \nu_e + N &\rightarrow e^- + N' + \pi^+ \\
 &\quad \downarrow \mu^+ + \nu_\mu \\
 &\quad \downarrow e^+ + \nu_e + \bar{\nu}_\mu.
 \end{aligned} \tag{6.1}$$

¹⁷⁶³ The π^- emitted from a $\bar{\nu}_e$ interaction is more likely to be absorbed within the
¹⁷⁶⁴ oxygen nucleus than the π^+ from ν_e interactions [189]. These pions then decay,
¹⁷⁶⁵ mostly through muons, to electrons. Therefore the number of tagged decay
¹⁷⁶⁶ electrons associated with an event gives an indication of whether the interaction
¹⁷⁶⁷ was due to a neutrino or antineutrino: zero for $\bar{\nu}_e$ events, and one for ν_e events.
¹⁷⁶⁸ The ability to separate neutrino from antineutrino events is illustrated in Table 6.4,
¹⁷⁶⁹ where the MultiGeV-*e*like-nue has 78% purity of CC neutrino interactions with
¹⁷⁷⁰ only 7% antineutrino background, the rest consisting of NC backgrounds.

1771 The number of decay electrons discriminator works reasonably well for single-
1772 ring events. However, this is not the case for multi-ring events. A multiGeV
1773 multiring electron-like (MME) likelihood cut was introduced in [190, 191]. This
1774 is a two-stage likelihood selection cut. Four observables are used in the first
1775 likelihood cut to distinguish $CC\nu_e$ and $CC\bar{\nu}_e$ events from background:

- 1776 • The number of decay electrons
- 1777 • The maximum distance between the vertex of the neutrino and the decay
1778 electrons
- 1779 • The energy deposited by the highest energy ring
- 1780 • The particle identification of that highest energy ring

1781 Background events consist of $CC\nu_\mu$ and NC interactions. Typically, the
1782 majority of the energy in these background events is carried by the hadronic
1783 system. Additionally, muons tend to travel further than the pions from $CC\nu_e$
1784 before decaying. Thus, the parameters used within the likelihood cut target these
1785 typical background interaction kinematics.

Sample Name	Description
MultiGeV-elike-nue	Single ring e -like events with zero decay electrons
MultiGeV-elike-nuebar	Single ring e -like events with one or more decay electrons
MultiGeV-mulike	Single ring μ -like events
MultiRing-elike-nue	Two or more ring events with leading energy e -like ring and passed both MME and $\nu/\bar{\nu}$ separation cuts
MultiRing-elike-nuebar	Two or more ring events with leading energy e -like ring and passed MME and failed $\nu/\bar{\nu}$ separation cuts
MultiRing-mulike	Two or more ring events with leading energy μ -like ring and only requires $E_{vis} > 0.6\text{GeV}$ DB: Why is this not }1.33\text{GeV
MultiRing-Other1	Two or more ring events with leading energy e -like ring and failed the MME likelihood cut

Table 6.3: The fully contained multiGeV samples used within this oscillation analysis. Both the sample name and description are given.

1786 Neutrino and antineutrino events are then separated by a second likelihood
1787 method ($\nu/\bar{\nu}$ separation) detailed in [61]. This uses the number of decay electrons,

1788 the number of reconstructed rings, and the event’s transverse momentum. The
1789 last two parameters are used because higher-energy samples tend to have more
1790 pions produced above the Cherenkov threshold which results in more rings
1791 compared to an antineutrino interaction. Furthermore, the angular distribution
1792 also tends to be more forward peaked in antineutrino interactions as compared
1793 to neutrino interactions [86]. These FC multiGeV sample definitions are de-
1794 tailed in Table 6.3.

1795 The PC and up- μ samples are split by the amount of energy deposited within
1796 the outer detector, into “stopping” and “through-going” samples. If an event
1797 leaves the detector, the energy it takes with it has to be estimated which increases
1798 the systematic uncertainty compared to events entirely contained within the
1799 inner detector. This estimation is particularly poor at high energies, thus the
1800 up- μ through-going events are not binned in reconstructed momentum. The
1801 through-going up- μ are further separated by the presence of any electromagnetic
1802 showering in the event, as the assumption of non-showering muon does not give
1803 reliable reconstruction for these types of events [56]. In total, 13 FC, 2 PC, and
1804 3 up- μ atmospheric samples are included within this analysis.

1805 The atmospheric samples are binned in direct observables: reconstructed
1806 lepton momentum and direction, as given by Table A.1. The distribution of
1807 the reconstructed lepton momentum (for samples that only have one bin in
1808 reconstructed zenith angle) and reconstructed direction for each atmospheric
1809 sample used within this analysis is illustrated in Figure 6.2. The by-mode
1810 breakdown of each of the atmospheric samples is given in Appendix A.

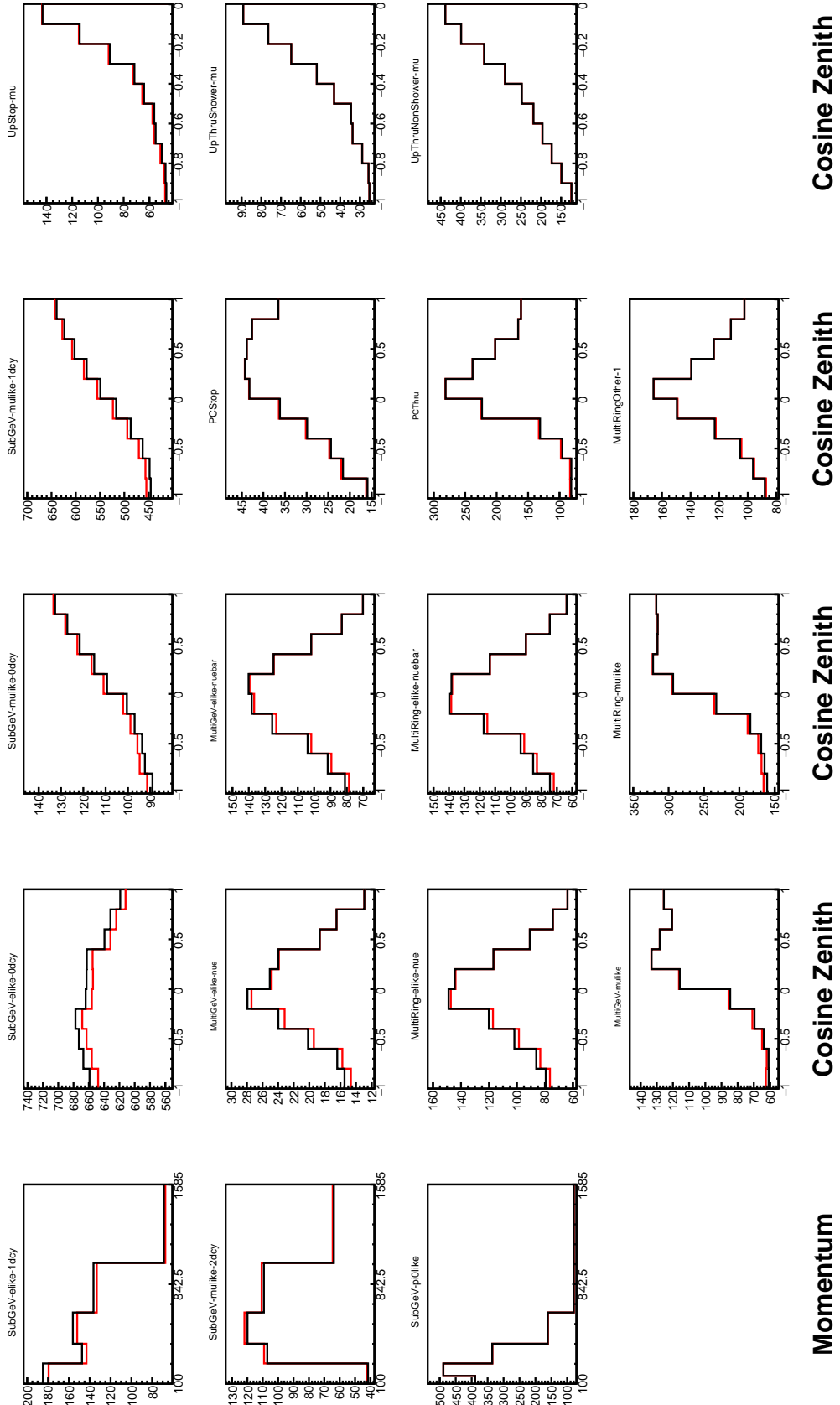


Figure 6.2: Comparison of the SK-IV atmospheric samples between predictions made with the CP-violating Asimov A (Black) and CP-conserving Asimov B (Red) oscillation parameter sets (given in Table 2.2). The subGeV samples CCRES and π^0 -like samples are given in their reconstructed lepton momentum. All other samples are presented in their reconstructed zenith angle projection.

Sample	$CC\nu_e$	$CC\bar{\nu}_e$	$CC(\nu_\mu + \bar{\nu}_\mu)$	$CC(\nu_\tau + \bar{\nu}_\tau)$	NC
SubGeV- <i>elike</i> -0dcy	72.17	23.3	0.724	0.033	3.77
SubGeV- <i>elike</i> -1dcy	86.81	1.773	7.002	0.062	4.351
SubGeV- <i>mulike</i> -0dcy	1.003	0.380	90.07	0.036	8.511
SubGeV- <i>mulike</i> -1dcy	0.023	0.	98.46	0.029	1.484
SubGeV- <i>mulike</i> -2dcy	0.012	0.	99.25	0.030	0.711
SubGeV- <i>pi0like</i>	6.923	2.368	0.928	0.011	89.77
MultiGeV- <i>elike</i> -nue	78.18	7.041	3.439	1.886	9.451
MultiGeV- <i>elike</i> -nuebar	56.68	37.81	0.174	0.614	4.718
MultiGeV- <i>mulike</i>	0.024	0.005	99.67	0.245	0.058
MultiRing- <i>elike</i> -nue	59.32	12.39	4.906	3.385	20
MultiRing- <i>elike</i> -nuebar	52.39	31.03	1.854	1.585	13.14
MultiRing- <i>mulike</i>	0.673	0.080	97.33	0.342	1.578
MultiRingOther-1	27.98	2.366	34.93	4.946	29.78
PCStop	8.216	3.118	84.45	0.	4.214
PCThrus	0.564	0.207	98.65	0.	0.576
UpStop-mu	0.829	0.370	98.51	0.	0.289
UpThruNonShower-mu	0.206	0.073	99.62	0.	0.103
UpThruShower-mu	0.128	0.054	99.69	0.	0.132

Table 6.4: The purity of each atmospheric sample used within this analysis, broken down by charged current (CC) and neutral current (NC) interactions and which neutrino flavour interacted within the detector. Asimov A oscillation parameter sets are assumed (given in Table 2.2). Electron neutrino and antineutrino events are separated to illustrate the ability of the separation likelihood cuts used within the multiGeV and multiring sample selections.

1811 6.2 Near Detector Beam Samples

1812 The near detector sample selections are documented in detail within [192] and
1813 summarised below. Samples are selected based upon the which Fine Grained
1814 Detector (FGD) that the vertex is reconstructed in as well as the operating mode
1815 of the beam: FHC or RHC. Wrong-sign neutrino samples are considered in the
1816 RHC mode in order to add additional constraints on model parameters. Samples
1817 from the wrong-sign component of the FHC beam mode are not included as they
1818 are statistically insignificant compared to those samples already listed.

1819 For additional constraints on model parameters, wrong-sign neutrino samples
1820 are also considered when the beam is operating in RHC mode.

1821 The reconstruction algorithm uses a clustering algorithm to group hits within
1822 the TPC. It then adds information from the upstream FGD to form a track
1823 which passes through both sub-detectors. In FHC(RHC), the highest momentum
1824 negative(positive) curvature track is defined as the muon candidate. Before
1825 being assigned a sample, these candidate muon events must pass CC-inclusive
1826 cuts, as defined in [193]:

- 1827 • Event Timing: The DAQ must be operational and the event must occur
1828 within the expected beam time window consistent with the beam spill
- 1829 • TPC Requirement: The muon-candidate track path must intercept one or
1830 more TPCs
- 1831 • Fiducial volume: The event must originate from within the fiducial volume
1832 defined in [194].
- 1833 • Upstream Background: Remove events that have muon tracks that originate
1834 upstream of the FGDs by requiring no high-momentum tracks within
1835 150mm upstream of the candidate vertex. Additionally, events that occur
1836 within the downstream FGD are vetoed if a secondary track starts within
1837 the upstream FGD

- 1838 • Broken track removal: All candidates where the muon candidate is broken
1839 in two are removed

- 1840 • Muon PID: Measurements of dE/dx in a TPC are used to distinguish muon-
1841 like events, from electron-like or proton-like, using a likelihood cut

1842 In addition to these cuts, RHC neutrino events also have to undergo the
1843 following cuts to aid in the separation of neutrino and antineutrino [195]:

- 1844 • TPC Requirement: The track path must intercept TPC2

- 1845 • Positive Track: The highest momentum track must have positive recon-
1846 structed charge

- 1847 • TPC1 Veto: Remove any events originating upstream of TPC1

1848 Once all CC-inclusive events have been determined, they are further split by
1849 pion multiplicity: CC0 π , CC1 π , and CCOther. These target specific interaction
1850 modes CCQE, CCRES, and other CC background interactions, respectively. Pions
1851 in the TPCs and FGDs are selected by requiring a second track to be observed,
1852 which is separate from the muon track and is in the same beam spill window and
1853 sub-detector. If the pion originated within a FGD, it must also pass through the
1854 sequential downstream TPC (TPC2 for FGD1, TPC3 for FGD2).

1855 CC0 π , CC1 π , and CCOther samples are defined with the following cuts:

1856 **DB: Understand pion cuts at ND**

- 1857 • ν_μ CC0 π **Selection:** No electrons in TPC and no charged pions or decay
1858 electrons within the TPC or FGD

- 1859 • ν_μ CC1 π **Selection:** Exactly one charged pion in either the TPC or FGD,
1860 where the number of charged pions in the FGD is equal to the number of
1861 decay electrons

- 1862 • ν_μ CCOther **Selection:** All events which are not classified into the above
1863 two selections.

Counting the three selections for each FGD in FHC and RHC running, including the wrong-sign background in RHC, 18 near detector samples are used within this analysis. These samples are binned in reconstructed lepton momentum (illustrated in Figure 6.3) and direction with respect to the beam. The binning is chosen such that each event has at least 20 Monte Carlo events in each bin [194]. This is to ensure that the bins are coarse enough to ensure the reduction of statistical errors, whilst also being fine enough to sample the high-resolution peak regions. The exact binning is detailed in [194].

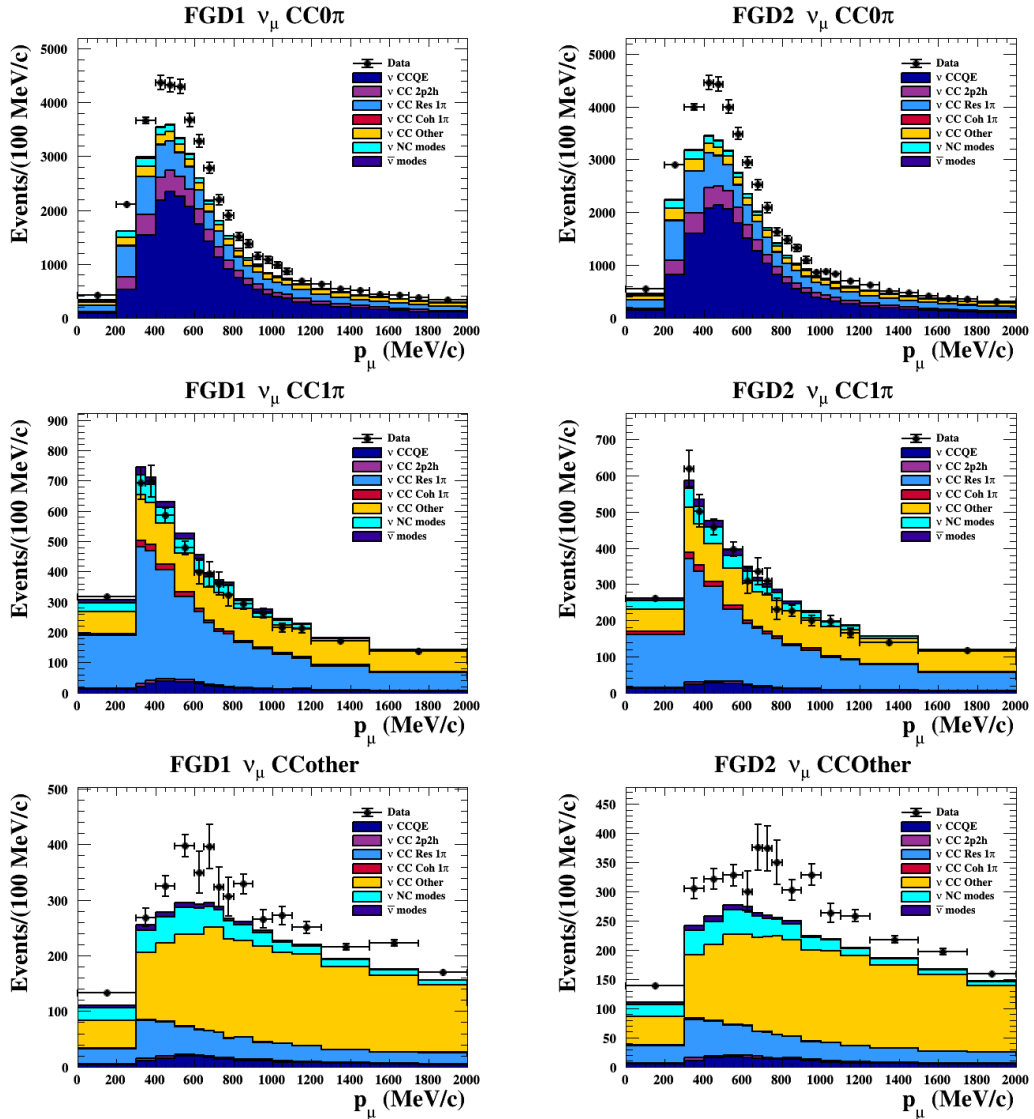


Figure 6.3: The nominal Monte Carlo predictions compared to data for the FGD1 and FGD2 samples in neutrino beam mode, broken down into the $CC\nu_\mu 0\pi$, $CC\nu_\mu 1\pi$ and $CC\nu_\mu$ Other categories. Figures taken from [192].

1872 6.3 Far Detector Beam Samples

1873 The beam neutrino events which occur at the SK detector, which pass the
 1874 reduction cuts detailed in section 5.3, are separated based on whether the beam
 1875 was operating in FHC or RHC mode. The events are then separated into three
 1876 samples: electron-like ($1Re$), muon-like ($1R\mu$), and $CC1\pi^+$ -like ($1Re1de$) which
 1877 are observed as electron-like events with an associated decay electron [183].
 1878 As discussed in section 6.1, positively charged pions emitted from neutrino
 1879 interactions are more likely to produce decay electrons than negatively charged
 1880 pions. Consequently, the $CC1\pi^+$ -like sample is only selected when the beam is
 1881 operating in FHC mode. Therefore, five beam samples measured at SK are
 1882 used in this analysis.

1883 The fiducial volume definition for beam samples is slightly different from that
 1884 used for the atmospheric samples. It uses both the distance to the closest wall
 1885 (`dWall`) and the distance to the wall along the trajectory of the particle (`toWall`).
 1886 This allows events that originate close to the wall but are facing into the tank to be
 1887 included within the analysis, which would have otherwise been removed. These
 1888 additional events are beneficial for a statistics-limited experiment. The exact
 1889 cut values for both `dWall` and `toWall` are different for each of the three types of
 1890 sample and are optimised based on T2K sensitivity to δ_{CP} [181, 196]. They are:

1891 **1Re event selection** For an event to be classified as a $1Re$ -like, the event must sat-
 1892 isfy:

- 1893 • Fully-contained and have $dWall > 80\text{cm}$ and $toWall > 170\text{cm}$
- 1894 • Total of one ring which is reconstructed as electron-like with reconstructed
 1895 momentum $P_e > 100\text{MeV}$
- 1896 • Zero decay electrons are associated with the event
- 1897 • Passes π^0 rejection cut discussed in section 5.2

1898 The zero decay electron cut removes non-CCQE interactions and the π^0
 1899 rejection cut is designed to remove neutral current π^0 background events which
 1900 can be easily reconstructed as 1Re-like events.

1901 The zero decay electron cut removes non-CCQE interactions and the π^0
 1902 rejection cut is designed to remove neutral current π^0 background events which
 1903 can be easily reconstructed as 1Re-like events.

1904 **CC1 π^+ event selection** This event selection is very similar to that of the 1Re
 1905 sample. The only differences are that the `dWall` and `toWall` criteria are changed
 1906 to $> 50\text{cm}$ and $> 270\text{cm}$, respectively, and exactly one decay electron is required
 1907 from the π^+ decay.

1908 **1R μ event selection** A 1R μ -like event is determined by the following cuts:

- 1909 • Fully-contained and have `dWall` $> 50\text{cm}$ and `toWall` $> 250\text{cm}$
- 1910 • Total of one ring which is reconstructed as muon-like with reconstructed
 1911 momentum $P_\mu > 200\text{MeV}$
- 1912 • Fewer than two decay electrons are associated with the event
- 1913 • Passes π^+ rejection cut discussed in section 5.2

1914 All of these samples are binned in reconstructed neutrino energy. This is
 1915 possible under a particular interaction mode assumption, as the direction from
 1916 the source is known extremely well. For the 1Re-like and 1R μ -like samples,

$$E_\nu^{rec} = \frac{(M_N - V_{nuc})E_l - m_l^2/2 + M_N V_{nuc} - V_{nuc}^2/2 + (M_P^2 + M_N^2)/2}{M_N - V_{nuc} - E_l + P_l \cos(\theta_{beam})} \quad (6.2)$$

1917 Where M_N , M_P and m_l are the masses of the neutron, proton and outgoing
 1918 lepton, respectively. $V_{nuc} = 27\text{MeV}$ is the binding energy of the oxygen nucleus
 1919 [183], θ_{beam} is the angle between the beam and the direction of the outgoing
 1920 lepton, and E_l and P_l are the energy and momentum of that outgoing lepton.

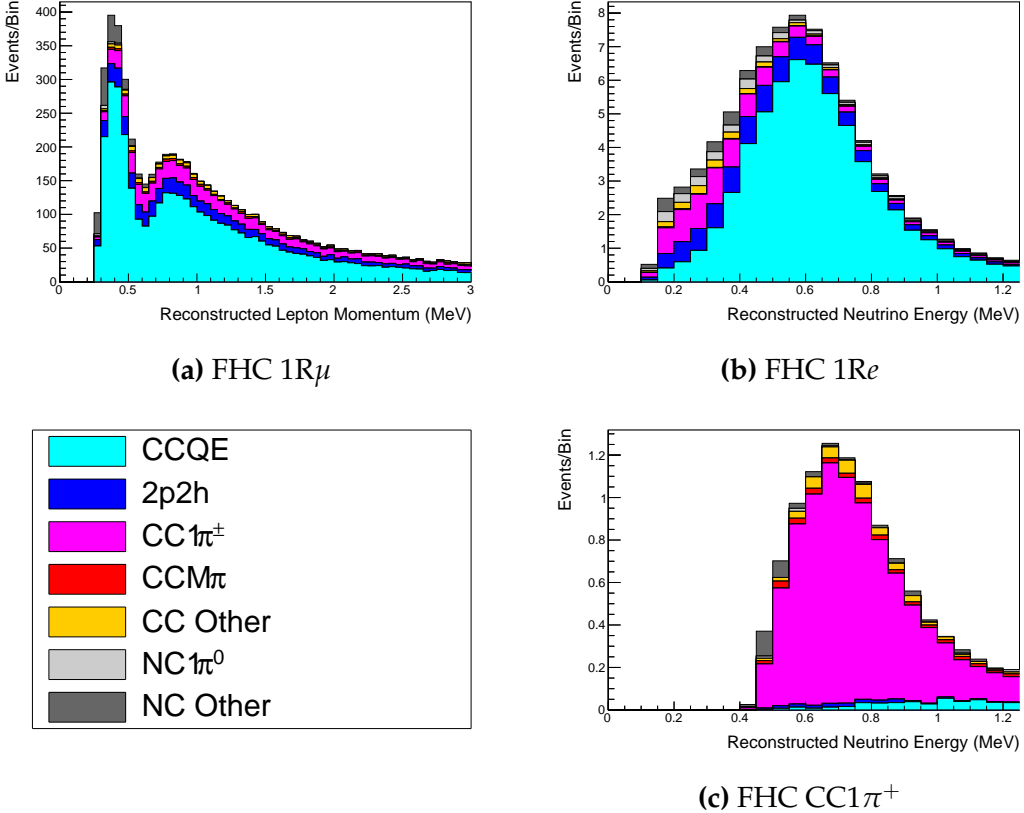


Figure 6.4: The reconstructed neutrino energy, as defined by Equation 6.2 and Equation 6.3, for the 1R μ -like, 1Re-like and CC1 π^+ -like samples. Asimov A oscillation parameter sets are assumed (given in Table 2.2). These samples are the FHC mode samples. For ease of viewing, the 1R μ sample only shows the $0 \leq E_\nu^{rec} < 3.0\text{GeV}$ but the binning extends to 30.0GeV.

1921 The reconstructed neutrino energy of the CC1 π^+ -like events also accounts
 1922 for the delta resonance produced within the interaction,

$$E_\nu^{rec} = \frac{2M_N E_l + M_{\Delta^{++}}^2 - M_N^2 - m_l^2}{2(M_N - E_l + P_l \cos(\theta_{beam}))} \quad (6.3)$$

1923 Where $M_{\Delta^{++}}$ is the mass of the delta baryon. Binding energy effects are not
 1924 considered as a two-body process with the delta baryon is assumed. This follows
 1925 the T2K oscillation analysis presented in [76], although recent developments
 1926 of the interaction model in the latest T2K oscillation analysis do include effects
 1927 from binding energy in this calculation [197].

1928 The reconstructed neutrino energy for the FHC samples is illustrated in
 1929 Figure 6.4. As expected, the 1R μ -like and 1Re-like samples are heavily dominated

by CCQE interactions, with smaller contributions from 2p2h meson exchange and resonant pion production interactions. The CC $1\pi^+$ -like sample predominantly consists of charged current resonant pion production interactions. The 1Re-like and CC $1\pi^+$ -like samples are also binned by the angle between the neutrino beam and the reconstructed lepton momentum. This is to aid in charged current and neutral current separation, as indicated in Figure 6.5. This is because the neutral current backgrounds are predominantly due to π^0 -decays, where the opening angle of the two gammas alongside the different final state kinematics produces a slightly broader angular distribution compared to the final state particles originating from charged current ν_e interactions.

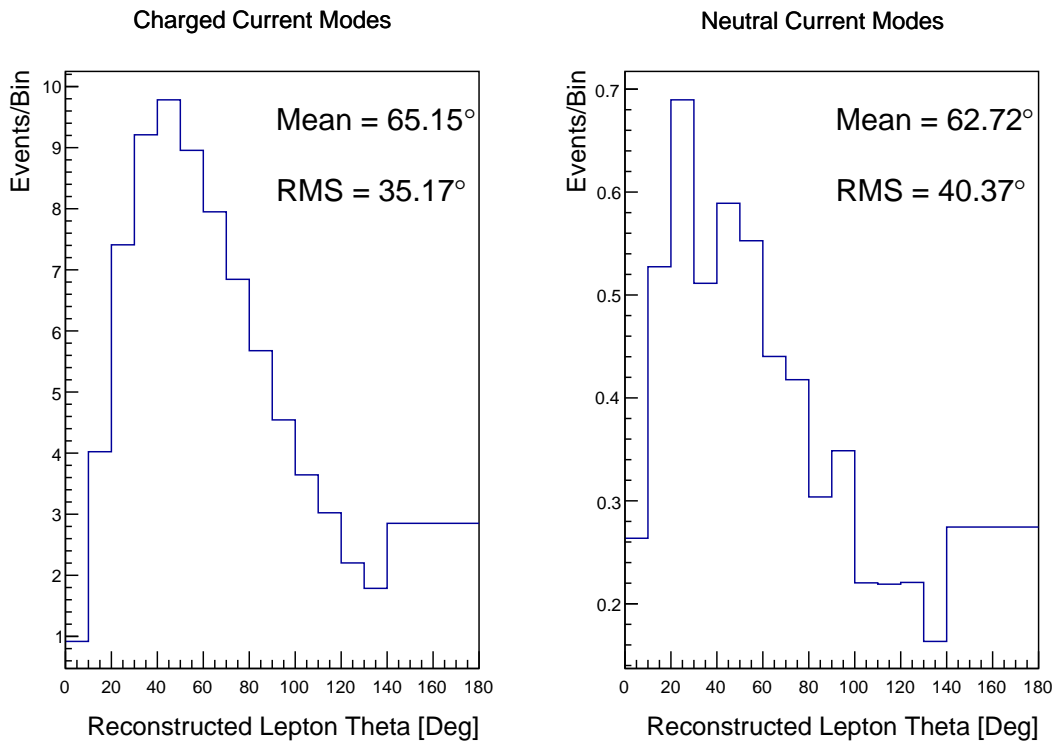


Figure 6.5: The distribution of the angle between the neutrino beam direction and the reconstructed final state lepton, for the FHC 1Re-like sample. The distribution is broken down by neutrino interaction mode into charged current (left) and neutral current (right) components. Asimov A oscillation parameter sets are assumed (given in Table 2.2). The RMS of the charged and neutral current plots are 35.17° and 40.37° , respectively.

1940 6.4 Systematic Uncertainties

1941 The systematic model parameters for this analysis are split into groups, or blocks,
 1942 depending on their purpose. They consist of flux uncertainties, neutrino-matter
 1943 interaction systematics, and detector efficiencies. There are also uncertainties on
 1944 the oscillation parameters which this analysis is not sensitive to, namely Δm_{12}^2
 1945 and $\sin^2(\theta_{12})$. These oscillation parameters uncertainties are taken from the 2020
 1946 PDG measurements [77]. As described in chapter 4, each model parameter used
 1947 within this analysis requires a prior uncertainty. This is provided via separate
 1948 covariance matrices for each block. The covariance matrices can include prior
 1949 correlations between parameters within a single block, but the separate treatment
 1950 means prior correlations can not be included for parameters in different groups.
 1951 Some parameters in these models have no reasonably motivated uncertainties
 1952 and are assigned flat priors which do not modify the likelihood penalty. In
 1953 practice, these flat prior parameters are actually assigned a Gaussian with a
 1954 very large width to ensure the covariance matrix is positive definite. They are
 1955 then checked at run time to determine if they contribute to the likelihood. The
 1956 flux, neutrino interaction, and detector modeling simulations have already been
 1957 discussed in section 5.1 and section 5.2. The uncertainties invoked within each
 1958 of these models are described below.

1959 6.4.1 Beam Flux

1960 The neutrino beam flux systematics are based upon the uncertainty in the mod-
 1961 eling of the components of the beam simulation. This includes the model of
 1962 hadron productions and reinteractions, the shape, intensity, and alignment of
 1963 the beam with respect to the target, and the uniformity of the magnetic field
 1964 produced by the horn, alongside other effects. The uncertainty, as a function
 1965 of neutrino energy, is illustrated in Figure 6.6 which includes a depiction of
 1966 the total uncertainty as well as the contribution from individual components.
 1967 The uncertainty around the peak of the energy distribution ($E_\nu \sim 0.6\text{GeV}$) is

1968 dominated by uncertainties in the beam profile and alignment. Outside of this
1969 region, uncertainties on hadron production dominate the error.

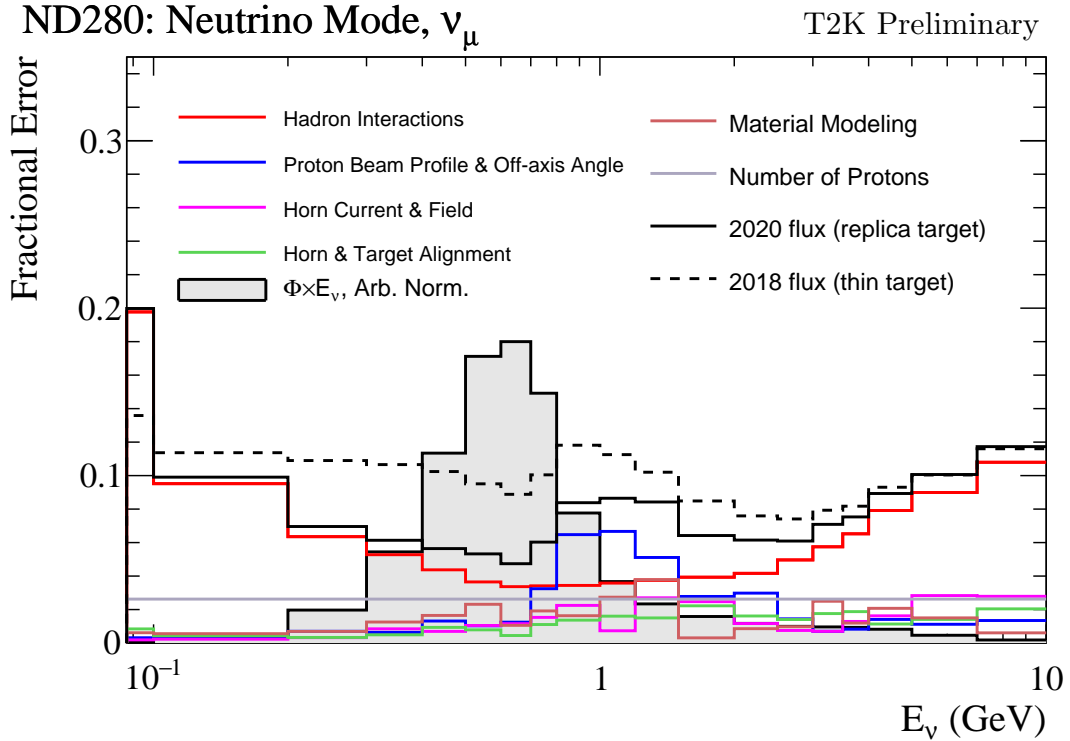


Figure 6.6: The total uncertainty evaluated on the near detector ν_μ flux prediction constrained by the replica-target data, illustrated as a function of neutrino energy. The solid(dashed) line indicates the uncertainty used within this analysis(the T2K 2018 analysis [198]). The solid histogram indicates the neutrino flux as a function of energy. Figure taken from [199].

1970 The beam flux uncertainties are described by one hundred parameters. They
1971 are split between the ND280 and SK detectors and binned by neutrino flavour:
1972 ν_μ , $\bar{\nu}_\mu$, ν_e and $\bar{\nu}_e$. The response is then broken down as a function of neutrino
1973 energy. The bin density in the neutrino energy is the same for the ν_μ in FHC
1974 and $\bar{\nu}_\mu$ in RHC beams, and narrows for neutrino energies close to the oscillation
1975 maximum of $E_\nu = 0.6\text{GeV}$. This binning is specified in Table 6.5. All of these
1976 systematic uncertainties are applied as normalisation parameters with Gaussian
1977 priors centered at 1.0 and error specified from a covariance matrix provided
1978 by the T2K beam group [199].

Neutrino Flavour	Sign	Neutrino Energy Bin Edges (GeV)
μ	Right	0., 0.4, 0.5, 0.6, 0.7, 1., 1.5, 2.5, 3.5, 5., 7., 30.
μ	Wrong	0., 0.7, 1., 1.5, 2.5, 30.
e	Right	0., 0.5, 0.7, 0.8, 1.5, 2.5, 4., 30.
e	Wrong	0., 2.5, 30.

Table 6.5: The neutrino energy binning for the different neutrino flavours. “Right” sign indicates neutrinos in the FHC beam and antineutrinos in the RHC beam. “Wrong” sign indicates antineutrinos in the FHC beam and neutrinos in the RHC beam. The binning of the detector response is identical for the FHC and RHC modes as well as at ND280 and SK.

1979 6.4.2 Atmospheric Flux

1980 The atmospheric neutrino flux is modeled by the HKKM model [52]. 16 systematic
 1981 uncertainties are applied to control the normalisation of each neutrino flavour,
 1982 energy, and direction. They are summarised below:

- 1983 • **Absolute Normalisation:** The overall normalisation of each neutrino flavour
 1984 is controlled by two independent systematic uncertainties, for $E_\nu < 1\text{GeV}$
 1985 and $E_\nu > 1\text{GeV}$, respectively. This is driven mostly by hadronic interaction
 1986 uncertainties for the production of pions and kaons [52]. The strength of
 1987 the response is dependent upon the neutrino energy. The uncertainty is
 1988 parameterized following Figure 11 in [52].
- 1989 • **Relative Normalisation:** Uncertainties on the ratio of $(\nu_\mu + \bar{\nu}_\mu) / (\nu_e + \bar{\nu}_e)$
 1990 are controlled by the difference between the HKKM model [52], FLUKA
 1991 [55] and Bartol models [51]. Three independent parameters are applied in
 1992 the energy ranges: $E_\nu < 1\text{GeV}$, $1\text{GeV} < E_\nu < 10\text{GeV}$, and $E_\nu > 10\text{GeV}$.
- 1993 • **$\nu/\bar{\nu}$ Normalisation:** The uncertainties in the π^+/π^- (and kaon equivalent)
 1994 production uncertainties in the flux of $\nu/\bar{\nu}$. The response is applied using
 1995 the same methodology as the relative normalisation parameters.
- 1996 • **Up/Down and Vertical/Horizontal Ratio:** Similar to the above two sys-
 1997 tematics, the difference between the HKKM, FLUKA, and Bartol model

1998 predictions, as a function of $\cos(\theta_Z)$, is used to control the normalisation of
 1999 events as a function of zenith angle.

- 2000 • **K/π Ratio:** Higher energy neutrinos ($E_\nu > 10\text{GeV}$) mostly originate in
 2001 kaon decay. Measurements of the ratio of K/π production [200] are used to
 2002 control the systematic uncertainty of the expected ratio of pion and kaon
 2003 production.
- 2004 • **Solar Activity:** As the 11-year solar cycle can affect the Earth's magnetic
 2005 field, the flux of primary cosmic rays varies across the same period. The
 2006 uncertainty is calculated by taking a ± 1 year variation, equating to a 10%
 2007 uncertainty for the SK-IV period.
- 2008 • **Atmospheric Density:** The height of the interaction of the primary cosmic
 2009 rays is dependent upon the atmospheric density. The HKKM assumes the
 2010 US standard 1976 [151] profile. This systematic controls the uncertainty in
 2011 that model.

2012 The total uncertainty is dominated by the absolute and relative normalisation
 2013 parameters. The effect of which is illustrated in Figure 6.7. Generally, the
 2014 uncertainty is large at low energy, reducing to $O(10\%)$ around the peak of the
 2015 flux distribution and then increasing once the neutrino energy exceeds 10GeV.

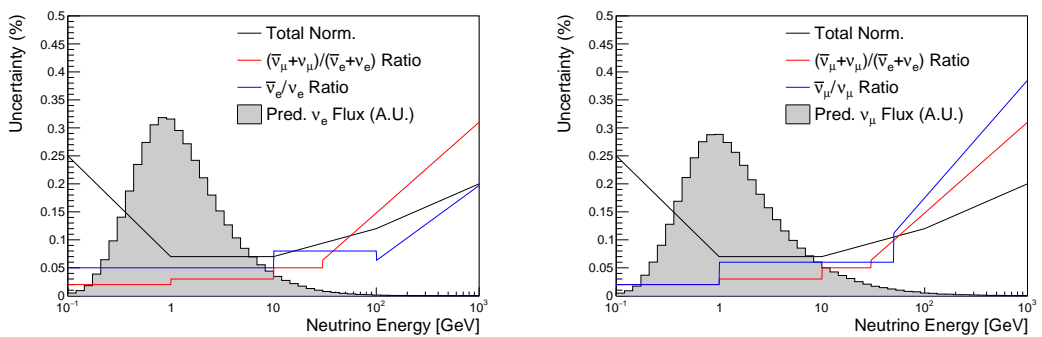


Figure 6.7: The uncertainty evaluated on the atmospheric ν_e (left) and ν_μ (right) flux predictions. The absolute normalisation and flavour ratio uncertainties are given. The solid histogram indicates the neutrino flux as a function of energy.

2016 Updates to the HKKM and Bartol models are underway [156] to use a similar
2017 tuning technique to that used in the beam flux predictions. After those updates,
2018 it may be possible to include correlations in the hadron production uncertainty
2019 systematics for beam and atmospheric flux predictions.

2020 **6.4.3 Neutrino Interaction**

2021 Neutrino interactions in the detectors are modeled by NEUT. The two indepen-
2022 dent oscillation analyses, T2K-only [201] and the SK-only [61], have developed
2023 separate interaction models. To maximise sensitivity out of this simultaneous
2024 beam and atmospheric analysis, a correlated interaction model has been defined
2025 in [202]. Where applicable, correlations allow the systematic uncertainties applied
2026 to the atmospheric samples to be constrained by near detector neutrino beam
2027 measurements. This can lead to stronger sensitivity to oscillation parameters
2028 as compared to an uncorrelated model.

2029 The low-energy T2K systematic model has a more sophisticated treatment
2030 of CCQE, 2p2h, and CCRES uncertainties, where extensive comparisons of
2031 this model have been performed to external data [201]. However, the model
2032 is not designed for high-energy atmospheric events, like those illustrated in
2033 Figure 5.11. Therefore the high energy systematic model from the SK-only
2034 analysis is implemented for the relevant multiGeV, PC, and up- μ samples. The
2035 T2K CCQE model is more sophisticated so it has been implemented for all
2036 samples within this analysis, where separate low-energy and high-energy dials
2037 have been implemented. The low-energy dials are constrained by the near
2038 detector measurements and are uncorrelated to their high-energy counterparts.
2039 The author of this thesis was responsible for implementing and validating the
2040 combined cross section model as documented in [202, 203].

2041 The high energy systematic model includes parameters developed from
2042 comparisons of Nieves and Rein-Seghal models which affect resonant pion
2043 producing interactions, comparisons of the GRV98 and CKMT models which
2044 control DIS interactions, and hadron multiplicity measurements which modulate

the normalisation of multi-pion producing events. The uncertainty on the ν_τ cross-section is particularly large and is controlled by a 25% normalisation uncertainty. These uncertainties are applied via normalisation or shape parameters. The former linearly scales the weight of all affected Monte-Carlo events, whereas the latter can increase or decrease a particular event's weight depending on its neutrino energy and mode of interaction. The response of the shape parameters is defined by third-order polynomial splines which return a weight for a particular neutrino energy. To reduce computational resources for the far detector fit, the response is binned by neutrino energy and sample binning: lepton momentum and cosine zenith binning for atmospheric splined responses and reconstructed neutrino energy and direction binning for beam samples. In total, 17 normalisation and 15 shape parameters are included in the high-energy model within this analysis.

Figure 6.8 indicates the predicted neutrino energy distribution for both beam and subGeV atmospheric samples. There is clearly significant overlap in neutrino energy between the subGeV atmospheric and beam samples, allowing similar kinematics in the final state particles. Figure 6.9 illustrates the fractional contribution of the different interaction modes per sample.

Comparing beam and atmospheric samples which target CCQE interactions (S.G. e-like 0de, S.G. μ -like [0,1]de, [FHC,RHC] 1R μ -like and [FHC,RHC] 1R e-like samples), there is a very similar contribution of CCQE, CC 2p2h, and CC1 π^\pm interactions. The samples which target CC1 π^\pm interactions, (S.G. e-like 0de, S.G. μ -like 2de and FHC 1R+1d.e e-like) also consist of very similar mode interactions.

As a consequence of the similarity in energy and mode contributions, correlating the systematic model between the beam and subGeV atmospheric samples ensures that this analysis attains the largest sensitivity to oscillation parameters while still ensuring neutrino interaction systematics are correctly accounted for. Due to its more sophisticated CCQE and 2p2h model, the T2K systematic model was chosen as the basis of the correlated model.

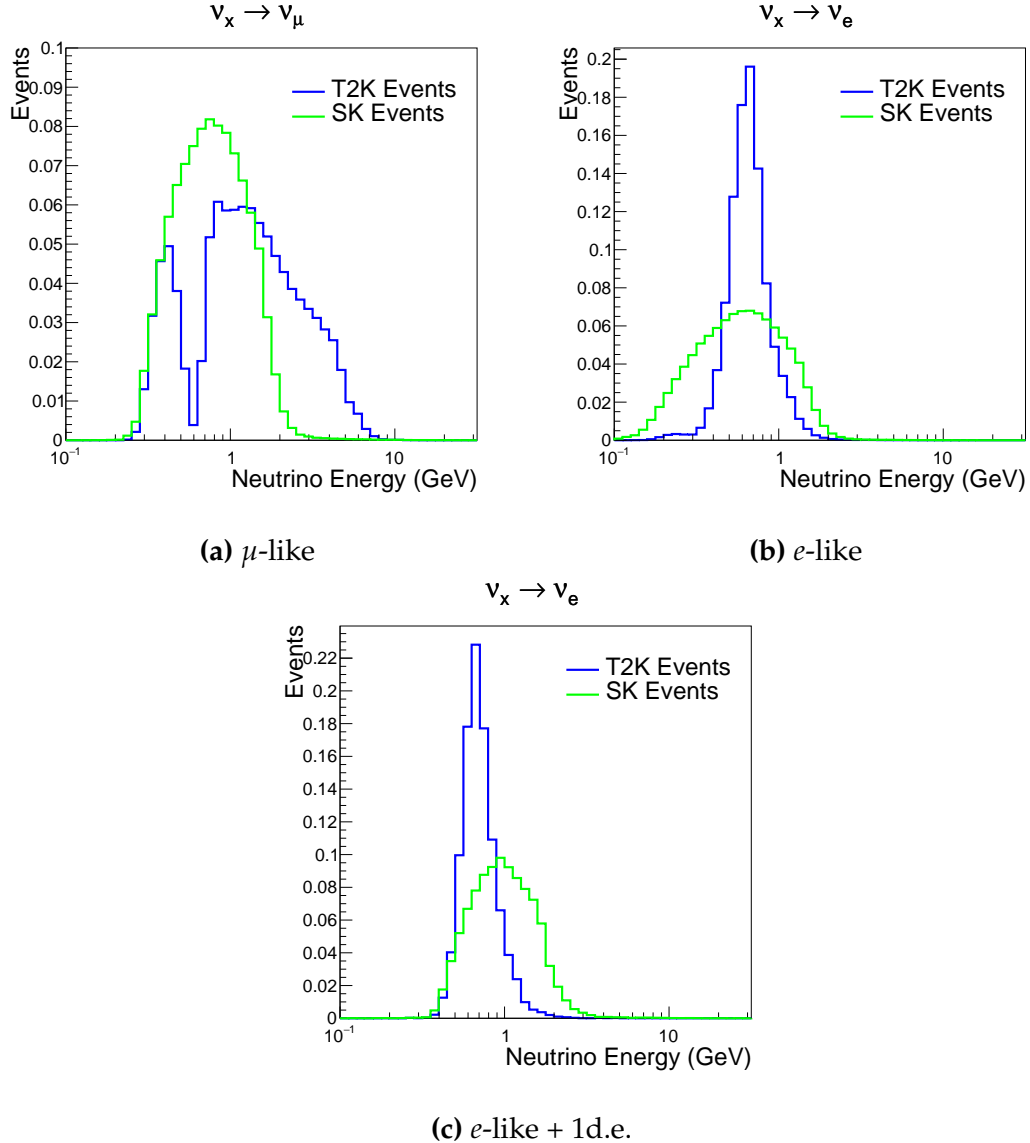


Figure 6.8: The predicted neutrino energy distribution for subGeV atmospheric and beam samples. FHC and RHC beam samples are summed together Asimov A oscillation parameters are assumed (given in Table 2.2). Beam and atmospheric samples with similar cuts are compared against one another.

The T2K systematic model [201] is applied in a similar methodology to the SK model parameters. It consists of 19 shape parameters and 24 normalisation parameters. Four additional parameters, which model the uncertainty in the binding energy, are applied in a way to shift the momentum of the lepton emitted from a nucleus. This controls the uncertainty specified on the 27MeV binding energy assumed within Equation 6.2. The majority of these parameters are

	CC QE	CC 2p2h	CC $1\pi^\pm$	CC $M\pi$	CC Other	NC $1\pi^0$	NC $1\pi^\pm$	NC $M\pi$	NC Coh.	NC Other
FHC 1R+1d.e. e-like	0.04	0.02	0.83	0.03	0.04	0.01	0.01	0.01	0.00	0.01
RHC 1R e-like	0.62	0.12	0.11	0.01	0.02	0.06	0.01	0.01	0.01	0.04
FHC 1R e-like	0.68	0.12	0.10	0.00	0.02	0.04	0.01	0.00	0.00	0.02
RHC 1R μ -like	0.62	0.13	0.17	0.02	0.03	0.00	0.02	0.00	0.00	0.00
FHC 1R μ -like	0.62	0.12	0.16	0.02	0.03	0.00	0.03	0.00	0.00	0.00
S.G. π^0 -like	0.05	0.01	0.02	0.00	0.01	0.68	0.06	0.07	0.06	0.04
S.G. μ -like 2de	0.04	0.01	0.80	0.10	0.04	0.00	0.00	0.00	0.00	0.00
S.G. μ -like 1de	0.72	0.11	0.12	0.01	0.02	0.00	0.01	0.00	0.00	0.00
S.G. μ -like 0de	0.68	0.11	0.10	0.01	0.02	0.01	0.05	0.01	0.00	0.02
S.G. e-like 1de	0.05	0.01	0.75	0.10	0.05	0.00	0.01	0.02	0.00	0.01
S.G. e-like 0de	0.73	0.11	0.10	0.01	0.02	0.02	0.00	0.00	0.00	0.00

Figure 6.9: The interaction mode contribution of each sample given as a fraction of the total event rate in that sample. Asimov A oscillation parameters are assumed (given in Table 2.2). The Charged Current (CC) modes are broken into quasi-elastic (QE), 2p2h, resonant charged pion production ($1\pi^\pm$), multi-pion production ($M\pi$), and other interaction categories. Neutral Current (NC) interaction modes are given in interaction mode categories: π^0 production, resonant charged pion production, multi-pion production, and others.

2081 assigned a Gaussian prior uncertainty. Those that have no reasonably motivated
 2082 uncertainty, or those which have not been fit to external data, are assigned a
 2083 flat prior which does not affect the penalty term.

2084 On top of the combination of the SK and T2K interaction models, several
 2085 other parameters have been specifically developed for the joint oscillation anal-
 2086 ysis. The majority of the atmospheric samples' δ_{CP} sensitivity comes from the
 2087 normalisation of subGeV electron-like events. These are modeled using a spectral
 2088 function to approximate the nuclear ground state. However, the near detector is
 2089 not able to constrain the model so an additional systematic is introduced which
 2090 models applies an alternative Continuous Random Phase Approximation (CRPA)
 2091 nuclear ground state. This dial approximates the event weights if a CRPA model

had been assumed rather than a spectral function. This dial only applies to ν_e and $\bar{\nu}_e$ as the near detector does not constraint ν_e cross-section measurements. It is applied as a shape parameter.

Further additions to the model have been introduced due to the inclusion of the subGeV π^0 atmospheric sample. This particularly targets charged current and neutral current π^0 producing interactions to help constrain the systematic uncertainties. Therefore, an uncertainty that affects neutral current resonant π^0 production is incorporated into this analysis. Comparisons of NEUT's NC resonant pion production predictions have been made to MiniBooNE [204] data and a consistent 16% to 21% underprediction is observed [202]. Consequently, a conservative 30% normalisation parameter is invoked.

Down-going events are mostly insensitive to oscillation parameters and can act similar to the near detector within an accelerator experiment (Details will be discussed in chapter 7). This region of phase space can act as a sideband and allows the cross-section model and near detector constraint to be studied. The distribution of events in this region is calculated using the technique outlined in subsection 4.3.4. The results are illustrated in Figure 6.10. For CCQE-targeting samples, the application of the near detector constraint is well within the statistical fluctuation of the down-going data such that no significant tension is observed between the data and the Monte Carlo prediction after the near detector constraint is applied. This is not the case for samples with target CCRES interactions. The electron-like data is consistent with the constrained prediction at high reconstructed momenta but diverges at lower momentum, whereas the muon-like sample is under-predicted throughout the range of momenta. To combat this disagreement, an additional cross-section systematic dial, specifically designed to inflate the low pion momentum systematics was developed in [202]. This is a shape parameter implemented through a splined response.

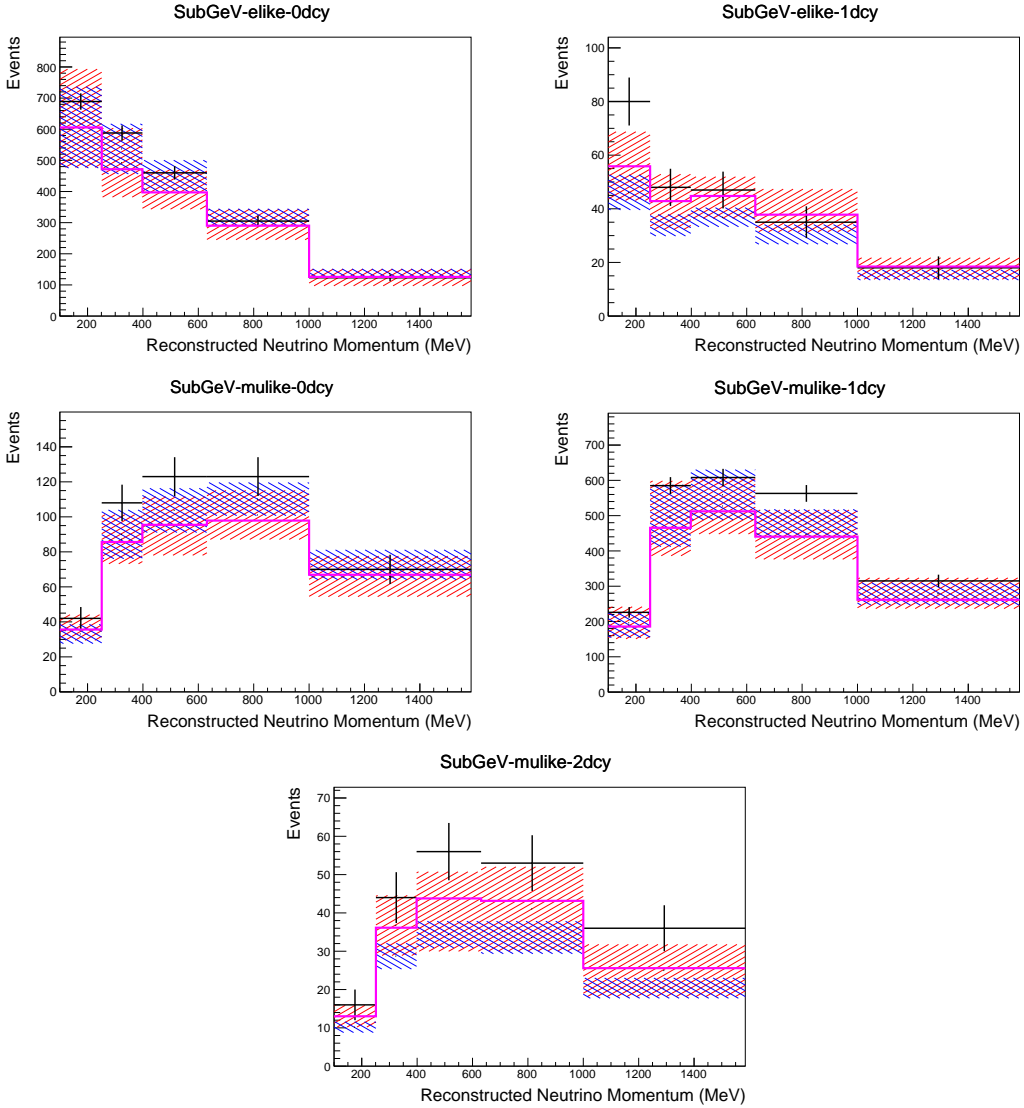


Figure 6.10: Down-going atmospheric subGeV single-ring samples comparing the mean and error of the pre-fit and post-fit Monte Carlo predictions in red and blue, respectively. The magenta histogram illustrates the Monte Carlo prediction using the generated dial values. The black points illustrate the down-going data with statistical errors given. The mean and errors of the Monte Carlo predictions are calculated by the techniques documented in subsection 4.3.4. The pre-fit spectrum is calculated by throwing the cross-section and atmospheric flux dial values from the pre-fit covariance matrix. The post-fit spectrum is calculated by sampling the cross-section dial values from an ND fit MCMC chain, whilst still throwing the atmospheric flux dials from the pre-fit covariance.

2119 6.4.4 Near Detector

2120 The systematics applied due to uncertainties arising from the response of the near
 2121 detector is documented in [131]. The response is described by 574 normalisation
 2122 parameters binned in the selected sample as well as momentum and angle,

2123 P_μ and $\cos(\theta_\mu)$, of the final-state muon. These are applied via a covariance
2124 matrix with each parameter being assigned a Gaussian prior from that covariance
2125 matrix. These normalisation parameters are built from underlying systematics,
2126 e.g. pion secondary interaction systematics, which are randomly thrown and
2127 the variation in each $P_\mu \times \cos(\theta_\mu)$ bin is determined. Two thousand throws are
2128 evaluated and a covariance matrix response is created. This allows significant
2129 correlations between FGD1 and FGD2 samples, as well as adjacent $P_\mu \times \cos(\theta_\mu)$
2130 bins. Statistical uncertainties are accounted for by including fluctuations of each
2131 event's weight from a Poisson distribution.

2132 Similar to the cross-section systematics, MaCh3 and BANFF are used to
2133 constrain the uncertainty of these systematics through independent validations.
2134 Each fitter generates a post-fit covariance matrix which is compared and passed
2135 to the far-detector oscillation analysis working group. As the analysis presented
2136 within this thesis uses the MaCh3 framework, a joint oscillation analysis fit of all
2137 three sets of samples and their respective systematics is performed.

2138 6.4.5 Far Detector

2139 Two configurations of the far detector systematic model implementation have
2140 been considered. Firstly, the far detector systematic uncertainties for beam and
2141 atmospheric samples are taken from their respective analysis inputs, denoted
2142 “official inputs” analysis, with no correlations assumed between the beam and at-
2143 mospheric samples. The beam- and atmospheric-specific inputs are documented
2144 in subsubsection 6.4.5.1 and subsubsection 6.4.5.2. Secondly, an alternative
2145 detector model has been developed which correlates the response of the SK
2146 detector systematics between the beam and atmospheric samples. Here, the
2147 distribution of parameters used for applying event cuts (e.g. electron-muon
2148 PID separation) is modified within the fit. It follows a similar methodology to
2149 the beam far detector systematics implementation but performs a joint fit of
2150 the beam and atmospheric data. This alternative implementation is detailed
2151 in subsubsection 6.4.5.3.

2152 **6.4.5.1 Beam Samples**

2153 There are 45 systematics which describe the response of the far detector to
2154 beam events [183], split into 44 normalisation parameters and one energy scale
2155 systematic. The energy scale systematic is applied as a multiplicative scaling
2156 of the reconstructed neutrino energy. It is estimated from data-to-Monte Carlo
2157 differences in the stopping muon sample in [185] and found to be 2.1%. The
2158 normalisation parameters are assigned a Gaussian error centred at one with
2159 width taken from a covariance matrix. A detailed breakdown of the generation
2160 of the covariance matrix is found in [196]. To build the covariance matrix, a fit
2161 is performed on atmospheric data which has been selected using beam sample
2162 selection cuts. These cuts use the variables, L^i , where the index i is detailed in
2163 Table 6.6. Each L^i is a smear, α , and shift, β parameter such that,

$$L_j^i \rightarrow \bar{L}_j^i = \alpha_j^i L + \beta_j^i \quad (6.4)$$

2164 Where L_j^i (\bar{L}_j^i) correspond to nominal(varied) PID cut parameters given in
2165 Table 6.6. The shift and smear parameters are nuisance parameters with no prior
2166 constraints. They are binned by final-state topology, j , where the binning is given
2167 in Table 6.7. The final-state topology binning is because the detector will respond
2168 differently to events that have one or multiple rings. For example, the detector
2169 will be able to distinguish single-ring events better than two overlapping ring
2170 events, resulting in different systematic uncertainty for one-ring events compared
2171 to two-ring events. This approach is used to allow the cut parameter distributions
2172 to be modified within the fit, allowing for better data to Monte Carlo agreement.

Cut Variable	Parameter Name
0	<code>fitQun e/mu PID</code>
1	<code>fitQun e/pi0 PID</code>
2	<code>fitQun mu/pi PID</code>
3	<code>fitQun Ring-Counting Parameter</code>

Table 6.6: List of cut variables that are included within the shift/smear fit documented in [196].

Category	Description
1e	Only one electron above Cherenkov threshold in the final state
1 μ	Only one muon above Cherenkov threshold in the final state
1e+other	One electron and one or more other charged particles above Cherenkov threshold in the final state
1 μ +other	One muon and one or more other charged particles above Cherenkov threshold in the final state
1 π^0	Only one π^0 in the final state
1 π^\pm or 1p	Only one hadron (typically charged pion or proton) in the final state
Other	Any other final state

Table 6.7: Reconstructed event topology categories on which the SK detector systematics [196] are based.

2173 The mis-modeling of π^0 events is also considered. If one of the two rings
 2174 from a π^0 event is missed, this will be reconstructed as a CC ν_e -like event. This
 2175 is one of the largest systematics hindering the electron neutrino appearance
 2176 analyses. Consequently, additional systematics have been introduced to con-
 2177 strain the mis-modeling of π^0 events in SK, binned by reconstructed neutrino
 2178 energy. To evaluate this systematic uncertainty, a set of “hybrid- π^0 ” samples is
 2179 constructed. These events are built by overlaying one electron-like ring from
 2180 the SK atmospheric neutrino samples or decay electron ring from a stopping
 2181 cosmic ray muon with one simulated photon ring. Both rings are chosen so
 2182 that momenta and opening angle follow the decay kinematics of NC π^0 events
 2183 from the T2K-MC. Hybrid- π^0 Monte Carlo samples with both rings from the
 2184 SK Monte Carlo are produced to compare with the hybrid- π^0 data samples and
 2185 the difference in the fraction of events that pass the ν_e selection criteria is used
 2186 to assign the systematic errors. In order to investigate any data to Monte Carlo
 2187 differences that may originate from either the higher energy ring or lower energy
 2188 ring, two samples are built; a sample in which the electron constitutes the higher
 2189 energy ring from the π^0 decay (called the primary sample) and another one in
 2190 which it constitutes the lower energy ring (called the secondary sample). The
 2191 standard T2K ν_e fitQun event selection criteria are used to select events.

2192 Final contributions to the covariance matrix are determined by supplemen-
 2193 tary uncertainties obtained by comparing stopping muon data to Monte Carlo

2194 prediction, as first introduced in section 5.2. The efficiency of tagging decay
2195 electrons is estimated by the stopping muon data to Monte Carlo differences by
2196 comparing the number of one decay electron events to the number of events with
2197 one or fewer decay electrons. Similarly, the rate at which fake decay electrons
2198 are reconstructed by `f iTQun` is estimated by comparing the number of two decay
2199 electron events to the number of events with one or two reconstructed decay
2200 electrons. The two sources of systematics are added in quadrature weighted by
2201 the number of events with one true decay electron yielding a 0.2% systematic
2202 uncertainty. A fiducial volume systematic of $\pm 2.5\text{cm}$ which corresponds to a 0.5%
2203 shift in the normalisation of events is also applied. Additional normalisation
2204 uncertainties based on neutrino flavour and interaction mode are also defined
2205 in [183, 205, 206].

2206 Two additional sources of uncertainty are included: secondary and photo-
2207 nuclear interactions. These are estimated by varying the underlying parameters
2208 are building a distribution of sample event rates. These contributions are then
2209 added in quadrature to the above covariance matrix.

2210 **DB: Matrix Diagonals from SK Det Matrix**

2211 6.4.5.2 Atmospheric Samples

2212 The detector systematics for atmospheric samples, documented in [86], are split
2213 into two sub-groups: those which are related to particle identification and ring
2214 counting systematics, and those which are related to calibration, separation,
2215 and reduction uncertainties.

2216 The particle identification systematics consist of five parameters. The ring sep-
2217 aration systematic enforces an anti-correlated response between the single-ring
2218 and multi-ring samples. This is implemented as a fractional increase/decrease
2219 in the overall normalisation of each sample, depending on the distance to the
2220 nearest wall from an event's vertex. The coefficients of the normalisation are
2221 estimated prior to the fit and depend on the particular atmospheric sample. Two
2222 electron-muon separation systematics are included within this model which

2223 anti-correlate the response of the electron-like and muon-like samples: one for
2224 single-ring events and another for multi-ring events.

2225 The multi-ring electron-like separation likelihood, discussed in section 6.1,
2226 encodes the ability of the detector to separate neutrino from anti-neutrino events.
2227 Two normalisation parameters vary the relative normalisation of multi-ring ν_e
2228 and $\bar{\nu}_e$ samples whilst keeping a consistent overall event rate.

2229 There are 22 systematics related to calibration measurements, including effects
2230 from backgrounds, reduction, and showering effects. They are documented in
2231 [86] and are briefly summarised in Table 6.8. They are applied via normalisation
2232 parameters, with the separation systematics requiring the conservation of event
2233 rate across all samples.

2234 6.4.5.3 Correlated Detector Model

2235 A complete uncertainty model of the SK detector would be able to determine
2236 the systematic shift on the sample spectra for a variation of the underlying
2237 parameters, e.g. PMT angular acceptance. However, this is computationally
2238 intensive, requiring Monte Carlo predictions to be made for each plausible
2239 variation. Consequently, an effective parameter model has been utilised for
2240 a correlated detector model following from the T2K-only model implementation
2241 documented in subsubsection 6.4.5.1. It correlates the detector systematics
2242 between the far-detector beam and subGeV atmospheric samples due to their
2243 similar energies and interaction types. As there are no equivalent beam samples,
2244 the multiGeV, multiring, PC, and Up- μ samples will be subject to the particle
2245 identification systematics implementation as described in subsubsection 6.4.5.2
2246 rather than using this correlated detector model. The calibration systematics also
2247 described in the aforementioned chapter still apply to all atmospheric samples.

2248 The correlated detector model utilises the same smear and shift parameters
2249 documented in subsubsection 6.4.5.1, split by final state topology. Beyond this,
2250 the shift and smear parameters are split by visible energy deposited within the
2251 detector, with binning specified in Table 6.9. This is because atmospheric events

Index	Description
0	Partially contained reduction
1	Fully contained reduction
2	Separation of fully contained and partially contained events
3	Separation of stopping and through-going partially contained events in top of detector
4	Separation of stopping and through-going partially contained events in barrel of detector
5	Separation of stopping and through-going partially contained events in bottom of detector
6	Background due to cosmic rays
7	Background due to flasher events
8	Vertex systematic moving events into and out of fiducial volume
9	Upward going muon event reduction
10	Separation of stopping and through-going in upward going muon events
11	Energy systematic in upward going muon events
12	Reconstruction of the path length of upward going muon events
13	Separation of showering and non-showering upward going muon events
14	Background of stopping upward going muon events
15	Background of non-showering through-going upward going muon events
16	Background of showering through-going upward going muon events
17	Efficiency of tagging two rings from π^0 decay
18	Efficiency of decay electron tagging
19	Background from downgoing cosmic muons
20	Asymmetry of energy deposition in tank
21	Energy scale deposition

Table 6.8: Sources of systematic errors specified within the grouped into the “calibration” systematics model.

are categorised by subGeV and multiGeV events based on visible energy, so this splitting is required when correlating the systematic model for beam and atmospheric events. Alongside the technical requirement, higher energy events will be better reconstructed due to fractionally less noise within the detector. As a result of the inclusion of visible energy binning, Equation 6.4 becomes

$$L_{jk}^i \rightarrow \bar{L}_{jk}^i = \alpha_{jk}^i L + \beta_{jk}^i, \quad (6.5)$$

where k is the visible energy bin.

The implementation of this systematic model takes the events reconstructed values of the cut parameters, modifies them by the particular shift and smear

Index	Range (MeV)
0	$30 \geq E_{vis} > 300$
1	$300 \geq E_{vis} > 700$
2	$700 \geq E_{vis} > 1330$
3	$E_{vis} \geq 1330$

Table 6.9: Visible energy binning for which the correlated SK detector systematics are based

parameter for that event, and then re-applies event selection. This causes event migration, which is a new feature incorporated into the MaCh3 framework which is only achievable due to the event-by-event reweighting scheme.

Particular care has to be taken when varying the ring counting parameter. This is because the number of rings is a finite value (one-ring, two-rings, etc.) which can not be continuously varied through this shift and smear technique. Consequently a continuous ring counting parameter, RC_i , is calculated for the i^{th} event, following the definition in [182]: the preferred likelihoods from all considered one-ring (L_{1R}) and two-ring (L_{2R}) fits are determined. The difference is computed as $\Delta_{LLH} = \log(L_{1R}) - \log(L_{2R})$. The ring counting parameter is then defined as

$$RC_i = \text{sgn}(\Delta_{LLH}) \times \sqrt{|\Delta_{LLH}|}, \quad (6.6)$$

where $\text{sgn}(x) = x/|x|$. This ring counting parameter corresponds to an intermediate likelihood value used within the `fitQun` algorithm to decide the number of rings associated with a particular event. However, fake-ring merging algorithms are applied after this likelihood value is used. Consequently, this ring counting parameter does not always exactly correspond to the number of reconstructed rings. This can be seen in Figure 6.11.

As the `fitQun` algorithm does not provide a likelihood value after the fake-ring algorithms have been applied, the ring counting parameter distribution is correlated to the final number of reconstructed rings through “maps”. These are two-dimensional distributions of the ring counting parameter and the final number of reconstructed rings. An example is illustrated in Figure 6.12. In principle,

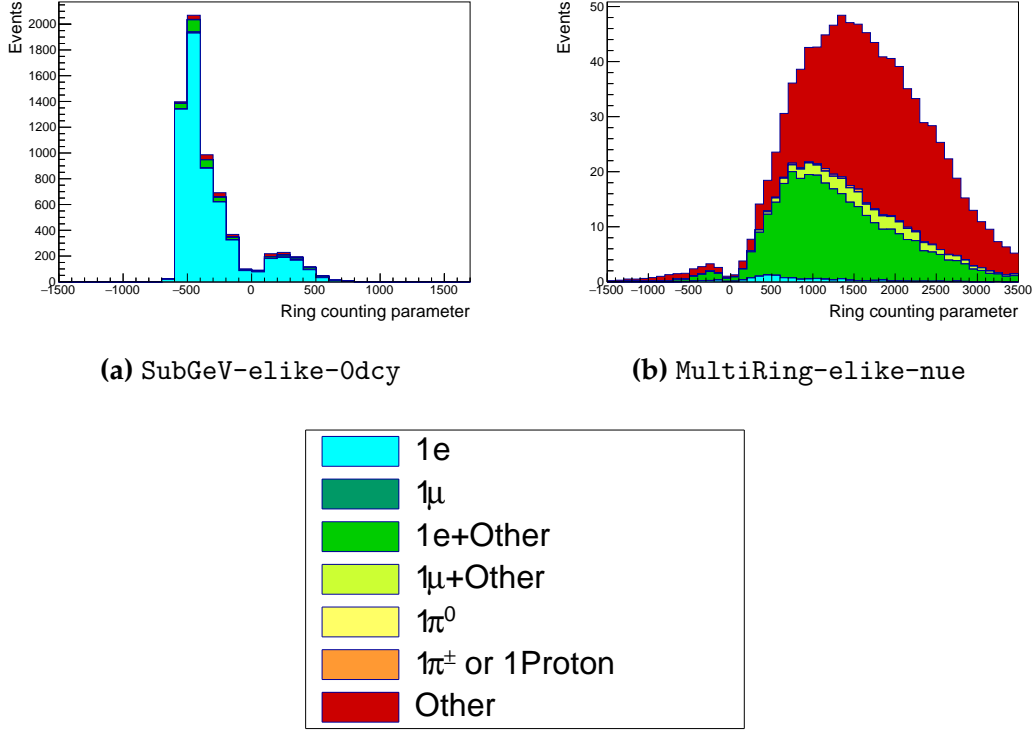


Figure 6.11: The ring counting parameter as defined in Equation 6.6 for the SubGeV-else-like-0dcy and MultiRing-else-like-nue samples.

the `fitQun` reconstruction algorithm should be re-run after the variation in the ring counting parameter. However, this is not computationally viable. Therefore the “maps” are used as a reweighting template.

The maps are split by final state topology and true neutrino flavour and all `fitQun`-reconstructed Monte Carlo events are used to fill them. The maps are row-normalised to represent the probability of X rings for a given RC_i value. Prior to the oscillation fit, an event’s nominal weight is calculated as $W^i(N_{Rings}^i, L_{jk}^i)$, where N_{Rings}^i is the reconstructed number of rings for the i^{th} event and $W^i(x, y)$ is the bin content in map associated with the i^{th} event, where x is the number of rings and y is the ring counting parameter. Then during the fit, the value of $R = W^i(N_{Rings}^i, \bar{L}_{jk}^i) / W^i(N_{Rings}^i, L_{jk}^i)$ is calculated as the event weight for the i^{th} event. This is the only cut variable that uses a reweighting technique rather than event migration.

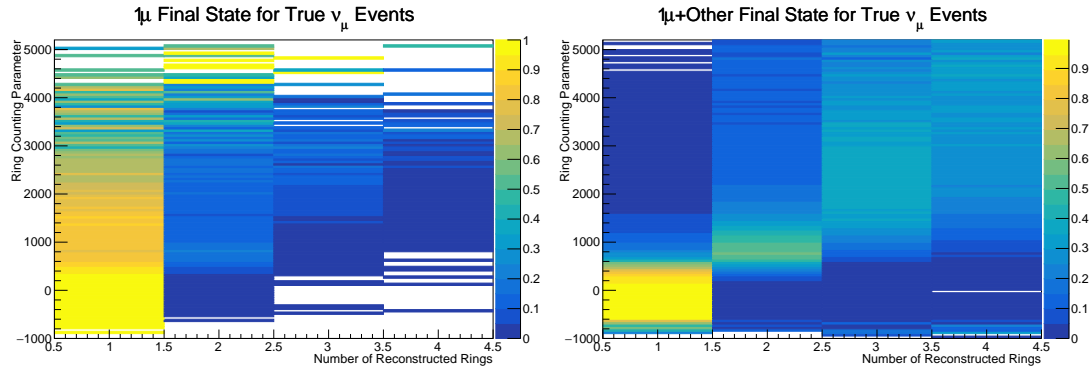


Figure 6.12: The ring counting parameter, defined in Equation 6.6, as a function of the number of reconstructed rings as found by the `fitQun` reconstruction algorithm. Left: true ν_μ events with only one muon above the Cherenkov threshold in the final state. Right: true ν_μ events with one muon and at least one other charged particle above the Cherenkov threshold in the final state.

2295 The π^0 systematics introduced in subsection 6.4.4 are applied via a covariance
 2296 matrix. This is not possible in the alternative model as no covariance matrix
 2297 is used. Thus, the implementation of the π^0 systematics has been modified.
 2298 The inputs from the hybrid π^0 sample are included via the use of “ χ^2 maps”,
 2299 which are two-dimensional histograms in α_{jk}^i and β_{jk}^i parameters over some
 2300 range. Illustrative examples of the χ^2 maps are given in Figure 6.13. Due to
 2301 their nature, the shift and smear parameters are typically very correlated. A
 2302 map is produced for each cut parameter given in Table 6.6 and for each visible
 2303 energy bin given in Table 6.9.

2304 The maps are filled through the χ^2 comparison of the hybrid π^0 Monte Carlo
 2305 and data in the particle identification parameters documented in Table 6.6. The
 2306 Monte Carlo distribution is modified by the α_{jk}^i and β_{jk}^i scaling, whilst cross-
 2307 section and flux nuisance parameters are thrown from their prior uncertainties.
 2308 The χ^2 between the scaled Monte Carlo and data is calculated and the relevant
 2309 point in the χ^2 map is filled.

2310 The implementation within this alternative detector model is to add the bin
 2311 contents of the maps, for the relevant values of the α_{jk}^i and β_{jk}^i parameters, to
 2312 the likelihood penalty. Only 1 π^0 final state topology shift and smear parameters
 2313 use this prior uncertainty.

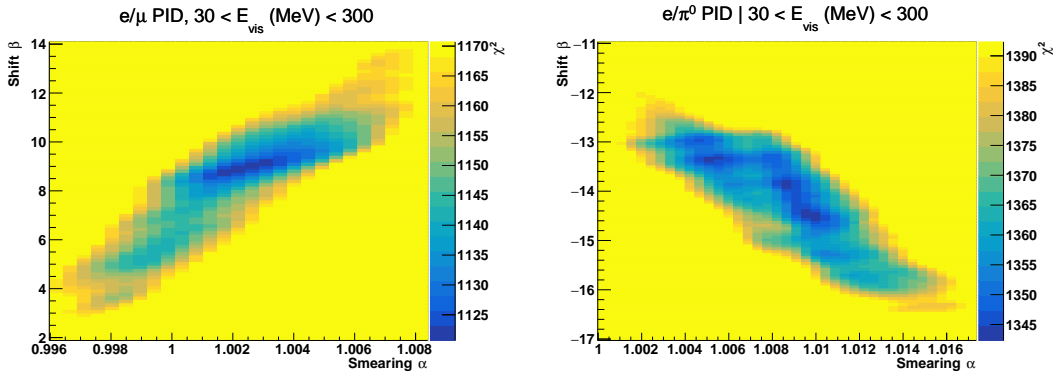


Figure 6.13: The χ^2 between the hybrid- π^0 Monte Carlo and data samples, as a function of smear (α) and shift (β) parameters, for events which have $1\pi^0$ final state topology. Left: Electron-muon separation PID parameter for events with $30 \leq E_{\text{vis}}(\text{MeV}) < 300$. Right: Electron- π^0 separation PID parameter for events with $30 \leq E_{\text{vis}}(\text{MeV}) < 300$.

Similarly, the implementation of the supplementary systematics documented in subsubsection 6.4.5.1 needs to be modified. A new framework [207] was built in tandem with the T2K-SK working group [183] so the additional parameters can be incorporated into the MaCh3 framework. These are applied as normalisation parameters, depending on the particular interaction mode, number of tagged decay electrons, and whether the primary particle generated Cherenkov light. They are assigned Gaussian uncertainties with widths described by a covariance matrix. Furthermore, the secondary interaction and photo-nuclear effects need to be accounted for in this detector model using a different implementation than that in subsubsection 6.4.5.1. This was done by including a shape parameter for each of the secondary interactions and the photo-nuclear systematic parameters.

There are a total of 224 α_{jk}^i and β_{jk}^i parameters, of which 32 have prior constraints from the hybrid π^0 samples.

One final complexity of this correlated detector model is that the two sets of samples, beam and subGeV atmospheric, use slightly different parameters to distinguish electron and muon-like events. The T2K samples use the value of $\log(L_e/L_\mu)$ whereas the atmospheric samples use the value of $\log(L_e/L_\pi)$, where L_X is the likelihood for hypothesis X. This is because the T2K fits use single-ring `f1TQun` fitting techniques, whereas multi-ring fits are applied to the atmospheric samples where only the electron and pion hypothesis are considered.

2334 The correlation between the two likelihood ratios is illustrated in Figure 6.14. As
 2335 discussed in section 5.2, the pion hypothesis is a very good approximation of the
 2336 muon hypothesis due to their similar mass. Consequently, using the same shift
 2337 and smear parameters correlated between the beam and subGeV atmospheric
 2338 samples is deemed a good approximation.

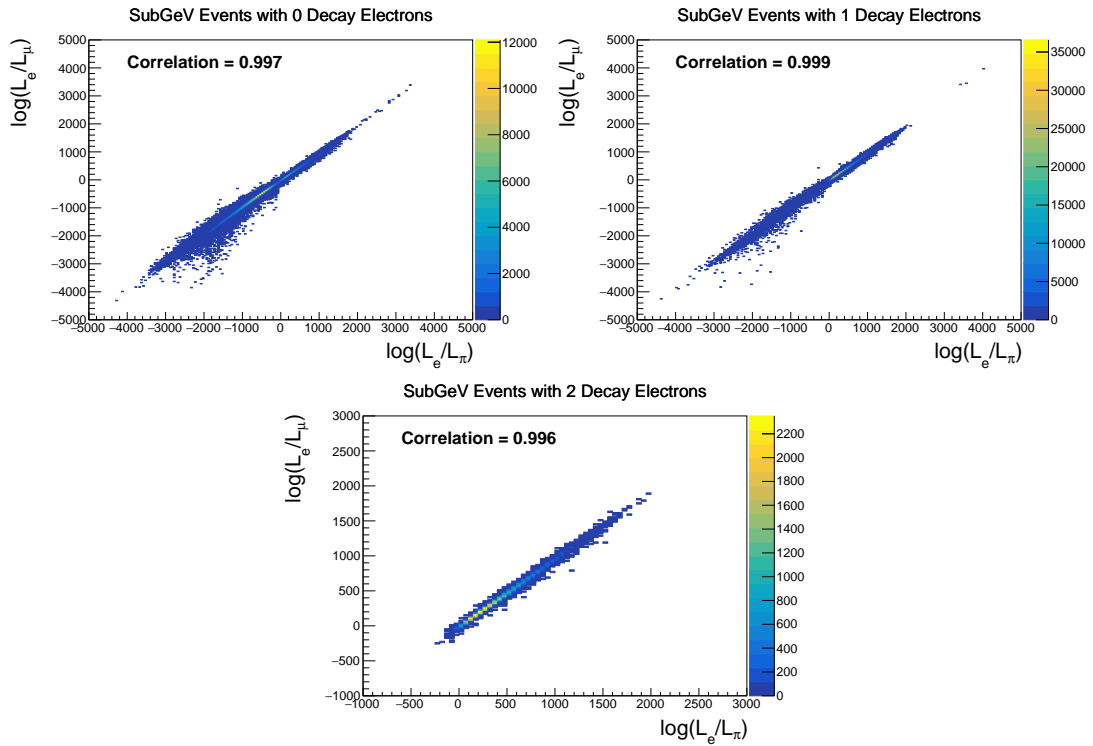


Figure 6.14: The distribution of $\log(L_e/L_\mu)$ compared to $\log(L_e/L_\pi)$ for subGeV events with zero (top left), one (top right) or two (bottom) decay electrons. The correlation in the distribution is calculated as 0.997, 0.999 and 0.996, respectively.

7

2339

2340

Oscillation Probability Calculation

2341 It is important to understand how and where the sensitivity to the oscillation
2342 parameters comes from for both atmospheric and beam samples. An overview
2343 of how these samples observe changes in δ_{CP} , Δm^2_{23} , and $\sin^2(\theta_{23})$ affect
2344 these samples is given in section 7.1. This section also explains the additional
2345 complexities involved when performing an atmospheric neutrino analysis as
2346 compared to a beam-only analysis.

2347 Without additional techniques, atmospheric sub-GeV upward-going neutrinos ($E_\nu < 1.33\text{GeV}, \cos(\theta_Z) < 0.$) can artificially inflate the sensitivity to δ_{CP}
2348 due to the quickly varying oscillation probability in this region. Therefore, a
2349 “sub-sampling” approach has been developed to reduce these biases ensuring
2350 accurate and reliable sensitivity measurements. This technique ensures that small-
2351 scale unresolvable features of the oscillation probability have been averaged over
2352 whilst the large-scale features in the oscillation probability are unaffected. The
2353 documentation and validation of this technique are found in section 7.2. The
2354 oscillation probability calculation is computationally intensive due to the large
2355 number of matrix multiplications needed. Consequently, the CUDAProb3 imple-
2356 mentation choice made within the fitting framework, as detailed in section 7.3,
2357 ensures that the analysis can be done in a timely manner.

Whilst the beam neutrinos are assumed to propagate through a constant density slab of material, the density variations through the Earth result in more complex oscillation patterns for atmospheric neutrinos. Furthermore, the uncertainty in the electron density can modify the oscillation probability for the denser core layers of the Earth. The model of the Earth used within this analysis is detailed in section 7.4. This includes information about the official SK-only methodology as well as improvements that have been made to remove some of the approximations used in that analysis. Another complexity of atmospheric neutrinos oscillation studies is that the height of production in the atmosphere is not known on an event-by-event basis. An analytical averaging technique that approximates the uncertainty of the oscillation probability has been followed, with the author of this thesis being responsible for the implementation and validation.

This implementation of an external technique is illustrated in section 7.5.

7.1 Overview

DB: Should this be moved into an earlier chapter? The selections chapter references the matter resonance which has not yet been explained at that point

The analysis presented within this thesis focuses on the determination of oscillation parameters from atmospheric and beam neutrinos. Whilst subject to the same oscillation formalism, the way in which the two samples have sensitivity to the different oscillation parameters differs significantly.

Atmospheric neutrinos have a varying baseline, or “path length”, L , such that the distance each neutrino travels before interacting is dependent upon the zenith angle, θ_Z . As primary cosmic rays can interact anywhere between the Earth’s surface and $\sim 50\text{km}$ above that, the height, h , in the atmosphere at which the neutrino was generated also affects the path length,

$$L = \sqrt{(R_E + h)^2 - R_E^2 (1 - \cos^2(\theta_Z))} - R_E \cos(\theta_Z). \quad (7.1)$$

2384 Where $R_E = 6,371\text{km}$ is the Earth's radius. Consequently, the oscillation
 2385 probability is dependent upon two parameters, $\cos(\theta_Z)$ and E_ν .

2386 The oscillation probability used within this analysis is based on [21]. The
 2387 neutrino wavefunction in the vacuum Hamiltonian evolves in each layer of
 2388 constant matter density via

$$i \frac{d\psi_j(t)}{dt} = \frac{m_j^2}{2E_\nu} \psi_j(t) - \sum_k \sqrt{2} G_F N_e U_{ej} U_{ke}^\dagger \psi_k(t), \quad (7.2)$$

2389 where m_j^2 is the square of the j^{th} vacuum eigenstate mass, E_ν is the neutrino
 2390 energy, G_F is Fermi's constant, N_e is the electron number density and U is the
 2391 PMNS matrix. The transformation $N_e \rightarrow -N_e$ and $\delta_{CP} \rightarrow -\delta_{CP}$ is applied
 2392 for antineutrino propagation. Thus, a model of the Earth's density is required
 2393 for neutrino propagation. Following the official SK-only methodology [208],
 2394 this analysis uses the Preliminary Reference Earth Model (PREM) [209] which
 2395 provides piecewise cubic polynomials as a function of the Earth's radius. This
 2396 density profile is illustrated in Figure 7.1. As the propagator requires layers of
 2397 constant density, the SK methodology approximates the PREM model by using
 2398 four layers of constant density [208], detailed in Table 7.1.

Layer	Outer Radius [km]	Density [g/cm ³]	Chemical composition (Z/A)
Inner Core	1220	13	0.468 ± 0.029
Outer Core	3480	11.3	0.468 ± 0.029
Lower Mantle	5701	5.0	0.496
Transition Zone	6371	3.3	0.496

Table 7.1: Description of the four layers of the Earth invoked within the constant density approximation of the PREM model [209].

2399 The atmospheric neutrino oscillation probabilities can be presented as two di-
 2400 mensional “oscillograms” as illustrated in Figure 7.2. The distinct discontinuities,
 2401 as a function of $\cos(\theta_Z)$, are due to the discontinuous density in the PREM model.

2402 Atmospheric neutrinos have sensitivity to δ_{CP} through the overall event
 2403 rate. Figure 7.3 illustrates the difference in oscillation probability between CP-
 2404 conserving ($\delta_{CP} = 0$) and a CP-violating ($\delta_{CP} = -1.601$) value taken from

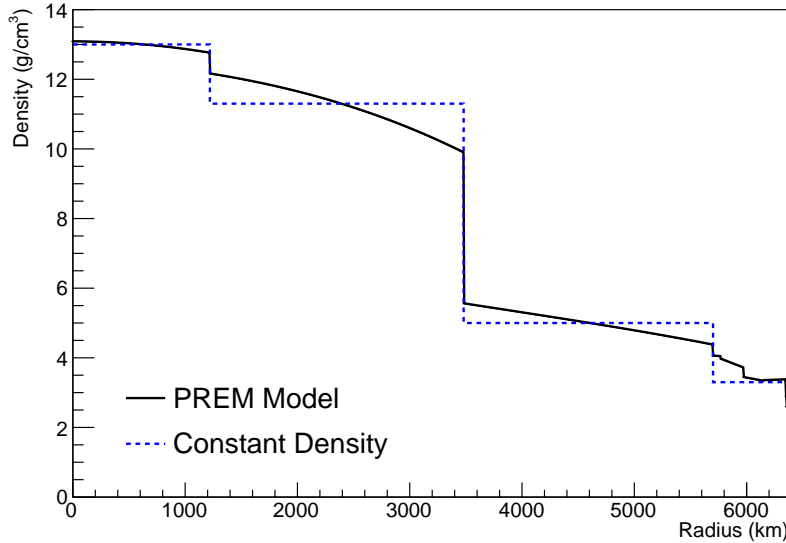


Figure 7.1: The density of the Earth given as a function of the radius, as given by the PREM model (Black), and the constant density four-layer approximation (Blue), as used in the official SK-only analysis.

2405 Asimov A oscillation parameter set (Table 2.2). The result is a complicated
 2406 oscillation pattern in the appearance probability for sub-GeV upgoing neutrinos.
 2407 The detector does not have sufficient resolution to resolve these individual
 2408 patterns so the sensitivity to δ_{CP} for atmospheric neutrinos comes via the overall
 2409 normalisation of these events.

2410 The presence of matter means that the effect δ_{CP} has on the oscillation
 2411 probability is not equal between neutrinos and antineutrinos. Furthermore,
 2412 the interaction cross-section for neutrinos is larger than antineutrinos so the
 2413 two effects have to be disentangled. These effects are further convoluted by
 2414 detector efficiencies as SK cannot distinguish neutrinos and antineutrinos well.
 2415 Furthermore, the sample selections discussed in section 6.1 have difference
 2416 efficiencies for neutrino-antineutrino selections. All of these effects lead to
 2417 a difference in the number of neutrinos detected compared to antineutrinos.
 2418 This changes how the δ_{CP} normalisation term is observed, resulting in a very
 2419 complex sensitivity to δ_{CP} .

2420 The vacuum and matter oscillation probabilities for $P(\nu_e \rightarrow \nu_e)$ and $P(\bar{\nu}_e \rightarrow$

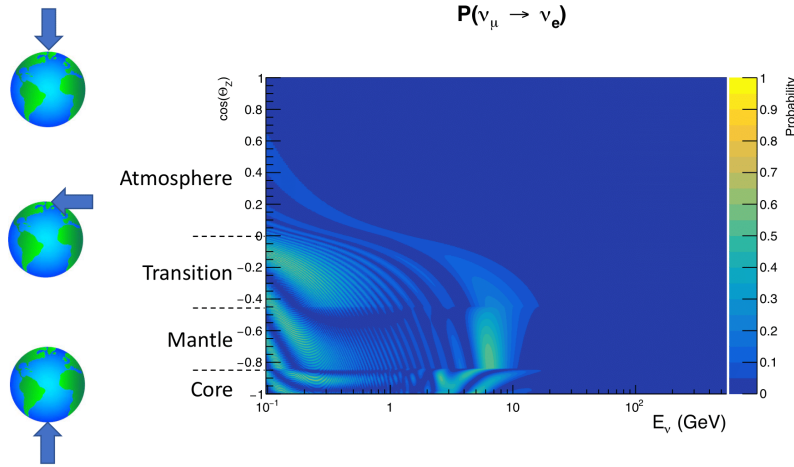


Figure 7.2: An “oscillogram” that depicts the $P(\nu_\mu \rightarrow \nu_e)$ oscillation probability as a function of neutrino energy and cosine of the zenith angle. The zenith angle is defined such that $\cos(\theta_Z) = 1.0$ represents neutrinos that travel from directly above the detector. The four-layer constant density PREM model approximation is used and Asimov A oscillation parameters are assumed (Table 2.2).

$\bar{\nu}_e$) are presented in Figure 7.4, where the PREM model has been assumed.
 The oscillation probability for both neutrinos and antineutrinos is affected in the presence of matter. However, the resonance effects around $O(5)\text{GeV}$ only occur for neutrinos in normal mass hierarchy and antineutrinos in inverse mass hierarchy. The exact position and amplitude of the resonance depend on $\sin^2(\theta_{23})$, further increasing the atmospheric neutrinos’ sensitivity to the parameter.

As the T2K beam flux is centered at the first oscillation maximum ($E_\nu = 0.6\text{GeV}$), the sensitivity to δ_{CP} is predominantly observed as a change in the event-rate of e-like samples in $\nu/\bar{\nu}$ modes. Figure 7.5 illustrates the $P(\nu_\mu \rightarrow \nu_e)$ oscillation probability for a range of δ_{CP} values. A circular modulation of the first oscillation peak (in both magnitude and position) is observed when varying throughout the allowable values of δ_{CP} . The CP-conserving values of $\delta_{CP} = 0, \pi$ have a lower(higher) oscillation maximum than the CP-violating values of $\delta_{CP} = -\pi/2(\delta_{CP} = \pi/2)$. A sub-dominant shift in the energy of the oscillation peak is also present, which aids in separating the two CP-conserving values of δ_{CP} .

T2K’s sensitivity to $\sin^2(\theta_{23})$ and Δm_{23}^2 is observed as a shape-based variation

$$\mathbf{P}(\nu_\mu \rightarrow \nu_e; \delta_{CP} = -1.601) - \mathbf{P}(\nu_\mu \rightarrow \nu_e; \delta_{CP} = 0.)$$

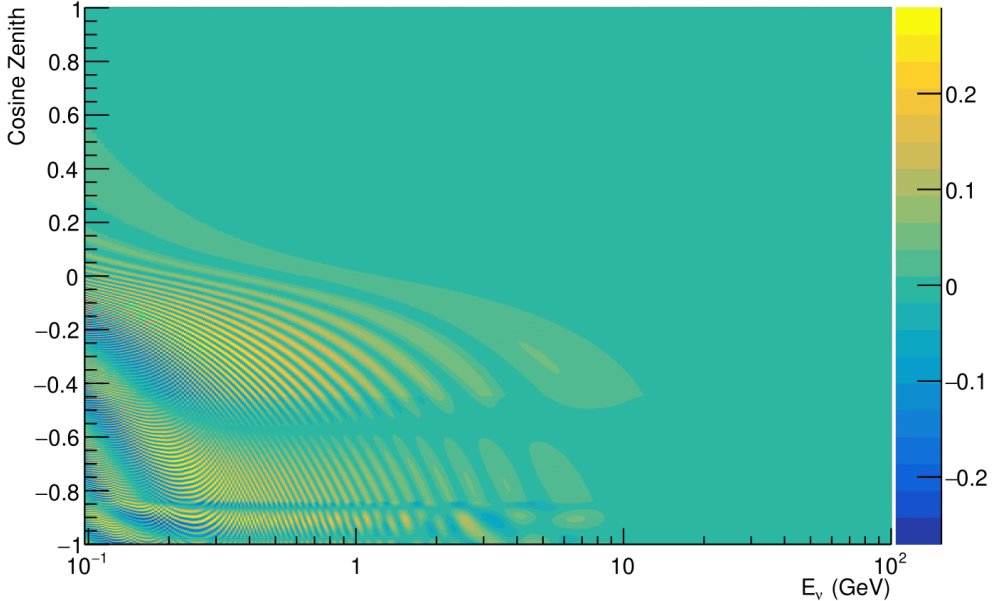


Figure 7.3: The effect of δ_{CP} for atmospheric neutrinos given in terms of the neutrino energy and zenith angle. This oscillogram compares the $P(\nu_\mu \rightarrow \nu_e)$ oscillation probability for a CP conserving ($\delta_{CP} = 0.0$) and a CP violating ($\delta_{CP} = -1.601$) value taken from the Asimov A parameter set. The other oscillation parameters assume the Asimov A oscillation parameter set given in Table 2.2.

of the muon-like samples, as illustrated in Figure 7.5. The value of Δm_{32}^2 laterally shifts the position of the oscillation dip (around $E_\nu \sim 0.6\text{GeV}$) in the $P(\nu_\mu \rightarrow \nu_\mu)$ oscillation probability. A variation of $\sin^2(\theta_{23})$ is predominantly observed as a vertical shift of the oscillation dip with second-order horizontal shifts being due to matter effects. The beam neutrinos have limited sensitivity to matter effects due to the relatively shorter baseline as well as the Earth's mantle being a relatively low-density material (as compared to the Earth's core). For some values of δ_{CP} , the degeneracy in the number of e-like events allows the mass hierarchy to be broken. This leads to a δ_{CP} -dependent mass hierarchy sensitivity which can be seen in Figure 7.6.

Whilst all oscillation channels should be included for completeness, the computational resources required to run a fit are limited and any reasonable approximations which reduce the number of oscillation probability calculations

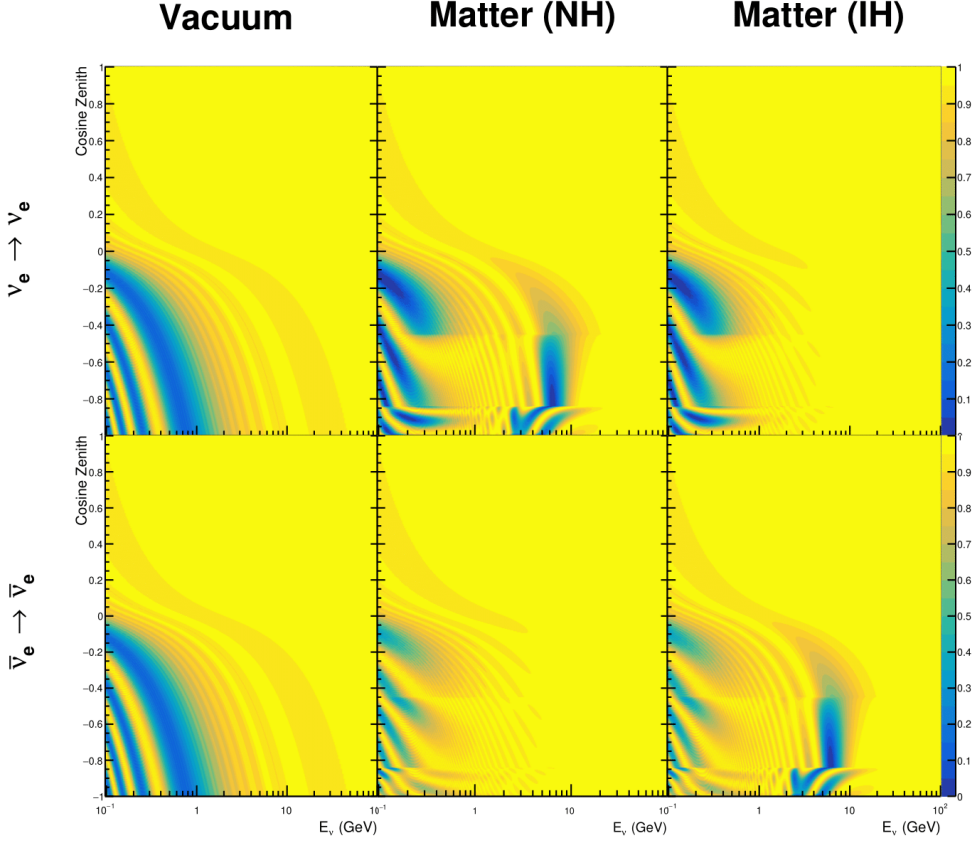


Figure 7.4: An illustration of the matter-induced effects on the oscillation probability, given as a function of neutrino energy and zenith angle. The top row of panels gives the $P(\nu_e \rightarrow \nu_e)$ oscillation probability and the bottom row illustrates the $P(\bar{\nu}_e \rightarrow \bar{\nu}_e)$ oscillation probability. The left column highlights the oscillation probability in a vacuum, whereas the middle and right column represents the oscillation probabilities when the four-layer fixed density PREM model is assumed. All oscillation probabilities assume the “Asimov A” set given in Table 2.2, but importantly, the right column sets an inverted mass hierarchy. The “matter resonance” effects at $E_\nu \sim 5\text{GeV}$ can be seen in the $P(\nu_e \rightarrow \nu_e)$ for normal mass hierarchy and $P(\bar{\nu}_e \rightarrow \bar{\nu}_e)$ for inverted hierarchy.

that need to be made should be applied. The $\nu_e \rightarrow \nu_{e,\mu,\tau}$ (and antineutrino equivalent) oscillations can be ignored for beam neutrinos as the $\nu_e/\bar{\nu}_e$ fluxes are approximately two orders of magnitude smaller than the corresponding $\nu_\mu/\bar{\nu}_\mu$ flux. Furthermore, as the peak neutrino energy of the beam is well below the threshold for charged current tau production ($E_\nu = 3.5\text{GeV}$ [60], only a small proportion of the neutrinos produced in the beam have the required energy. For the few neutrinos that have sufficient energy, the oscillation probability is very

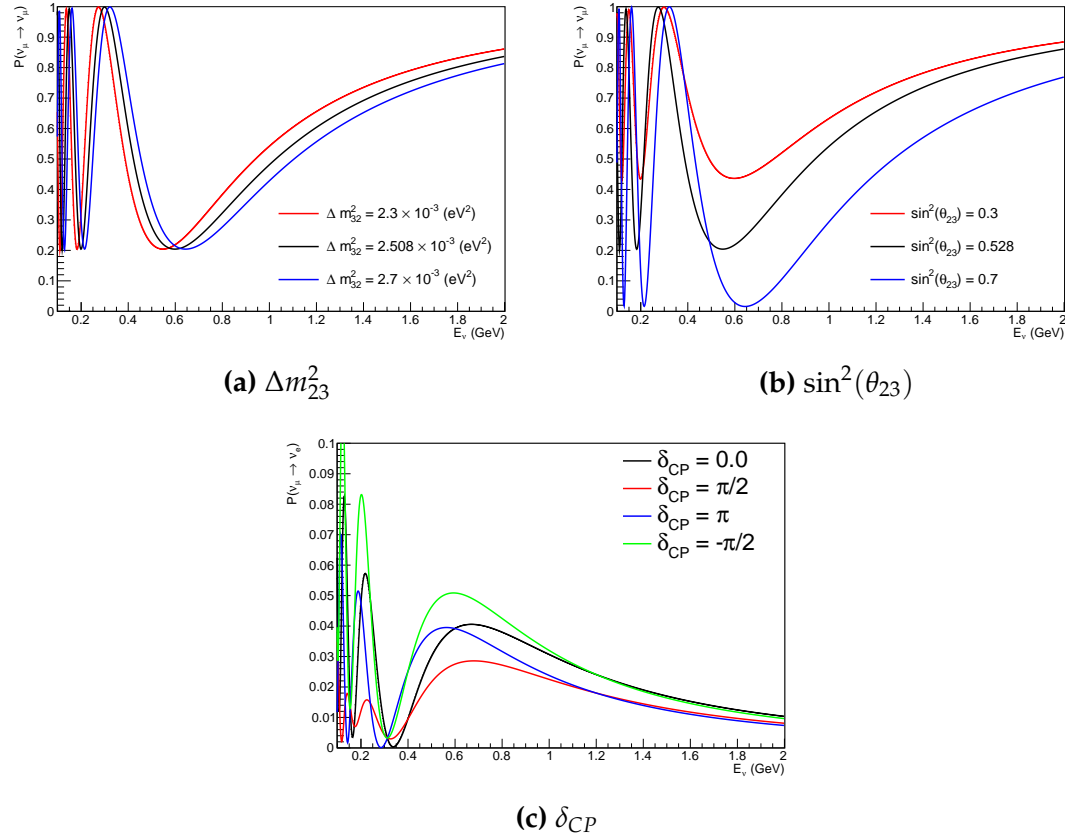


Figure 7.5: The oscillation probability for beam neutrino events given as a function of neutrino energy. All oscillation parameters assume the “Asimov A” set given in Table 2.2 unless otherwise stated. Each panel represents a change in one of the oscillation parameters whilst keeping the remaining parameters fixed.

2457 small due to the short baseline. Whilst these approximations have been made for
 2458 the beam neutrinos, the atmospheric flux of ν_e is of the same order of magnitude
 2459 as the ν_μ flux and the energy distribution of atmospheric neutrinos extends well
 2460 above the tau production threshold.

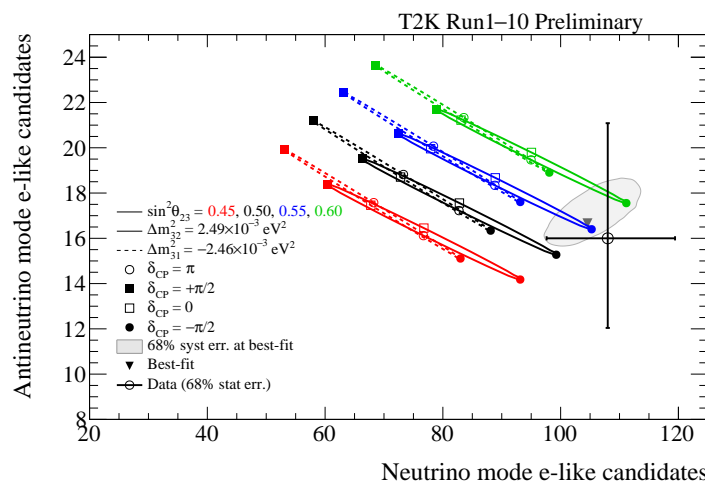


Figure 7.6: The number of electron-like events in the FHC and RHC operating mode of the beam, as a function of the oscillation probabilities. Both normal hierarchy (Solid) and inverse hierarchy (Dashed) values of Δm_{23}^2 are given.

2461 7.2 Treatment of Fast Oscillations

2462 As shown in Figure 7.7, atmospheric neutrino oscillations have a significantly
 2463 more complex structure for upgoing neutrinos with energy below 1GeV. This is
 2464 because the L/E dependence of the oscillation probability in this region induces
 2465 rapid variations for small changes in L or E . As discussed in section 7.1, this
 2466 is also the region in which atmospheric neutrinos have sensitivity to δ_{CP} . In
 2467 practice, the direction of the neutrino is inferred from the direction of the final
 2468 state particles traveling in the detector, which can be poor for low-energy neutrino
 2469 interactions. This creates a distinct difference from the beam neutrinos where
 2470 the position of the source is very precisely known.

2471 As a consequence of the unresolvable structure, an event rate consistent with
 2472 the averaged oscillation probability is observed in the subGeV upgoing region.
 2473 This creates a computational problem: A significantly large amount of Monte
 2474 Carlo statistics would be required to accurately predict the number of events
 2475 if Monte Carlo averaging was the only technique used. This section describes
 2476 the ‘sub-sampling’ approach developed for this analysis and compares it to the
 2477 methodology used within the SK-only analysis.

2478 The official SK-only analysis uses the osc3++ oscillation parameter fitter
 2479 [208]. To perform the fast oscillation averaging, it uses a ‘nearest-neighbour’
 2480 technique. For a given Monte Carlo neutrino event, the nearest twenty Monte
 2481 Carlo neighbours in reconstructed lepton momentum and zenith angle are
 2482 found and a distribution of their neutrino energies is built. The RMS, σ , of
 2483 this distribution is then used to compute an average oscillation probability for
 2484 the given neutrino Monte Carlo event.

2485 For the i^{th} event, the oscillation weight is calculated as

$$2486 W_i = \frac{1}{5}P(E_i, \bar{L}_i) + \frac{1}{5}\sum_{\beta=-1, -0.5, 0.5, 1} P(E_i + \beta\sigma_i, L_\beta), \quad (7.3)$$

2486 where $P(E, L)$ is the oscillation probability calculation for neutrino energy
 2487 E and path length L and the two path lengths, \bar{L}_i and L_β are discussed below.

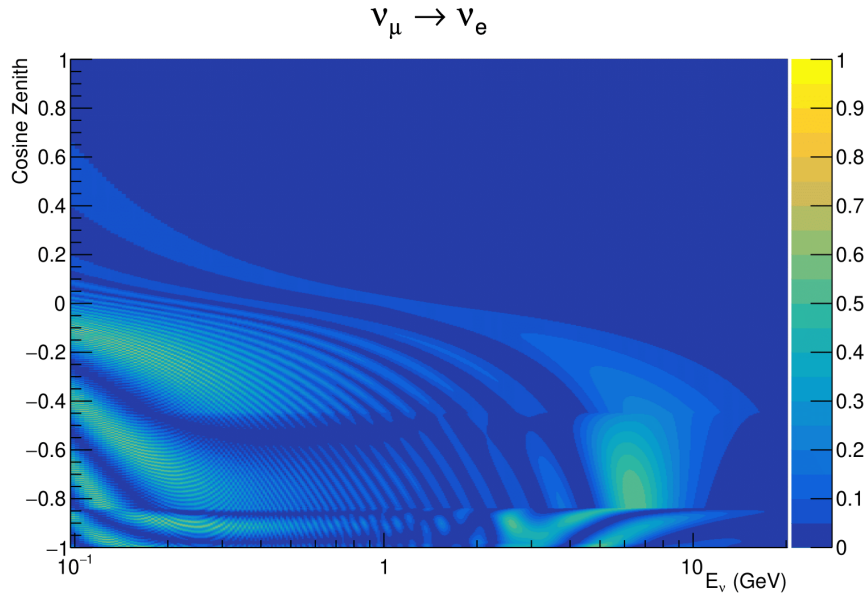


Figure 7.7: The oscillation probability $P(\nu_\mu \rightarrow \nu_e)$, given as a function of neutrino energy and zenith angle, which highlights an example of the “fast” oscillations in the sub-GeV upgoing region.

2488 All of the oscillation probability calculations are performed with a fixed zenith
2489 angle such that the same density profile is used.

2490 The uncertainty in the production height is controlled by using an “average”
2491 production height, \bar{L}_i , which represents the average path length computed using
2492 twenty production heights taken from the Honda flux model’s prediction [54].
2493 For a given event, the production heights are sampled in steps of 5% of their
2494 cumulative distribution function. L_β values are similarly calculated but instead
2495 use different combinations of four production heights,

$$\begin{aligned}
 L_{-1.0} &= \frac{1}{4}L(45, 50, 55, 60), \\
 L_{-0.5} &= \frac{1}{4}L(35, 40, 65, 70), \\
 L_{+0.5} &= \frac{1}{4}L(25, 30, 75, 68), \\
 L_{+1.0} &= \frac{1}{4}L(15, 20, 85, 89).
 \end{aligned} \tag{7.4}$$

2496 This averaging technique works because of the inference between the zenith
2497 angle and the reconstructed direction of final state particles in the detector. For

2498 low-energy neutrinos, where the resolution of the true neutrino direction is poor,
2499 σ_i will be large, resulting in significant averaging effects. Contrary to this, the
2500 inferred direction of high-energy neutrinos will be much closer to the true value,
2501 meaning that σ_i will be smaller, culminating in small averaging effects.

2502 In practice, these calculations are performed prior to the fit as only oscillation
2503 parameters at fixed points are considered. The MCMC technique used in this
2504 thesis requires oscillation probabilities to be evaluated at arbitrary parameter
2505 values, not known *a priori*. Calculating the five oscillation probabilities per
2506 event required by the SK technique is computationally infeasible, so a differencct
2507 averaging technique is used. However, the concept of the averaging technique
2508 can be taken from it.

2509 To perform a similar averaging as the SK analysis, a sub-sampling approach
2510 using binned oscillograms has been devised. A coarsly binned oscillogram is
2511 defined in $\cos(\theta_Z)$ and E_ν . For a given set of oscillation parameters, a single
2512 oscillation probability will be assigned to each coarse bin. This value will then
2513 apply to all Monte Carlo events which fall into that bin. To assign these oscillation
2514 probabilities, the probability is calculated at $N \times N$ points on a grid within a
2515 particular bin. This ensemble of oscillation probabilities is averaged to define
2516 the coarse bin's oscillation probability, assuming a flat prior in E_ν and $\cos(\theta_Z)$.
2517 Figure 7.8 illustrates the $N = 2$ example where the assigned value to a coarse
2518 bin is the average of the four fine bins which fall in that coarse bin. Whilst the
2519 coarse bin edges do not have to be linear on either axis, the sub-division of the
2520 fine bins is linear over the range of a coarse bin.

2521 The coarse binning is defined with 67×52 bins in true neutrino energy \times
2522 cosine zenith. It is picked to be identical to that provided in [210]. In general, the
2523 binning is logarithmically spaced in neutrino energy but has some hand-picked
2524 bin edges around the matter resonance to smoothly increased the bin density.
2525 This is to avoid smearing this region which can be well sampled by the Monte
2526 Carlo. The cosine zenith binning is approximately linearly spaced across the

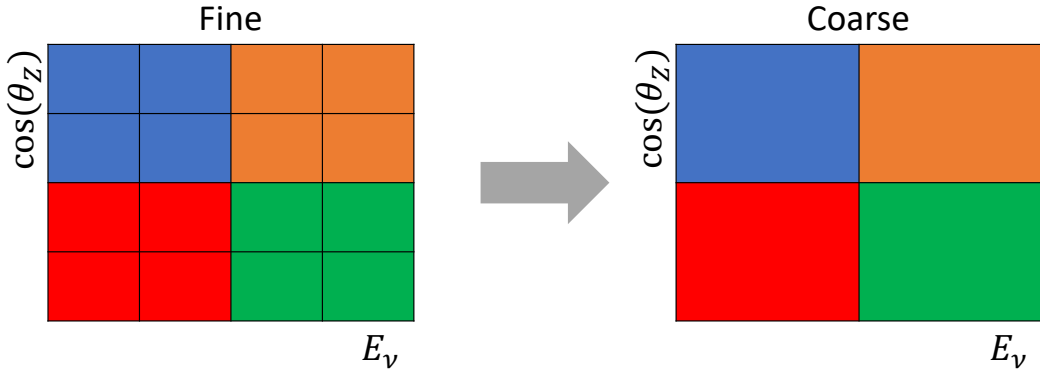


Figure 7.8: Illustration of the averaging procedure for $N = 2$. The oscillation probabilities calculated on the finer left binning are averaged to obtain the oscillation probabilities in the coarser right binning. These averaged oscillation probabilities with the coarser binning are then applied to each event during the fit.

allowable range but the values of layer transitions are hit precisely: -0.8376 (core-mantle) and -0.4464 (mantle/transition zone). Bins are spread further apart for downgoing events as this is a region unaffected by the fast oscillation wavelengths and reduces the total number of calculations required to perform the calculation.

The choice of N is justified based on two studies. Firstly, the variation of event rates of each sample is studied as a function of N . For a given set of oscillation parameters thrown from the PDG prior constraints (detailed in Table 2.1), the oscillation probabilities are calculated using a given value of N . Each sample is re-weighted and the event rate is stored. The value of N is scanned from 1, which corresponds to no averaging, to 19, which corresponds to the largest computationally viable subdivision binning. The event rate of each sample at large N is expected to converge to a stationary value due to the fine binning fully sampling the small-scale structure. Figure 7.9 illustrates this behaviour for the SubGeV_elike_0dcy sample for 9 different throws of the oscillation parameters.

Denoting the event rate for one sample for a given throw t at each N by λ_t^N , the average over all considered N values ($\bar{\lambda}_t = \frac{1}{24} \sum_{N=1}^{24} \lambda_t^N$) is computed. The variance in the event rate at each N is then calculated as

$$\text{Var}[\lambda^N] = \frac{1}{N_{\text{throws}}} \sum_{t=1}^{N_{\text{throws}}} (\lambda_t^N - \bar{\lambda}_t)^2 - \left[\frac{1}{N_{\text{throws}}} \sum_{t=1}^{N_{\text{throws}}} (\lambda_t^N - \bar{\lambda}_t) \right]^2. \quad (7.5)$$

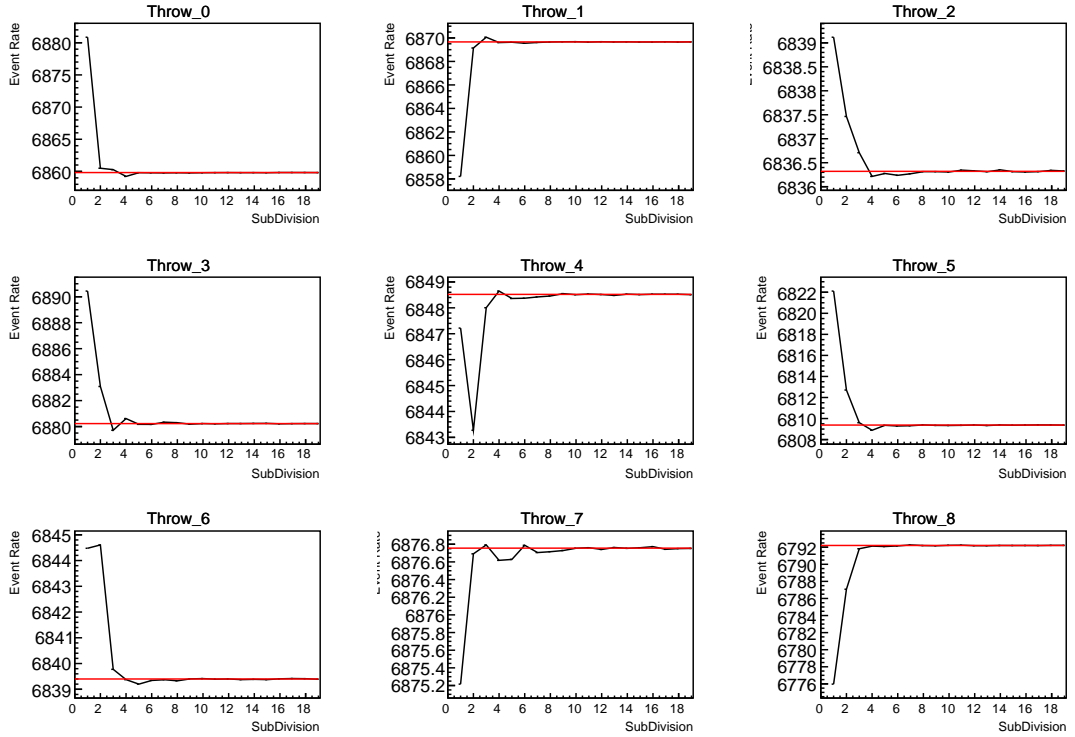


Figure 7.9: Event rate of the SubGeV_elike_0dcy sample as a function of the number of sub-divisions per coarse bin. Each subplot represents the event rate of the sample at a different oscillation parameter set thrown from the PDG priors detailed in Table 2.1. The red line in each subplot represents the mean of the event rate over the different values of sub-divisions for that particular oscillation parameter throw.

2544 In practice the following procedure is undertaken. For a particular throw,
 2545 the difference between the event rate at a particular choice of N and the mean
 2546 of the distribution is calculated. This is illustrated in Figure 7.10. This value
 2547 is then calculated for all the 2000 throws, generating a distribution of $\lambda_t^N - \bar{\lambda}_t$.
 2548 This is repeated for each of the values of N considered within this study. The
 2549 distributions of this value, for $N = \{1, 5\}$, are given in Figure 7.11. As expected,
 2550 the distribution gets narrower and tends towards zero for the higher values of N .

2551 The aim of the study is to find the lowest value of N such that this variance
 2552 is below 0.001. This utilises the width of the distributions given in Figure 7.11.
 2553 This is the typical threshold used by T2K fitters to validate systematic imple-
 2554 mentation so has been set as the same criteria. The results of this study for
 2555 each atmospheric sample used within this thesis are illustrated in Figure 7.12 for
 2556 2000 throws of the oscillation parameters. As can be seen, the variance is below

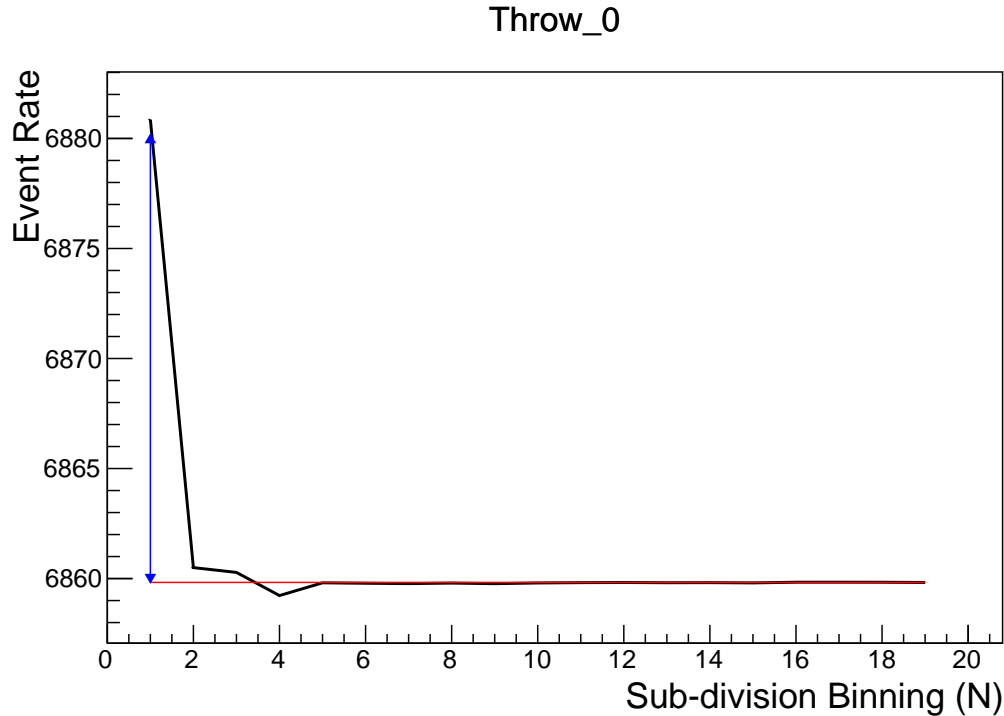


Figure 7.10: Event rate of the SubGeV_elike_0dcy sample, for a particular oscillation parameter throw, as a function of the number of sub-divisions, N , per coarse bin. The difference between the mean event rate (red), $\bar{\lambda}$, and the event rate at $N = 1$, $\lambda^{N=1}$ is defined as $\lambda^N - \bar{\lambda}$ and illustrated by the blue arrow.

2557 the threshold at $N = 10$, and is driven primarily by the SubGeV_mulike_1dcy
 2558 and SubGeV_elike_0dcy samples.

2559 The second study to determine the value of N is as follows. The likelihood
 2560 for each sample is computed against an Asimov data set created with Asimov
 2561 A oscillation parameters (Table 2.2). Following Equation 7.5, the variance of
 2562 the log-likelihood over all considered N is computed. The results are shown
 2563 in Figure 7.13.

2564 A choice of $N = 10$ sub-divisions per coarse bin has a variance in both
 2565 event rate and log-likelihood residuals less than the required threshold of 0.001.
 2566 The largest value of the likelihood variance is of order 10^{-7} , corresponding to
 2567 an error on the log-likelihood of about 3×10^{-4} which is small enough to be
 2568 negligible for the oscillation analysis.

2569 Figure 7.14 illustrates the effect of the smearing using $N = 10$. The fast oscil-

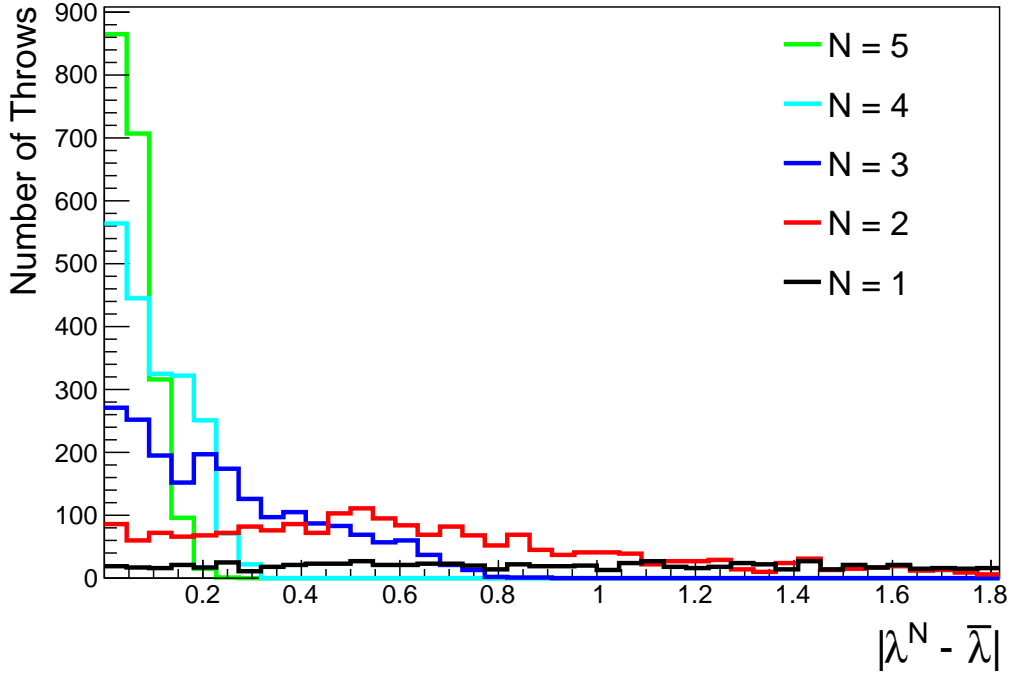


Figure 7.11: The distribution of $\lambda^N - \bar{\lambda}$ for various values of N . As expected, the distribution gets narrower for larger values of N .

2570 lations in the sub-GeV upgoing region have been replaced with a normalisation
 2571 effect whilst the large matter resonance structure remains.

2572 7.3 Calculation Engine

2573 As previously discussed in section 7.2, the calculation of oscillation probabilities
 2574 is performed at run-time. Consequently, the time per calculation is crucial for fit
 2575 performance. The initial fitting framework used for this analysis was developed
 2576 with ProbGPU [211]. This is a GPU-only implementation of the prob3 engine
 2577 [212]. It is primarily designed for neutrino propagation in a beam experiment
 2578 (single layer of constant density) with the atmospheric propagation code not
 2579 being used prior to the analysis in this thesis.

2580 Another engine, CUDAProb3 [213], has been interfaced with the fitting frame-
 2581 work used in this analysis. It has been specifically optimised for atmospheric
 2582 neutrino oscillation calculation so does not contain the code to replace the

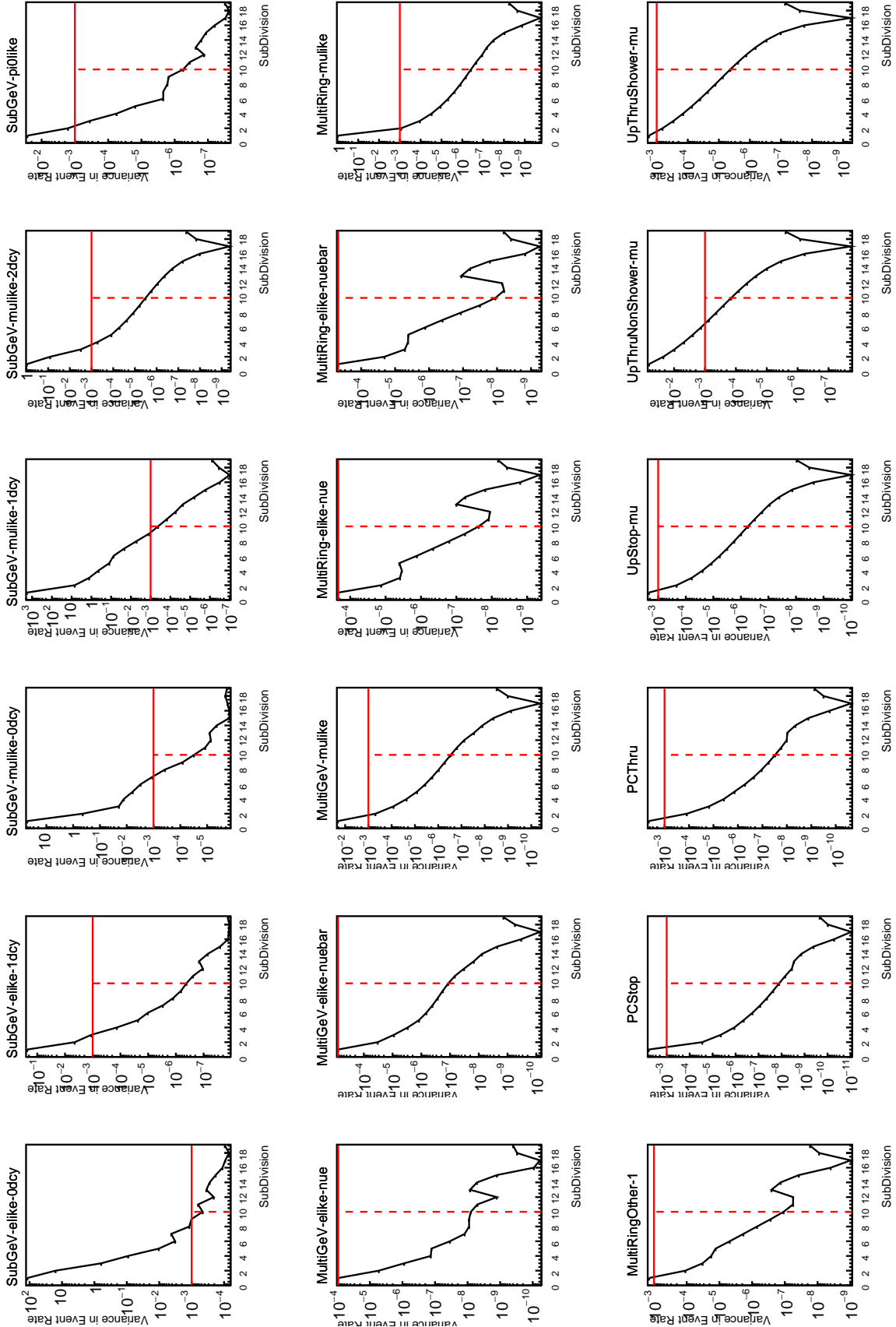


Figure 7.12: Variance of event rate for each atmospheric sample as a function of the number of sub-divisions per coarse bin. The solid red line indicates the 0.1% threshold and the dashed red line indicates the variance at a sub-division $N = 10$.

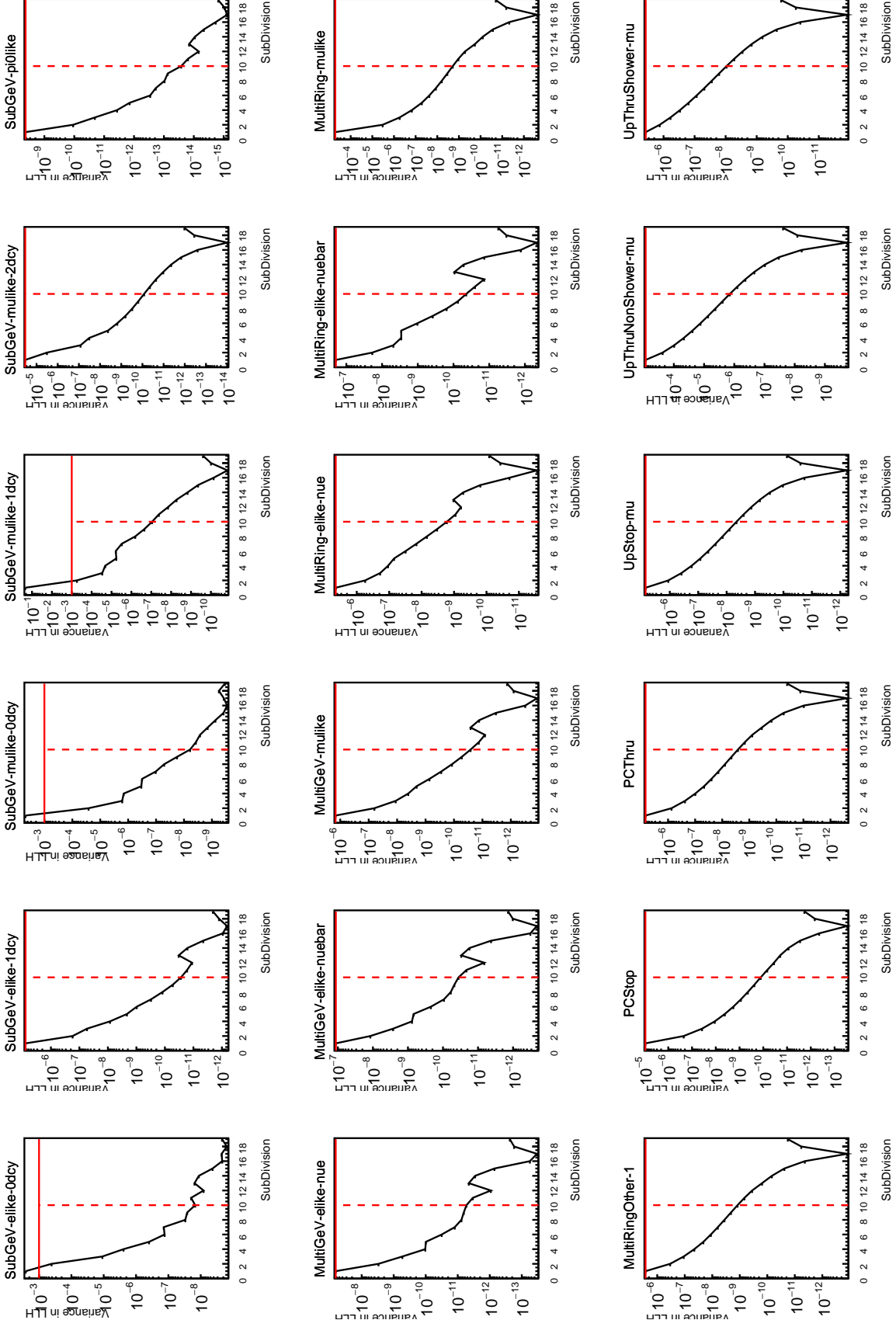


Figure 7.13: Variance of sample likelihood, when compared to ‘Asimov data’ set at Asimov A, for each atmospheric sample as a function of the number of sub-divisions per coarse bin. The solid red line indicates the 0.1% threshold and the dashed red line is a graphical indication of the variance at a sub-division $N = 10$.

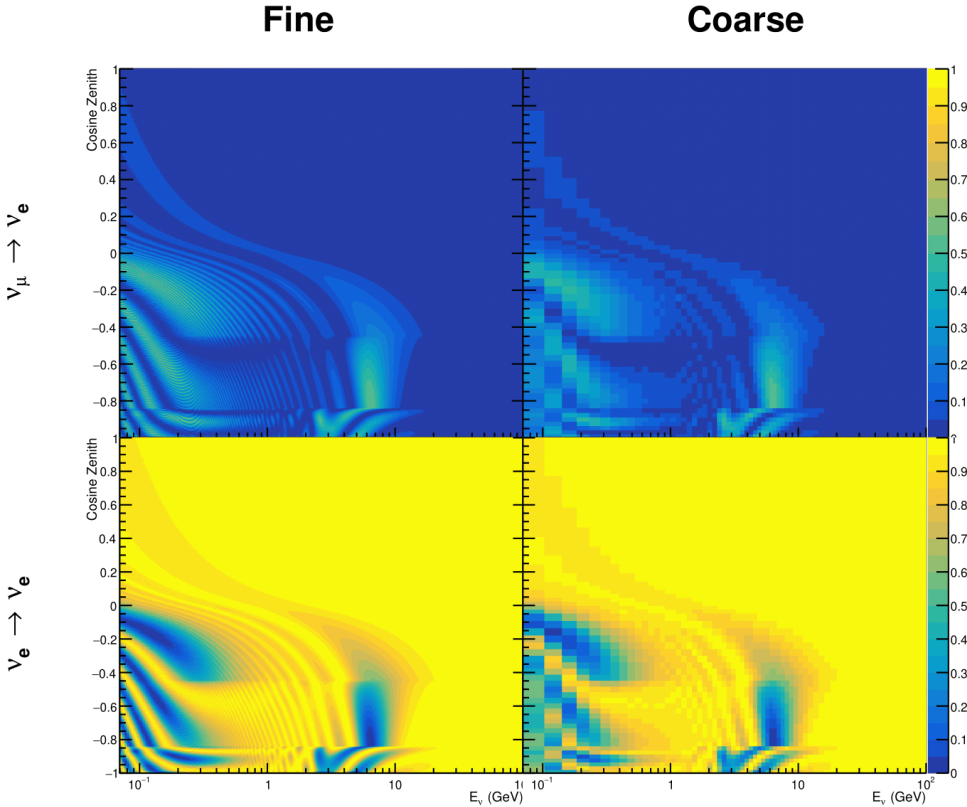


Figure 7.14: The oscillation probability, $P(\nu_\mu \rightarrow \nu_e)$ (top row) and $P(\nu_e \rightarrow \nu_e)$ (bottom row), given as a function of neutrino energy and zenith angle. The left column gives the “fine” binning used to calculate the oscillation probabilities and the right column illustrates the “coarse” binning used to reweight the Monte Carlo events. The fine binning choice is given with $N = 10$, which was determined to be below the threshold from Figure 7.12 and Figure 7.13.

beam oscillation calculation. The engine utilises object-orientated techniques as compared to the functional implementation of ProbGPU. This allows the energy and cosine zenith arrays to be kept on GPU memory, rather than having to load these arrays onto GPU memory for each calculation. Reducing the memory transfer between CPU and GPU significantly reduces the time required for calculation. This can be seen in Figure 7.15, where the GPU implementation of CUDAProb3 is approximately three times faster than the ProbGPU engine.

Another significant advantage of CUDAProb3 is that it contains a CPU multithreaded implementation which is not possible with the ProbGPU or prob3

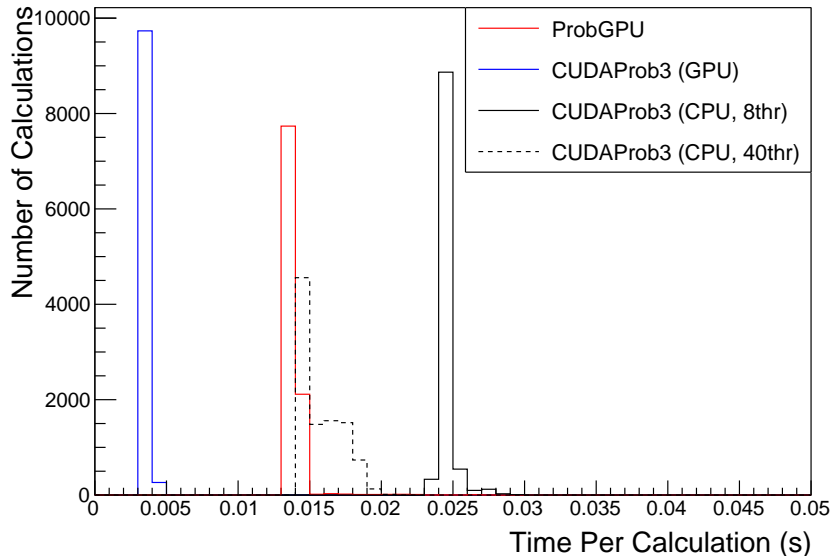


Figure 7.15: The calculation time taken to both calculate the oscillation probabilities and fill the “coarse” oscillograms, following the technique given in section 7.2, for the CUDAProb3 and ProbGPU (Red) calculation engines. CUDAProb3 has both a GPU (Blue) and CPU (Black) implementation, where the CPU implementation is multithreaded. Therefore, 8-threads (solid) and 40-threads (dashed) configurations have been tested. Prob3, which is a CPU single-thread implementation has a mean step time of 1.142s.

2592 engines. This eliminates the requirement for GPU resources when submitting
 2593 jobs to batch systems. As illustrated in Figure 7.15, the calculation speed depends
 2594 on the number of available threads. Using 8 threads (which is typical of the
 2595 batch systems being used) is approximately twice as slow as the ProbGPU engine
 2596 implementation, but would allow the fitting framework to be run on many more
 2597 resources. This fact is utilised for any SK-only fits but GPU resources are required
 2598 for any fits which include beam samples due to the ProbGPU requirement. Based
 2599 on the benefits shown by the implementation in this section, efforts are being
 2600 placed into including linear propagation for beam neutrino propagation into
 2601 the engine [214].

2602 7.4 Matter Density Profile

2603 For an experiment observing neutrinos propagating through the Earth, a model
 2604 of the Earth’s density profile is required. The model used within this analysis is

2605 based on the Preliminary Reference Earth Model (PREM) [209], as illustrated in
 2606 Figure 7.1. Table 7.1 documents the density and radii of the layers used within
 2607 the constant density approximaton used by the SK-only analysis [208]. The
 2608 density measurements provided in the PREM model are provided in terms of
 2609 mass density, whereas neutrino oscillations are sensitive to the electron number
 2610 density. This value can be computed as the product of the chemical composition,
 2611 or the Z/A value, and the mass density of each layer. Currently, the only
 2612 way to measure the chemical composition value for layers close to the Earth's
 2613 core is through neutrino oscillations. The chemical composition of the upper
 2614 layers of the Earth's Mantle and the Transition zone is well known due to it
 2615 being predominantly pyrolite which has a chemical composition value of 0.496
 2616 [215]. The chemical composition dial for the core layers is set to a value of
 2617 0.468, as calculated in [216]. As this value is lesss well known, it is assigned a
 2618 Gaussian error with a standard deviation equivalent to the difference in chemical
 2619 composition in core and mantle layers. Figure 7.16 illustrates the effect of moving
 2620 from the $Z/A = 0.5$ method which is used in the official SK-only analysis
 2621 to these more precise values.

2622 The beam oscillation probability in this thesis uses a baseline of 295km, density
 2623 $2.6\text{g}/\text{cm}^3$, and chemical composition 0.5 as is done by the official T2K-only
 2624 analysis [217].

2625 For a neutrino with given E_ν , $\cos(\theta_Z)$, the oscillation probability calculation
 2626 engine must be passed a list of the matter regions that the neutrino traversed,
 2627 with the path length and fixed density in each region. However, a neutrino
 2628 passing through the earth experiences a range of radii, and thus a range of
 2629 densities, in each region. In the SK-only analysis, the earth density model used
 2630 is piecewise-constant, thereby ignoring this effect. For this thesis, the density
 2631 values for the calculation engine are found by averaging the earth density along
 2632 the neutrino's path,

$$\langle \rho \rangle_i = \frac{1}{t_{i+1} - t_i} \int_{t_i}^{t_{i+1}} \rho(t) dt \quad (7.6)$$

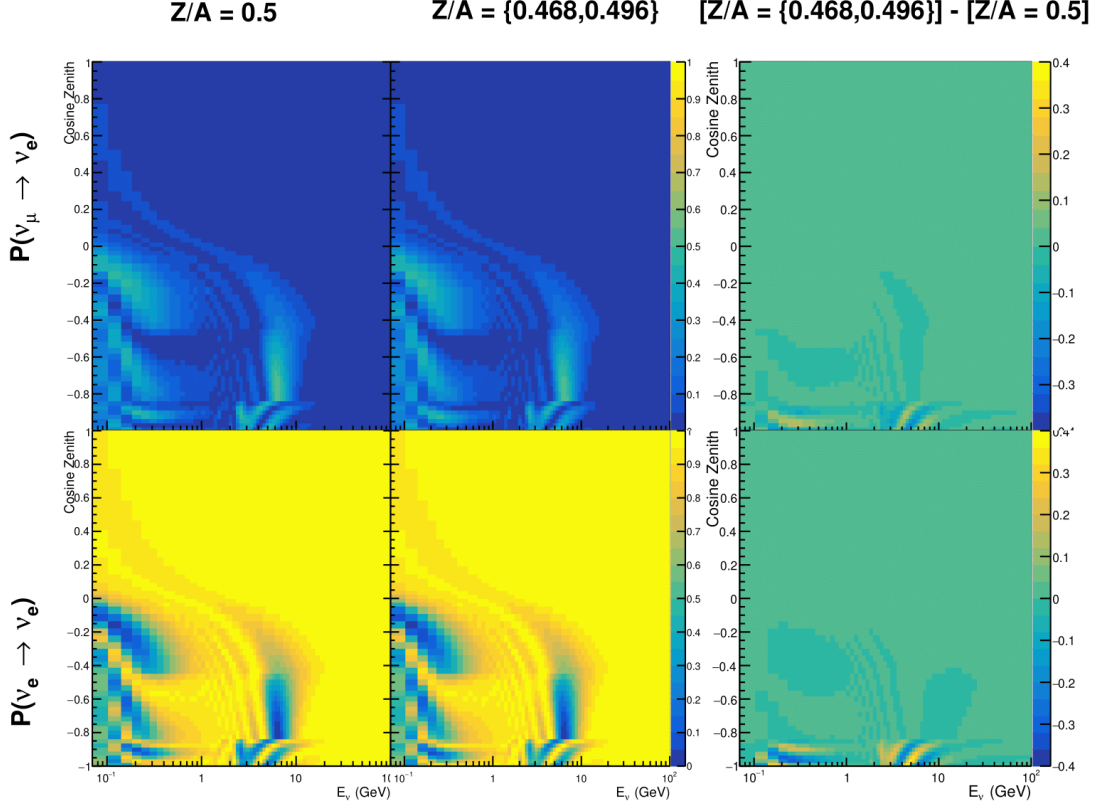


Figure 7.16: The oscillation probability, $P(\nu_\mu \rightarrow \nu_e)$ (top row) and $P(\nu_e \rightarrow \nu_e)$ (bottom row), given as a function of neutrino energy and zenith angle. The left column gives probabilities where the constant $Z/A = 0.5$ approximation which is used in the official SK-only analysis. The middle column gives the probabilities where $Z/A = [0.468, 0.498]$ values are used, as given in Table 7.1. The right column illustrates the difference in oscillation probability between the two different techniques.

where t_i are the intersection points between each layer and t is the path length of the trajectory across the layer. This leads to an improved approximation. For this averaging, the simplification of the PREM model developed in [218] is used. The layers of the prem model are combined into four to reduce calculation time, with a quadratic fit to each section. This fit was not performed by the author of the thesis and is documented in [210]. The coefficients of the quadratic fit to each layer are given in Table 7.2 with the final distribution illustrated in Figure 7.17. The quadratic approximation is clearly much closer to the PREM model as compared to the constant density approximation.

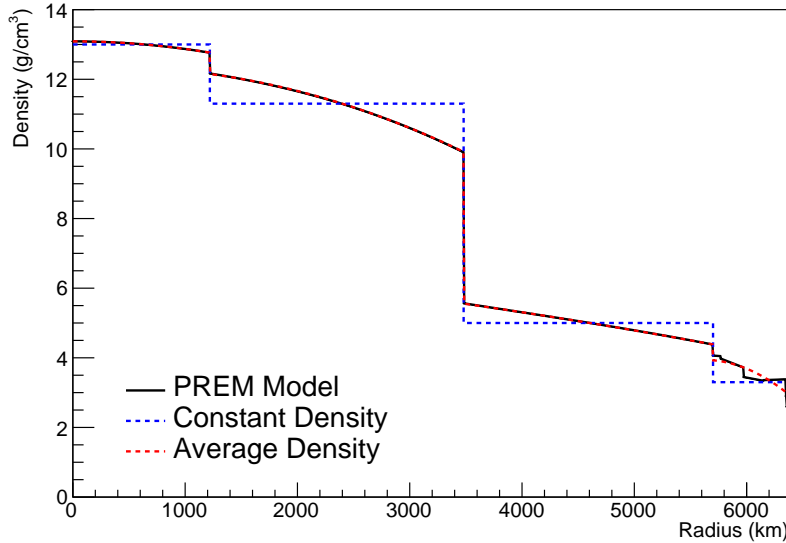


Figure 7.17: The density of the Earth given as a function of the radius, as given by the PREM model (Black), the constant density four-layer approximation (Blue), as used in the official SK-only analysis, and the quadratic approximation of the PREM model (Red).

Layer	Outer Radius [km]	Density [g/cm ³]
Inner Core	1220	$13.09 - 8.84x^2$
Outer Core	3480	$12.31 + 1.09x - 10.02x^2$
Lower Mantle	5701	$6.78 - 1.56x - 1.25x^2$
Transition Zone	6371	$-50.42 + 123.33x - 69.95x^2$

Table 7.2: The quadratic polynomial fits to the PREM model for four assumed layers of the PREM model. The fit to calculate the coefficients is given in [210], where $x = R / R_{\text{Earth}}$.

The effect of using the quadratic density per $\cos(\theta_Z)$ model is highlighted in Figure 7.18. The slight discontinuity in the oscillation probability around $\cos(\theta_Z) \sim -0.45$ in the fixed density model, which is due to the transition to mantle layer boundary, has been reduced. This is expected as the difference in density across this boundary is significantly smaller in the quadratic density model as compared to the constant density model. Whilst the difference in density across the other layer transitions is reduced, there is still a significant difference. This means the discontinuities in the oscillation probabilities remain but are significantly reduced. However, as the quadratic density approximation matches the PREM model well in this region, these discontinuities are due to the Earth model rather than an artifact of the oscillation calculation.

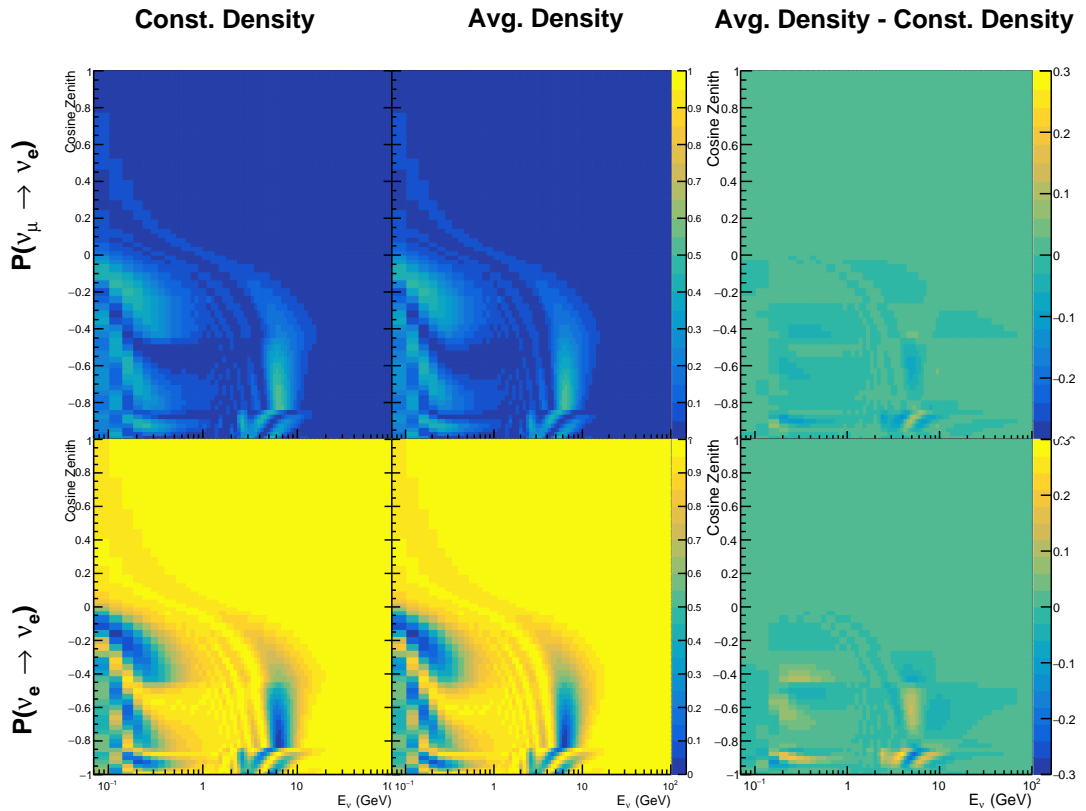


Figure 7.18: The oscillation probability, $P(\nu_\mu \rightarrow \nu_e)$ (top row) and $P(\nu_e \rightarrow \nu_e)$ (bottom row), given as a function of neutrino energy and zenith angle. The left column gives probabilities where the four-layer constant density approximation is used. The middle column gives the probabilities where the density is integrated over the trajectory, using the quadratic PREM approximation, for each $\cos(\theta_Z)$ is used. The right column illustrates the difference in oscillation probability between the two different techniques.

2653 7.5 Production Height Averaging

2654 As discussed in section 7.1, the height at which the cosmic ray flux interacts
 2655 in the atmosphere is not known on an event-by-event basis. The production
 2656 height can vary from the Earth's surface to $\sim 50\text{km}$ above that. The SK-only
 2657 analysis methodology (described in section 7.2) for including the uncertainty
 2658 on the production height is to include variations from the Honda model when
 2659 pre-calculating the oscillation probabilities prior to the fit. This technique is not
 2660 possible for this analysis which uses continuous oscillation parameters that can
 2661 not be known prior to the fit. Consequently, an analytical averaging technique
 2662 was developed in [210]. The author of this thesis was not responsible for the
 2663 derivation of the technique but has performed the implementation and validation
 2664 of the technique for this analysis alone.

2665 Using the 20 production heights per Monte Carlo neutrino event, provided
 2666 as 5% percentiles from the Honda flux model, a production height distribution
 2667 $p_j(h|E_\nu, \cos \theta_Z)$ is built for each neutrino flavour $j = \nu_e, \bar{\nu}_e, \nu_\mu, \bar{\nu}_\mu$. In practice, a
 2668 histogram is filled with 20 evenly spaced bins in production height h between
 2669 0 and 50km. The neutrino energy and cosine zenith binning of the histogram
 2670 is the same as that provided in section 7.2. The average production height,
 2671 $\bar{h} = \int dh \frac{1}{4} \sum_j p_j(h|E_\nu, \cos(\theta_Z))$, is calculated. The production height binning
 2672 of this histogram is then translated into $\delta t(h) = t(\bar{h}) - t(h)$, where $t(h)$ is the
 2673 distance travelled along the trajectory.

2674 For the i^{th} traversed layer, the transition amplitude, $D_i(t_{i+1}, t_i)$, is computed.
 2675 The time-ordered product of these is then used as the overall transition amplitude
 2676 via

$$A(t_{n+1}, t_0) = D_n(t_{n+1}, t_n) \dots D_1(t_2, t_1) D_0(t_1, t_0), \quad (7.7)$$

2677 where,

$$\begin{aligned} D_n(t_{n+1}, t_n) &= \exp[-iH_n(t_{n+1} - t_n)] \\ &= \sum_{k=1}^3 C_k \exp[ia_k(t_{n+1} - t_n)] \end{aligned} \quad (7.8)$$

2678 is expressed as a diagonalised time-dependent solution to the Schrodinger
 2679 equation. The 0th layer is the propagation through the atmosphere and is the
 2680 only term that depends on the production height. Using the substitution $t_0 =$
 2681 $t(\bar{h}) - \delta t(h)$, it can be shown that

$$D_0(t_1, t_0) = D_0(t_1, \bar{h})D_0(\delta t). \quad (7.9)$$

2682 Thus Equation 7.7 becomes

$$\begin{aligned} A(t_{n+1}, t_0) &= D_n(t_{n+1}, t_n) \dots D_1(t_2, t_1) D_0(t_1, \bar{h}) D(\delta t) \\ &= A(t_{n+1}, \bar{h}) \sum_{k=1}^3 C_k \exp[ia_k \delta t], \\ &= \sum_{k=1}^3 B_k \exp[ia_k \delta t]. \end{aligned} \quad (7.10)$$

2683 The oscillation probability averaged over production height is then calculated
 2684 as

$$\begin{aligned} \bar{P}(\nu_j \rightarrow \nu_i) &= \int d(\delta t) p_j(\delta t | E_\nu, \cos \theta_Z) P(\nu_j \rightarrow \nu_i) \\ &= \int d(\delta t) p_j(\delta t | E_\nu, \cos \theta_Z) A(t_{n+1}, t_0) A^*(t_{n+1}, t_0) \\ &= \sum_{km} (B_k)_{ij} (B_m)^*_{ij} \int d(\delta t) p_j(\delta t | E_\nu, \cos \theta_Z) \exp[i(a_k - a_m)\delta t] \end{aligned} \quad (7.11)$$

2685 In practice, implementation in CUDAProb3 [213] is relatively straightforward
 2686 as the majority of these terms are already calculated in the standard oscillation
 2687 calculation. Figure 7.19 illustrates the results of the production height averaging.
 2688 As expected, the main effect is observed in the low-energy downward-going
 2689 and horizontal-going events. Upward-going events have to travel the radius
 2690 of the Earth, $R_E = 6371\text{km}$, where the production height uncertainty is a small
 2691 fraction of the total path length.

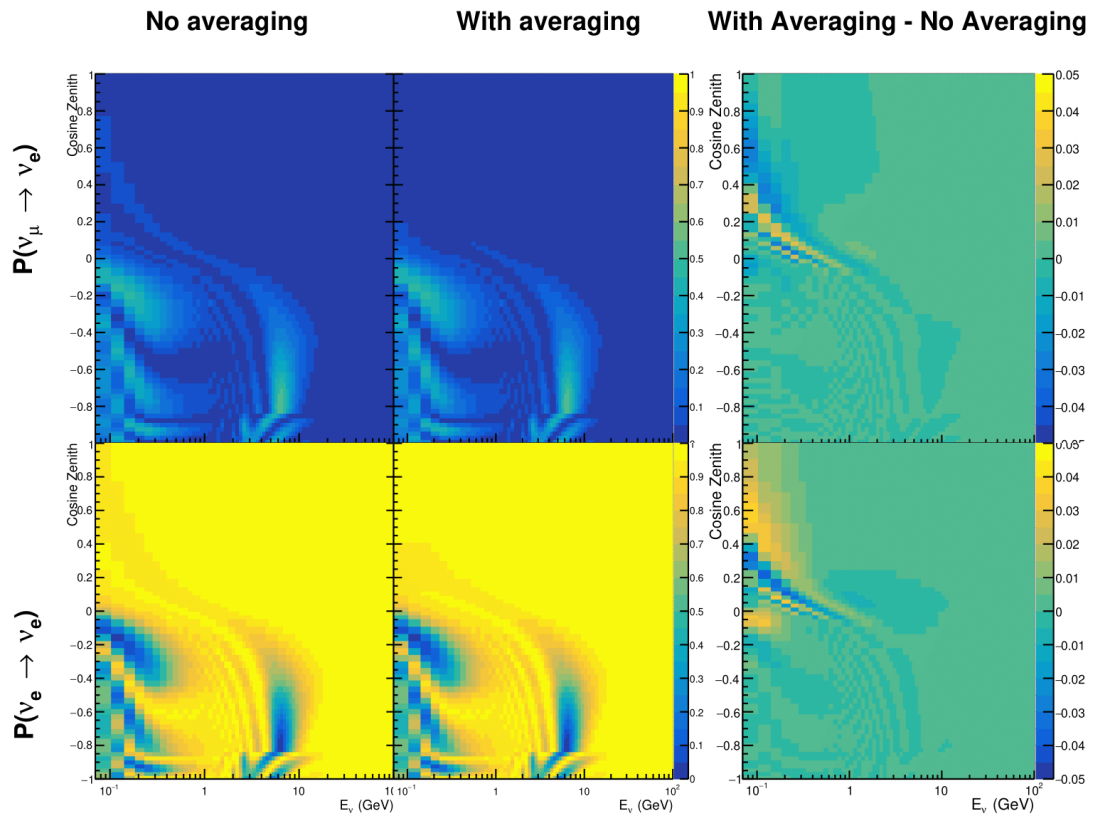


Figure 7.19: The oscillation probability, $P(\nu_\mu \rightarrow \nu_e)$ (top row) and $P(\nu_e \rightarrow \nu_e)$ (bottom row), given as a function of neutrino energy and zenith angle. The left column gives probabilities where a fixed production height of 25km is used. The middle column gives the probabilities where the production height is analytically averaged. The right column illustrates the difference in oscillation probability between the two different techniques.

8

2692

2693

Oscillation Analysis

2694 Using the samples and systematics defined in chapter 6, this chapter documents
2695 a simultaneous beam and atmospheric oscillation analysis from the T2K and SK
2696 experiments. The MaCh3 Bayesian MCMC framework introduced in chapter 4
2697 is used for all studies performed within this thesis.

2698 The MaCh3 framework used throughout this thesis has been validated through
2699 many tests. The code which handles the beam far detector samples was developed
2700 by the author and validated by comparison to the 2020 T2K analysis [76]. The
2701 sample event rates and likelihood evaluations of beam samples generated by
2702 the framework used within this thesis were compared to those from the T2K
2703 analysis by the author of this thesis. Variations of the sample predictions were
2704 compared at $\pm 1\sigma$ and $\pm 3\sigma$ and good agreement was found in all cases. A similar
2705 study, led by Dr. C. Wret was used to validate the near detector portion of
2706 the code [203]. The implementation of the atmospheric samples within MaCh3
2707 was completed and cross-checked by the author of this thesis against the P-
2708 Theta framework (Introduced in section 3.2). Both fitters are provided with
2709 the same inputs and can therefore cross-validate each other. These validations
2710 compared the event rate and likelihood calculation. Documentation of all the
2711 above validations can be found in [203].

2712 8.1 Monte Carlo Prediction

2713 Using the three sets of dial values (generated, pre-BANFF, and post-BANFF tunes)
 2714 defined in subsection 6.4.3, the predicted event rates for each sample are defined
 2715 in Table 8.1. The oscillated (AsimovA defined in Table 2.2) and un-oscillated
 2716 event rates are calculated for each tune.

Sample	Total Predicted Events					
	Generated		Pre-fit		Post-fit	
	Osc	UnOsc	Osc	UnOsc	Osc	UnOsc
SubGeV- <i>elike</i> -0dcy	7121.0	7102.6	6556.8	6540.0	7035.2	7015.7
SubGeV- <i>elike</i> -1dcy	704.8	725.5	693.8	712.8	565.7	586.0
SubGeV- <i>mulike</i> -0dcy	1176.5	1737.2	1078.6	1588.1	1182.7	1757.1
SubGeV- <i>mulike</i> -1dcy	5850.7	8978.1	5351.7	8205.1	5867.0	9009.9
SubGeV- <i>mulike</i> -2dcy	446.9	655.2	441.6	647.7	345.9	505.6
SubGeV- <i>pi0like</i>	1438.8	1445.4	1454.9	1461.1	1131.1	1136.2
MultiGeV- <i>elike</i> -nue	201.4	195.6	201.1	195.3	202.6	196.7
MultiGeV- <i>elike</i> -nuebar	1141.5	1118.3	1060.7	1039.5	1118.5	1095.7
MultiGeV- <i>mulike</i>	1036.7	1435.8	963.1	1334.1	1015.2	1405.9
MultiRing- <i>elike</i> -nue	1025.1	982.2	1026.8	984.3	1029.8	986.4
MultiRing- <i>elike</i> -nuebar	1014.8	984.5	991.0	962.0	1008.9	978.5
MultiRing- <i>mulike</i>	2510.0	3474.4	2475.6	3425.8	2514.6	3480.4
MultiRingOther-1	1204.5	1279.1	1205.8	1280.3	1207.4	1281.0
PCStop	349.2	459.2	338.4	444.7	346.8	456.1
PCThru	1692.8	2192.5	1661.5	2149.8	1689.2	2187.8
UpStop-mu	751.2	1295.0	739.7	1271.6	750.4	1293.0
UpThruNonShower-mu	2584.4	3031.6	2577.9	3019.4	2586.8	3034.0
UpThruShower-mu	473.0	488.6	473.2	488.7	473.8	489.4
FHC1Rmu	328.0	1409.2	301.1	1274.7	345.1	1568.0
RHC1Rmu	133.0	432.3	122.7	396.2	135.0	443.9
FHC1Re	84.6	19.2	77.4	18.2	93.7	19.7
RHC1Re	15.7	6.4	14.6	6.1	15.9	6.3
FHC1Re1de	10.5	3.2	10.3	3.1	8.8	2.9

Table 8.1: The Monte Carlo predicted event rate of each far detector sample used within this analysis. Three model parameter tunes are considered, as defined in subsection 6.4.3. Un-oscillated and oscillated predictions are given, where the oscillated predictions assume Asimov A oscillation parameters provided in Table 2.2.

2717 Generally, the samples which target CCQE interaction modes observe a
 2718 decrease in prediction when using the pre-fit dial values. This is in accordance
 2719 with the Monte Carlo being produced assumed $M_A^{QE} = 1.21\text{GeV}$ [162] whilst

the pre-fit dial value is set to $M_A^{QE} = 1.03\text{GeV}$ as suggested by [201]. Furthermore, the predicted event rates of samples that target CCRES interaction modes are significantly reduced when considering the post-BANFF fit. This follows the observations in subsection 6.4.3. The strength of the accelerator neutrino experiment can be seen in the remarkable difference between the oscillated and unoscillated predictions in the FHC1Rmu and RHC1Rmu samples. There is a very clear decrease in the expected event rate between the oscillated and un-oscillated predictions which is not as obvious as in the atmospheric samples. This is due to the fact that the beam energy is tuned to the maximum disappearance probability which is not the case for the naturally generated atmospheric neutrinos.

8.2 Likelihood Calculation

This analysis performs a joint oscillation parameter fit of the ND280 beam samples, the T2K far detector beam samples, and the SK atmospheric samples.

Once the Monte Carlo predictions of each beam and atmospheric sample have been built (see chapter 6) a likelihood needs to be constructed. This is done by comparing the binned Monte Carlo prediction to binned data. The Monte Carlo prediction is calculated at a particular point, $\vec{\theta}$, in the model parameter space such that $N_i^{MC} = N_i^{MC}(\vec{\theta})$, where N_i represents the bin content of the i^{th} bin. The data and Monte Carlo spectra are represented by N_i^D and N_i^{MC} , respectively. The bin contents for the beam near detector, beam far detector and atmospheric samples are denoted with *ND*, *FD*, and *Atm*, respectively. The binning index, i , runs over all the bins within a sample. Taking the FHC1Rmu far detector sample as an example, the binning index runs over all the reconstructed neutrino energy bins. The likelihood calculation between the data and the Monte Carlo prediction for a particular bin follows a Poisson distribution, where the data is treated as a fluctuation of the simulation.

The data can consist of either real data or an ‘Asimov’ Monte Carlo prediction, which is typically used for sensitivity studies and denoted ‘Asimov data’. The process for building Asimov data is as follows. The Monte Carlo prediction is

2749 reweighted using a particular set of oscillation parameters (potentially those
 2750 listed in Table 2.2) and systematic parameter tune. The resulting spectra for each
 2751 sample is then defined to be the Asimov data for that sample. Whilst this results
 2752 in unphysical non-integer data predictions, it eliminates statistical fluctuations
 2753 from the data. Therefore, the results of a fit to Asimov data should not include any
 2754 biases from statistical fluctuations. Furthermore, these results should produce
 2755 posterior probability distributions consistent with the parameters which were
 2756 used to make the data prediction. That is to say, the fit results should return the
 2757 known parameters. Any biases seen would be attributed to correlations between
 2758 each oscillation parameter and correlations between oscillation and systematic
 2759 parameters. Consequently, Asimov fit results present the maximum precision
 2760 at which the oscillation parameters could be measured to.

2761 Following the T2K analysis presented in [76], the likelihood contribution for
 2762 the near detector samples also includes a Monte Carlo statistical uncertainty term,
 2763 derived from the Barlow and Beeston statistical treatment [219, 220]. In addition
 2764 to treating the data as a Poisson fluctuation of the Monte Carlo prediction, it
 2765 includes a contribution to the likelihood that which treats the generated Monte
 2766 Carlo prediction as a statistical fluctuation of the actual true simulation assuming
 2767 an infinite amount of statistics had been created. The technical implementation
 2768 of this additional likelihood term is documented in [192] and briefly summarised
 2769 as follows. The term is defined as,

$$\frac{(\beta_i - 1)^2}{2\sigma_{\beta_i}^2}, \quad (8.1)$$

2770 where β_i represents a scaling parameter for the i^{th} bin that relates the bin
 2771 content for the amount of Monte Carlo actually generated N_i^{MC} to the bin content
 2772 if an infinite amount of Monte Carlo statistics had been generated $N_{i,true}^{MC}$, such
 2773 that $N_{i,true}^{MC} = \beta_i \times N_i^{MC}$. In the case where a sufficient amount of Monte Carlo
 2774 statistics had been generated, $\beta_i = 1$. An analytical solution for β_i is given in
 2775 [192]. Additionally, $\sigma_{\beta_i} = \sqrt{\sum_i w_i^2 / N_i^{MC}}$ where $\sqrt{\sum_i w_i^2}$ represents the sum of
 2776 the square of the weights of the Monte Carlo events which fall into bin i .

An additional contribution to the likelihood comes from the variation of
 the systematic model parameters. For those parameters with well-motivated
 uncertainty estimates, a covariance matrix, V , describes the prior knowledge of
 each parameter as well as any correlations between the parameters. Due to a
 technical implementation, a single covariance matrix describes each “block” of
 model parameters, e.g. beam flux systematics. The covariance matrix associated
 with the k^{th} block is denoted V^k . This substitution results in $\vec{\theta} = \sum_k^{N_b} \vec{\theta}^k$ and
 $V = \sum_k^{N_b} V^k$ where N_b denotes the number of blocks. A single covariance
matrix is provided for: the oscillation parameters, the beam flux parameters,
the atmospheric flux parameters, the neutrino interaction systematics, the near
detector parameters, the beam far detector systematics, and the atmospheric
far detector systematics. All of these are detailed in section 6.4. The number
of parameters in the k^{th} block is defined as $n(k)$.

The equation for the likelihood \mathcal{L} includes all the terms discussed above.
 It is defined as,

$$\begin{aligned}
 -\ln(\mathcal{L}) = & \\
 & \sum_i^{\text{NDbins}} N_i^{\text{ND},MC}(\vec{\theta}) - N_i^{\text{ND},D} + N_i^{\text{ND},D} \times \ln \left[N_i^{\text{ND},D} / N_i^{\text{ND},MC}(\vec{\theta}) \right] + \frac{(\beta_i - 1)^2}{2\sigma_{\beta_i}^2} \\
 & + \sum_i^{\text{FDbins}} N_i^{\text{FD},MC}(\vec{\theta}) - N_i^{\text{FD},D} + N_i^{\text{FD},D} \times \ln \left[N_i^{\text{FD},D} / N_i^{\text{FD},MC}(\vec{\theta}) \right] \\
 & + \sum_i^{\text{Atmbins}} N_i^{\text{Atm},MC}(\vec{\theta}) - N_i^{\text{Atm},D} + N_i^{\text{Atm},D} \times \ln \left[N_i^{\text{Atm},D} / N_i^{\text{Atm},MC}(\vec{\theta}) \right] \\
 & + \frac{1}{2} \sum_k^{N_b} \sum_i^{n(k)} \sum_j^{n(k)} (\vec{\theta}^k)_i (V^k)_{ij}^{-1} (\vec{\theta}^k)_j.
 \end{aligned} \tag{8.2}$$

The negative log-likelihood value is determined at each step of the MCMC
 to build the posterior distribution defined in chapter 4. This value is minimised
 when the Monte Carlo prediction tends towards the data spectrum.

2795 8.2.1 Likelihood Scans

2796 Using the definition of the likelihood presented in section 8.2, the response of each
2797 sample to a variation of a particular parameter can be studied. Figure 8.1 presents
2798 the variation of all the samples (beam and atmospheric) at the far detector to the
2799 oscillation parameters of interest: δ_{CP} , $\sin^2(\theta_{13})$, $\sin^2(\theta_{23})$, and Δm_{32}^2 . These plots
2800 are colloquially called ‘likelihood scan’ (or ‘log-likelihood scans’). The process
2801 of making these plots is as follows. An Asimov data set (following technique
2802 detailed in section 8.2) is built using the AsimovA oscillation parameters and
2803 pre-fit systematic tune. The Monte Carlo is then reweighted using the value of
2804 the oscillation parameter at each point on the x-axis of the scan. The likelihood
2805 is then calculated between the Asimov data and Monte Carlo prediction and
2806 plotted. This process identifies which samples drive the determination of the
2807 oscillation parameters in the joint fit.

2808 Due to the caveat of fixed systematic parameters and the correlations between
2809 oscillation parameters being ignored when creating these likelihood scans, the
2810 value of $\chi^2 = 1$ (or $-2 \times \ln(\text{Likelihood}) = 1$) does not equate to the typical
2811 1σ sensitivity. However, it does give an indication of which samples respond
2812 the strongest to a variation in a particular oscillation parameter. The point at
2813 which the likelihood tends to zero illustrates the value of the parameter used
2814 to build the Asimov data prediction.

2815 The sensitivity to $\sin^2(\theta_{23})$ is mostly dominated by the beam muon-like
2816 samples. The response of an individual atmospheric sample is small but non-
2817 negligible such that the summed response over all atmospheric samples becomes
2818 comparable to that of the muon-like beam samples. Consequently, the sensitivity
2819 of the joint fit to $\sin^2(\theta_{23})$ would be expected to be greater than the beam-only
2820 analysis. The only sample which respond to the $\sin^2(\theta_{13})$ oscillation parameter is
2821 the electron-like beam samples. Consequently, no increase in sensitivity beyond
2822 that of the T2K-only analysis would be expected from the joint fit. Regardless, the
2823 sensitivity of the beam sample is significantly weaker than the external reactor
2824 constraint so prior knowledge will dominate any measurement that is included

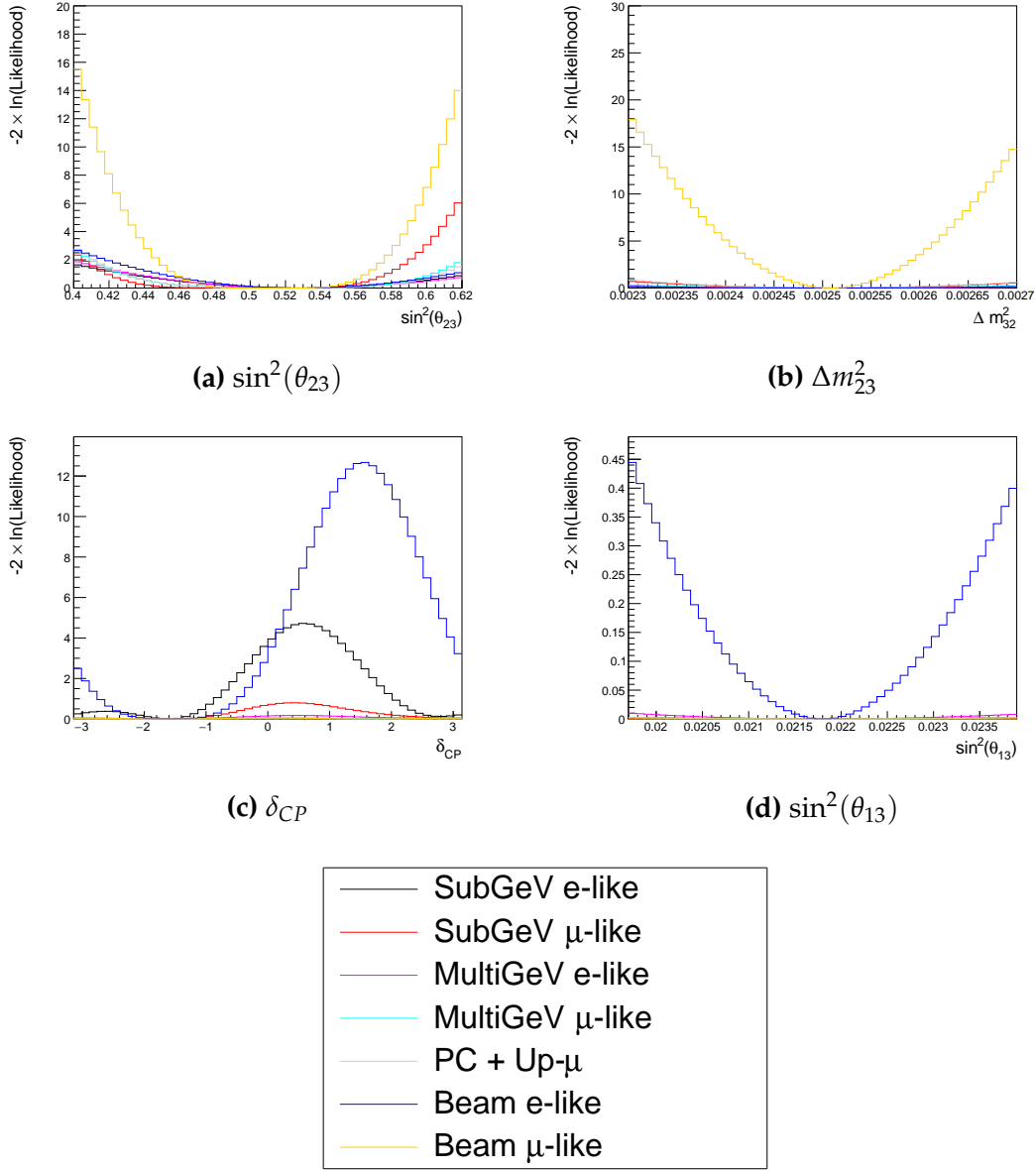


Figure 8.1: The response of the likelihood, as defined in section 8.2, illustrating the response of the samples to a variation of an oscillation parameter.

within this thesis. The Δm_{21}^2 and $\sin^2(\theta_{12})$ parameters are not considered as there is simply no sensitivity in any sample considered within this analysis. The response to Δm_{32}^2 is completely dominated by the beam muon-like samples. This is because the beam neutrino energy can be specifically tuned to match the maximal disappearance probability. Despite this, improvements to the $|\Delta m_{32}^2|$ sensitivity may be expected due to additional mass hierarchy determination

2831 added by the atmospheric samples.

2832 Two-dimensional scans of the appearance ($\sin^2(\theta_{13})$ - δ_{CP}) and disappearance
2833 ($\sin^2(\theta_{23})$ - Δm_{32}^2) parameters are illustrated in Figure 8.2 and Figure 8.3, respec-
2834 tively. The caveat of fixed systematic parameters and correlations between other
2835 oscillation parameters being neglected still apply.

2836 The appearance log-likelihood scans show the distinct difference in how
2837 the beam and atmospheric samples respond. The beam samples have an ap-
2838 proximately constant width of the 2σ and 3σ contours, throughout all ranges
2839 of δ_{CP} . The response of the atmospheric samples to $\sin^2(\theta_{13})$ is very strongly
2840 correlated to the value of δ_{CP} being evaluated, with the strongest constraints
2841 around $\delta_{CP} \sim 1$. Consequently, this difference allows some of the degeneracy in
2842 a beam-only fit to be broken. Comparing the beam-only and joint fit likelihood
2843 scans, the 2σ continuous contour in δ_{CP} for beam samples is broken when the
2844 atmospheric samples are added. This may result in a stronger sensitivity to
2845 δ_{CP} . Similarly, the width of the 3σ contours also becomes dependent upon the
2846 value of δ_{CP} . Whilst these are encouraging results for the joint fit, these are
2847 not sensitivity measurements as the systematic parameters are fixed and the
2848 correlation between oscillation parameters is neglected. An interesting point to
2849 note is that the atmospheric samples have little sensitivity to $\sin^2(\theta_{13})$ on their
2850 own, as evidenced in Figure 8.1, but can improve sensitivity to the parameter
2851 when combined within the simultaneous fit.

2852 The response of the atmospheric samples in Figure 8.2 shows an interesting
2853 behaviour when considering the application of the reactor constraint. At higher
2854 values of $\sin^2(\theta_{13})$, two lobes appear around $\delta_{CP} \sim -\pi/2$ and $\delta_{CP} \sim 2.4$. If this
2855 distribution was projected onto the δ_{CP} axis, these lobes would mean the posterior
2856 distribution would have a significant dip between these values. However, the
2857 region of $\sin^2(\theta_{13})$ near the reactor constraint ($\sin^2(\theta_{13}) = (2.18 \pm 0.08) \times 10^{-2}$)
2858 is flatter across the range of δ_{CP} . Therefore, if we were to project only this
2859 region onto the δ_{CP} axis, the dip between the peaks would not be as significant.
2860 If this behaviour was to be seen in the results of a fit, these marginalisation

2861 effects would actually conspire to reduce the sensitivity to δ_{CP} if the reactor
2862 constraint was to be applied.

2863 The disappearance log-likelihood scans in $\sin^2(\theta_{23})$ - Δm_{32}^2 space (Figure 8.3)
2864 show the expected behaviour when considering the one-dimensional scans
2865 already discussed. The uncertainty on the width of $|\Delta m_{32}^2|$ is mostly driven
2866 by the beam-only sensitivities. However, the width of this contour in the
2867 inverted mass region ($\Delta m_{32}^2 < 0$) is significantly reduced due to the ability
2868 of the atmospheric samples to select the correct (normal) mass hierarchy. The
2869 width of the uncertainty in $\sin^2(\theta_{23})$ is also reduced compared to the beam-only
2870 sensitivities, with a further decrease in the inverted hierarchy region due to the
2871 better mass hierarchy determination.

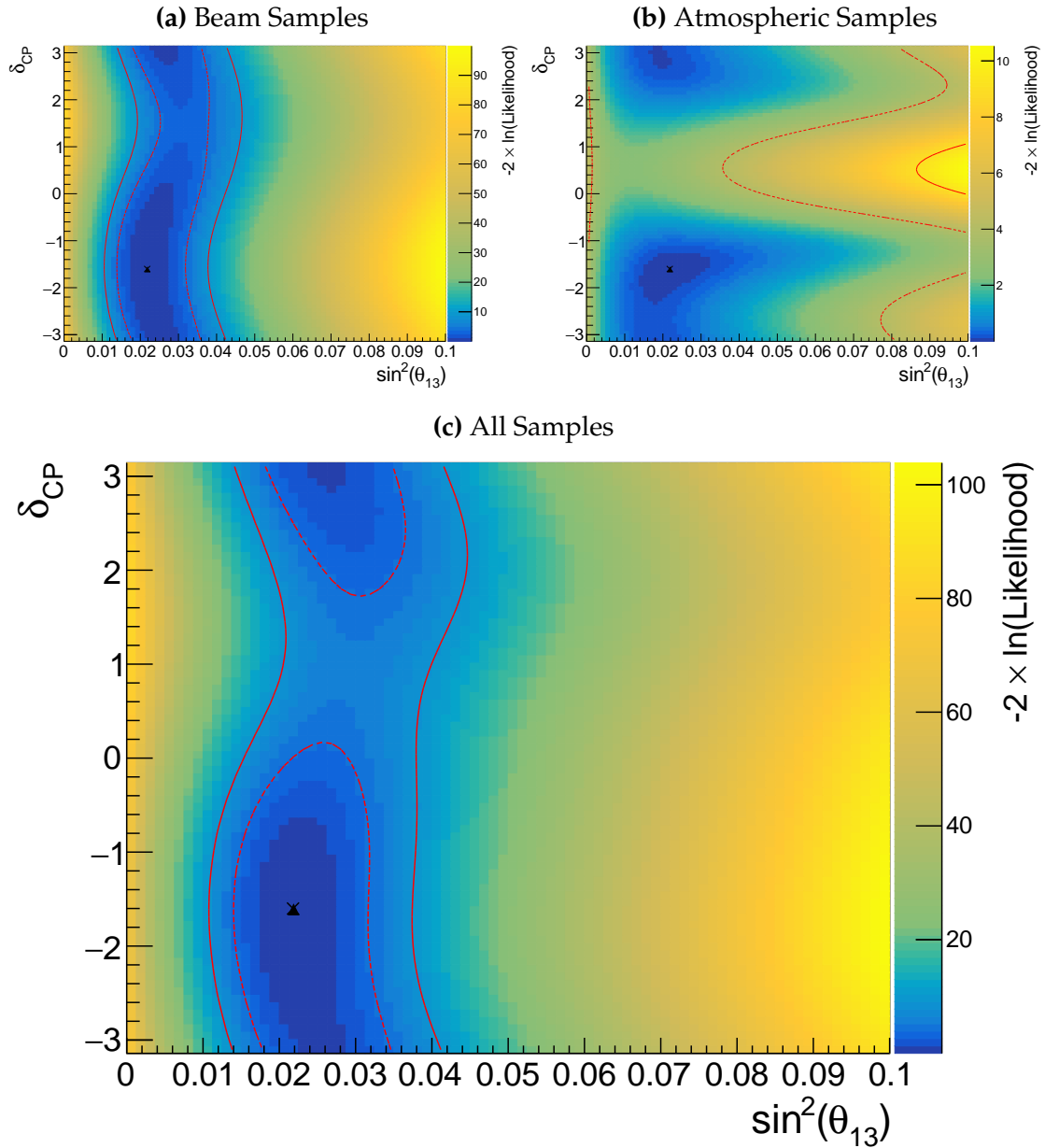


Figure 8.2: Two-dimensional log-likelihood scan of the appearance ($\sin^2(\theta_{13})$ - δ_{CP}) parameters showing the response of the beam samples (top left), atmospheric samples (top right) and the summed response (bottom). The Asimov A oscillation parameters, defined in Table 2.2, are known to be the true point (Black Cross). The position of the smallest log-likelihood is highlighted with the triangle. Prior uncertainty terms of the oscillation parameters are neglected. The two(three) sigma contour levels are illustrated with the dashed(solid) red line.

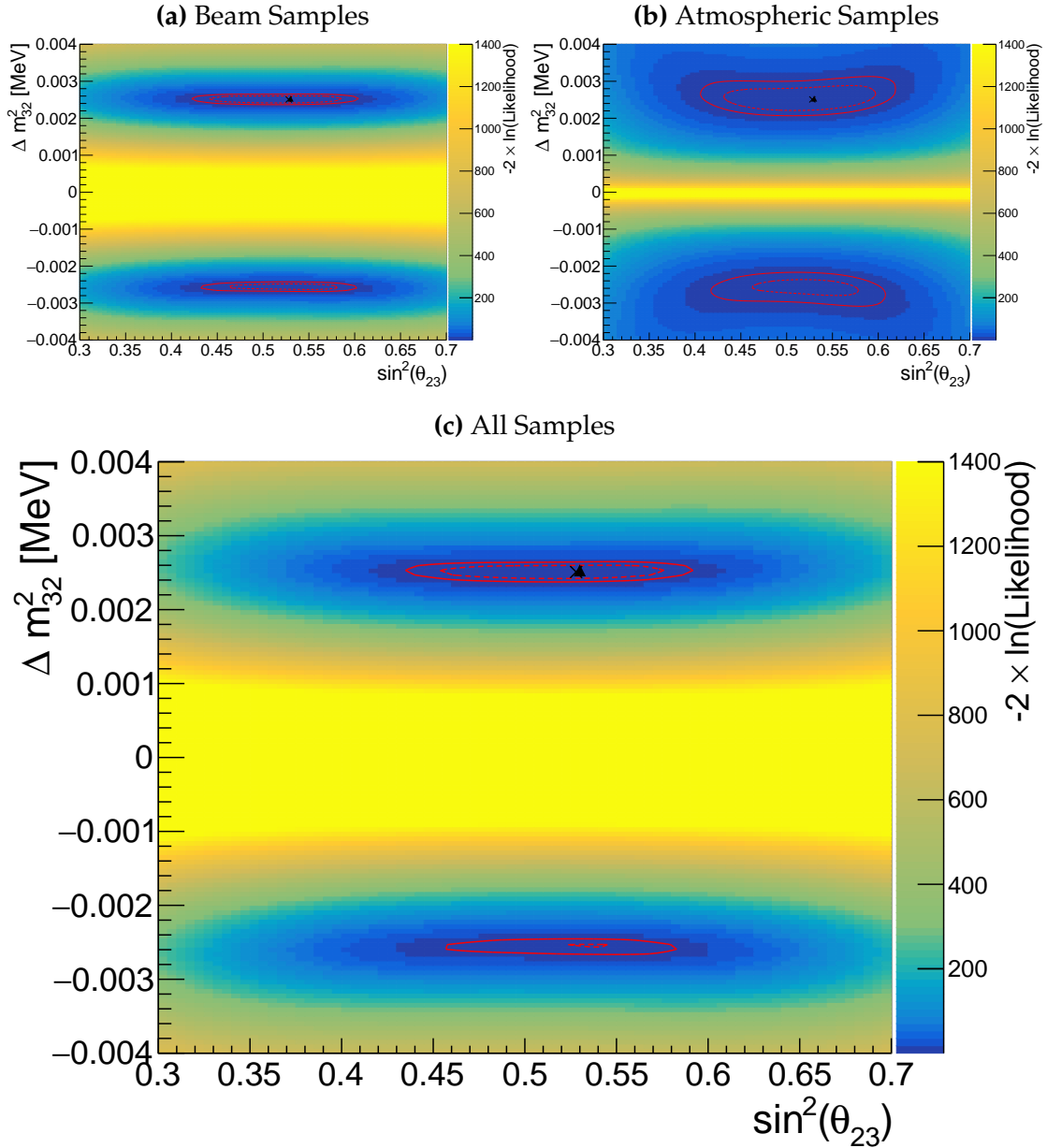


Figure 8.3: Two-dimensional log-likelihood scan of the disappearance ($\sin^2(\theta_{23})$ - Δm_{32}^2) parameters showing the response of the beam samples (top left), atmospheric samples (top right) and the summed response (bottom). The Asimov A oscillation parameters, defined in Table 2.2, are known to be the true point (Black Cross). The position of the smallest log-likelihood is highlighted with the triangle. Prior uncertainty terms of the oscillation parameters are neglected. The two(three) sigma contour levels are illustrated with the dashed(solid) red line.

2872 The likelihood scans illustrated thus far only consider the sensitivity of this
2873 analysis for a fixed set of true oscillation parameters, namely Asimov A defined in
2874 Table 2.2. Whilst computational infeasible to run many fits at different parameter
2875 sets, it is possible to calculate the likelihood response to different Asimov data
2876 sets. Figure 8.4 and Figure 8.5 illustrate how the sensitivity changes for differing
2877 true values of δ_{CP} and $\sin^2(\theta_{23})$, respectively. For both of these plots, the other
2878 oscillation parameters are fixed at their Asimov A values. Consequently, the
2879 caveat of fixed systematic parameters and correlations between other oscillation
2880 parameters being neglected still applies.

2881 To explain how these plots are made, consider Figure 8.4. This plot is built
2882 by considering multiple one-dimensional log-likelihood scans, each creating
2883 an Asimov data with the value of δ_{CP} taken from the x-axis. The likelihood to
2884 a particular Asimov data set is calculated after reweighting the Monte Carlo
2885 prediction to each value of δ_{CP} on the y-axis.

2886 Figure 8.4 illustrates the sensitivity to δ_{CP} . Notably, the 1σ intervals contain
2887 regions in the off-diagonal for which the beam and atmospheric samples have
2888 broken and discontinuous contours. This indicates that there are regions of δ_{CP}
2889 which are degenerate. For example, for the x-axis value of $\delta_{CP} = 0$, the beam
2890 samples sensitivity would include two discontinuous regions excluded from
2891 the 1σ interval: $\delta_{CP} \sim 0$ and $\delta_{CP} \sim \pi$. The offset in δ_{CP} between the beam
2892 and atmospheric samples allows the joint fit to have increased sensitivity in
2893 these regions. Consequently, the difference between the beam-only and joint
2894 beam-atmospheric fit should be studied using multiple Asimov data sets.

2895 Despite the increased sensitivity at 1σ , the 2σ intervals from the joint fit
2896 are more similar to the two independent sensitivities and the off-diagonal de-
2897 generacies mostly remain. This indicates that the joint fit has the strength to
2898 aid parameter determination but can not entirely break the degeneracies in δ_{CP}
2899 at higher confidence levels.

2900 Figure 8.5 illustrates a similar analysis as above, although the value of $\sin^2(\theta_{23})$
2901 is varied and δ_{CP} is fixed to the Asimov A parameter value. Due to the beam

parameters and baseline being tuned to specifically target this oscillation parameter, the average sensitivity of the beam samples is stronger than the atmospheric samples. However, the degeneracy around maximal mixing ($\sin^2(\theta_{23}) = 0.5$) is significantly more peaked in the beam samples compared to the atmospheric samples. This behaviour is strengthened when considering the 2σ intervals, to the point where two distinct discontinuous regions of the 2σ intervals exist around the Asimov point $\sin^2(\theta_{23}) \sim 0.41, 0.6$. Given the caveat of only considering likelihood scans, the joint analysis would mostly eliminate the discontinuous intervals in these regions. This means that the joint fit could feasibly have an increased preference for the correct octant hypothesis.

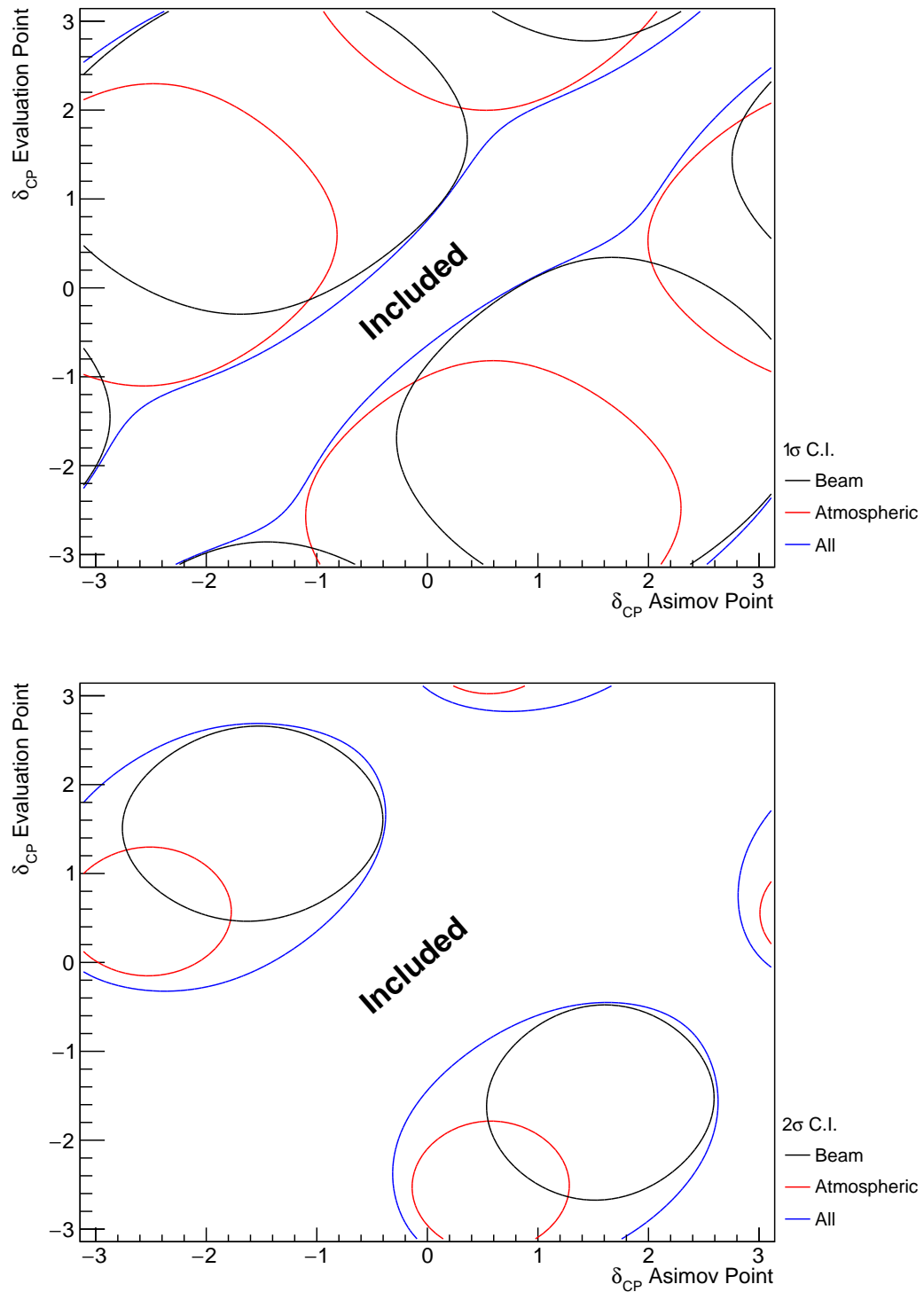


Figure 8.4: A series of one-dimensional likelihood scans over δ_{CP} , where an Asimov data set is built for each value of δ_{CP} on the x-axis and the likelihood is evaluated for each value of δ_{CP} on the y-axis. The diagonal represents the minimum log-likelihood and defines the region included within the 1σ (Top) and 2σ (Bottom) confidence intervals. The beam (black) and atmospheric (red) samples are individually plotted and the joint fit (blue) is the sum of the two.

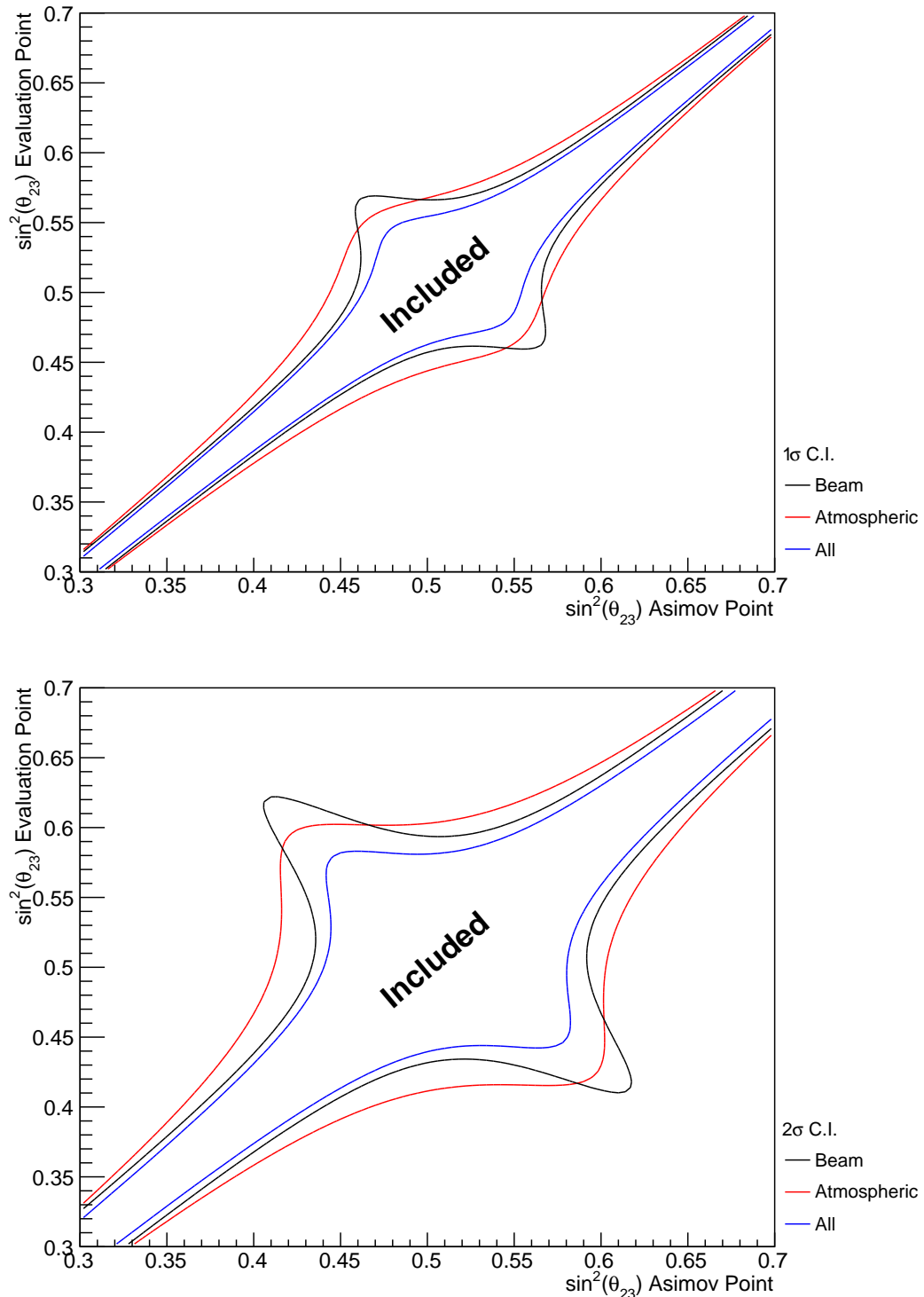


Figure 8.5: A series of one-dimensional likelihood scans over $\sin^2(\theta_{23})$, where an Asimov data set is built for each value of $\sin^2(\theta_{23})$ on the x-axis and the likelihood is evaluated for each value of $\sin^2(\theta_{23})$ on the y-axis. The diagonal represents the minimum log-likelihood and defines the region included within the 1σ (Top) and 2σ (Bottom) confidence intervals. The beam (black) and atmospheric (red) samples are individually plotted and the joint fit (blue) is the sum of the two.

Alongside oscillation parameters (Figure 8.1), the sensitivity to systematic parameters can also be studied for the joint fit. As some of these parameters are correlated between the beam and atmospheric events, the response of the atmospheric samples can modify the constraint. This means the systematics can have additional constraints than what they would from a beam-only analysis. Therefore, the response from the beam and the atmospheric samples to various systematic parameters has been compared in Figure 8.6. The Asimov data set has been created using the AsimovA oscillation parameter and the pre-fit systematic tune. For example, the systematic parameter controlling the effective axial mass coupling in CCQE interactions, M_A^{QE} , is clearly dominated by the ND constraint. An example where the response of the atmospheric sample is approximately similar to the near detector constraint is the 2p2h_Cto0 normalisation systematic. This systematic models the scaling of the 2p2h interaction cross-section on a carbon target to an oxygen target. There are also systematics which have no near detector constraint. For example, the systematic parameters which describe the normalisation of the NC1Gamma and NCOther interaction modes. The atmospheric samples are significantly more sensitive to these systematics than the beam samples due to their similar interaction contributions but relatively higher statistics (Table 8.1). As an example of how the atmospheric samples can help constrain systematic parameters used within the T2K-only analysis, these NC background events in beam electron-like samples will be considerably more constrained with the additional sensitivity of atmospheric samples. This would be expected to reduce the overall uncertainty of the beam electron-like event rates in the joint analysis compared to the beam-only studies. This could modify the sensitivity of the beam samples due to the more constrained background events.

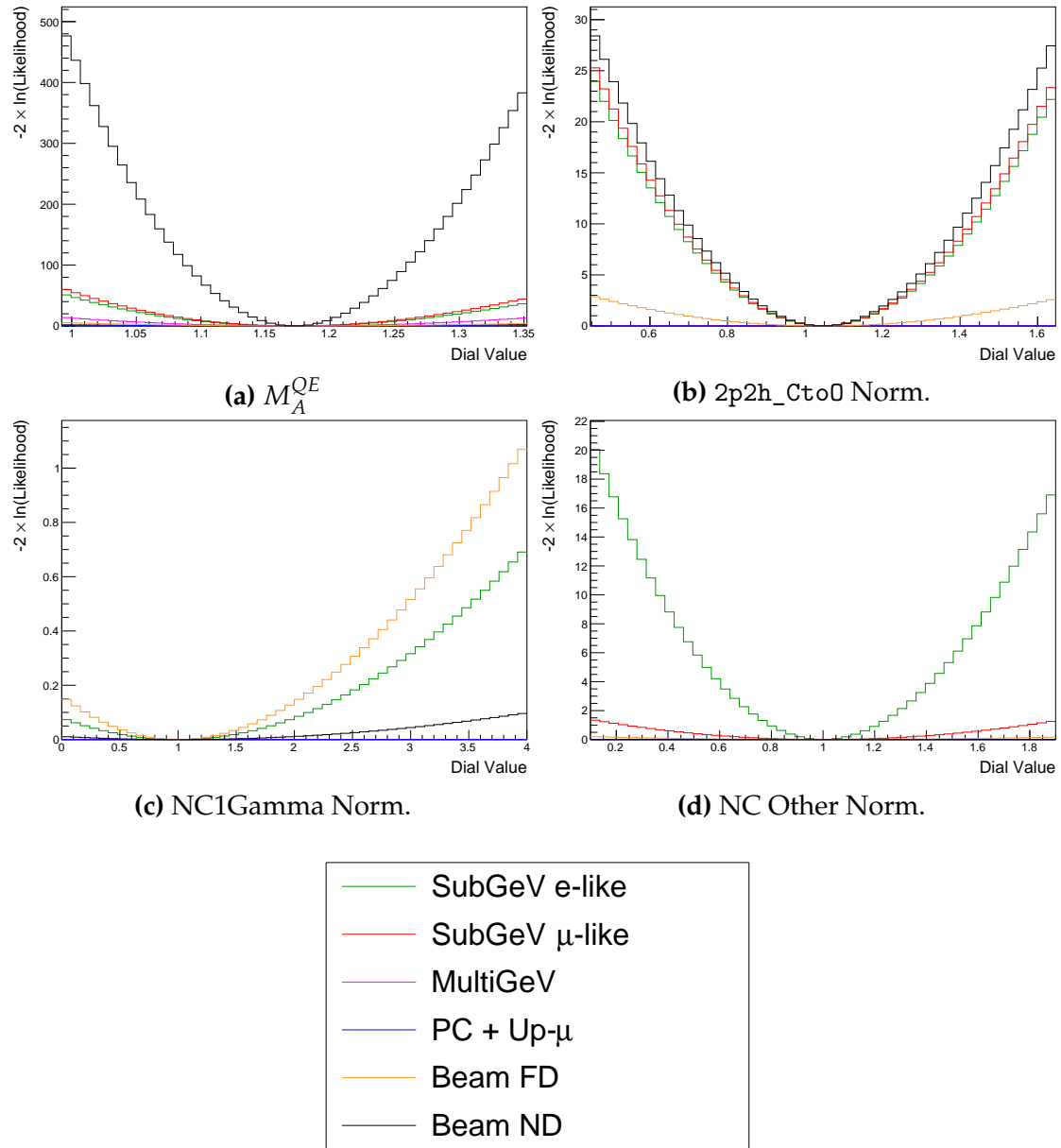


Figure 8.6: The response of the likelihood, as defined in section 8.2, illustrating the response of the samples to the various cross-section systematic parameters.

2937 8.3 Sensitivities

2938 The sensitivities of the joint T2K and SK oscillation analysis are presented in
2939 the form of Asimov fits. This technique builds an Asimov data set (follow-
2940 ing section 8.2) using the AsimovA oscillation parameters and post-BANFF
2941 systematic tune.

2942 In practice, the Asimov fits presented within this analysis are modified from
2943 the above definition. An Asimov prediction of both beam and atmospheric far
2944 detector samples is fit whilst the true data is used for near detector samples.
2945 The Asimov predictions at the far detector are built using the BANFF tuning (as
2946 discussed in section 3.2). These modifications mean that the results are equivalent
2947 to performing a far detector Asimov fit using inputs from the BANFF data fit.
2948 Consequently, this allows the results to be cross-checked with the results from
2949 the P-Theta analysis. The comparison has been performed and is documented in
2950 [221]. No significant discrepancies were found between the fitters.

2951 This section proceeds with the following studies. Firstly, the sensitivity of
2952 the atmospheric samples after the T2K cross-section has been applied to the low-
2953 energy events is detailed in subsection 8.3.1. This includes studying the choice of
2954 applying the 2020 PDG reactor constraint [77] to the atmospheric samples, which
2955 is documented in subsection 8.3.2. Additionally, the effect of applying the near-
2956 detector constraints onto the atmospheric samples is discussed in subsection 8.3.3.
2957 The main result is the sensitivity of the simultaneous beam and atmospheric fit.
2958 The sensitivities, both with and without the application of the reactor constraint,
2959 are presented in subsection 8.3.4 and subsection 8.3.5, respectively. To indicate
2960 the benefit of the joint analysis, the sensitivities are compared to the 2020 T2K
2961 sensitivities [76, 183] in subsection 8.3.6 and subsection 8.3.7. As shown in
2962 subsection 8.2.1, the response of the beam and atmospheric samples change
2963 depending upon the true set of oscillation parameters assumed. Therefore,
2964 subsection 8.3.8 documents the sensitivities at an alternative oscillation parameter

²⁹⁶⁵ set. It is important to note that these results have been published at the Neutrino
²⁹⁶⁶ 2022 conference on behalf of the T2K and SK collaborations [109].

2967 8.3.1 Atmospheric-Only Sensitivity Without Reactor Constraint

2968 This section presents the results of an Asimov fit using samples from the near
 2969 detector and only atmospheric samples from the far detector. The results are
 2970 presented as one-dimensional or two-dimensional histograms which have been
 2971 marginalised over all other parameters using the technique outlined in sub-
 2972 section 4.3.1. Each histogram displays the posterior probability density and
 2973 illustrates the credible intervals, calculated using the technique in subsection 4.3.2.
 2974 For these fits in this subsection, a flat penalty term is used for $\sin^2(\theta_{13})$ such the
 2975 reactor constraint is not applied. The Asimov data is generated assuming the
 2976 AsimovA oscillation parameter set defined in Table 2.2 and the post-BANFF
 2977 systematic parameter tune.

Without Reactor Constraint, Both Hierarchies

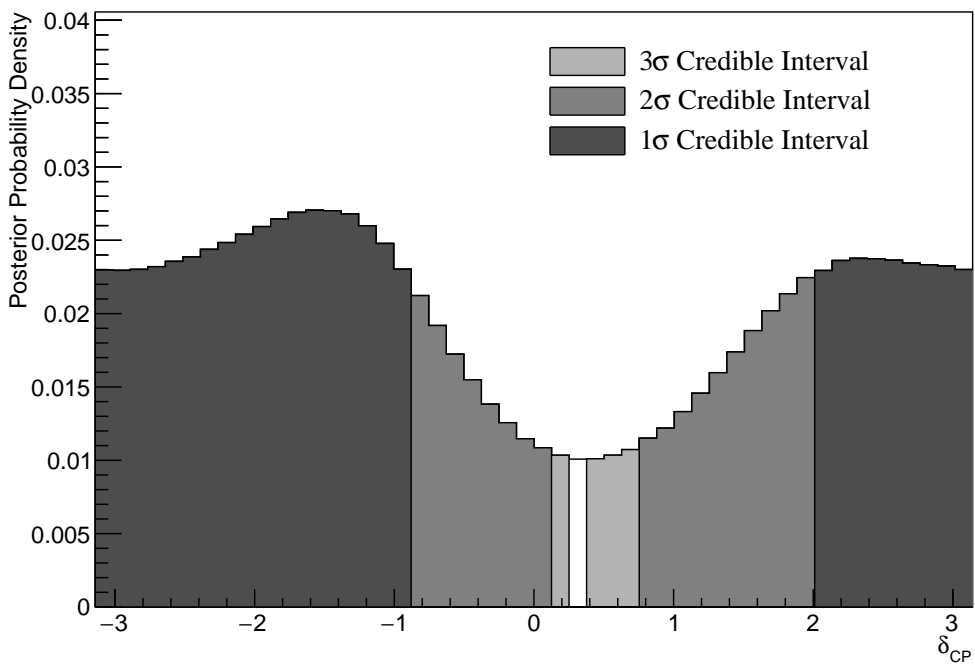


Figure 8.7: The one-dimensional posterior probability density distribution in δ_{CP} , marginalised over both hierarchies, from the SK atmospheric-only fit. The reactor constraint is not applied.

2978 Figure 8.7 illustrates the posterior probability density for δ_{CP} , marginalised
 2979 over both hierarchies. If instead, only steps in the normal hierarchy were
 2980 considered, the shape of the contours would change. The fit favours the known

oscillation parameter ($\delta_{CP} = -1.601$) although the posterior probability is very flat through the range of $-\pi < \delta_{CP} < -1$ and $2 < \delta_{CP} < \pi$. There is also a region around $\delta_{CP} \sim 0.4$ which is disfavoured at 2σ . This indicates that the SK samples can rule out some parts of the CP conserving parameter space reasonably well, near $\delta_{CP} \sim 0.4$, when the true value of $\delta_{CP} \sim \pi/2$.

Without Reactor Constraint, Both Hierarchies

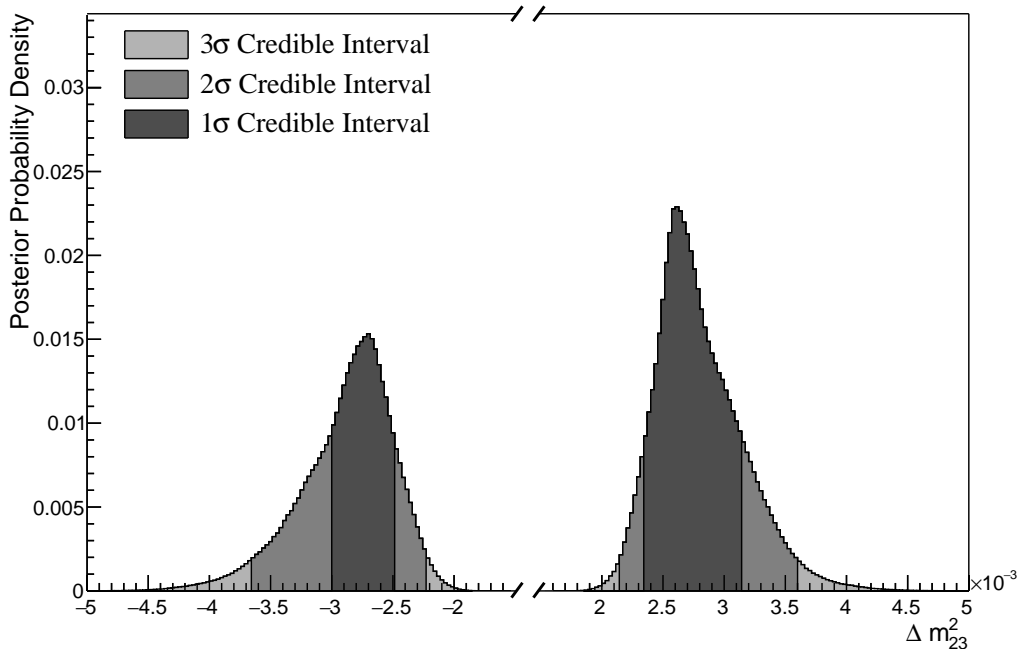


Figure 8.8: The one-dimensional posterior probability density distribution in Δm_{32}^2 , marginalised over both hierarchies, from the SK atmospheric-only fit. The reactor constraint is not applied.

The posterior probability density in Δm_{32}^2 is given in Figure 8.8. This distribution includes steps in both the normal hierarchy (NH, $\Delta m_{32}^2 > 0$) and the inverse hierarchy (IH, $\Delta m_{32}^2 < 0$). The highest posterior probability density is found within the NH, which agrees with the known oscillation parameter value. However, all of the credible intervals span both of the hierarchies hypotheses. If instead, only steps in the normal hierarchy were considered, the shape of the contours would change. The known oscillation parameter is $2.509 \times 10^{-3} \text{ eV}^2$, which is contained within the 1σ credible interval.

	LO ($\sin^2 \theta_{23} < 0.5$)	UO ($\sin^2 \theta_{23} > 0.5$)	Sum
NH ($\Delta m_{32}^2 > 0$)	0.17	0.40	0.58
IH ($\Delta m_{32}^2 < 0$)	0.13	0.29	0.42
Sum	0.31	0.69	1.00

Table 8.2: The distribution of steps in an SK atmospheric-only fit, presented as the fraction of steps in the upper (UO) and lower (LO) octants and the normal (NH) and inverted (IH) hierarchies. The reactor constraint is not applied. The Bayes factors are calculated as $B(\text{NH}/\text{IH}) = 1.37$ and $B(\text{UO}/\text{LO}) = 2.24$.

Following the discussion in subsection 4.3.3, the Bayes factor for hierarchy preference can be calculated by determining the fraction of steps that fall into the NH and the IH regions, as an equal prior is placed on both hypotheses. A similar calculation can be performed by calculating the fraction of steps which fall in the lower octant (LO, $\sin^2 \theta_{23} < 0.5$) or upper octant (UO, $\sin^2 \theta_{23} > 0.5$). The fraction of steps, broken down by hierarchy and octant, are given in Table 8.2. The Bayes factor for preferred hierarchy model is $B(\text{NH}/\text{IH}) = 1.37$. Table 4.1 states this value of the Bayes factor indicates a weak preference for the normal hierarchy model. The Bayes factor for choice of octant is $B(\text{UO}/\text{LO}) = 2.24$. This is also classified as a weak preference for the UO. Both of these show that the fit is returning the correct choice of models (NH and UO) for the known Asimov A oscillation parameters defined in Table 2.2.

The 1σ credible intervals, broken down by hierarchy, and position in parameter space of the highest posterior probability density is given in Table 8.3. These are taken from the one-dimensional projections of the oscillation parameters, marginalised over all other parameters within the fit. For the known Asimov value of $\delta_{CP} = -1.601$, the 1σ credible interval rules out a region between $\delta_{CP} = -0.86$ and $\delta_{CP} = 1.96$, when marginalising over both hierarchies. The position of the highest posterior density is $\delta_{CP} = -1.57$ which is clearly compatible with the known oscillation parameter value.

The sensitivity of the atmospheric samples to $\sin^2(\theta_{13})$ is presented in Figure 8.9. The likelihood scans presented in Figure 8.1 suggest that the sensitivity

Parameter	Interval	HPD
δ_{CP} , (BH)	$[-\pi, -0.86], [1.96, \pi]$	-1.57
δ_{CP} , (NH)	$[-\pi, -0.86], [1.88, \pi]$	-1.57
δ_{CP} , (IH)	$[-\pi, -0.94], [1.96, \pi]$	-1.57
Δm_{32}^2 (BH) [$\times 10^{-3}\text{eV}^2$]	$[-3.00, -2.50], [2.35, 3.15]$	2.65
Δm_{32}^2 (NH) [$\times 10^{-3}\text{eV}^2$]	$[2.39, 3.04]$	2.64
Δm_{32}^2 (IH) [$\times 10^{-3}\text{eV}^2$]	$[-3.15, -2.45]$	-2.70
$\sin^2(\theta_{23})$ (BH)	$[0.476, 0.59]$	0.542
$\sin^2(\theta_{23})$ (NH)	$[0.476, 0.59]$	0.554
$\sin^2(\theta_{23})$ (IH)	$[0.476, 0.59]$	0.542

Table 8.3: The position of the highest posterior probability density (HPD) and width of the 1σ credible interval for the SK atmospheric-only fit. The reactor constraint is not applied. The values are presented by which hierarchy hypothesis is assumed: marginalised over both hierarchies (BH), normal hierarchy only (NH), and inverted hierarchy only (IH).

3016 to $\sin^2(\theta_{13})$ will be small. This behaviour is also seen in the fit results, where the
 3017 width of the 1σ credible intervals span the region of $\sin^2(\theta_{13}) = [0.008, 0.08]$. This
 3018 is more than an order of magnitude worse than the constraint from reactor
 3019 experiments [77].

3020 As previously discussed, the correlations between oscillation parameters are
 3021 also important to understand how the atmospheric samples respond. Figure 8.10
 3022 illustrates the two dimensional $\sin^2(\theta_{13}) - \delta_{CP}$ sensitivity, marginalised over all
 3023 other parameters. The displayed contours are calculated by marginalising over
 3024 both hierarchies. The shape of the 1σ credible interval shows that the constraining
 3025 power of the fit on δ_{CP} is dependent upon the value of $\sin^2(\theta_{13})$. Furthermore,
 3026 they show a strong resemblance to the likelihood scans illustrated in Figure 8.2.
 3027 Whilst the atmospheric samples do not strongly constrain the value of $\sin^2(\theta_{13})$,
 3028 the value of $\sin^2(\theta_{13})$ does impact the atmospheric sensitivity to δ_{CP} . A value of
 3029 $\sin^2(\theta_{13}) \sim 0.02$ would select a continuous contour over all values of δ_{CP} . This
 3030 shows the effect of the marginalisation effect previously described.

Without Reactor Constraint, Both Hierarchies

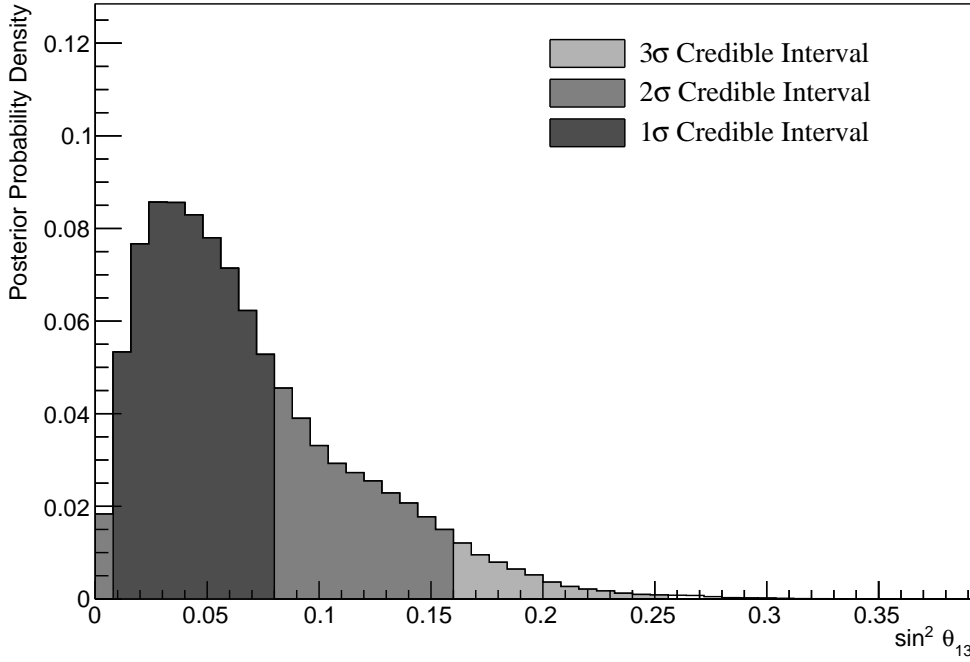


Figure 8.9: The one-dimensional posterior probability density distribution in $\sin^2(\theta_{13})$, marginalised over both hierarchies, from the SK atmospheric-only fit. The reactor constraint is not applied.

3031 The $\sin^2(\theta_{23}) - \Delta m_{32}^2$ disappearance contours are illustrated in Figure 8.11.
 3032 As expected, the area contained in the inverted hierarchy 1σ credible interval is
 3033 slightly smaller than that in the normal hierarchy. This follows from the Bayes
 3034 factor showing a weak preference for NH meaning that more of the steps will exist
 3035 in the $\Delta m_{32}^2 > 0$ region. The known oscillation parameters of $\sin^2(\theta_{23}) = 0.528$
 3036 and $\Delta m_{32}^2 = 2.509 \times 10^{-3} \text{ eV}^2$ are contained within the 1σ credible interval.

3037 Figure 8.12 illustrates the two-dimensional projections for each permutation of
 3038 oscillation parameters which this analysis is sensitive to: δ_{CP} , $\sin^2(\theta_{13})$, $\sin^2(\theta_{23})$,
 3039 and Δm_{32}^2 . The purpose of this plot is to illustrate the correlations between the
 3040 oscillation parameters. The contours are calculated whilst marginalising over
 3041 both hierarchies, however, only the NH is illustrated when plotting the Δm_{32}^2
 3042 parameter. As expected the correlations play a significant role in these sensitivity
 3043 measurements, especially the choice of the $\sin^2(\theta_{13})$ constraint. The application
 3044 of reactor constraint would be expected to alter both the width and position of the

Without Reactor Constraint, Both Hierarchies

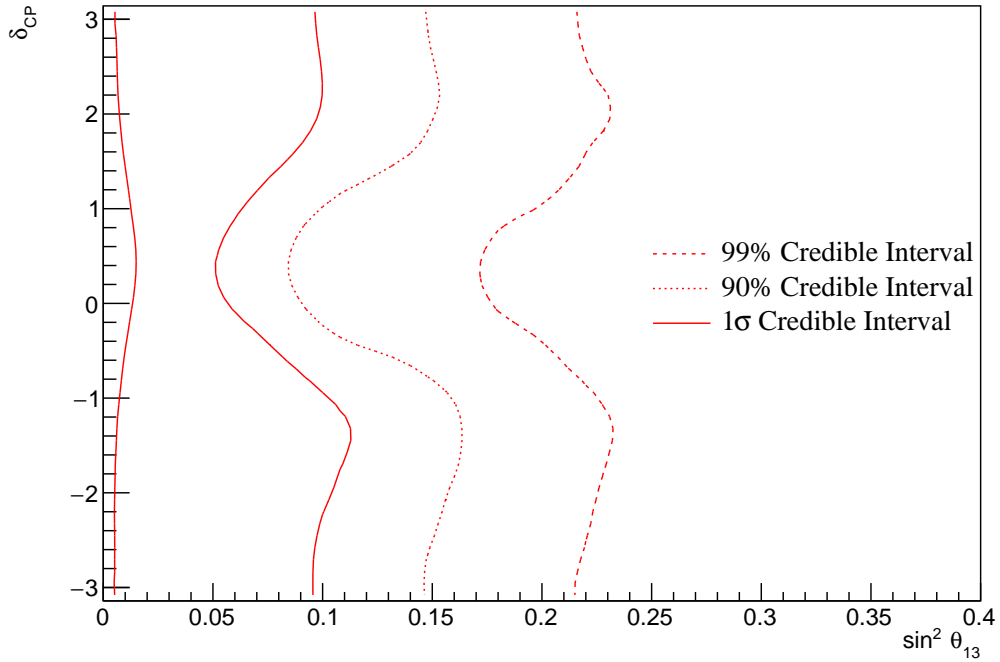


Figure 8.10: The two-dimensional posterior probability density distribution in δ_{CP} – $\sin^2(\theta_{13})$, marginalised over both hierarchies, from the SK atmospheric-only fit. The reactor constraint is not applied.

3045 Δm_{32}^2 , δ_{CP} , and $\sin^2(\theta_{23})$ constraints. The majority of the octant model preference
 3046 comes from the region of $\sin^2(\theta_{13}) \sim 0.03$ such that the application of the reactor
 3047 constraint would not be expected to significantly change the octant preference.
 3048 The reactor constraint would result in lower values of $|\Delta m_{32}^2|$. Interestingly, the
 3049 distribution of steps in the δ_{CP} - $\sin^2(\theta_{13})$ plot is slightly flatter in the region of the
 3050 reactor constraint. Both the posterior distribution from this fit and the distribution
 3051 in Figure 8.2 show a region of low negative log-likelihood extending out towards
 3052 higher values of $\sin^2(\theta_{13})$ in the $\delta_{CP} \sim -\pi/2$ and $\delta_{CP} \sim 2$ region. Consequently,
 3053 the reactor constraint could feasibly reduce the sensitivity of the atmospheric
 3054 samples to δ_{CP} , due to the previously discussed marginalisation effects.

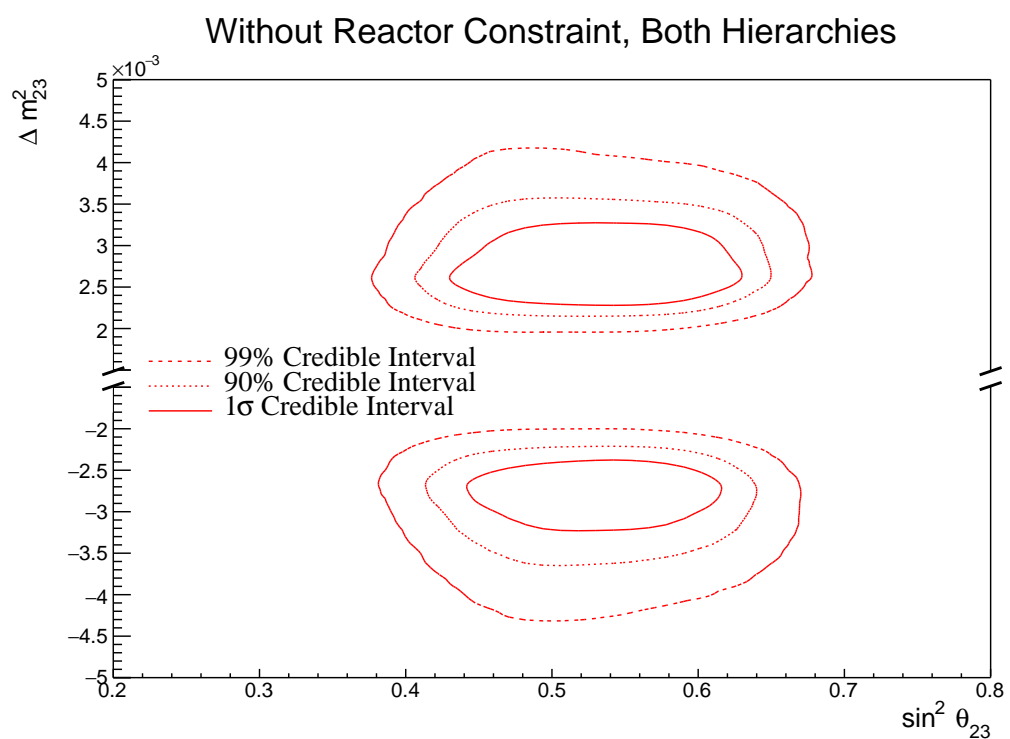


Figure 8.11: The two-dimensional posterior probability density distribution in $\Delta m_{32}^2 - \sin^2(\theta_{23})$, marginalised over both hierarchies, from the SK atmospheric-only fit. The reactor constraint is not applied.

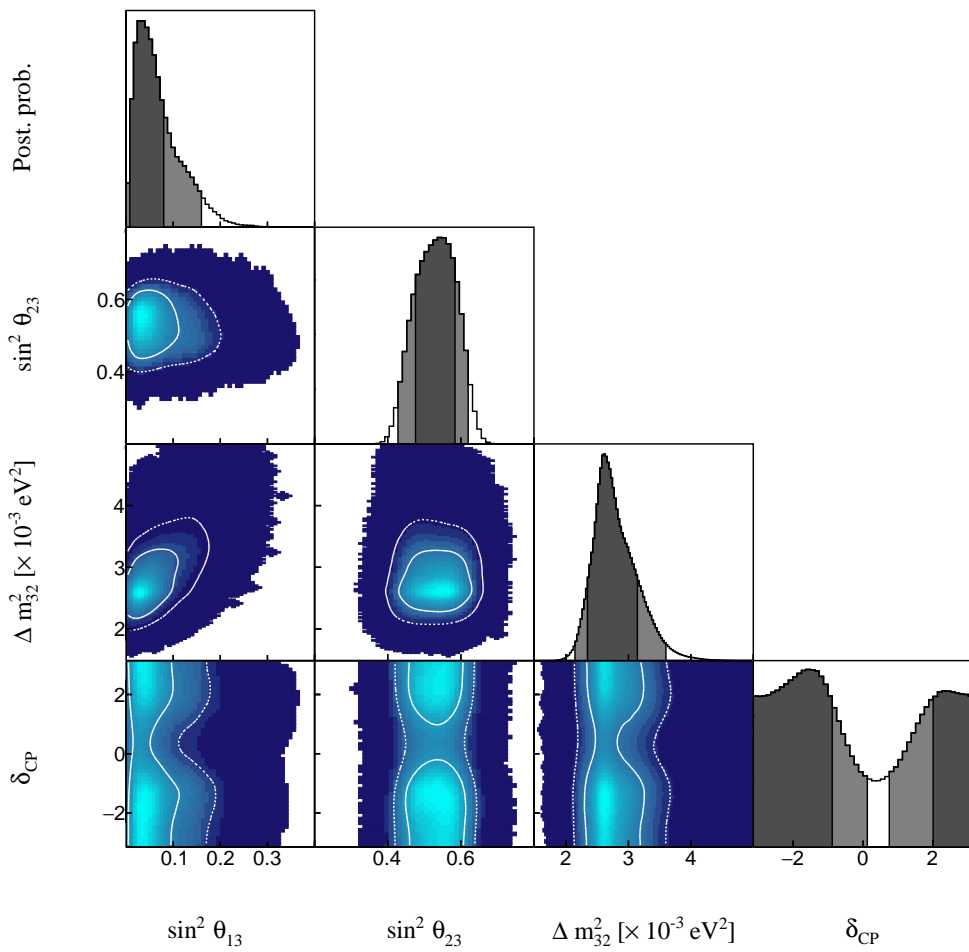


Figure 8.12: The posterior probability density distribution from the SK atmospheric-only fit. The reactor constraint is not applied. The distribution is given for each two-dimensional permutation of the oscillation parameters of interest. The one-dimensional distribution of each parameter is also given.

3055 8.3.2 Atmospheric-Only Sensitivity With Reactor Constraint

3056 The results in subsection 8.3.1 discuss the atmospheric sensitivity when the reactor
 3057 constraint is not applied. The correlations illustrated in Figure 8.12 indicate that
 3058 the marginalisation effects could contribute to differing sensitivities when the
 3059 external reactor constraint is applied. Using the technique discussed in subsec-
 3060 tion 4.1.1, the posterior distribution of the fit in subsection 8.3.1 can be reweighted
 3061 to include the reactor constraint of $\sin^2(\theta_{13}) = (2.18 \pm 0.08) \times 10^{-2}$ [77].

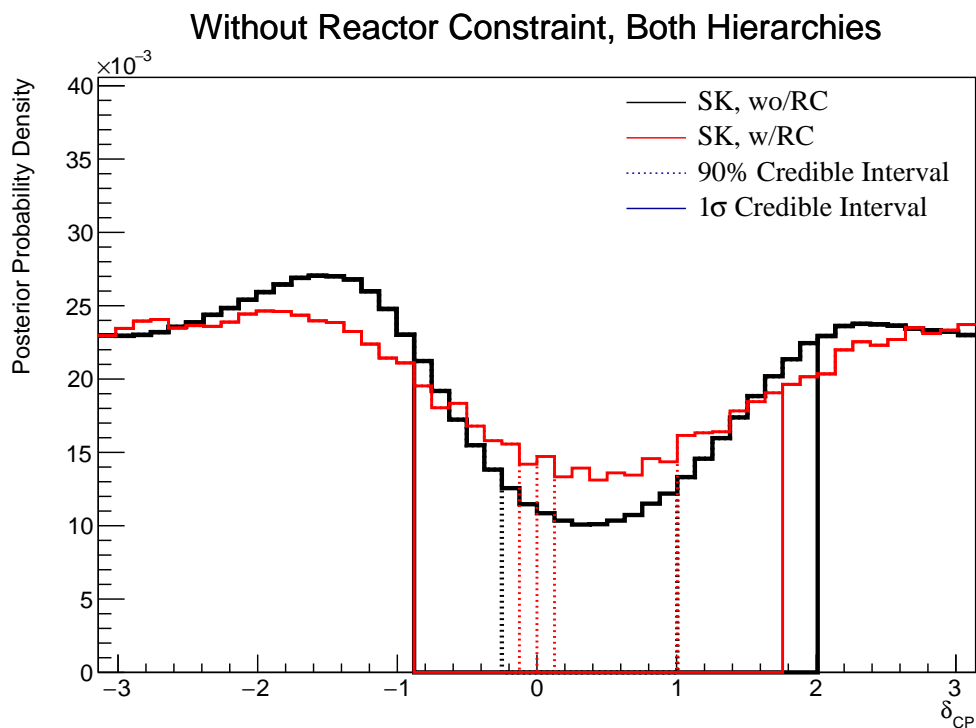


Figure 8.13: The one-dimensional posterior probability density distribution in δ_{CP} compared between the SK atmospheric-only fit (Black) and the SK atmospheric fit with the reactor constraint applied (Red). The distributions are marginalised over both hierarchies.

3062 Figure 8.13 illustrates the sensitivity to δ_{CP} of the atmospheric fit with reactor
 3063 constraint applied. The distribution is less peaked than the previous results.
 3064 This is due to the expected marginalisation effect previously discussed. The
 3065 width of the 1σ credible interval is increased when the reactor constraint is
 3066 applied, indicating less sensitivity to δ_{CP} in the region of $\sin^2(\theta_{13})$ preferred
 3067 by the reactor constraint.

Without Reactor Constraint, Both Hierarchies

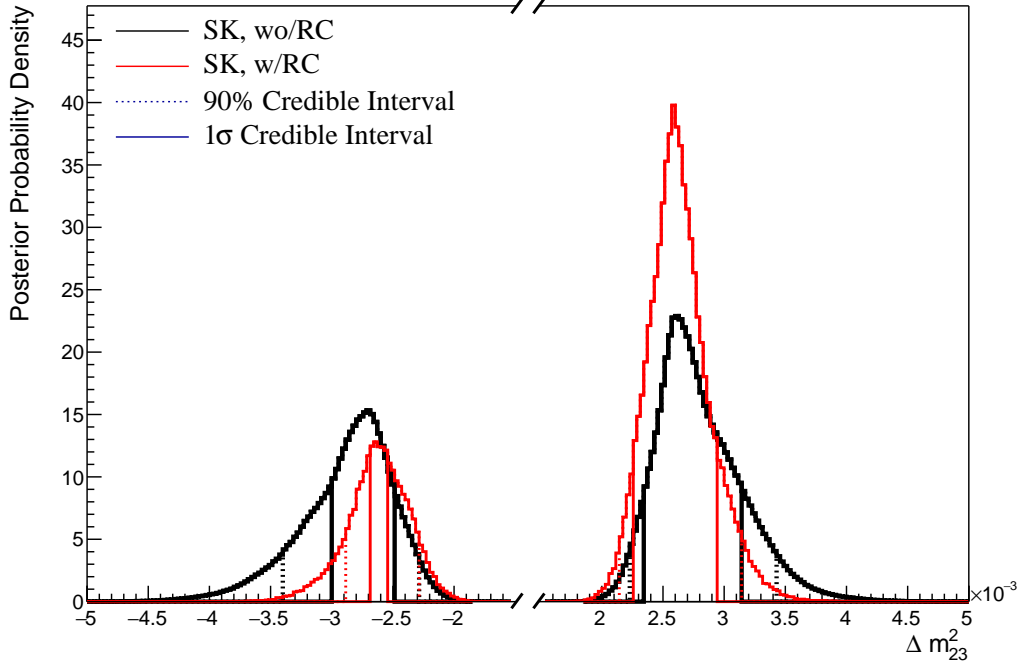


Figure 8.14: The one-dimensional posterior probability density distribution in Δm_{32}^2 compared between the SK atmospheric-only fit (Black) and the SK atmospheric fit with the reactor constraint applied (Red). The distributions are marginalised over both hierarchies.

The reactor constraint increases the sensitivity of the atmospheric samples to Δm_{32}^2 as illustrated in Figure 8.14. The 1σ credible interval in Δm_{32}^2 is determined to be $[-2.70, -2.55] \times 10^{-3}\text{eV}^2$ and $[2.25, 2.95] \times 10^{-3}\text{eV}^2$. The width of the IH credible interval is reduced by $\sim 70\%$ when the reactor constraint is applied. Due to the marginalisation effects observed in Figure 8.12, the favoured region of Δm_{32}^2 moves closer to zero for both hierarchies. A clear explanation of this behaviour is illustrated in Figure 8.15 which illustrates the posterior distribution in the $\Delta m_{32}^2 - \sin^2(\theta_{13})$ parameters, marginalised over both hierarchies. The correlation between Δm_{32}^2 and $\sin^2(\theta_{13})$ is such that lower values of $\sin^2(\theta_{13})$ tend towards lower values of $|\Delta m_{32}^2|$. This moves the posterior distribution towards the known oscillation parameter $\Delta m_{32}^2 = 2.509 \times 10^{-3}\text{eV}^2$.

Table 8.4 presents the fraction of steps in each hierarchy and octant model for the fit after the reactor constraint has been applied. The reactor constraint significantly increases the NH preference, increasing the Bayes factor from

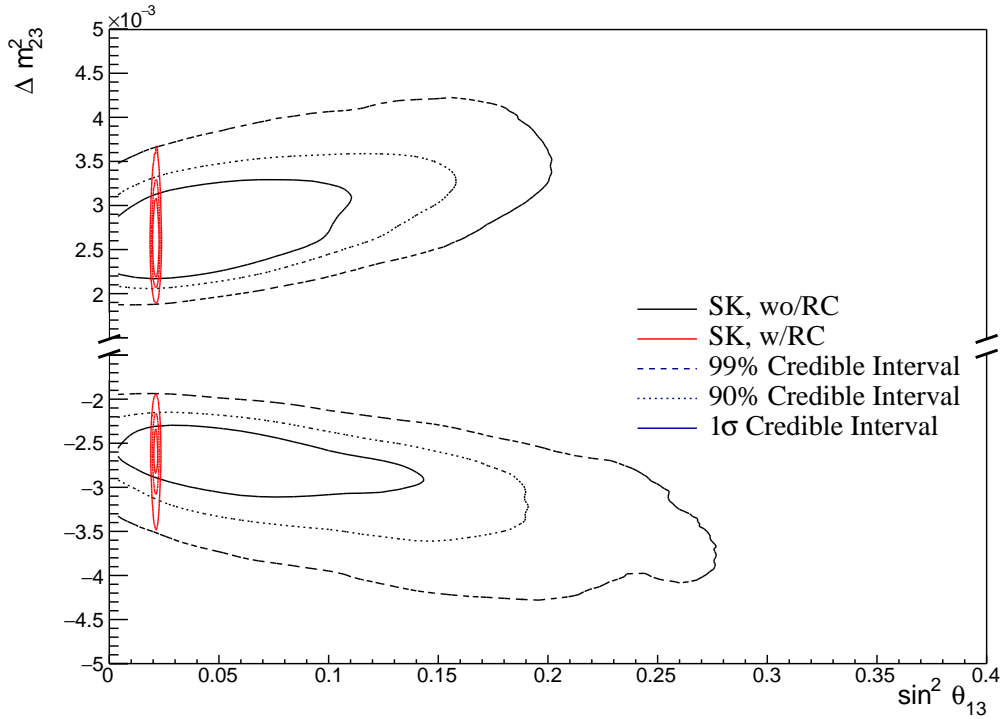


Figure 8.15: The two-dimensional posterior probability density distribution in Δm_{32}^2 – $\sin^2(\theta_{13})$ compared between the SK atmospheric-only fit (Black) and the SK atmospheric fit with the reactor constraint (Red). The distributions are marginalised over both hierarchies.

	LO ($\sin^2 \theta_{23} < 0.5$)	UO ($\sin^2 \theta_{23} > 0.5$)	Sum
NH ($\Delta m_{32}^2 > 0$)	0.21	0.53	0.74
IH ($\Delta m_{32}^2 < 0$)	0.08	0.18	0.26
Sum	0.29	0.71	1.00

Table 8.4: The distribution of steps in an SK atmospheric with reactor constraint fit, presented as the fraction of steps in the upper (UO) and lower (LO) octants and the normal (NH) and inverted (IH) hierarchies. The Bayes factors are calculated as $B(\text{NH}/\text{IH}) = 2.86$ and $B(\text{UO}/\text{LO}) = 2.39$.

3082 $B(\text{NH}/\text{IH}) = 1.37$ to $B(\text{NH}/\text{IH}) = 2.86$ when the reactor constraint is applied.

3083 This is still defined as a weak preference for NH hypothesis according to Jeffrey's

3084 scale (see Table 4.1), however, it is a stronger preference than when the constraint

3085 is not applied. The preference for the correct octant model is slightly increased

3086 by the application of the reactor constraint which is consistent with expectation.

3087 However, the conclusion that would be made does not significantly change.

3088 8.3.3 Application of Near Detector Constraints for Atmospheric 3089 Samples

3090 The choice of applying the near detector constraints to the low-energy atmo-
3091 spheric samples was introduced in subsection 6.4.3. This subsection illustrates
3092 the effect of that choice on the sensitivities of the atmospheric samples to the
3093 oscillation parameters. This Asimov data was generated assuming the ‘AsimovA’
3094 oscillation parameter set defined in Table 2.2 and the post-BANFF systematic
3095 parameter tune.

3096 The change in sensitivity on δ_{CP} is given in Figure 8.16. The reactor constraint
3097 is not applied in either of the fits within this comparison. The shape of the
3098 posterior is similar although less peaked at the Asimov point ($\delta_{CP} = -1.601$)
3099 and more symmetric between the regions of $\delta_{CP} = -1.601$ and $\delta_{CP} \sim 2.5$. The
3100 width of the 1σ credible intervals are approximately the same (identical to within
3101 a bin width) and the same conclusion holds for the higher credible intervals. The
3102 change in sensitivity to other oscillation parameters has been studied and no
3103 significant discrepancies were found. As expected, the sensitivities are statistics
3104 dominated and the exact choice of systematic model and constraint does not
3105 significantly affect the physics conclusions one would make from this analysis.

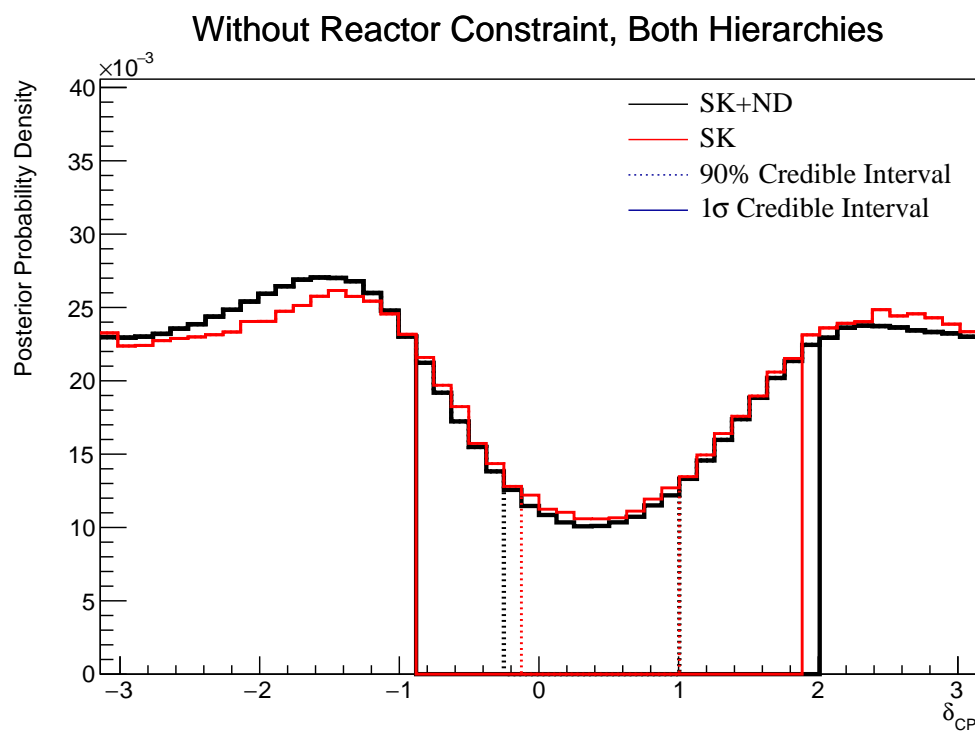


Figure 8.16: The one-dimensional posterior probability density distribution in δ_{CP} compared between the SK atmospheric-only fit where the near detector constraint is (Black) and is not (Red) applied. The distributions are marginalised over both hierarchies.

3106 8.3.4 Atmospheric and Beam Sensitivity without Reactor Con- 3107 straint

3108 This section presents the sensitivities of the simultaneous beam and atmospheric
 3109 analysis where the reactor constraint is not applied. Similar to the previous
 3110 studies, the Asimov data is built assuming the post-BANFF cross-section tune
 3111 and Asimov A oscillation parameters defined in Table 2.2. This fit uses all 18 near
 3112 detector beam samples, 5 far detector beam samples, and 18 atmospheric samples.
 3113 The sensitivity to δ_{CP} , marginalised over both hierarchies, is given in Figure 8.17.

Without Reactor Constraint, Both Hierarchies

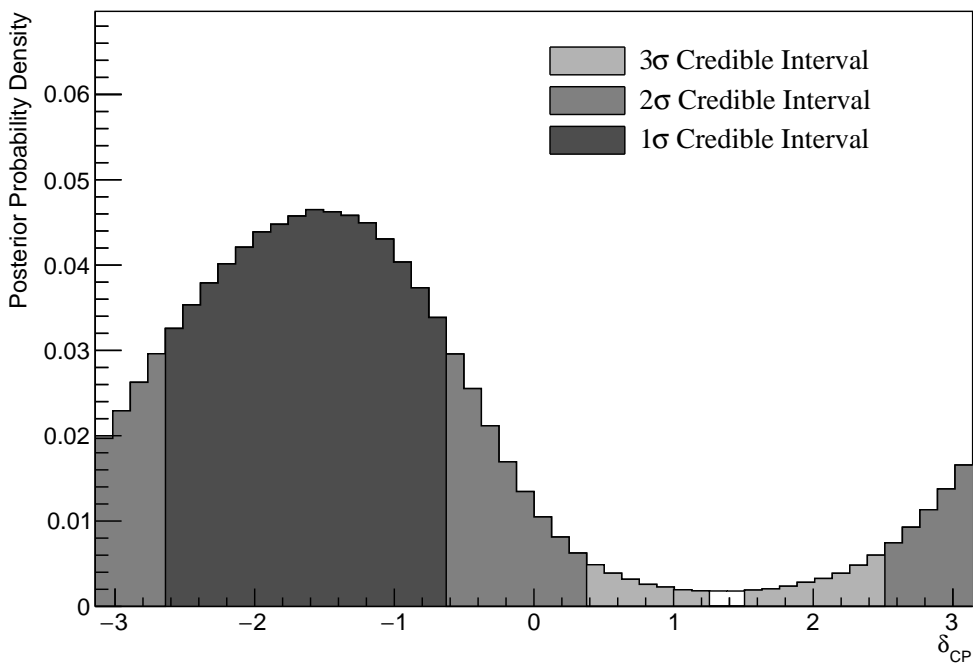


Figure 8.17: The one-dimensional posterior probability density distribution in δ_{CP} , marginalised over both hierarchies, from the joint beam and atmospheric fit. The reactor constraint is not applied.

3114 The credible intervals and highest posterior distribution for each oscillation
 3115 parameter is given in Table 8.5. The highest posterior probability density is
 3116 $\delta_{CP} = -1.58$ and is compatible with the known Asimov A value of $\delta_{CP} = -1.601$.
 3117 The CP-conserving values of $\delta_{CP} = 0, \pi, -\pi$ are disfavoured at 1 σ credible
 3118 interval. There is also a region around $\delta_{CP} = 1.4$ which is disfavoured at more
 3119 than 3 σ . Whilst these conclusions can only be made at this particular Asimov

point, it does show that if the true value of δ_{CP} was CP-violating, this joint analysis would be able to disfavour CP conserving values at over 1σ without any external constraints. The highest posterior probability density does move further away from the Asimov point when only steps in the NH region are considered. This is due to the correlations between the value of δ_{CP} and the mass hierarchy, as will be later discussed.

Parameter	Interval	HPD
δ_{CP} , (BH)	$[-2.64, -0.63]$	-1.57
δ_{CP} , (NH)	$[-2.76, -0.63]$	-1.45
δ_{CP} , (IH)	$[-2.39, -0.88]$	-1.57
Δm_{32}^2 (BH) [$\times 10^{-3}\text{eV}^2$]	[2.46, 2.58]	2.49
Δm_{32}^2 (NH) [$\times 10^{-3}\text{eV}^2$]	[2.48, 2.56]	2.51
Δm_{32}^2 (IH) [$\times 10^{-3}\text{eV}^2$]	$[-2.60, -2.52]$	-2.55
$\sin^2(\theta_{23})$ (BH)	[0.48, 0.55]	0.509
$\sin^2(\theta_{23})$ (NH)	[0.48, 0.55]	0.509
$\sin^2(\theta_{23})$ (IH)	[0.48, 0.55]	0.521

Table 8.5: The position of the highest posterior probability density (HPD) and width of the 1σ credible interval for the joint beam and atmospheric fit. The reactor constraint is not applied. The values are presented by which hierarchy hypothesis is assumed: marginalised over both hierarchies (BH), normal hierarchy only (NH), and inverted hierarchy only (IH).

The sensitivity to Δm_{32}^2 is illustrated in Figure 8.18, marginalised over both hierarchies. Notably, the 1σ credible interval is entirely contained within the normal hierarchy region, as illustrated in Table 8.5. This illustrates reasonable sensitivity to the mass hierarchy model. This is also reflected in the 1σ credible intervals being approximately the same when they are made considering both hierarchies and when considering only the NH. The known oscillation parameter is $\Delta m_{32}^2 = 2.509 \times 10^{-3}\text{eV}^2$. The normal hierarchy distribution favours this value with the highest posterior probability density of $\Delta m_{32}^2 = 2.51 \times 10^{-3}\text{eV}^2$.

The fraction of steps in each of the mass hierarchy regions and octants of $\sin^2(\theta_{23})$ is given in Table 8.6. The Bayes factors are determined to be $B(\text{NH}/\text{IH}) =$

3136 3.67 and $B(\text{UO}/\text{LO}) = 1.74$. Jeffrey's scale (presented in Table 4.1) states that
 3137 this value of the hierarchy Bayes factor illustrates substantial evidence for the
 3138 normal hierarchy hypothesis. This corresponds to the correct hypothesis given
 3139 the known oscillation parameters. It is a stronger statement than the atmospheric-
 3140 only analysis can provide. It is important to note that this is a substantial
 3141 preference that requires no external constraints required. The Bayes factor for
 3142 octant determination represents a weak preference for the upper octant but does
 3143 select the correct octant model.

	LO ($\sin^2 \theta_{23} < 0.5$)	UO ($\sin^2 \theta_{23} > 0.5$)	Sum
NH ($\Delta m_{32}^2 > 0$)	0.29	0.50	0.79
IH ($\Delta m_{32}^2 < 0$)	0.08	0.13	0.21
Sum	0.37	0.63	1.00

Table 8.6: The distribution of steps in a joint beam and atmospheric fit, presented as the fraction of steps in the upper (UO) and lower (LO) octants and the normal (NH) and inverted (IH) hierarchies. The reactor constraint is not applied. The Bayes factors are calculated as $B(\text{NH}/\text{IH}) = 3.67$ and $B(\text{UO}/\text{LO}) = 1.74$.

3144 The sensitivity to $\sin^2(\theta_{23})$ is presented in Figure 8.19. There is a clear
 3145 preference for the upper octant but the peak of the distribution is relatively
 3146 flat. It peaks at $\sin^2(\theta_{23}) = 0.509$ which is in the region of the known value of
 3147 $\sin^2(\theta_{23}) = 0.528$. The difference in the highest posterior distribution and the
 3148 width of the credible interval is relatively unchanged when considering different
 3149 hierarchy models showing no strong correlation between $\sin^2(\theta_{23})$ and $|\Delta m_{32}^2|$.
 3150 The sensitivity presented as a function of the appearance parameters ($\sin^2(\theta_{13}) -$
 3151 δ_{CP}) is given in Figure 8.20. As expected, the contours follow that given in
 3152 Figure 8.2, where the 2σ credible intervals have a closed contour excluding the
 3153 region around $\delta_{CP} \sim 1.2$. The width of the 3σ credible interval is also clearly
 3154 dependent upon the value of δ_{CP} . Close to the Asimov point, $\delta_{CP} = -1.601$, the
 3155 width of the 3σ credible interval approximately spans $\sin^2(\theta_{13}) = [0.013, 0.04]$.
 3156 This is reduced to a region of $\sin^2(\theta_{13}) = [0.023, 0.042]$ at the most disfavoured
 3157 value of δ_{CP} . This follows the behaviour shown in the likelihood scans. The 1σ

Without Reactor Constraint, Both Hierarchies

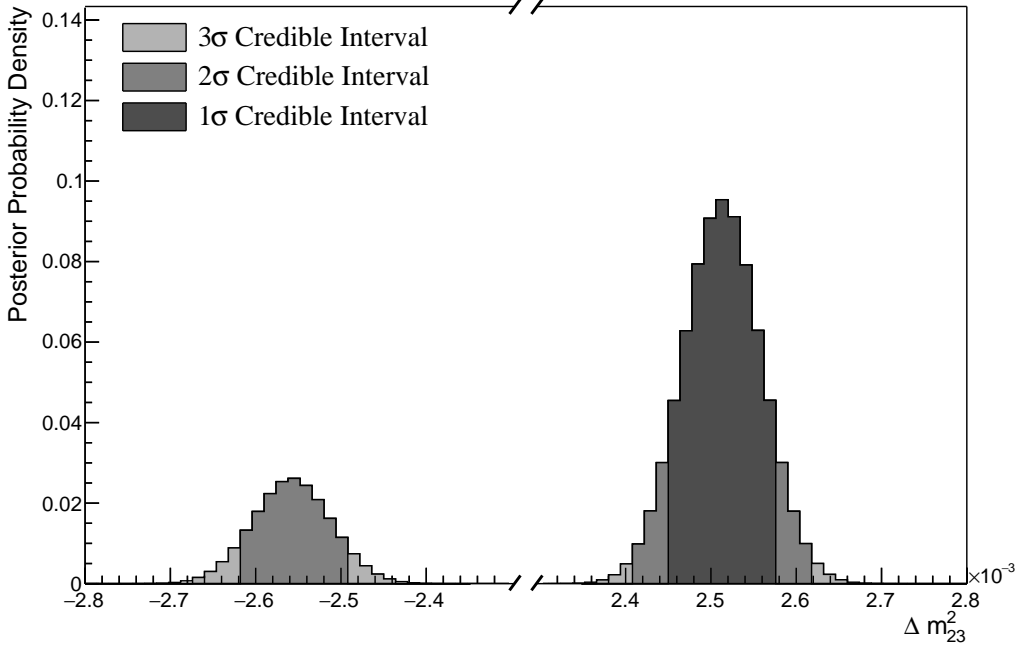


Figure 8.18: The one-dimensional posterior probability density distribution in Δm_{32}^2 , marginalised over both hierarchies, from the joint beam and atmospheric fit. The reactor constraint is not applied.

credible interval is consistent with both the known oscillation parameter and the reactor constraint ($\sin^2(\theta_{13}) = (2.18 \pm 0.08) \times 10^{-2}$). Application of the reactor constraint would be expected to decrease the width of the 1 σ credible intervals of δ_{CP} due to the triangular shape of the posterior probability.

The sensitivity in terms of the ‘disappearance’ parameters marginalised over both hierarchies is given in Figure 8.21. The area contained within the IH credible intervals is significantly smaller than those in the NH region. This is reflected in the IH credible intervals being tighter in the $\sin^2(\theta_{23})$ dimension. No significant correlation is observed between the value of $\sin^2(\theta_{23})$ and $|\Delta m_{32}^2|$.

The two-dimensional posterior distribution for each permutation of the oscillation parameters of interest is given in Figure 8.22. The most notable observation is that the $\sin^2(\theta_{13})$ and $\sin^2(\theta_{23})$ are anti-correlated. If the value of $\sin^2(\theta_{13})$ was known to be closer to the known oscillation parameter value, the preferred value of $\sin^2(\theta_{23})$ would increase furthering the preference for the UO. That

Without Reactor Constraint, Both Hierarchies

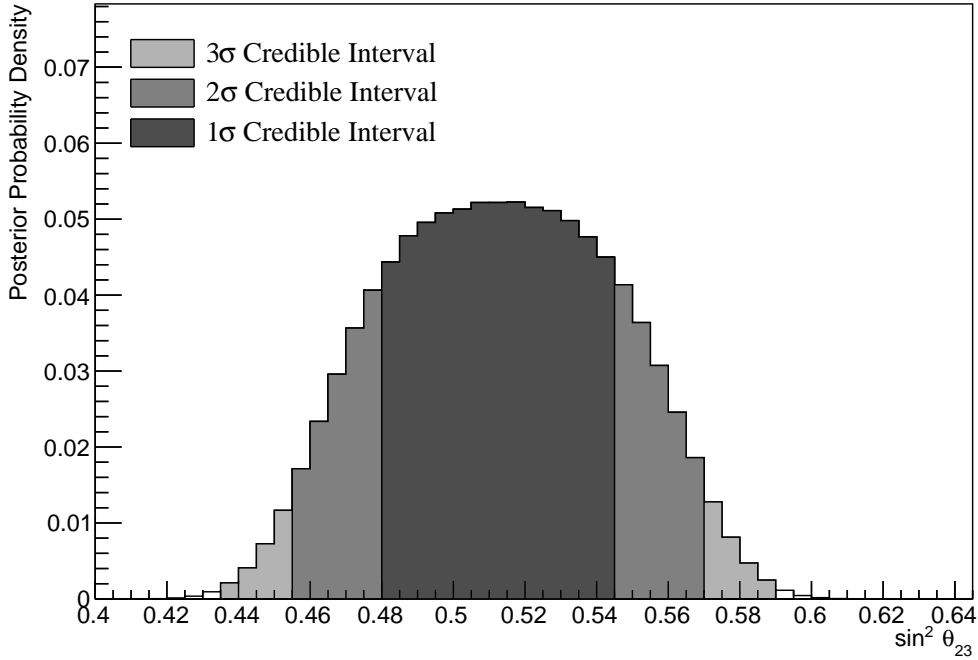


Figure 8.19: The one-dimensional posterior probability density distribution in $\sin^2(\theta_{23})$, marginalised over both hierarchies, from the joint beam-atmospheric fit. The reactor constraint is not applied.

would move the highest posterior probability closer in line with the Asimov value. This also means that the preference for the UO would be increased if the reactor constraint was to be applied.

Furthermore, the δ_{CP} and $|\Delta m_{32}^2|$ oscillation parameters are anti-correlated, such that higher values of $|\Delta m_{32}^2|$ prefer lower values of δ_{CP} . Whilst this is an interesting result on its own, the width of the Δm_{32}^2 contours also depend on $\sin^2(\theta_{13})$. This introduces another correlation effect that could modify the sensitivity to δ_{CP} once the reactor constraint is applied.

The correlation between $\sin^2(\theta_{13})$ and Δm_{32}^2 can be seen in Figure 8.23. A much larger fraction of the posterior distribution is contained in the NH for lower values of $\sin^2(\theta_{13})$. Consequently, the application of the reactor constraint would be expected to significantly increase the preference for NH.

Without Reactor Constraint, Both Hierarchies

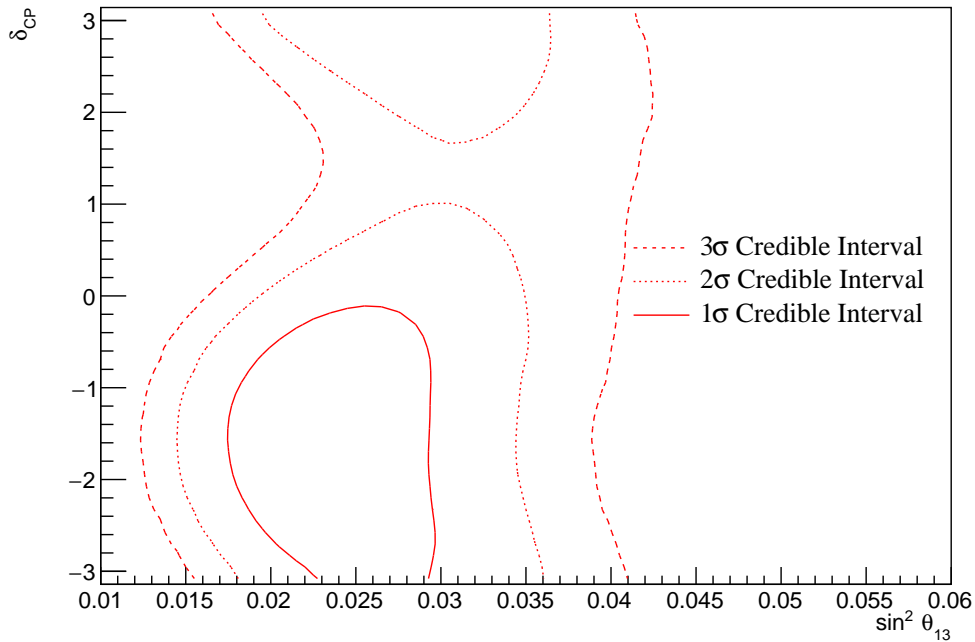


Figure 8.20: The two-dimensional posterior probability density distribution in δ_{CP} – $\sin^2(\theta_{13})$, marginalised over both hierarchies, from the joint beam and atmospheric fit. The reactor constraint is not applied.

Without Reactor Constraint, Both Hierarchies

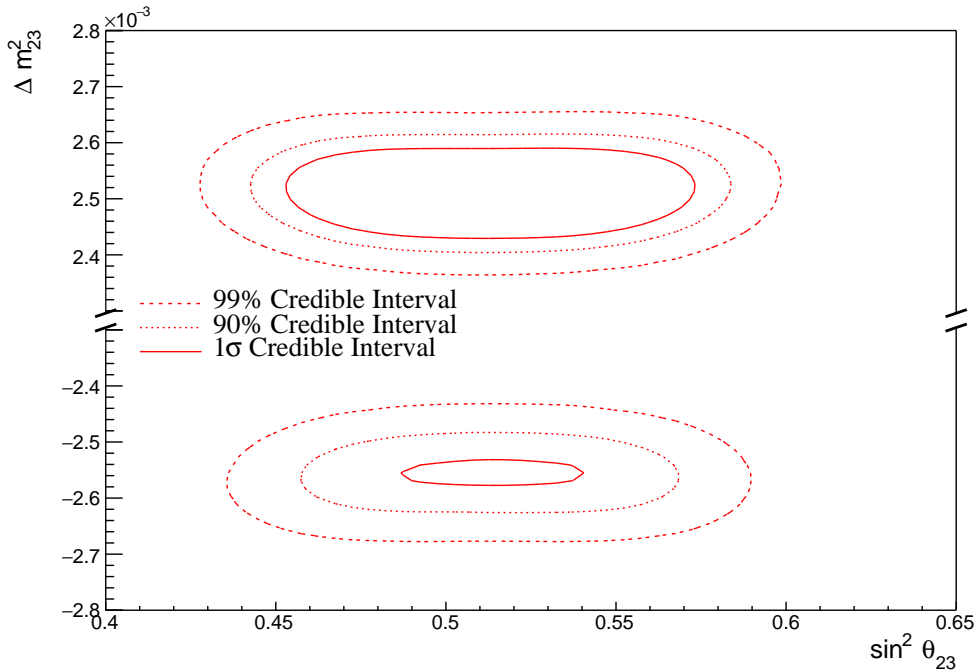


Figure 8.21: The two-dimensional posterior probability density distribution in Δm_{32}^2 – $\sin^2(\theta_{23})$, marginalised over both hierarchies, from the joint beam and atmospheric fit. The reactor constraint is not applied.

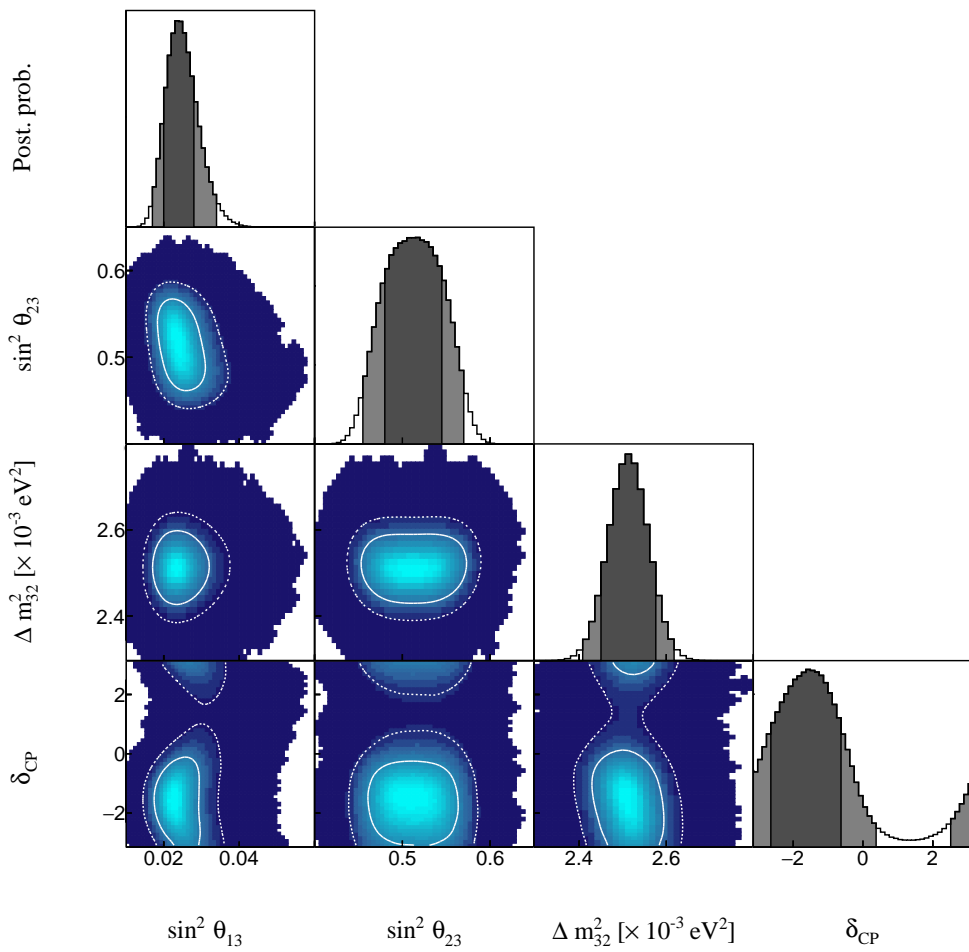


Figure 8.22: The posterior probability density distribution from the joint beam and atmospheric fit. The reactor constraint is not applied. The distribution is given for each two-dimensional permutation of the oscillation parameters of interest. The one-dimensional distribution of each parameter is also given.

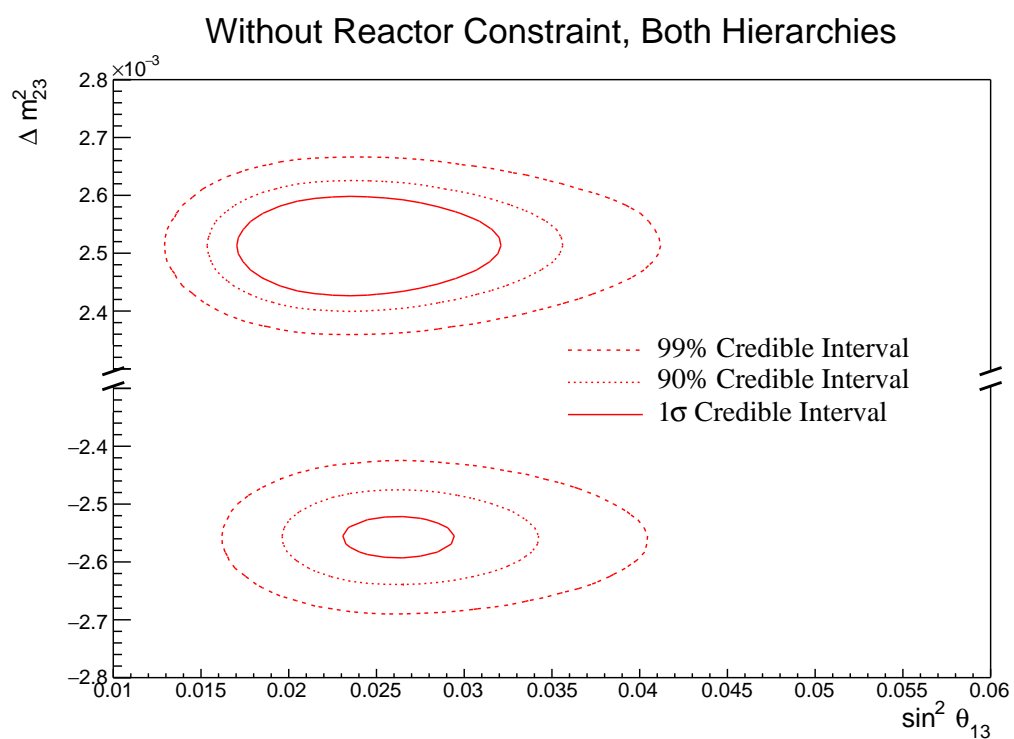


Figure 8.23: The two-dimensional posterior probability density distribution in $\Delta m_{32}^2 - \sin^2(\theta_{13})$, marginalised over both hierarchies, from the joint beam and atmospheric fit. The reactor constraint is not applied.

3184 8.3.5 Atmospheric and Beam Sensitivity with Reactor Constraint

3185 This section presents the sensitivities of the joint beam and atmospheric fit when
 3186 the reactor constraint is applied to $\sin^2(\theta_{13})$. As with the previous studies, the
 3187 Asimov data is made using the AsimovA oscillation parameter set defined in
 3188 Table 2.2 and the post-BANFF systematic parameter tune.

With Reactor Constraint, Both Hierarchies

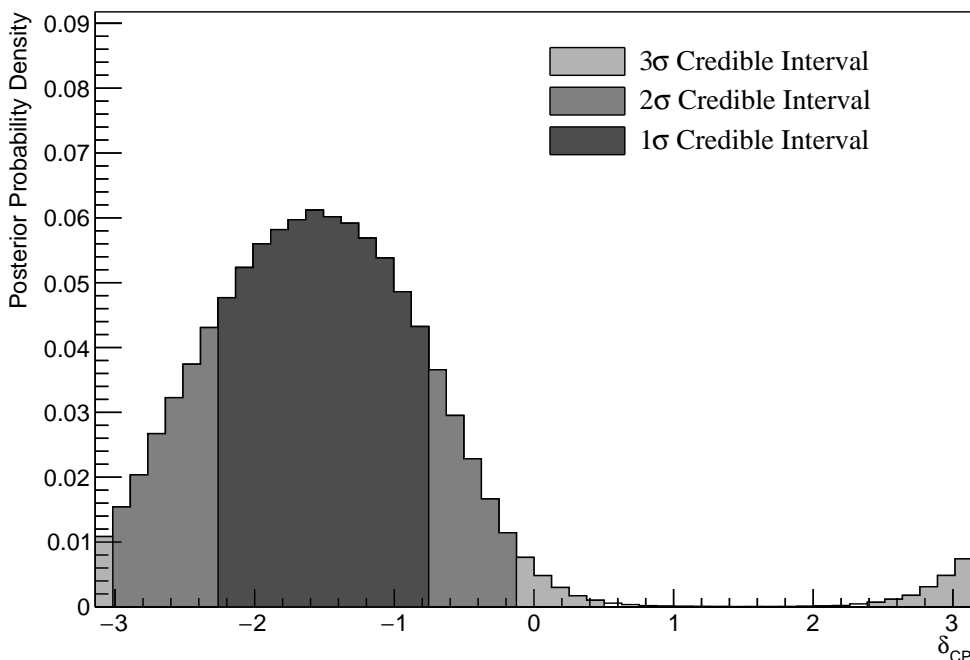


Figure 8.24: The one-dimensional posterior probability density distribution in δ_{CP} , marginalised over both hierarchies, from the joint beam and atmospheric fit where the reactor constraint is applied.

3189 Figure 8.24 illustrates the sensitivity to δ_{CP} , marginalised over both hierarchies.
 3190 The CP-conserving values of $\delta_{CP} = -\pi, 0, \pi$ are disfavoured at 2σ . Furthermore,
 3191 the 3σ credible interval excludes the region of $\delta_{CP} = [0.50, 2.39]$. Thus clearly
 3192 disfavouring the region of $\delta_{CP} = \pi/2$ at more than 3σ for this particular set
 3193 of known oscillation parameters. The width of the 1σ credible intervals and
 3194 the position of the highest posterior probability density is given in Table 8.7.
 3195 The highest posterior probability density in δ_{CP} is calculated as $\delta_{CP} = -1.57$
 3196 showing no significant biases in the determination of the known oscillation

parameters. The posterior distribution is more peaked around the known oscillation parameter value of $\delta_{CP} = -1.601$, as compared to the sensitivities when the reactor constraint is not applied (subsection 8.3.4). This follows from the correlations shown in Figure 8.20, where a lower value of $\sin^2(\theta_{13})$ results in tighter constraints on δ_{CP} .

The effect of applying the reactor constraint for δ_{CP} in the joint beam-atmospheric fit is presented in Figure 8.25. The posterior distribution from the two fits are marginalised over both hierarchies. Clearly, the reactor constraint improves the ability of the fit to select the known oscillation parameter as the shape of the distribution is much more peaked. This is also evidenced by the tightening of the 1σ and 90% credible intervals. Additionally, the disfavoured region of $1 < \delta_{CP} < 2$ is wider when the reactor constraint is applied.

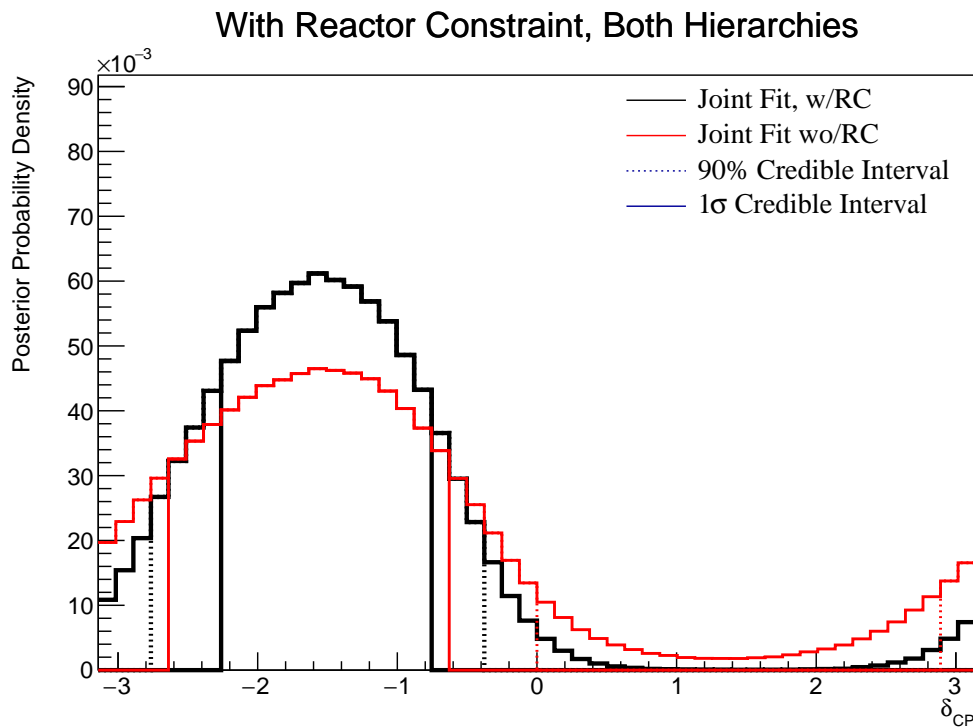


Figure 8.25: The one-dimensional posterior probability density distribution in δ_{CP} compared between the joint beam-atmospheric fit (Red) and the joint beam and atmospheric fit with the reactor constraint (Black). The distributions are marginalised over both hierarchies.

The sensitivity to $\sin^2(\theta_{23})$, marginalised over both hierarchies, is given in Figure 8.26. The highest posterior probability density is located at $\sin^2(\theta_{23}) = 0.527$

Parameter	Interval	HPD
δ_{CP} , (BH)	[-2.26, -0.75]	-1.57
δ_{CP} , (NH)	[-2.26, -0.75]	-1.57
δ_{CP} , (IH)	[-2.13, -1.00]	-1.57
Δm_{32}^2 (BH) [$\times 10^{-3}\text{eV}^2$]	[2.46, 2.52]	2.49
Δm_{32}^2 (NH) [$\times 10^{-3}\text{eV}^2$]	[2.48, 2.56]	2.51
Δm_{32}^2 (IH) [$\times 10^{-3}\text{eV}^2$]	[-2.60, -2.52]	-2.55
$\sin^2(\theta_{23})$ (BH)	[0.49, 0.55]	0.527
$\sin^2(\theta_{23})$ (NH)	[0.49, 0.55]	0.527
$\sin^2(\theta_{23})$ (IH)	[0.50, 0.56]	0.539

Table 8.7: The position of the highest posterior probability density (HPD) and width of the 1σ credible interval for the joint beam and atmospheric fit where the reactor constraint is applied. The values are presented by which hierarchy hypothesis is assumed: marginalised over both hierarchies (BH), normal hierarchy only (NH), and inverted hierarchy only (IH).

which agrees with the known value of $\sin^2(\theta_{23}) = 0.528$. The distribution clearly favours the UO with almost the entirety of the 1σ credible interval contained in the region. Figure 8.27 highlights the sensitivity of the joint fit both with and without the reactor constraint. The fit where the reactor constraint is applied selects the known value much better ($\sin^2(\theta_{23}) = 0.528$). Furthermore, the reactor constraint increases the UO preference which is evidenced by the distribution moving further away from the octant boundary. This indicates that there are marginalisation effects between the two mixing parameters. This follows from the correlation illustrated between $\sin^2(\theta_{23}) - \sin^2(\theta_{13})$ in Figure 8.22. The posterior distribution of the fit with reactor constraint is more peaked compared to the flatter distribution when the reactor constraint is not applied.

The fraction of steps contained within the two hierarchy and two octant models is given in Table 8.8. The reactor constraint significantly reduces the fraction of steps that are contained within the IH-LO region from 0.08 to 0.02, whilst significantly increasing the fraction of steps within the NH-UO region from 0.53 to 0.64. The application of the reactor constraint increases the Bayes factor

With Reactor Constraint, Both Hierarchies

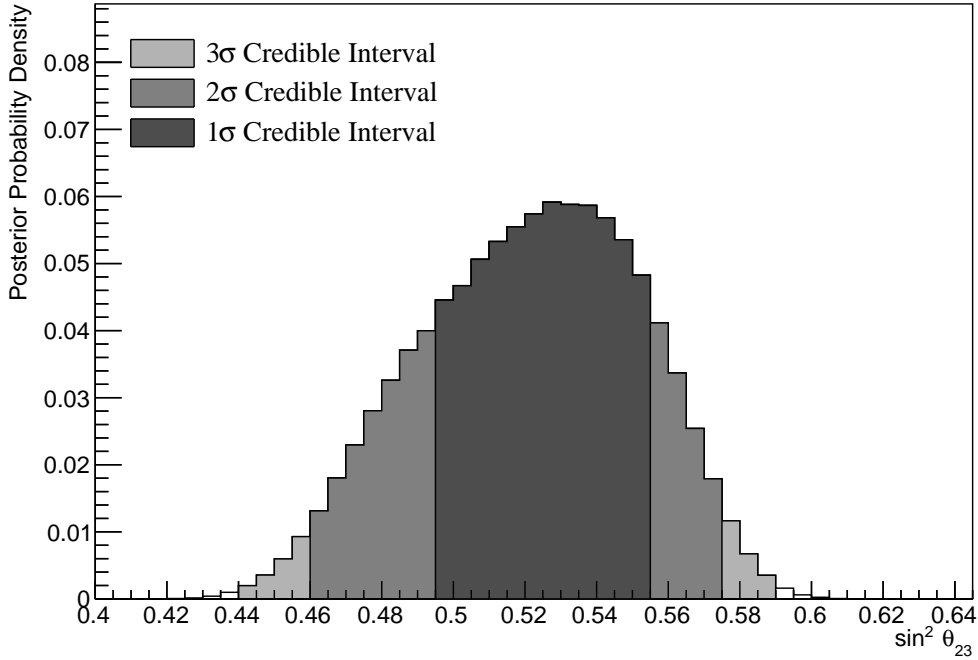


Figure 8.26: The one-dimensional posterior probability density distribution in $\sin^2(\theta_{23})$, marginalised over both hierarchies, from the joint beam and atmospheric fit where the reactor constraint is applied.

from $B(\text{NH}/\text{IH}) = 3.67$ to $B(\text{NH}/\text{IH}) = 7.29$. There is a very clear preference for the NH, with the Jeffreys scale stating a substantial preference for both fits (see subsection 4.3.3). The Bayes factor for UO preference is calculated as $B(\text{UO}/\text{LO}) = 2.86$. Whilst still a weak preference, this is certainly a stronger statement than the sensitivity when the reactor constraint is not applied.

	LO ($\sin^2 \theta_{23} < 0.5$)	UO ($\sin^2 \theta_{23} > 0.5$)	Sum
NH ($\Delta m_{32}^2 > 0$)	0.24	0.64	0.88
IH ($\Delta m_{32}^2 < 0$)	0.02	0.10	0.12
Sum	0.26	0.74	1.00

Table 8.8: The distribution of steps in a joint beam and atmospheric with the reactor constraint fit applied, presented as the fraction of steps in the upper (UO) and lower (LO) octants and the normal (NH) and inverted (IH) hierarchies. The Bayes factors are calculated as $B(\text{NH}/\text{IH}) = 7.29$ and $B(\text{UO}/\text{LO}) = 2.86$.

The sensitivity to Δm_{32}^2 , with the reactor constraint applied, is presented in

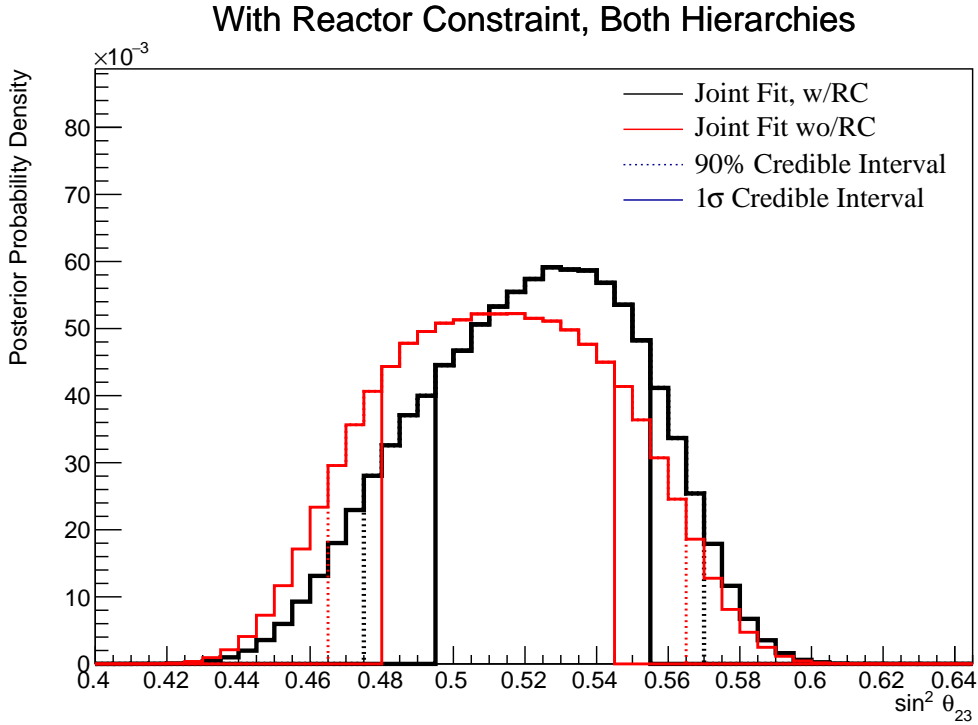


Figure 8.27: The one-dimensional posterior probability density distribution in $\sin^2(\theta_{23})$ compared between the joint beam-atmospheric fit (Red) and the joint beam and atmospheric fit with the reactor constraint (Black). The distributions are marginalised over both hierarchies.

3233 Figure 8.28. The posterior distribution is marginalised over both hierarchies. As
 3234 expected, the 1σ credible interval is entirely contained within the NH region. The
 3235 position of the highest posterior probability density is given as $2.49 \times 10^{-3} \text{ eV}^2$,
 3236 illustrating no significant bias between the fit results and the known oscillation
 3237 parameters. The application of the reactor constraint does move significantly the
 3238 position of the credible intervals but does reduce their width.

3239 The sensitivity to the appearance parameters ($\sin^2(\theta_{13}) - \delta_{CP}$) is given in
 3240 Figure 8.29. The distribution is mostly uncorrelated between the two parameters
 3241 and is centered at the known oscillation parameters. The 1σ credible interval
 3242 excludes $\delta_{CP} = 0$ and $\delta_{CP} = (-)\pi$. Furthermore, the 3σ credible intervals
 3243 exclude the region of $\delta_{CP} = \pi/2$.

3244 The sensitivity to the disappearance parameters ($\sin^2(\theta_{23}) - \Delta m_{32}^2$) is illus-
 3245 trated in Figure 8.30. As expected from the one-dimensional distribution, the 1σ
 3246 credible interval is entirely contained within the NH region. Both the NH and

With Reactor Constraint, Both Hierarchies

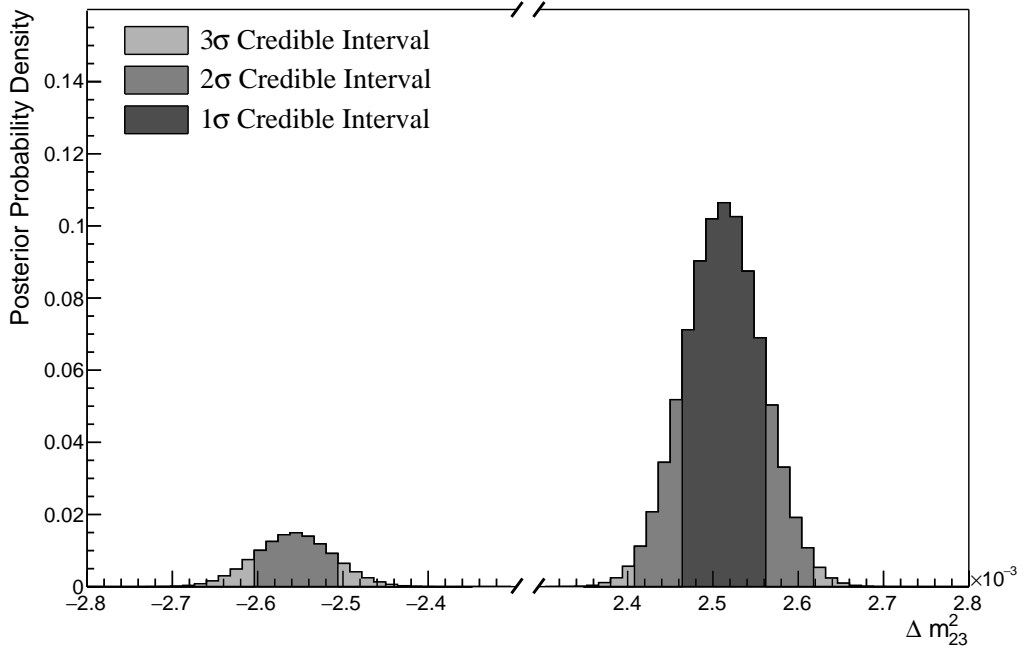


Figure 8.28: The one-dimensional posterior probability density distribution in Δm_{32}^2 , marginalised over both hierarchies, from the joint beam and atmospheric fit where the reactor constraint is applied.

3247 IH regions favour the UO, with a visually similar preference in both hierarchies.
 3248 The width of the Δm_{32}^2 1 σ credible interval does not significantly depend upon
 3249 the value or octant of $\sin^2(\theta_{23})$. This shows that there are no strong correlations
 3250 between these two parameters.

3251 Figure 8.31 illustrates the posterior distribution for each permutation of
 3252 two oscillation parameters of interest. The application of the reactor constraint
 3253 significantly reduces the correlations previously seen in Figure 8.22. There is
 3254 still a small correlation between δ_{CP} and Δm_{32}^2 . The application of the reactor
 3255 constraint has not significantly affected this correlation. The width of the 1 σ
 3256 credible interval in Δm_{32}^2 is wider for a value of $\delta_{CP} = 0$ as compared to a value
 3257 of $\delta_{CP} = \pi$. Similarly, the width of the 1 σ credible interval in δ_{CP} is smaller
 3258 for lower values of $\sin^2(\theta_{23})$.

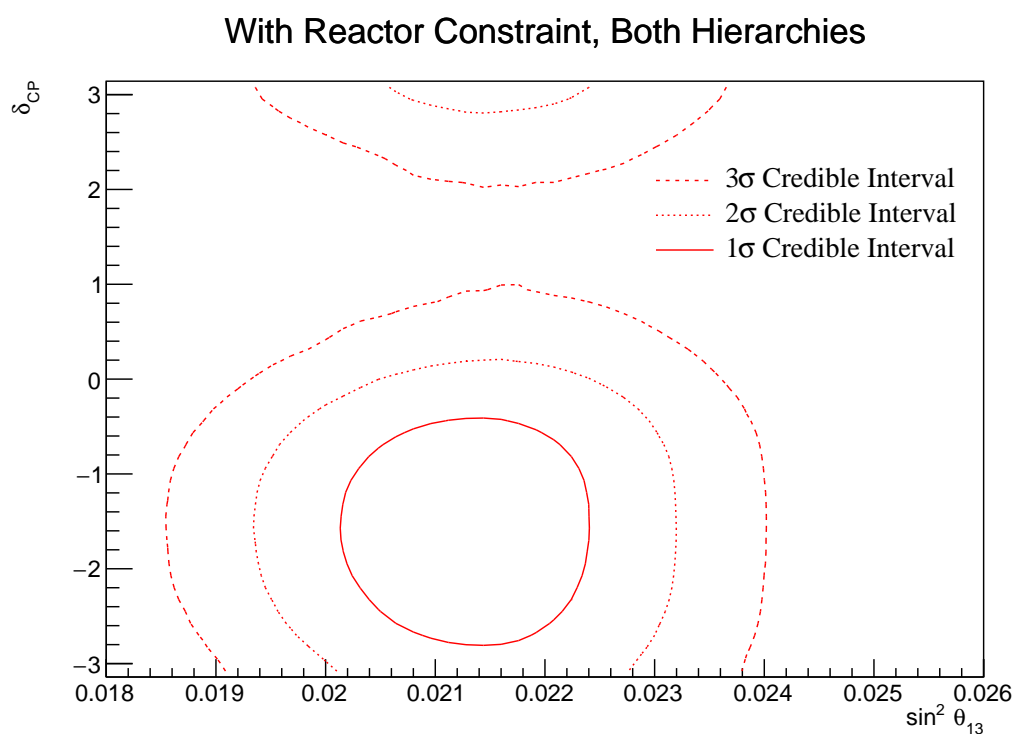


Figure 8.29: The two-dimensional posterior probability density distribution in $\delta_{CP} - \sin^2(\theta_{13})$, marginalised over both hierarchies, from the joint beam and atmospheric fit where the reactor constraint is applied.

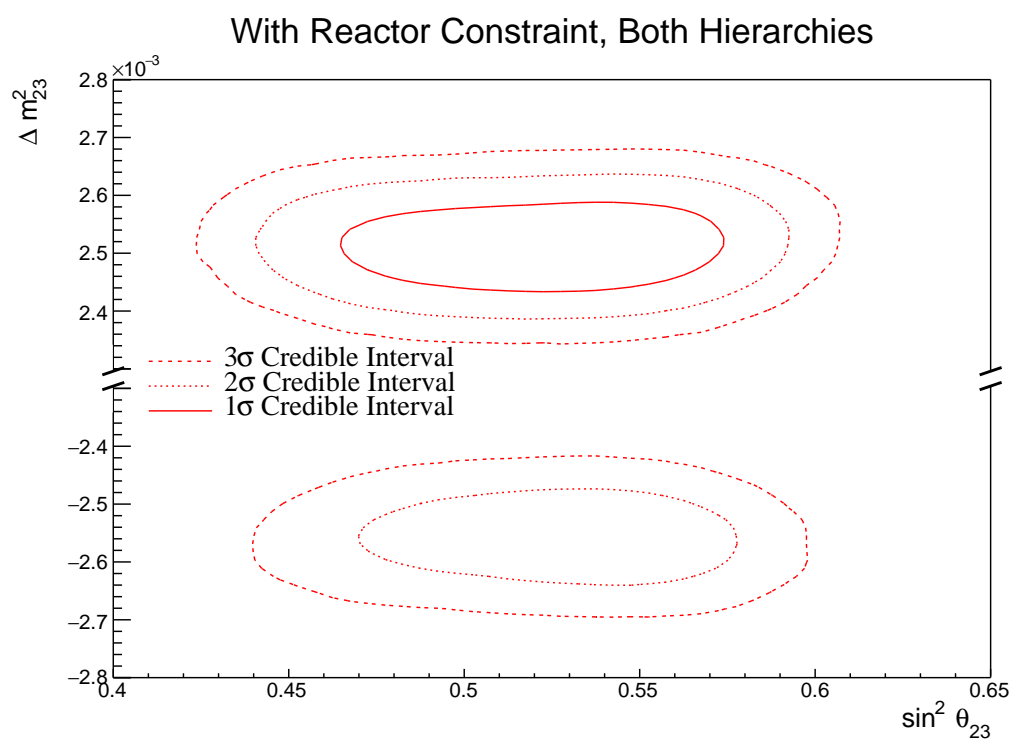


Figure 8.30: The two-dimensional posterior probability density distribution in $\Delta m_{32}^2 - \sin^2(\theta_{23})$, marginalised over both hierarchies, from the joint beam and atmospheric fit where the reactor constraint is applied.

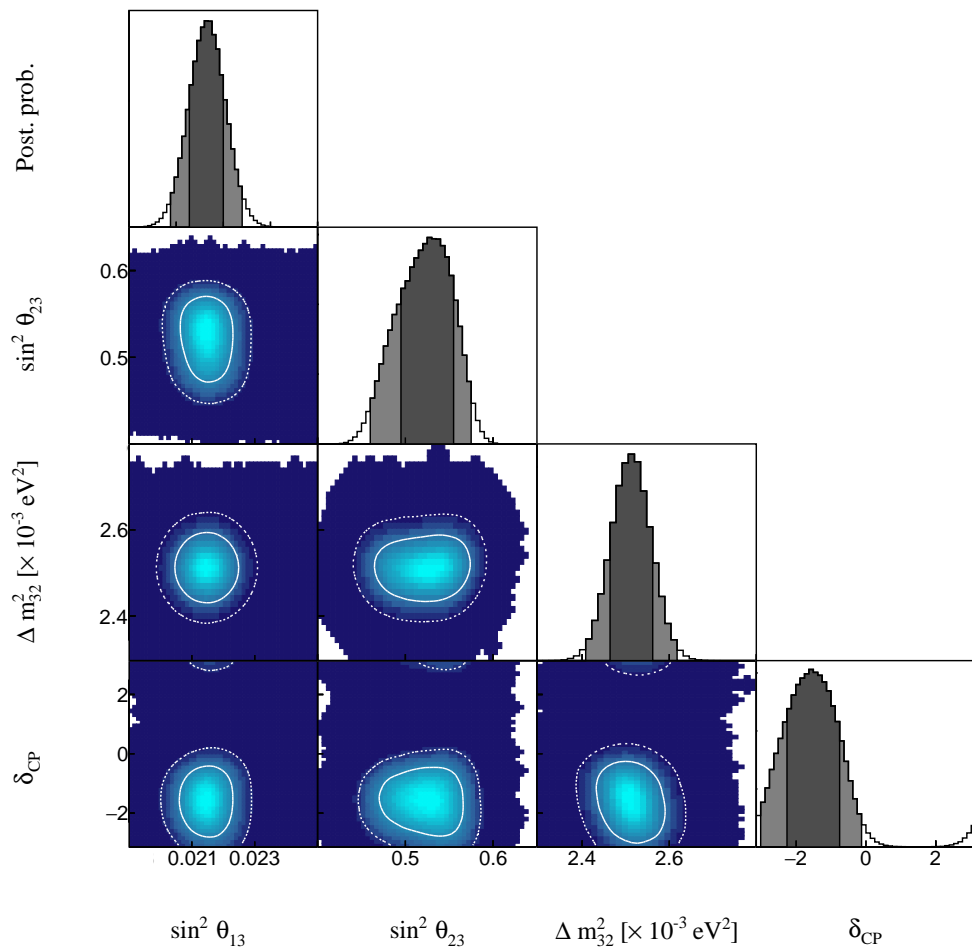


Figure 8.31: The posterior probability density distribution from the joint beam and atmospheric fit where the reactor constraint is applied. The distribution is given for each two-dimensional permutation of the oscillation parameters of interest. The one-dimensional distribution of each parameter is also given.

3259 8.3.6 Comparison to Latest T2K Sensitivities without Reactor 3260 Constraint

3261 The benefits of the joint beam and atmospheric analysis can be determined by
 3262 comparing the sensitivities to the beam-only analysis. This section presents those
 3263 comparisons for sensitivities built using the Asimov A oscillation parameters
 3264 defined in Table 2.2 and the post-BANFF systematic tune. The reactor constraint
 3265 is not applied within either of the fits used in these comparisons.

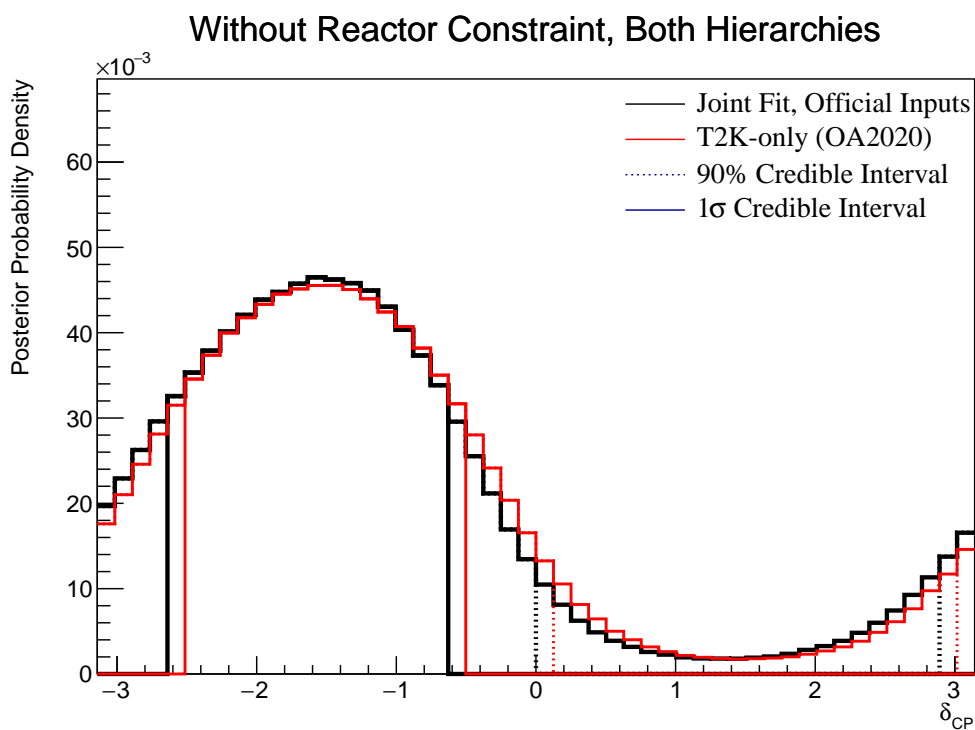


Figure 8.32: The one-dimensional posterior probability density distribution in δ_{CP} compared between the joint beam-atmospheric fit (Black) and the latest T2K sensitivities (Red) [183]. The reactor constraint is not applied in either fit. The distributions are marginalised over both hierarchies.

3266 The sensitivity, marginalised over both hierarchies, to δ_{CP} from the joint
 3267 beam-atmospheric and beam-only fits is presented in Figure 8.32. As expected
 3268 from the likelihood scans (Figure 8.4), the sensitivity to δ_{CP} is not significantly
 3269 increased. This is because the known oscillation parameter value ($\delta_{CP} = -1.601$)
 3270 lies at the position where the beam samples dominate the sensitivity compared
 3271 to the SK samples.

The sensitivity to Δm_{32}^2 of the joint beam-atmospheric fit is illustrated in Figure 8.33, where the posterior distribution has been marginalised over both hierarchies. The 1σ credible interval of the joint beam and atmospheric fit is entirely contained within the NH region. This shows the significant increase in the ability of the fit to determine the correct mass hierarchy, as compared to the beam-only analysis. This is further evidenced by the fact that the 90% credible intervals from the joint fit are also tighter in the IH region as compared to the beam-only analysis. The Bayes factor for mass hierarchy determination for the beam-only and joint beam and atmospheric are $B(\text{NH}/\text{IH}) = 1.91$ and $B(\text{NH}/\text{IH}) = 3.67$, respectively. According to Jeffrey's scale (Table 4.1), the beam-only analysis represents a weak preference for the NH hypothesis whereas the joint fit returns a substantial preference for the NH hypothesis. To summarise, the joint beam-atmospheric fit has a substantial preference for the correct hierarchy without the requirement of external constraints.

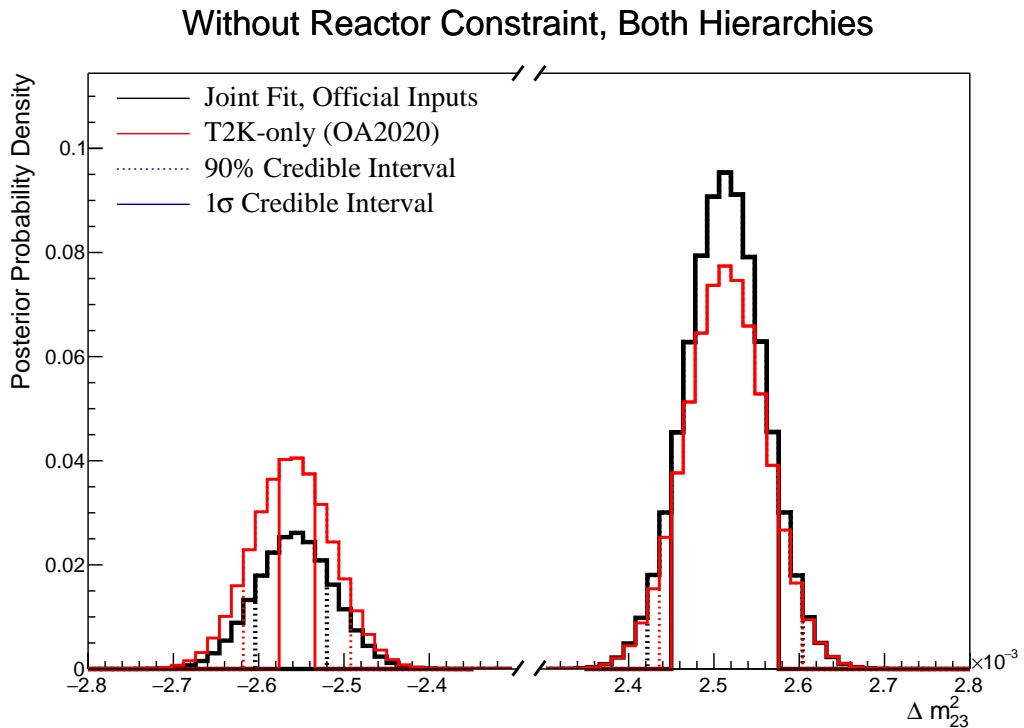


Figure 8.33: The one-dimensional posterior probability density distribution in Δm_{32}^2 compared between the joint beam-atmospheric fit (Black) and the latest T2K sensitivities (Red) [183]. The reactor constraint is not applied in either fit. The distributions are marginalised over both hierarchies.

The sensitivity to $\sin^2(\theta_{23})$, marginalised over both hierarchies, for both the beam-only and joint beam and atmospheric analysis are presented in Figure 8.34. The peak of the posterior distribution from the joint analysis is more aligned with the known value of $\sin^2(\theta_{23}) = 0.528$ as compared to the beam-only analysis. This indicates that the marginalisation effects from other oscillation parameters ($\sin^2(\theta_{13}) - \sin^2(\theta_{23})$) presented in Figure 8.22) are less prevalent in the projection of this parameter. The Bayes factors for the beam-only and joint beam-atmospheric fit are $B(\text{UO}/\text{LO}) = 1.56$ and $B(\text{UO}/\text{LO}) = 1.74$, respectively. Therefore, the joint beam-atmospheric fit does prefer the UO more strongly than the beam-only analysis, albeit slightly.

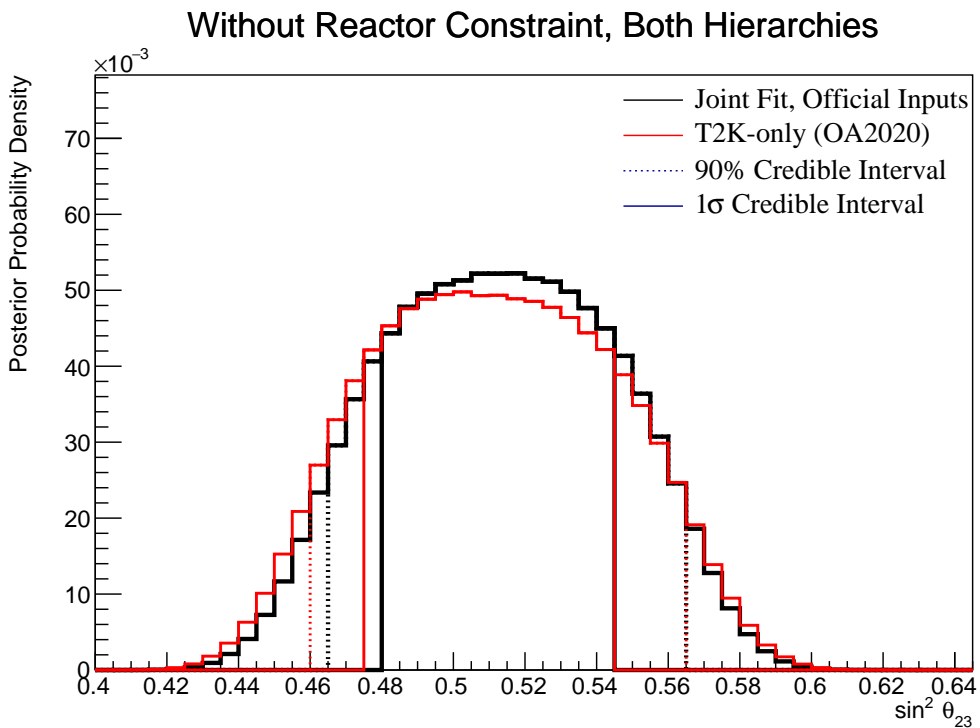


Figure 8.34: The one-dimensional posterior probability density distribution in $\sin^2(\theta_{23})$ compared between the joint beam-atmospheric fit (Black) and the latest T2K sensitivities (Red) [183]. The reactor constraint is not applied in either fit. The distributions are marginalised over both hierarchies.

Whilst the beam-only and joint beam-atmospheric fits have similar sensitivity to δ_{CP} and $\sin^2(\theta_{23})$ when projected in one-dimension, the benefit of the joint analysis becomes more obvious when the sensitivities are presented in two-

dimensions. The sensitivity of the two fits to the appearance parameters ($\delta_{CP} - \sin^2(\theta_{13})$) are illustrated in Figure 8.35.

The width of the 99% joint fit credible interval in $\sin^2(\theta_{13})$ is squeezed in the region of $\delta_{CP} \sim 0$ compared to the beam-only analysis. This is the same behaviour that is seen in the appearance likelihood scans presented in Figure 8.2. The 1σ and 90% also exhibit slightly tighter constraints on δ_{CP} . This is most prevalent in the region of $\delta_{CP} \sim 0$ and $\sin^2(\theta_{13}) \sim 0.03$. Whilst the atmospheric samples do not have significant sensitivity to $\sin^2(\theta_{13})$ (as shown in Figure 8.1), they aid in breaking the degeneracy between the oscillation parameters allowing for tighter constraints.

The sensitivity to the disappearance parameters $\sin^2(\theta_{23}) - \Delta m_{32}^2$, marginalised over both hierarchies, is presented in Figure 8.36 for both the beam-only and joint beam-atmospheric fits. Whilst the one-dimensional sensitivity comparisons considered so far show the improvements of the joint fit, the two-dimensional projection really shows the benefit of adding the atmospheric samples to the beam samples. The area contained within the IH credible intervals is drastically reduced in the joint fit. This follows from the better determination of the mass hierarchy seen in the Bayes factor comparisons. The 1σ joint fit credible interval in the IH region more strongly favours the UO as compared to the beam-only fit. Even in the NH region, the width of the credible intervals in $\sin^2(\theta_{23})$ decrease, albeit to a smaller extent.

The change in sensitivity to $\delta_{CP} - \Delta m_{32}^2$ is illustrated in Figure 8.37. As expected, the contours presented within the IH region are much smaller in the joint fit due to the increased sensitivity to mass hierarchy determination. This culminates in a region around $\delta_{CP} \sim \pi/2$ which is excluded at 3σ . This behaviour is not present within the beam-only analysis. Consistent with the previous observations, the area contained within the IH credible intervals is significantly reduced in comparison to the beam-only analysis.

The sensitivity to Δm_{32}^2 and $\sin^2(\theta_{23})$, as a function of $\sin^2(\theta_{13})$, is presented in Figure 8.38 and Figure 8.39, respectively. These sensitivities are marginalised

Without Reactor Constraint, Both Hierarchies

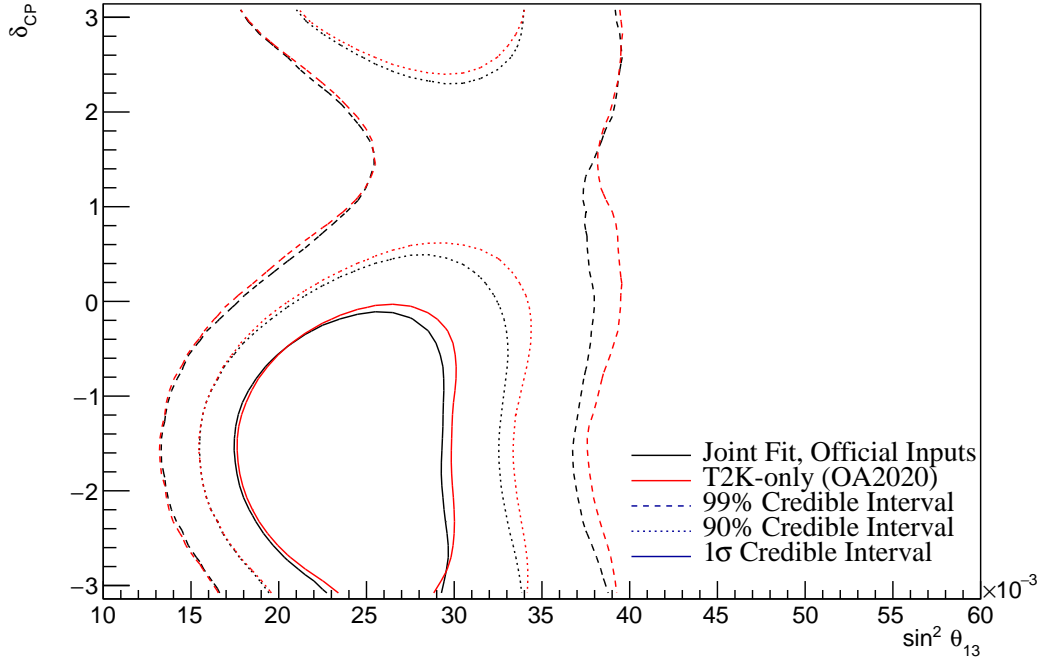


Figure 8.35: The two-dimensional posterior probability density distribution in δ_{CP} – $\sin^2(\theta_{13})$ compared between the joint beam-atmospheric fit (Black) and the latest T2K sensitivities (Red) [183]. The reactor constraint is not applied in either fit. The distributions are marginalised over both hierarchies.

over both hierarchies. As expected from the previous observations, the Δm_{32}^2 contours within IH region of the joint fit are much smaller than the beam-only analysis. Notably, the joint fit IH 1σ credible intervals exclude the region around the reactor constraint. This is not a bias from the fit as the known value for Δm_{32}^2 is in the NH region. This does suggest that the application of the reactor constraint would further increase the preference for NH in the joint fit as compared to its effect on the beam-only analysis.

The beam-only and joint beam-atmospheric fits have a slightly different contour shape between the $\sin^2(\theta_{13})$ and $\sin^2(\theta_{23})$ parameters, as illustrated by Figure 8.39. The joint analysis disfavours the wrong octant hypothesis more strongly in the region of high $\sin^2(\theta_{13})$. This suggests that the application of the reactor constraint will favour the UO more strongly in the joint analysis compared to the beam-only analysis.

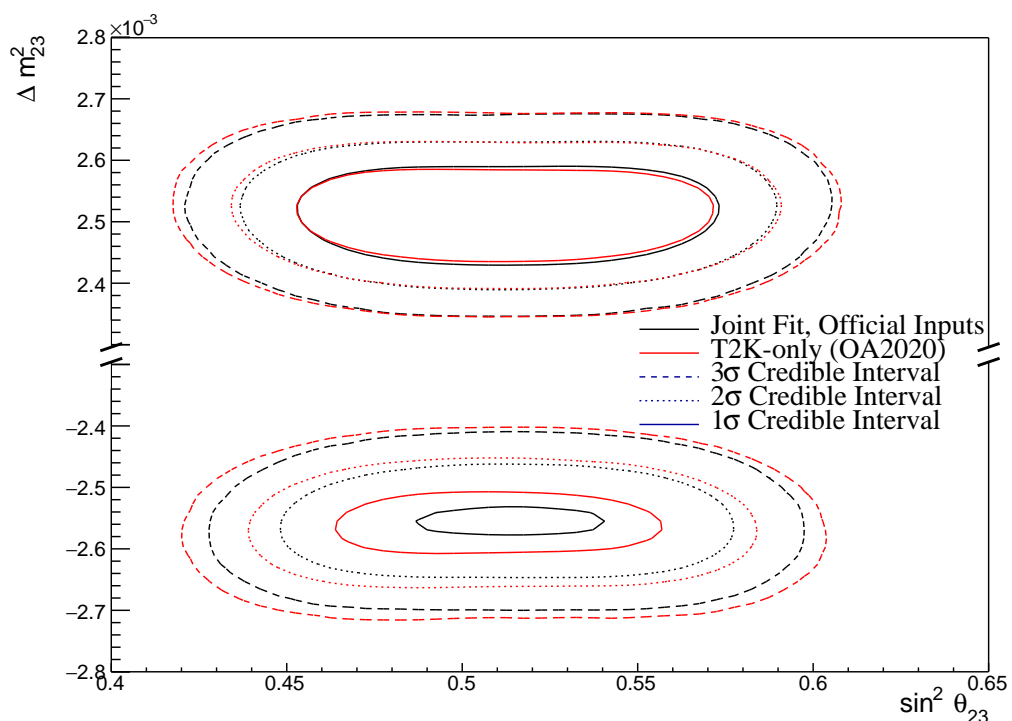


Figure 8.36: The two-dimensional posterior probability density distribution in $\Delta m_{32}^2 - \sin^2(\theta_{23})$ compared between the joint beam-atmospheric fit (Black) and the latest T2K sensitivities (Red) [183]. The reactor constraint is not applied in either fit. The distributions are marginalised over both hierarchies.

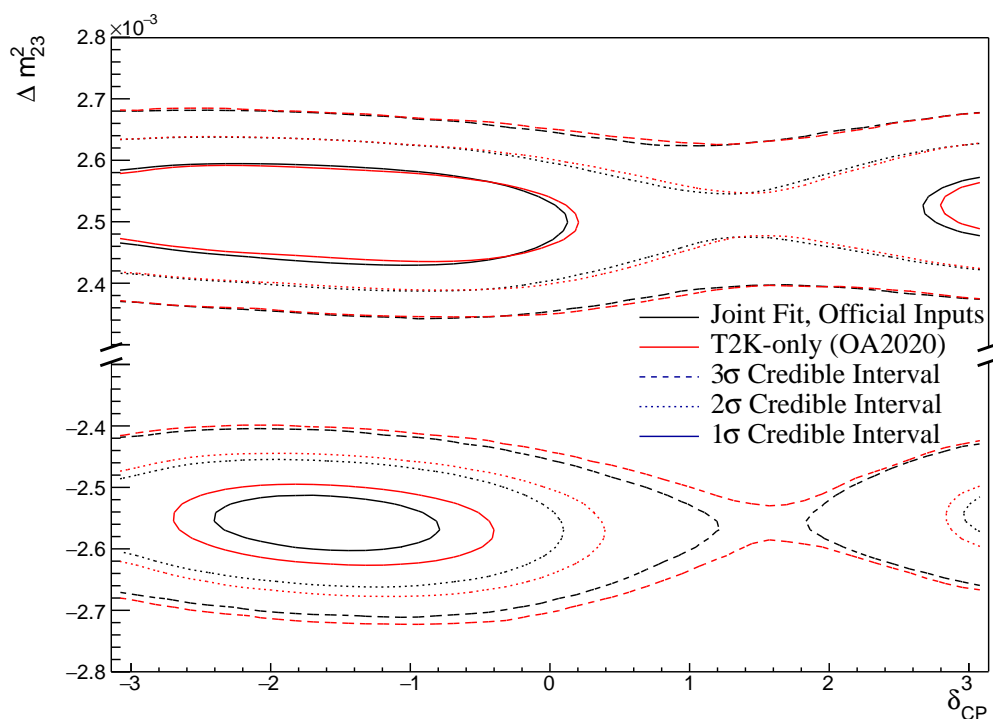


Figure 8.37: The two-dimensional posterior probability density distribution in Δm_{32}^2 – Δ_{CP} compared between the joint beam-atmospheric fit (Black) and the latest T2K sensitivities (Red) [183]. The reactor constraint is not applied in either fit. The distributions are marginalised over both hierarchies.

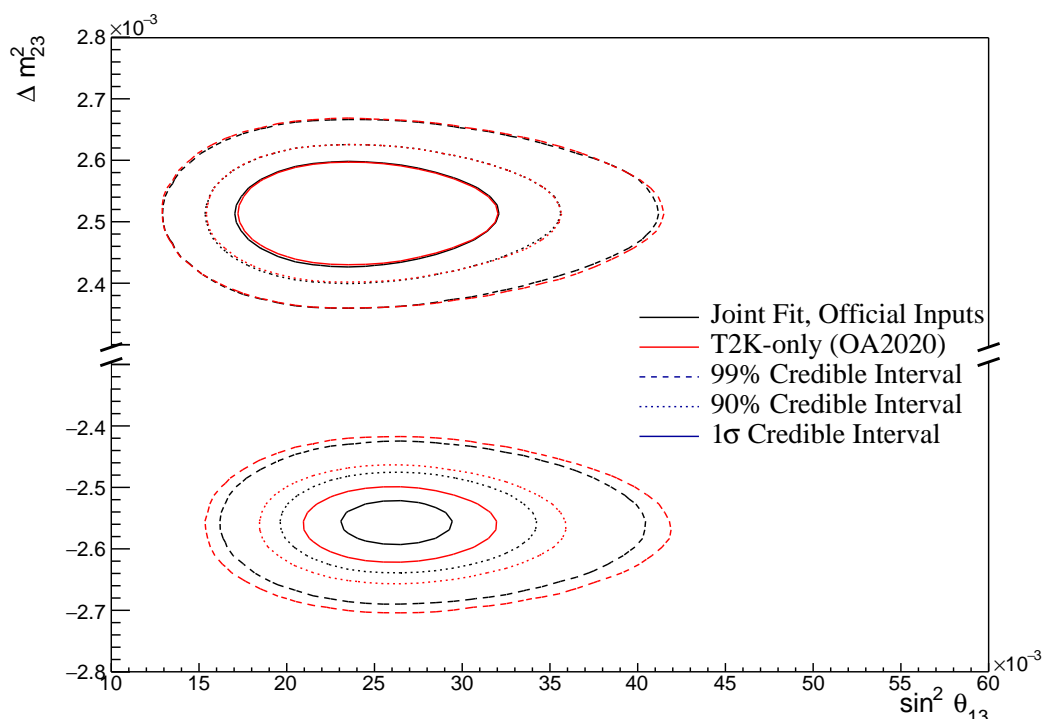


Figure 8.38: The two-dimensional posterior probability density distribution in Δm_{32}^2 – $\sin^2(\theta_{23})$ compared between the joint beam-atmospheric fit (Black) and the latest T2K sensitivities (Red) [183]. The reactor constraint is not applied in either fit. The distributions are marginalised over both hierarchies.

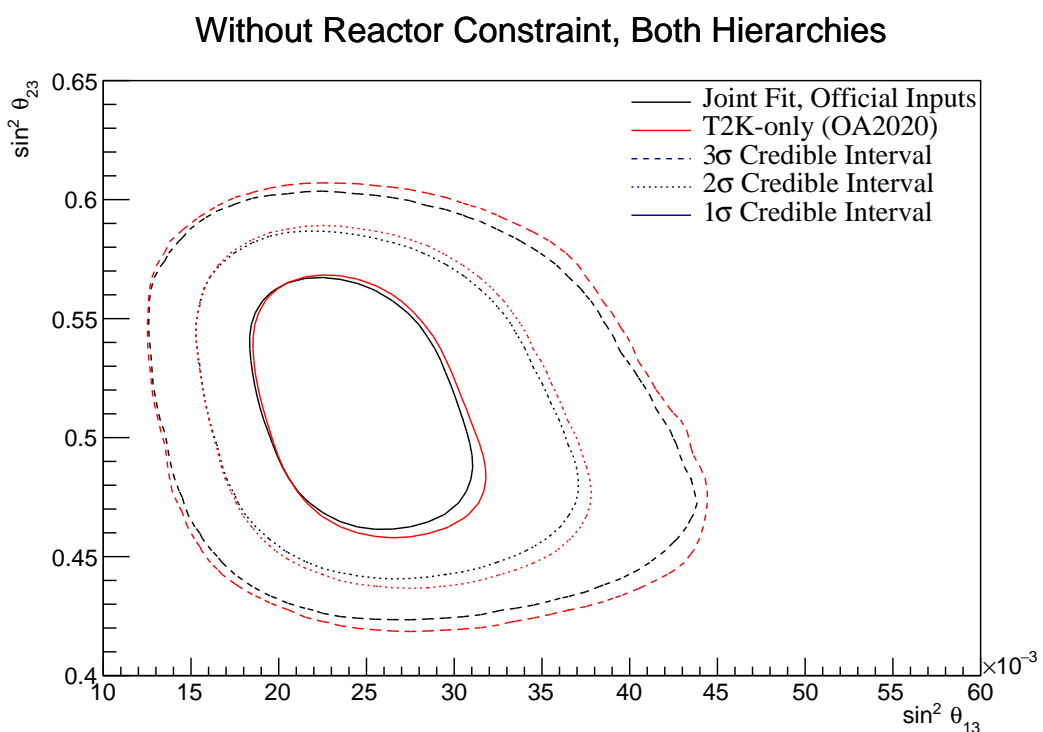


Figure 8.39: The two-dimensional posterior probability density distribution in $\sin^2(\theta_{23})$ – $\sin^2(\theta_{13})$ compared between the joint beam-atmospheric fit (Black) and the latest T2K sensitivities (Red) [183]. The reactor constraint is not applied in either fit. The distributions are marginalised over both hierarchies.

3342 8.3.7 Comparison to Latest T2K Sensitivities with Reactor Con- 3343 straint

3344 The comparison between the beam-only and joint beam-atmospheric fits are
 3345 compared in subsection 8.3.6. Those comparisons were made with the reactor
 3346 constraint not applied to either of the fits. This section illustrates the com-
 3347 parison when the reactor constraint is applied. As shown in Figure 8.38, the
 3348 application of the reactor constraint is expected to significantly increase the
 3349 joint fit's preference for the NH hypothesis, as compared to the beam-only
 3350 analysis. Figure 8.40 illustrates the sensitivities of the two fits to the disappearance
 3351 parameters ($\sin^2(\theta_{23}) - \Delta m_{32}^2$) marginalised over both hierarchies and with the
 3352 reactor constraint applied. This plot clearly illustrates the benefit of the joint
 3353 beam and atmospheric analysis. The 1σ credible interval in the IH region is
 3354 entirely removed in the joint analysis, illustrating the improved NH preference.

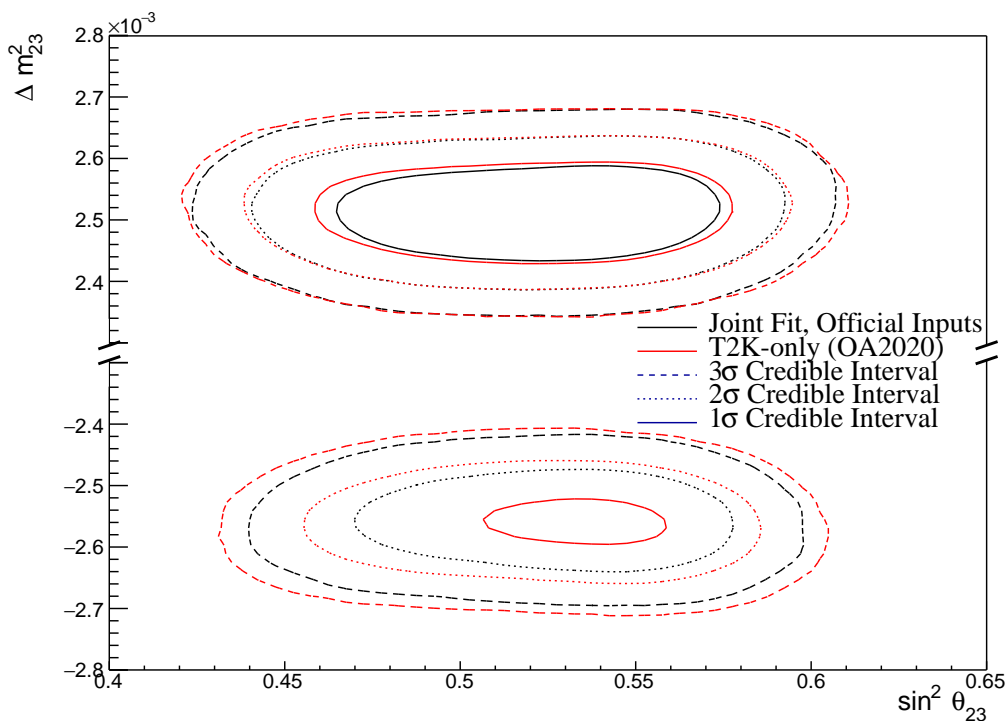


Figure 8.40: The two-dimensional posterior probability density distribution in $\Delta m_{32}^2 - \sin^2(\theta_{23})$ compared between the joint beam-atmospheric fit (Black) and the latest T2K sensitivities (Red) [183]. The reactor constraint is applied in both fits. The distributions are marginalised over both hierarchies.

3355 The credible intervals of the joint fit are also tighter in the $\sin^2(\theta_{23})$ dimension
3356 than the beam-only analysis in both mass hierarchy regions. This shows that
3357 beyond the ability of the joint fit to prefer the NH more strongly than the beam-
3358 only analysis, the precision to which it can measure $\sin^2(\theta_{23})$ is also improved.
3359 The Bayes factor for NH preference is calculated as $B(\text{NH}/\text{IH}) = 7.29$ and
3360 $B(\text{NH}/\text{IH}) = 3.41$ for the joint beam-atmospheric and beam-only analysis,
3361 respectively. Whilst both present a significant preference for the NH hypothesis
3362 (Table 4.1), the joint fit's preference is much stronger. A similar conclusion can be
3363 made regarding the Bayes factors for UO preference which are $B(\text{UO}/\text{LO}) = 2.86$
3364 and $B(\text{UO}/\text{LO}) = 2.67$ for the joint beam-atmospheric and beam-only analysis,
3365 respectively. Both of these represent a mild preference for the UO but there is
3366 a stronger preference observed in the joint analysis.

3367 The sensitivity of the beam-only and joint beam-atmospheric analyses, to the
3368 appearance parameters ($\delta_{CP} - \sin^2(\theta_{13})$), are compared in Figure 8.41. These
3369 results are marginalised over both hierarchies and include the reactor constraint
3370 on $\sin^2(\theta_{13})$. For this particular set of known oscillation parameters (AsimovA
3371 defined in Table 2.2), the beam-only analysis dominates the sensitivity. The
3372 joint fit does slightly increase the sensitivity to δ_{CP} but it does not change any
3373 conclusions that would be made.

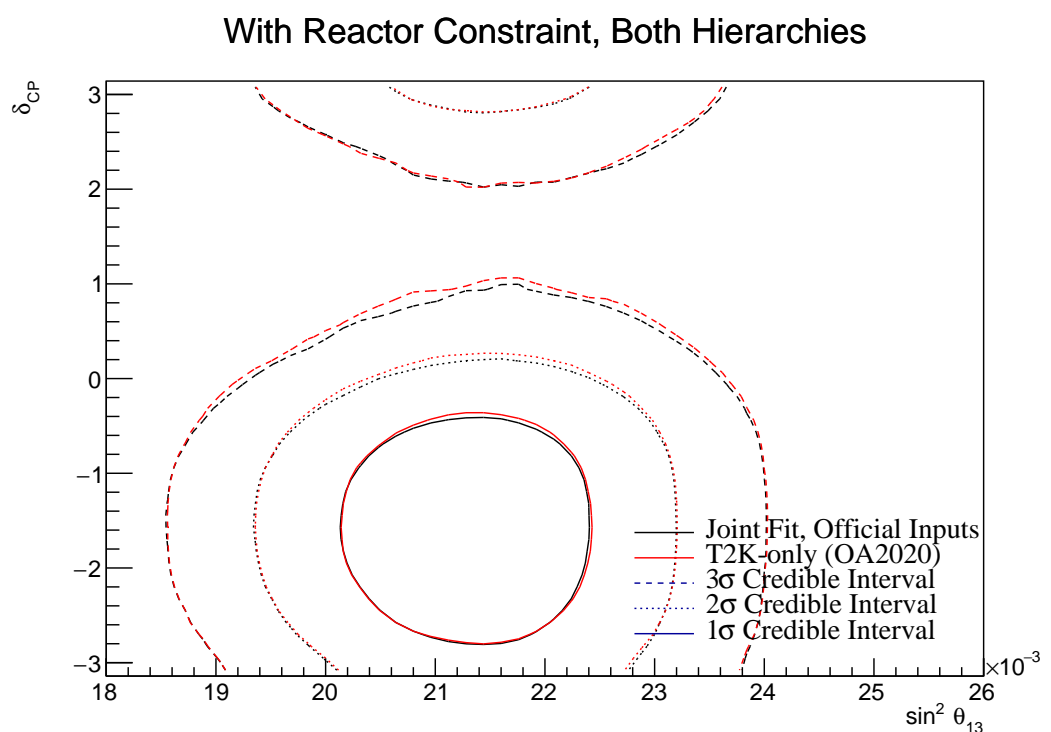


Figure 8.41: The two-dimensional posterior probability density distribution in δ_{CP} – $\sin^2(\theta_{13})$ compared between the joint beam-atmospheric fit (Black) and the latest T2K sensitivities (Red) [183]. The reactor constraint is applied in both fits. The distributions are marginalised over both hierarchies.

3374 8.3.8 Effect of Asimov Parameter Set

3375 Figure 8.4 and Figure 8.5 show that the choice of the parameter set at which the
 3376 Asimov data is made can affect the conclusion. ‘AsimovA’ oscillation parameters
 3377 are defined at a region of δ_{CP} which is dominated by the T2K experiment. This
 3378 explains why the addition of the atmospheric samples does not significantly in-
 3379 crease the sensitivity to δ_{CP} , as illustrated in subsection 8.3.6 and subsection 8.3.7.
 3380 This section presents the sensitivities when ‘AsimovB’ oscillation parameters,
 3381 as defined in Table 2.2, are assumed (alongside the post-BANFF tune) when
 3382 building the Asimov data.

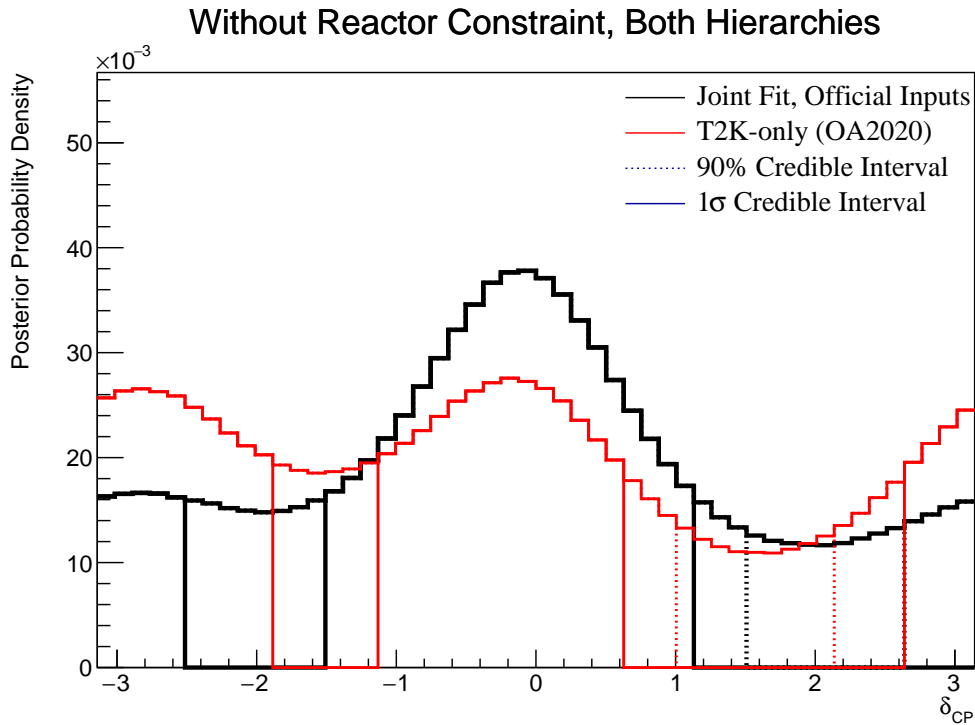


Figure 8.42: The one-dimensional posterior probability density distribution in δ_{CP} compared between the joint beam-atmospheric fit (Black) and the latest T2K sensitivities (Red) [183]. The reactor constraint is not applied in either fit. The distributions are marginalised over both hierarchies.

3383 The sensitivity to δ_{CP} for the joint beam and atmospheric fit is presented
 3384 in Figure 8.42. The results are compared to those from the beam-only analysis
 3385 in [183]. The reactor constraint is not applied in either of the fits. The known
 3386 oscillation parameter value is $\delta_{CP} = 0$. The shape of the posterior distribution

from the joint analysis is more peaked at $\delta_{CP} = 0$ as compared to the beam-only analysis which has approximately the same posterior probability density at $\delta_{CP} = 0$ and $\delta_{CP} = \pi$. This shows the ability of the joint analysis to better determine the correct phase of δ_{CP} if the true value was CP-conserving. The 1σ credible intervals and the position of the highest posterior probability density are given in Table 8.9.

Parameter	Interval	HPD
δ_{CP} , (BH)	$[-\pi, -2.51], [-1.51, 1.31]$	-0.06
δ_{CP} , (NH)	$[-1.13, 1.63]$	0.06
δ_{CP} , (IH)	$[-3.02, -1.88], [-1.76, 0.13]$	-0.44
Δm_{32}^2 (BH) [$\times 10^{-3}$ eV 2]	$[-2.60, -2.49], [2.46, 2.59]$	2.51
Δm_{32}^2 (NH) [$\times 10^{-3}$ eV 2]	$[2.47, 2.56]$	2.52
Δm_{32}^2 (IH) [$\times 10^{-3}$ eV 2]	$[-2.61, -2.52]$	-2.57
$\sin^2(\theta_{23})$ (BH)	$[0.43, 0.48], [0.55, 0.59]$	0.45
$\sin^2(\theta_{23})$ (NH)	$[0.43, 0.49], [0.55, 0.58]$	0.45
$\sin^2(\theta_{23})$ (IH)	$[0.44, 0.48], [0.54, 0.59]$	0.57

Table 8.9: The position of the highest posterior probability density (HPD) and width of the 1σ credible interval for the SK atmospheric-only fit. The reactor constraint is not applied. The values are presented by which hierarchy hypothesis is assumed: marginalised over both hierarchies (BH), normal hierarchy only (NH) and inverted hierarchy only (IH).

Naively, if just the 1σ credible interval were considered without observing the shape of the distribution, it would appear that the joint analysis would have a worse sensitivity to δ_{CP} due to the larger interval around δ_{CP} . The 1σ credible interval for the beam-only analysis is given as the range $\delta_{CP} = [-\pi, -1.88], [-1.13, 0.63]$ and $[2.64, \pi]$ which contains 56% of all values of δ_{CP} . The joint beam and atmospheric analysis contains 52% of all δ_{CP} values within the 1σ credible interval. Therefore, if the area within the 1σ credible interval were to be compared between the two fits, the joint analysis would be shown to have better precision.

This contradiction stems from the methodology in which the credible interval is calculated. The technique used in this analysis (documented in subsection 4.3.2)

3403 fills the credible interval by selecting bins in order of magnitude until 68% of the
 3404 posterior density is contained. If instead, the credible interval was calculated
 3405 by expanding around the highest posterior probability, the benefits of the joint
 3406 fit would be more obvious. In the case where the shape of the posterior was
 3407 Gaussian, these two techniques would be equivalent.

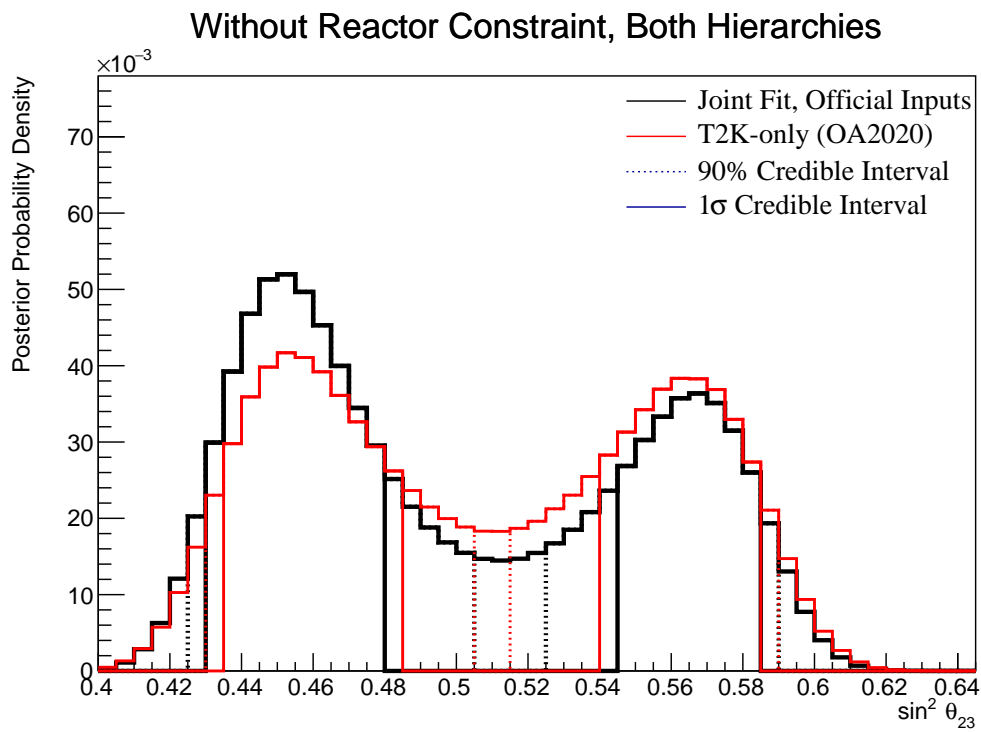


Figure 8.43: The one-dimensional posterior probability density distribution in $\sin^2(\theta_{23})$ compared between the joint beam-atmospheric fit (Black) and the latest T2K sensitivities (Red) [183]. The reactor constraint is not applied in either fit. The distributions are marginalised over both hierarchies.

3408 The sensitivity of the joint beam and atmospheric fit to $\sin^2(\theta_{23})$ is presented
 3409 in Figure 8.43. The sensitivity is compared to that of the beam-only analysis
 3410 in [183]. The reactor constraint is not applied in either of the fits being com-
 3411 pared. The Asimov parameter value is $\sin^2(\theta_{23}) = 0.45$ and the sensitivities are
 3412 marginalised over both hierarchies. Clearly, the joint beam and atmospheric
 3413 fit has a much larger probability density in the region surrounding the known
 3414 oscillation parameters. This shows the better octant determination of the joint
 3415 analysis compared to the beam-only fit. The ratio of the posterior density at

the peak of the lower octant to the peak of the upper octant from the joint fit is 1.43 compared to 1.09 from the beam-only analysis. This shows further support for the joint analysis in correctly selecting the lower octant, which is the correct hypothesis given the known oscillation parameters.

	LO ($\sin^2 \theta_{23} < 0.5$)	UO ($\sin^2 \theta_{23} > 0.5$)	Sum
NH ($\Delta m_{32}^2 > 0$)	0.35	0.24	0.59
IH ($\Delta m_{32}^2 < 0$)	0.19	0.22	0.41
Sum	0.54	0.46	1.00

Table 8.10: The distribution of steps in a joint beam and atmospheric fit, presented as the fraction of steps in the upper (UO) and lower (LO) octants and the normal (NH) and inverted (IH) hierarchies. The reactor constraint is not applied. The Bayes factors are calculated as $B(\text{NH}/\text{IH}) = 1.43$ and $B(\text{LO}/\text{UO}) = 1.19$.

The distribution of steps, split by hierarchy and octant hypothesis, is presented in Table 8.10. The Bayes factor for hierarchy and octant determination are $B(\text{NH}/\text{IH}) = 1.43$ and $B(\text{LO}/\text{UO}) = 1.19$, respectively. The octant Bayes factor is now presented as LO/UO as the known oscillation parameter is contained within the lower octant. These values compare to $B(\text{NH}/\text{IH}) = 1.08$ and $B(\text{LO}/\text{UO}) = 0.91$ from the beam-only analysis. This shows additional evidence of the joint analysis's preference for selecting the correct octant and hierarchy hypothesis. Comparisons to the AsimovA Bayes factors presented in Table 8.6 show how the preference for the correct octant and hierarchy depend on the true value of δ_{CP} and $\sin^2(\theta_{23})$.

The sensitivity of the beam-only and joint beam-atmospheric analysis to Δm_{32}^2 is given in Figure 8.44. Both of the results are marginalised over both hierarchies and the reactor constraint is not applied in either analysis. The joint analysis has a stronger preference for the correct hierarchy (NH) which is shown by the higher Bayes factor ($B(\text{NH}/\text{IH}) = 1.43$) compared to the beam-only analysis ($B(\text{NH}/\text{IH}) = 1.08$).

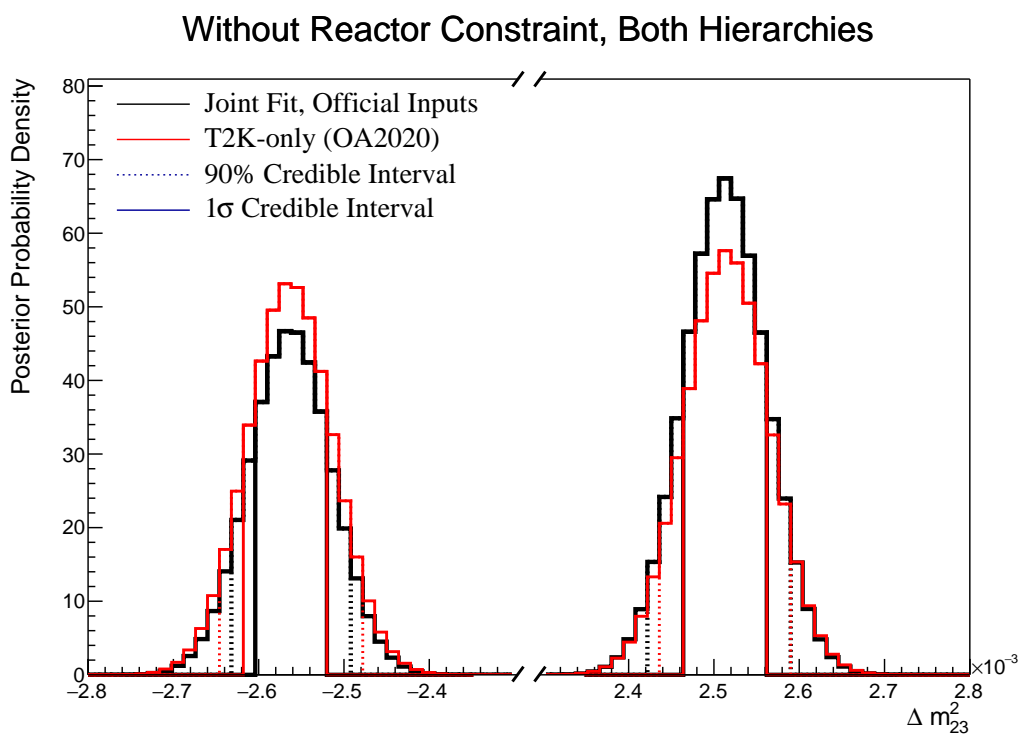


Figure 8.44: The one-dimensional posterior probability density distribution in Δm_{32}^2 compared between the joint beam-atmospheric fit (Black) and the latest T2K sensitivities (Red) [183]. The reactor constraint is not applied in either fit. The distributions are marginalised over both hierarchies.

9

3436

3437

Conclusions and Outlook

Appendices

A

3439

3440

Atmospheric Sample Spectra

3441 This appendix documents the interaction mode breakdown of all the atmospheric
3442 samples used within the analysis. The generated tune of the model parameters
3443 and the Asimov A oscillation parameter set (defined in Table 2.2) are assumed.
3444 The livetime of SK-IV is taken to be 3244.4 days.

3445 A.1 Binning

3446 The lepton momentum and cosine zenith binning edges for the atmospheric
3447 samples used within this analysis are defined in Table A.1.

3448 A.2 Fully Contained Sub-GeV Samples

3449 The interaction mode breakdown of the fully contained Sub-GeV samples are
3450 shown in Figure A.1 and Figure A.2, for the samples with enriched CC0 π and
3451 CC1 π^\pm respectively.

3452 The CC0 π sample are dominated by CCQE events ($\sim 70\%$) with smaller
3453 contributions of 2p2h ($\sim 12\%$) and CC1 π ($\sim 10\%$) components. The energy peaks
3454 around 300 MeV, which is slightly below that of the T2K samples but still has
3455 significant contribution upto 1 GeV which overlaps the T2K sample energy range.

Sample	$\cos(\theta_Z)$ Bins	Momentum Bin Edges ($\log_{10}(P)$ MeV)
SubGeV-elike-0dcy	10	2.0, 2.4, 2.6, 2.8, 3.0, 3.2
SubGeV-elike-1dcy	1	2.0, 2.4, 2.6, 2.8, 3.0, 3.2
SubGeV-mulike-0dcy	10	2.0, 2.4, 2.6, 2.8, 3.0, 3.2
SubGeV-mulike-1dcy	10	2.0, 2.4, 2.6, 2.8, 3.0, 3.2
SubGeV-mulike-2dcy	1	2.0, 2.4, 2.6, 2.8, 3.0, 3.2
SubGeV-pi0like	1	2.0, 2.2, 2.4, 2.6, 2.8, 3.2
MultiGeV-elike-nue	10	3.0, 3.4, 3.7, 4.0, 5.0
MultiGeV-elike-nuebar	10	3.0, 3.4, 3.7, 4.0, 5.0
MultiGeV-mulike	10	3.0, 3.4, 5.0
MultiRing-elike-nue	10	3.0, 3.4, 3.7, 5.0
MultiRing-elike-nuebar	10	3.0, 3.4, 3.7, 5.0
MultiRing-mulike	10	2.0, 3.124, 3.4, 3.7, 5.0
MultiRing-Other1	10	3.0, 3.4, 3.7, 4.0, 5.0
PC-Stop	10	2.0, 3.4, 5.0
PC-Through	10	2.0, 3.124, 3.4, 3.7, 5.0
Upmu-Stop	10	3.2, 3.4, 3.7, 8.0
Upmu-Through-Showering	10	2.0, 8.0
Upmu-Through-NonShowering	10	2.0, 8.0

Table A.1: The reconstructed cosine zenith and lepton momentum binning assigned to the atmospheric samples. The “ $\cos(\theta_Z)$ Bins” column illustrates the number of bins uniformly distributed over the $-1.0 \leq \cos(\theta_Z) \leq 1.0$ region for fully and partially contained samples and $-1.0 \leq \cos(\theta_Z) \leq 0.0$ region for up- μ samples.

3456 The one-ring CC1 π samples, where the pion is tagged via its decay electron,
 3457 are dominated by CC1 π events ($\sim 75\%$) with a small contribution of CCM π
 3458 ($\sim 10\%$). The two-ring pion sample is mostly dominated by the NC1 π^0 via
 3459 resonances, and has several equally-sized contributions from CCQE, NC1 π^\pm via
 3460 resonances, and NC coherent pion production, where the π^0 likely comes from
 3461 nucleon and π^\pm final state interactions in the nucleus.

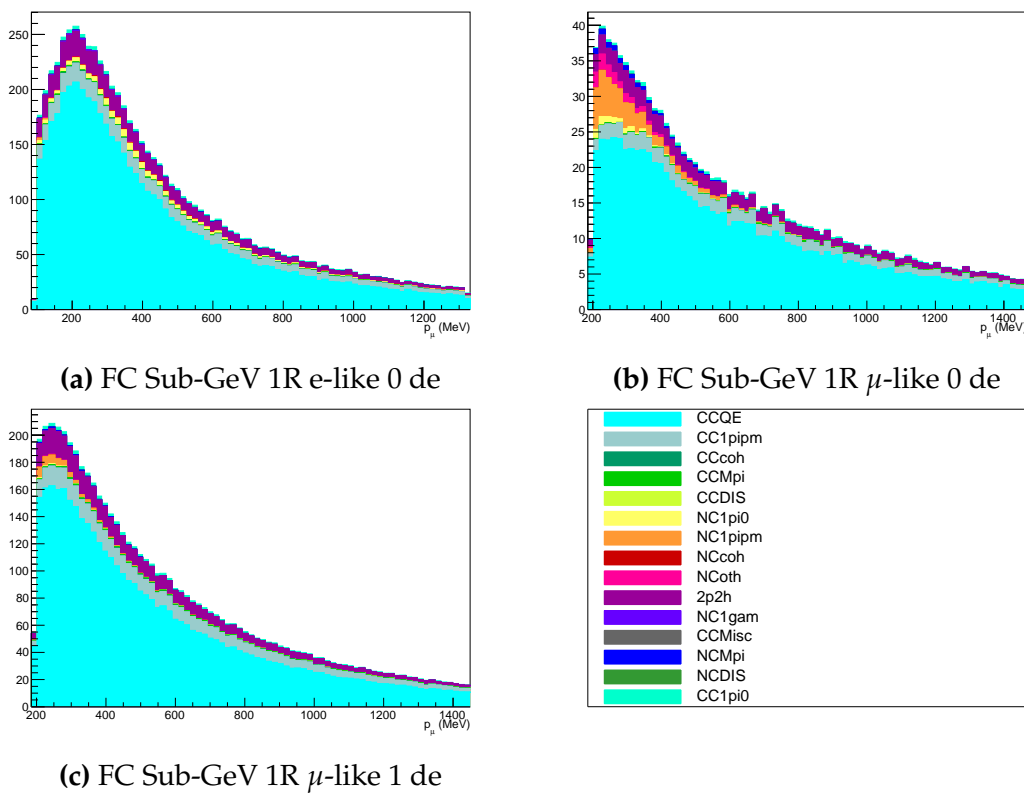


Figure A.1: Breakdown by interaction mode of the FC Sub-GeV atmospheric samples targeting CC 0π events.

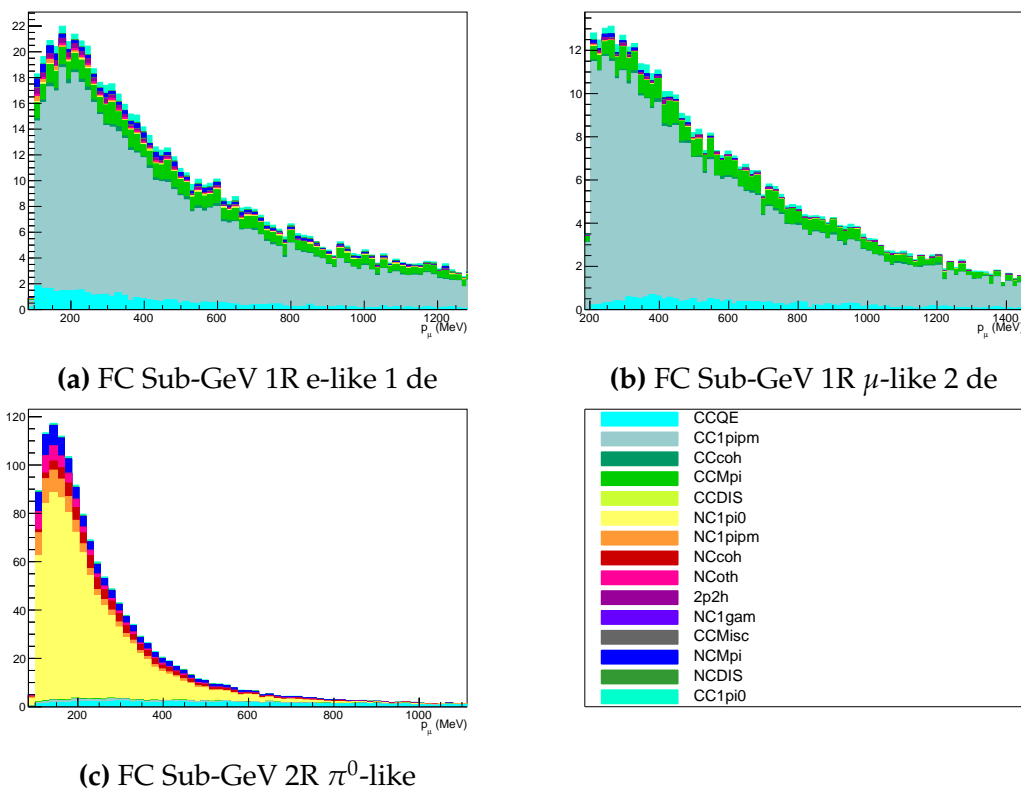


Figure A.2: Breakdown by interaction mode of the FC Sub-GeV atmospheric samples targeting single pion events.

3462 A.3 Fully Contained Multi-GeV Samples

3463 The interaction mode breakdown of fully contained multi-GeV samples is high-
 3464 lighted in Figure A.3. Due to the event selection applied in SK which targets π^+
 3465 and π^- separation, the ν_e sample mainly consists of events with pions (single pion
 3466 production or multi-pion/DIS interactions). The pion separation is explained in
 3467 Section section 6.1. This reasoning also explains the significant CCQE contribution
 3468 of the $\bar{\nu}_e$ sample. The muon-like sample is dominated by CCQE interactions with
 3469 $\sim 10 - 15\%$ 2p2h and CC1 π contribution of events.

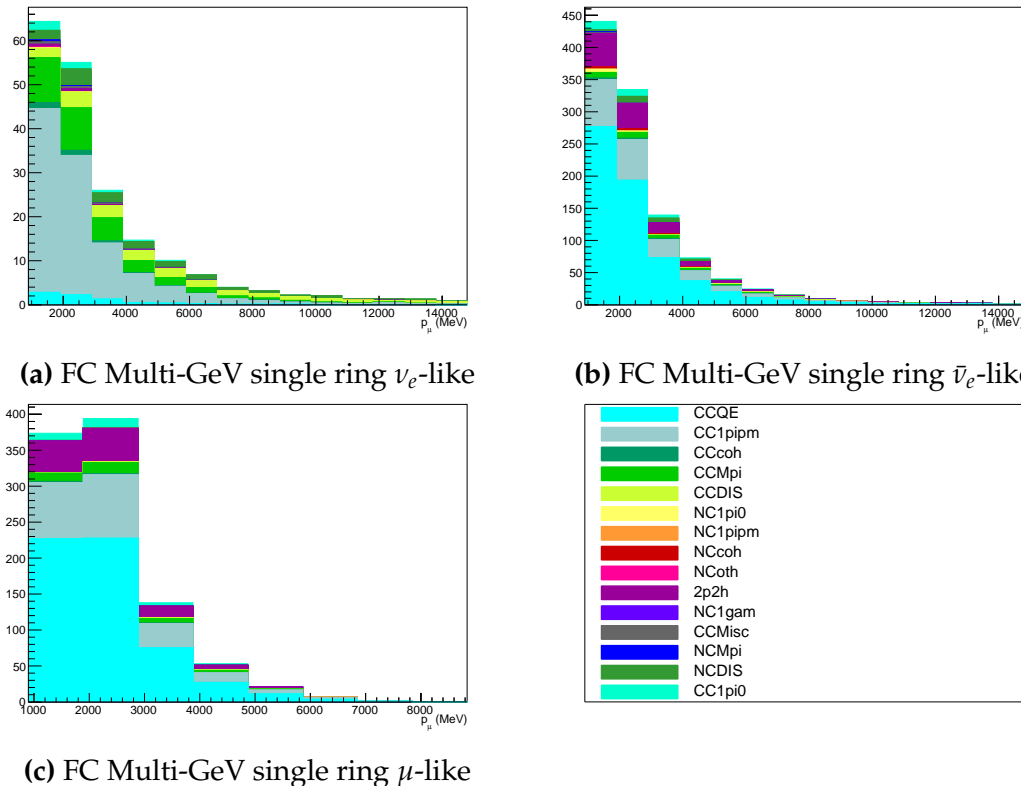


Figure A.3: Breakdown by interaction mode of the FC Multi-GeV single ring atmospheric samples.

A.4 Fully Contained Multi-Ring Samples

The interaction mode breakdown of fully contained multi-ring events is shown in Figure A.4. These samples see more interaction modes contributing in general, and there is a much larger contribution from multi-pion and DIS interaction modes, compared to the other samples.

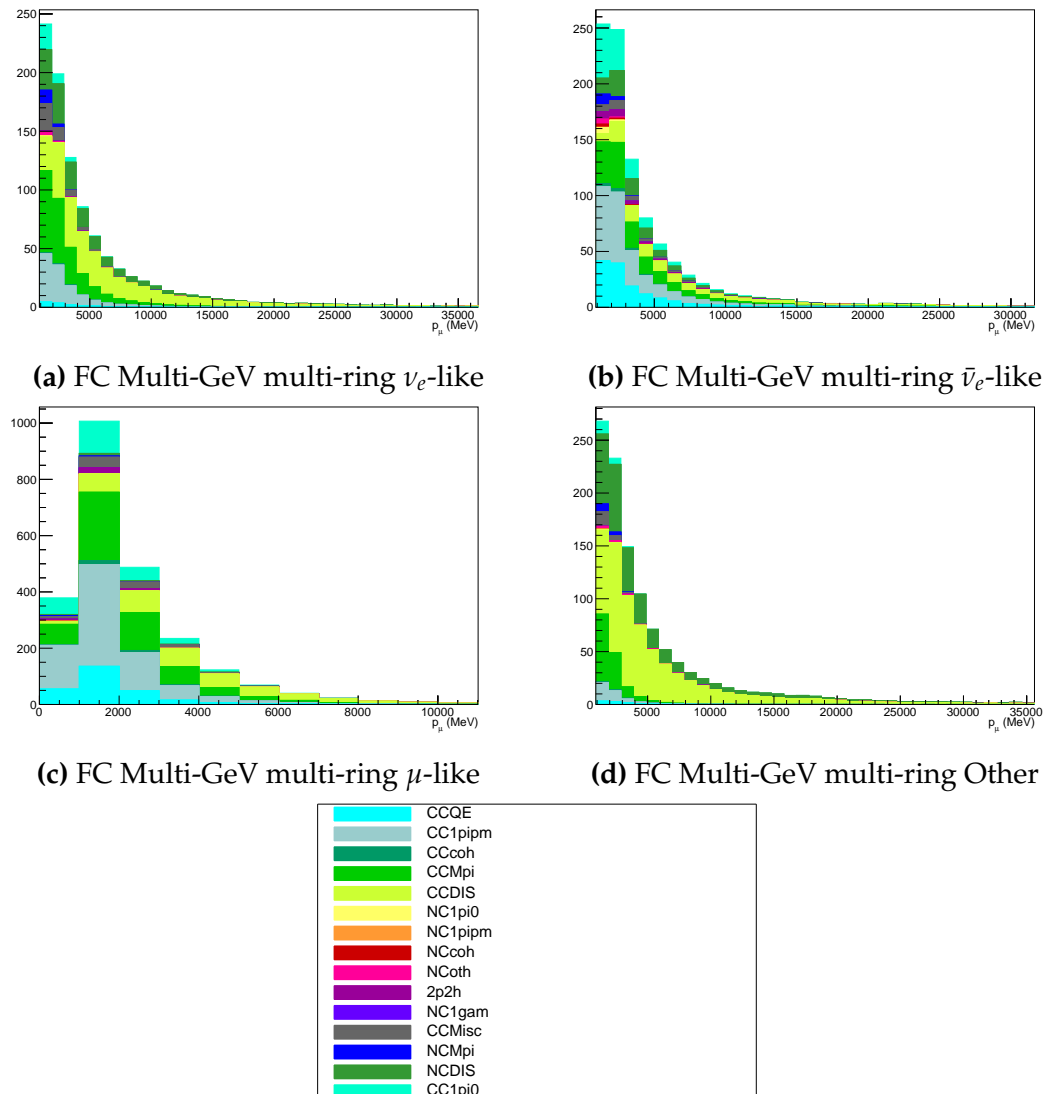


Figure A.4: Breakdown by interaction mode of the FC Multi-GeV multi-ring atmospheric samples.

3475 A.5 Partially Contained Samples

3476 The breakdown for partially contained samples is highlighted in Figure A.5.
 3477 As with the multi-ring samples, there is no dominating interaction mode. The
 3478 neutrino energies of events in this sample extend into the tens of GeV and become
 3479 dominated by DIS interaction modes in the high energy limit.

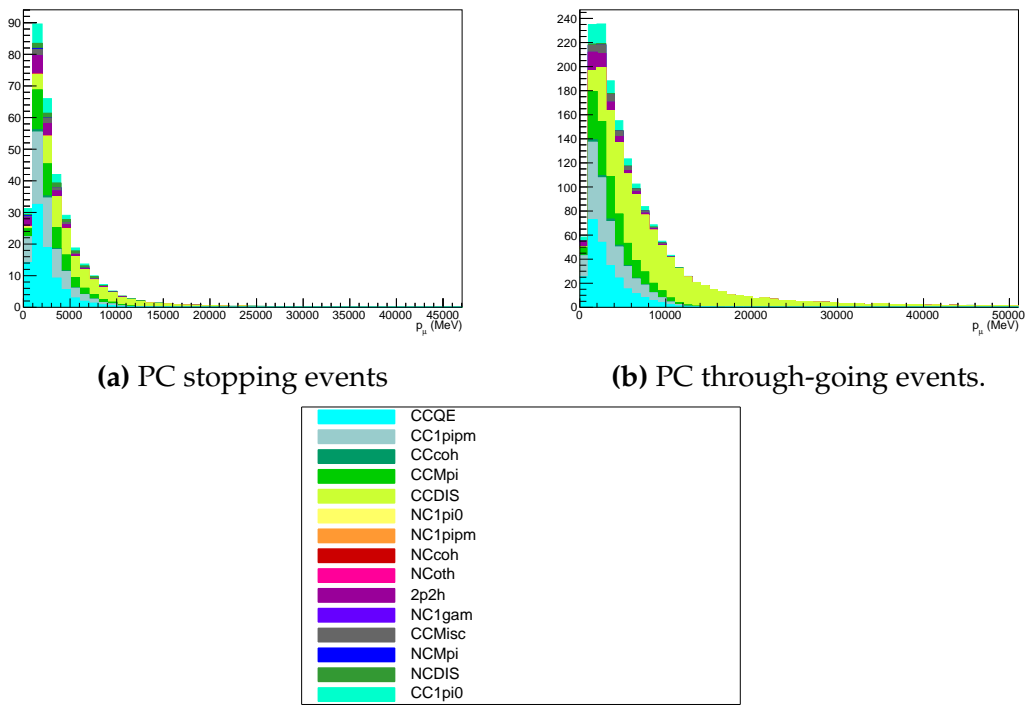


Figure A.5: Breakdown by interaction mode of the PC atmospheric samples.

3480 A.6 Upward-Going Muon Samples

3481 The breakdown for upward-going muons is illustrated in Figure A.6. These
 3482 samples are significantly dominated by DIS interactions with energies extending
 3483 up into the hundreds of GeV.

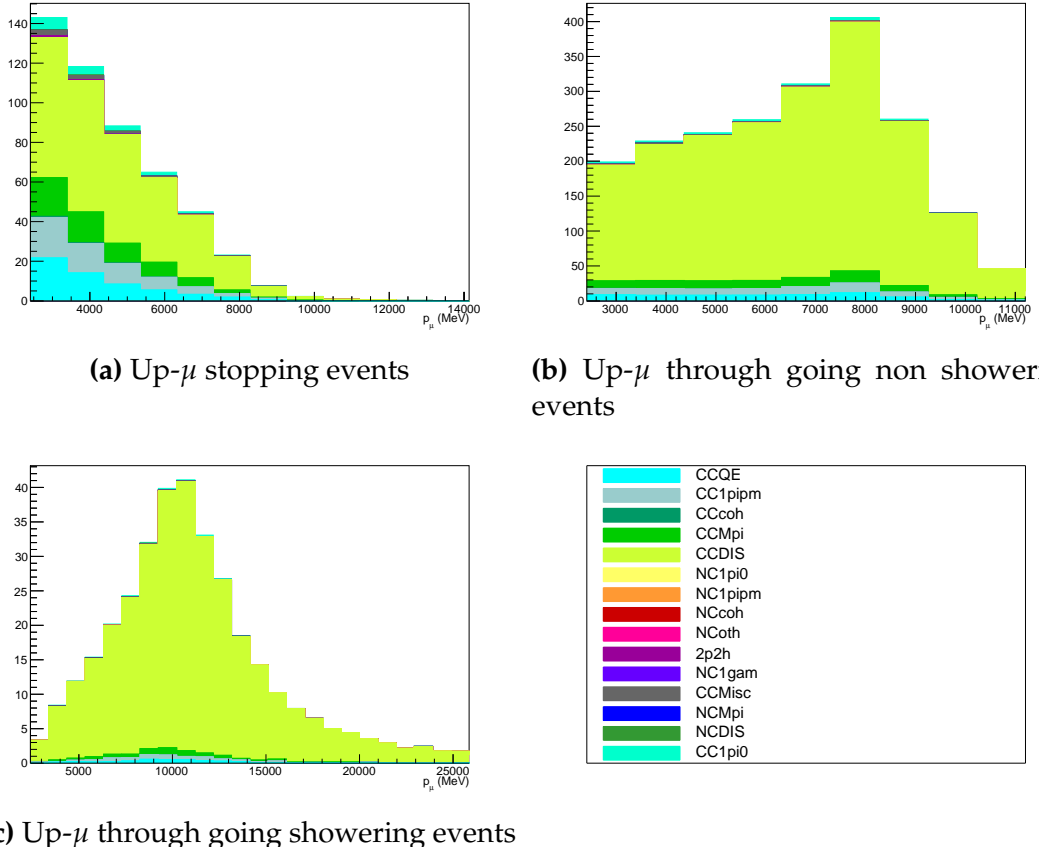


Figure A.6: Breakdown by interaction mode of the atmospheric upward going muon samples.

Bibliography

- [1] J Chadwick. "Intensitätsverteilung im magnetischen Spectrum der β -Strahlen von radium B + C". In: *Verhandl. Dtsc. Phys. Ges.* 16 (1914), p. 383. URL: <http://cds.cern.ch/record/262756>.
- [2] C D Ellis and W A Wooster. "The average energy of disintegration of radium E". en. In: *Proc. R. Soc. Lond. A Math. Phys. Sci.* 117.776 (Dec. 1927), pp. 109–123.
- [3] W. Pauli. "Dear radioactive ladies and gentlemen". In: *Phys. Today* 31N9 (1978), p. 27.
- [4] E. Fermi. "An attempt of a theory of beta radiation. 1." In: *Z. Phys.* 88 (1934), pp. 161–177.
- [5] F. Reines and C. L. Cowan. "Detection of the Free Neutrino". In: *Phys. Rev.* 92 (3 1953), pp. 830–831. URL: <https://link.aps.org/doi/10.1103/PhysRev.92.830>.
- [6] C. L. Cowan et al. "Detection of the Free Neutrino: a Confirmation". In: *Science* 124.3212 (1956), pp. 103–104. eprint: <http://science.sciencemag.org/content/124/3212/103.full.pdf>. URL: <http://science.sciencemag.org/content/124/3212/103>.
- [7] G. Danby et al. "Observation of High-Energy Neutrino Reactions and the Existence of Two Kinds of Neutrinos". In: *Phys. Rev. Lett.* 9 (1 1962), pp. 36–44. URL: <https://link.aps.org/doi/10.1103/PhysRevLett.9.36>.
- [8] K. Kodama et al. "Observation of tau neutrino interactions". In: *Physics Letters B* 504.3 (2001), pp. 218 –224. URL: <http://www.sciencedirect.com/science/article/pii/S0370269301003070>.
- [9] A. Aguilar-Arevalo et al. "Evidence for neutrino oscillations from the observation of anti-neutrino(electron) appearance in a anti-neutrino(muon) beam". In: *Phys. Rev.* D64 (2001), p. 112007. arXiv: [hep-ex/0104049](https://arxiv.org/abs/hep-ex/0104049) [hep-ex].
- [10] A. A. Aguilar-Arevalo et al. "Improved Search for $\bar{\nu}_\mu \rightarrow \bar{\nu}_e$ Oscillations in the MiniBooNE Experiment". In: *Phys. Rev. Lett.* 110 (16 2013), p. 161801. URL: <https://link.aps.org/doi/10.1103/PhysRevLett.110.161801>.
- [11] Planck Collaboration et al. "Planck 2018 results. VI. Cosmological parameters". In: *aap* 641 (Sept. 2020).
- [12] J. A. Bagger et al. "Precision electroweak measurements on the Z resonance". In: *Physics Reports* 427.5 (2006), pp. 257 –454. URL: <http://www.sciencedirect.com/science/article/pii/S0370157305005119>.
- [13] B. Pontecorvo. "Neutrino Experiments and the Problem of Conservation of Leptonic Charge". In: *Sov. Phys. JETP* 26 (1968). [Zh. Eksp. Teor. Fiz. 53, 1717(1967)], pp. 984–988.

- [14] B. Pontecorvo. "Inverse beta processes and nonconservation of lepton charge". In: *Sov. Phys. JETP* 7 (1958). [Zh. Eksp. Teor. Fiz.34,247(1957)], pp. 172–173.
- [15] Makoto Kobayashi and Toshihide Maskawa. "CP-Violation in the Renormalizable Theory of Weak Interaction". In: *Progress of Theoretical Physics* 49.2 (1973), pp. 652–657. URL: <http://dx.doi.org/10.1143/PTP.49.652>.
- [16] Nicola Cabibbo. "Unitary Symmetry and Leptonic Decays". In: *Phys. Rev. Lett.* 10 (12 1963), pp. 531–533. URL: <https://link.aps.org/doi/10.1103/PhysRevLett.10.531>.
- [17] A Maio and. "Search for Majorana neutrinos with the SNO+ detector at SNOLAB". In: *Journal of Physics: Conference Series* 587 (2015), p. 012030. URL: <https://doi.org/10.1088/1742-6596/587/1/012030>.
- [18] A Yu Smirnov. "The MSW effect and solar neutrinos". In: (2003).
- [19] S.P. Mikheyev and A.Y. Smirnov. "Resonance enhancement of oscillations in matter and solar neutrino spectroscopy". In: *Soviet Journal of Nuclear Physics* 42 (6 1985), pp. 913–917.
- [20] L. Wolfenstein. "Neutrino oscillations in matter". In: *Phys. Rev. D* 17 (9 1978), pp. 2369–2374. URL: <https://link.aps.org/doi/10.1103/PhysRevD.17.2369>.
- [21] Vernon D. Barger et al. "Matter Effects on Three-Neutrino Oscillations". In: *Phys. Rev. D* 22 (1980), p. 2718.
- [22] Y. Ashie et al. "Evidence for an Oscillatory Signature in Atmospheric Neutrino Oscillations". In: *Phys. Rev. Lett.* 93 (10 2004), p. 101801. URL: <https://link.aps.org/doi/10.1103/PhysRevLett.93.101801>.
- [23] Q. R. Ahmad et al. "Direct Evidence for Neutrino Flavor Transformation from Neutral-Current Interactions in the Sudbury Neutrino Observatory". In: *Phys. Rev. Lett.* 89 (1 2002), p. 011301. URL: <https://link.aps.org/doi/10.1103/PhysRevLett.89.011301>.
- [24] 2015 Nobel prize in Physics as listed by Nobelprize.org. https://www.nobelprize.org/nobel_prizes/physics/laureates/2015/. Accessed: 22-06-2022.
- [25] J. A. Formaggio and G. P. Zeller. "From eV to EeV: Neutrino Cross Sections Across Energy Scales". In: *Rev. Mod. Phys.* 84 (2012), pp. 1307–1341. arXiv: 1305.7513 [hep-ex].
- [26] A Bellerive. "Review of solar neutrino experiments". en. In: *Int. J. Mod. Phys. A* 19.08 (Mar. 2004), pp. 1167–1179.
- [27] Raymond Davis, Don S. Harmer, and Kenneth C. Hoffman. "Search for Neutrinos from the Sun". In: *Phys. Rev. Lett.* 20 (21 1968), pp. 1205–1209. URL: <https://link.aps.org/doi/10.1103/PhysRevLett.20.1205>.
- [28] Núria Vinyoles et al. "A new generation of standard solar models". In: *Astrophys. J.* 835.2 (Jan. 2017), p. 202.
- [29] V Gribov and B Pontecorvo. "Neutrino astronomy and lepton charge". en. In: *Phys. Lett. B* 28.7 (Jan. 1969), pp. 493–496.

- 3562 [30] K. S. Hirata et al. "Observation of ${}^8\text{B}$ solar neutrinos in the Kamiokande-II
3563 detector". In: *Phys. Rev. Lett.* 63 (1 1989), pp. 16–19. URL:
3564 <https://link.aps.org/doi/10.1103/PhysRevLett.63.16>.
- 3565 [31] W Hampel et al. "GALLEX solar neutrino observations: results for GALLEX IV".
3566 en. In: *Phys. Lett. B* 447.1-2 (Feb. 1999), pp. 127–133.
- 3567 [32] J. N. Abdurashitov et al. "Measurement of the solar neutrino capture rate with
3568 gallium metal". In: *Phys. Rev. C* 60 (5 1999), p. 055801. URL:
3569 <https://link.aps.org/doi/10.1103/PhysRevC.60.055801>.
- 3570 [33] Q R Ahmad et al. "Direct evidence for neutrino flavor transformation from
3571 neutral-current interactions in the Sudbury neutrino observatory". en. In: *Phys.*
3572 *Rev. Lett.* 89.1 (June 2002).
- 3573 [34] Borexino Collaboration. "Comprehensive measurement of pp-chain solar
3574 neutrinos". en. In: *Nature* 562.7728 (Oct. 2018), pp. 505–510.
- 3575 [35] B Aharmim et al. "A search for neutrinos from the SolarhepReaction and the
3576 diffuse supernova neutrino background with the Sudbury neutrino observatory".
3577 en. In: *Astrophys. J.* 653.2 (Dec. 2006), pp. 1545–1551.
- 3578 [36] M Agostini et al. "Experimental evidence of neutrinos produced in the CNO
3579 fusion cycle in the Sun". In: (2020).
- 3580 [37] S Andringa et al. "Current status and future prospects of the SNO+ experiment".
3581 In: *Adv. High Energy Phys.* 2016 (2016), pp. 1–21.
- 3582 [38] John F Beacom et al. "Physics prospects of the Jinping neutrino experiment". In:
3583 *Chin. phys. C* 41.2 (Feb. 2017), p. 023002.
- 3584 [39] Fengpeng An et al. "Neutrino physics with JUNO". In: *J. Phys. G Nucl. Part. Phys.*
3585 43.3 (Mar. 2016), p. 030401.
- 3586 [40] G Danby et al. "Observation of high-energy neutrino reactions and the existence
3587 of two kinds of neutrinos". In: *Phys. Rev. Lett.* 9.1 (July 1962), pp. 36–44.
- 3588 [41] K. Abe et al. "T2K neutrino flux prediction". In: *Physical Review D* 87.1 (2013).
3589 URL: <https://doi.org/10.1103%2Fphysrevd.87.012001>.
- 3590 [42] D. G. Michael et al. "Observation of Muon Neutrino Disappearance with the
3591 MINOS Detectors in the NuMI Neutrino Beam". In: *Phys. Rev. Lett.* 97 (19 2006),
3592 p. 191801. URL:
3593 <https://link.aps.org/doi/10.1103/PhysRevLett.97.191801>.
- 3594 [43] G. Danby et al. "Observation of High-Energy Neutrino Reactions and the
3595 Existence of Two Kinds of Neutrinos". In: *Phys. Rev. Lett.* 9 (1 1962), pp. 36–44.
3596 URL: <https://link.aps.org/doi/10.1103/PhysRevLett.9.36>.
- 3597 [44] M. A. Acero et al. "First measurement of neutrino oscillation parameters using
3598 neutrinos and antineutrinos by NOvA". In: *Phys. Rev. Lett.* 123 (15 2019),
3599 p. 151803. URL:
3600 <https://link.aps.org/doi/10.1103/PhysRevLett.123.151803>.
- 3601 [45] B Abi et al. "Long-baseline neutrino oscillation physics potential of the DUNE
3602 experiment". en. In: *Eur. Phys. J. C Part. Fields* 80.10 (Oct. 2020).

- 3603 [46] Hyper-Kamiokande Proto-Collaboration et al. "Physics potential of a
3604 long-baseline neutrino oscillation experiment using a J-PARC neutrino beam and
3605 Hyper-Kamiokande". In: *Prog. Theor. Exp. Phys.* 2015.5 (May 2015), pp. 53C02–0.
3606 [47] Carlos Blanco, Dan Hooper, and Pedro Machado. "Constraining sterile neutrino
3607 interpretations of the LSND and MiniBooNE anomalies with coherent neutrino
3608 scattering experiments". In: *Physical Review D* 101.7 (2020). URL:
3609 <https://doi.org/10.1103%2Fphysrevd.101.075051>.
3610 [48] MicroBooNE Collaboration et al. *Search for an Excess of Electron Neutrino*
3611 *Interactions in MicroBooNE Using Multiple Final State Topologies*. 2021. URL:
3612 <https://arxiv.org/abs/2110.14054>.
3613 [49] B. Armbruster et al. "Upper limits for neutrino oscillations $\bar{\nu}_\mu \rightarrow \bar{\nu}_e$ from muon
3614 decay at rest". In: *Phys. Rev. D* 65 (11 2002), p. 112001. URL:
3615 <https://link.aps.org/doi/10.1103/PhysRevD.65.112001>.
3616 [50] T K Gaisser and M Honda. "Flux of Atmospheric Neutrinos". In: (2002).
3617 [51] G. D. Barr et al. "Three-dimensional calculation of atmospheric neutrinos". In:
3618 *Physical Review D* 70.2 (2004). URL:
3619 <https://doi.org/10.1103/physrevd.70.023006>.
3620 [52] M. Honda et al. "Calculation of atmospheric neutrino flux using the interaction
3621 model calibrated with atmospheric muon data". In: *Physical Review D* 75.4 (2007).
3622 URL: <https://doi.org/10.1103/physrevd.75.043006>.
3623 [53] M. Honda et al. "New calculation of the atmospheric neutrino flux in a
3624 three-dimensional scheme". In: *Phys. Rev. D* 70 (4 2004), p. 043008. URL:
3625 <https://link.aps.org/doi/10.1103/PhysRevD.70.043008>.
3626 [54] M. Honda et al. "Improvement of low energy atmospheric neutrino flux
3627 calculation using the JAM nuclear interaction model". In: *Phys. Rev. D* 83 (12
3628 2011), p. 123001. URL:
3629 <https://link.aps.org/doi/10.1103/PhysRevD.83.123001>.
3630 [55] A. Fasso et al. "FLUKA: status and prospects for hadronic applications". In:
3631 (2001).
3632 [56] Y. Ashie et al. "Measurement of atmospheric neutrino oscillation parameters by
3633 Super-Kamiokande I". In: *Physical Review D* 71.11 (2005). URL:
3634 <https://doi.org/10.1103/physrevd.71.112005>.
3635 [57] F Reines et al. "Evidence for high-energy cosmic-ray neutrino interactions". In:
3636 *Phys. Rev. Lett.* 15.9 (Aug. 1965), pp. 429–433.
3637 [58] D. Casper et al. "Measurement of atmospheric neutrino composition with the
3638 IMB-3 detector". In: *Phys. Rev. Lett.* 66 (20 1991), pp. 2561–2564. URL:
3639 <https://link.aps.org/doi/10.1103/PhysRevLett.66.2561>.
3640 [59] K S Hirata et al. "Observation of a small atmospheric ν_μ/ν_e ratio in Kamiokande"
3641 en. In: *Phys. Lett. B* 280.1-2 (Apr. 1992), pp. 146–152.
3642 [60] Z. Li et al. "Measurement of the tau neutrino cross section in atmospheric
3643 neutrino oscillations with Super-Kamiokande". In: *Physical Review D* 98.5 (2018).
3644 URL: <https://doi.org/10.1103/physrevd.98.052006>.
3645 [61] Kamiokande Collaboration et al. "Atmospheric neutrino oscillation analysis with
3646 external constraints in Super-Kamiokande I-IV". In: (2017).

- 3647 [62] T2K Collaboration. "Constraint on the matter-antimatter symmetry-violating
3648 phase in neutrino oscillations". en. In: *Nature* 580.7803 (Apr. 2020), pp. 339–344.
- 3649 [63] M A Acero et al. "First measurement of neutrino oscillation parameters using
3650 neutrinos and antineutrinos by NOvA". en. In: *Phys. Rev. Lett.* 123.15 (Oct. 2019),
3651 p. 151803.
- 3652 [64] M G Aartsen et al. "Measurement of atmospheric neutrino oscillations at 6–56
3653 GeV with IceCube DeepCore". In: *Phys. Rev. Lett.* 120.7 (Feb. 2018).
- 3654 [65] P Adamson et al. "Combined analysis of $\nu\mu$ Disappearance
3655 and $\nu\mu \rightarrow \nu e$ Appearance in MINOS using accelerator and atmospheric neutrinos".
3656 In: *Phys. Rev. Lett.* 112.19 (May 2014).
- 3657 [66] M. Sajjad Athar et al. "Status and perspectives of neutrino physics". In: *Progress
3658 in Particle and Nuclear Physics* 124 (2022), p. 103947. URL:
3659 <https://doi.org/10.1016/Fj.pnpp.2022.103947>.
- 3660 [67] Soo-Bong Kim, Thierry Lasserre, and Yifang Wang. "Reactor Neutrinos". In: *Adv.
3661 High Energy Phys.* 2013 (2013), pp. 1–34.
- 3662 [68] Mohammad Sajjad Athar et al. "Status and perspectives of neutrino physics". In: *Prog. Part. Nucl. Phys.* 124 (2022), p. 103947. arXiv: 2111.07586 [hep-ph].
- 3664 [69] K Abe et al. "First gadolinium loading to Super-Kamiokande". en. In: *Nucl.
3665 Instrum. Methods Phys. Res. A* 1027.166248 (Mar. 2022), p. 166248.
- 3666 [70] F. P. An et al. "Observation of Electron-Antineutrino Disappearance at Daya Bay".
3667 In: *Phys. Rev. Lett.* 108 (17 2012), p. 171803. URL:
3668 <https://link.aps.org/doi/10.1103/PhysRevLett.108.171803>.
- 3669 [71] J. K. Ahn et al. "Observation of Reactor Electron Antineutrinos Disappearance in
3670 the RENO Experiment". In: *Phys. Rev. Lett.* 108 (19 2012), p. 191802. URL:
3671 <https://link.aps.org/doi/10.1103/PhysRevLett.108.191802>.
- 3672 [72] Y. Abe et al. "Indication of Reactor $\bar{\nu}_e$ Disappearance in the Double Chooz
3673 Experiment". In: *Phys. Rev. Lett.* 108 (13 2012), p. 131801. URL:
3674 <https://link.aps.org/doi/10.1103/PhysRevLett.108.131801>.
- 3675 [73] JUNO Collaboration et al. *TAO Conceptual Design Report: A Precision Measurement
3676 of the Reactor Antineutrino Spectrum with Sub-percent Energy Resolution*. 2020. arXiv:
3677 2005.08745 [physics.ins-det].
- 3678 [74] M P Decowski. "KamLAND's precision neutrino oscillation measurements". en.
3679 In: *Nucl. Phys. B*. 908 (July 2016), pp. 52–61.
- 3680 [75] A. Gando et al. "Constraints on θ_{13} from a three-flavor oscillation analysis of
3681 reactor antineutrinos at KamLAND". In: *Phys. Rev. D* 83 (5 2011), p. 052002. URL:
3682 <https://link.aps.org/doi/10.1103/PhysRevD.83.052002>.
- 3683 [76] Patrick Dunne. *Latest Neutrino oscillation results from T2K*. 2020.
- 3684 [77] Particle Data Group et al. "Review of particle physics". en. In: *Prog. Theor. Exp.
3685 Phys.* 2020.8 (Aug. 2020).
- 3686 [78] R. L. Workman and Others. "Review of Particle Physics". In: *PTEP* 2022 (2022),
3687 p. 083C01.

- 3688 [79] K. Abe et al. "Precise Measurement of the Neutrino Mixing Parameter θ_{23} from
3689 Muon Neutrino Disappearance in an Off-Axis Beam". In: *Phys. Rev. Lett.* 112 (18
3690 2014), p. 181801. URL:
3691 <https://link.aps.org/doi/10.1103/PhysRevLett.112.181801>.
- 3692 [80] Y Fukuda et al. "Evidence for oscillation of atmospheric neutrinos". In: *Phys. Rev.
3693 Lett.* 81.8 (Aug. 1998), pp. 1562–1567.
- 3694 [81] K. Abe et al. "Calibration of the Super-Kamiokande detector". In: *Nuclear
3695 Instruments and Methods in Physics Research Section A: Accelerators, Spectrometers,
3696 Detectors and Associated Equipment* 737 (2014), pp. 253–272. URL:
3697 <https://doi.org/10.1016/j.nima.2013.11.081>.
- 3698 [82] Linyan Wan. "Atmospheric Neutrino_Super-K". In: (2022). URL:
3699 <https://zenodo.org/record/6694761>.
- 3700 [83] Miao Jiang. "Study of the neutrino mass hierarchy with the atmospheric neutrino
3701 data collected in Super-Kamiokande IV". PhD thesis. Kyoto University, 2019.
- 3702 [84] S Fukuda et al. "The super-kamiokande detector". en. In: *Nucl. Instrum. Methods
3703 Phys. Res. A* 501.2-3 (Apr. 2003), pp. 418–462.
- 3704 [85] Y Itow et al. "The JHF-Kamioka neutrino project". In: (2001).
- 3705 [86] M Jiang et al. "Atmospheric neutrino oscillation analysis with improved event
3706 reconstruction in Super-Kamiokande IV". en. In: *Prog. Theor. Exp. Phys.* 2019.5
3707 (May 2019).
- 3708 [87] A. Suzuki et al. "Improvement of 20 in. diameter photomultiplier tubes". In:
3709 *Nuclear Instruments and Methods in Physics Research Section A: Accelerators,
3710 Spectrometers, Detectors and Associated Equipment* 329.1-2 (May 1993), pp. 299–313.
3711 URL: [https://doi.org/10.1016/0168-9002\(93\)90949-i](https://doi.org/10.1016/0168-9002(93)90949-i).
- 3712 [88] S. Fukuda et al. "The Super-Kamiokande detector". In: *Nuclear Instruments and
3713 Methods in Physics Research Section A: Accelerators, Spectrometers, Detectors and
3714 Associated Equipment* 501.2 (2003), pp. 418–462. eprint:
3715 <http://www.sciencedirect.com/science/article/pii/S016890020300425X>.
- 3716 [89] Y Nakano et al. "Measurement of the radon concentration in purified water in
3717 the Super-Kamiokande IV detector". en. In: *Nucl. Instrum. Methods Phys. Res. A*
3718 977.164297 (Oct. 2020), p. 164297.
- 3719 [90] Hamamatsu. *Hamamatsu Photonics Photomultiplier Tubes Handbook*. URL:
3720 [https://www.hamamatsu.com/content/dam/hamamatsu-photonics/sites/
documents/99\SALES_LIBRARY/etd/PMT_handbook_v4E.pdf](https://www.hamamatsu.com/content/dam/hamamatsu-photonics/sites/
3721 documents/99\SALES_LIBRARY/etd/PMT_handbook_v4E.pdf).
- 3722 [91] K Abe et al. "First gadolinium loading to Super-Kamiokande". en. In: *Nucl.
3723 Instrum. Methods Phys. Res. A* 1027.166248 (Mar. 2022), p. 166248.
- 3724 [92] John F. Beacom and Mark R. Vagins. "Antineutrino Spectroscopy with Large
3725 Water Čerenkov Detectors". In: *Phys. Rev. Lett.* 93 (17 2004), p. 171101. URL:
3726 <https://link.aps.org/doi/10.1103/PhysRevLett.93.171101>.
- 3727 [93] Ll Martí et al. "Evaluation of gadolinium's action on water Cherenkov detector
3728 systems with EGADS". en. In: *Nucl. Instrum. Methods Phys. Res. A* 959.163549
3729 (Apr. 2020), p. 163549.
- 3730 [94] Ll Martí et al. "Evaluation of gadolinium's action on water Cherenkov detector
3731 systems with EGADS". In: (2019).

- 3732 [95] Mark Vagins. *Solar/DSNB Neutrino_SK-Gd*. 2022.
- 3733 [96] John Focht. PhD thesis. Massachusetts Institute of Technology, 2004.
- 3734 [97] T. Tanimori et al. "Design and performance of semi-custom analog IC including
3735 two TACs and two current integrators for 'Super-Kamiokande'". In: *IEEE*
3736 *Transactions on Nuclear Science* 36.1 (1989), pp. 497–501.
- 3737 [98] J. Hosaka et al. "Solar neutrino measurements in Super-Kamiokande-I". In: *Phys.*
3738 *Rev. D* 73 (11 2006), p. 112001. URL:
3739 <https://link.aps.org/doi/10.1103/PhysRevD.73.112001>.
- 3740 [99] H Nishino et al. "High-speed charge-to-time converter ASIC for the
3741 Super-Kamiokande detector". en. In: *Nucl. Instrum. Methods Phys. Res. A* 610.3
3742 (Nov. 2009), pp. 710–717.
- 3743 [100] S. Yamada et al. "Commissioning of the New Electronics and Online System for
3744 the Super-Kamiokande Experiment". In: *IEEE Transactions on Nuclear Science* 57.2
3745 (2010), pp. 428–432.
- 3746 [101] Satoru Yamada et al. "New online system without hardware trigger for the
3747 Super-Kamiokande experiment". In: *2007 IEEE Nuclear Science Symposium
3748 Conference Record*. Honolulu, HI, USA: IEEE, Oct. 2007.
- 3749 [102] Giada Carminati. "The new wide-band solar neutrino trigger for
3750 super-kamiokande". In: *Phys. Procedia* 61 (2015), pp. 666–672.
- 3751 [103] P A Čerenkov. "Visible radiation produced by electrons moving in a medium
3752 with velocities exceeding that of light". In: *Phys. Rev.* 52.4 (Aug. 1937),
3753 pp. 378–379.
- 3754 [104] I Frank and Ig Tamm. "Coherent visible radiation of fast electrons passing
3755 through matter". In: *Selected Papers*. Berlin, Heidelberg: Springer Berlin
3756 Heidelberg, 1991, pp. 29–35.
- 3757 [105] The T2K Collaboration. "Letter of Intent: Neutrino Oscillation Experiment at
3758 JHF". In: *KEK Proposal* (2001). eprint:
3759 <http://neutrino.kek.jp/jhfnu/loi/loi.v2.030528.pdf>.
- 3760 [106] Y Itow et al. "The JHF-Kamioka neutrino project". In: (June 2001). arXiv:
3761 [hep-ex/0106019](https://arxiv.org/abs/hep-ex/0106019) [hep-ex].
- 3762 [107] The K2K Collaboration and S H Ahn. "Detection of Accelerator-Produced
3763 Neutrinos at a Distance of 250 km". In: (Feb. 2001). arXiv: [hep-ex/0103001](https://arxiv.org/abs/hep-ex/0103001)
3764 [hep-ex].
- 3765 [108] The T2K Collaboration. "Tokai-to-Kamioka (T2K) Long Baseline Neutrino
3766 Oscillation Experiment Proposal". In: *KEK Proposal* (2006). eprint: {{<http://j-parc.jp/researcher/Hadron/en/pac\0606/pdf/p11-Nishikawa.pdf>}}.
- 3767 [109] Christophe Bronner. *Accelerator Neutrino I_Recent results from T2K*. 2022.
- 3768 [110] K. Abe et al. "Observation of Electron Neutrino Appearance in a Muon Neutrino
3769 Beam". In: *Phys. Rev. Lett.* 112 (6 2014), p. 061802. eprint:
3770 <https://link.aps.org/doi/10.1103/PhysRevLett.112.061802>.
- 3771 [111] T. Fukuda et al. "Proposal for precise measurement of neutrino-water
3772 cross-section in NINJA physics run". Proposal for J-PARC and KEK. 2017.
- 3773

- 3774 [112] T. Ovsianikova et al. "New experiment WAGASCI to measure cross sections of
3775 neutrino interactions in water and hydrocarbon using J-PARC beam". In: *Physics*
3776 of Particles and Nuclei
- 3777 48.6 (2017), pp. 1014–1017. eprint:
<https://doi.org/10.1134/S1063779617060478>.
- 3778 [113] M. Antonova et al. "Baby MIND: a magnetized segmented neutrino detector for
3779 the WAGASCI experiment". In: *Journal of Instrumentation* 12.07 (2017), p. C07028.
3780 eprint: <http://stacks.iop.org/1748-0221/12/i=07/a=C07028>.
- 3781 [114] K. Abe et al. "First measurement of the charged current $\bar{\nu}_\mu$ double differential
3782 cross section on a water target without pions in the final state". In: *Phys. Rev. D*
3783 102 (1 2020), p. 012007. URL:
<https://link.aps.org/doi/10.1103/PhysRevD.102.012007>.
- 3785 [115] K Abe et al. "Measurements of $\bar{\nu}_\mu$ and $\bar{\nu}_\mu + \nu_\mu$ charged-current cross-sections
3786 without detected pions or protons on water and hydrocarbon at a mean
3787 anti-neutrino energy of 0.86 GeV". In: *Progress of Theoretical and Experimental*
3788 *Physics* 2021.4 (Mar. 2021). URL: <https://doi.org/10.1093/ptep/ptab014>.
- 3789 [116] K. Abe et al. "The T2K experiment". In: *Nuclear Instruments and Methods in Physics*
3790 *Research Section A: Accelerators, Spectrometers, Detectors and Associated Equipment*
3791 659.1 (2011), pp. 106 –135. eprint:
<http://www.sciencedirect.com/science/article/pii/S0168900211011910>.
- 3793 [117] K. Matsuoka et al. "Design and performance of the muon monitor for the T2K
3794 neutrino oscillation experiment". In: *Nuclear Instruments and Methods in Physics*
3795 *Research Section A: Accelerators, Spectrometers, Detectors and Associated Equipment*
3796 624.3 (2010), pp. 591 –600. eprint:
<http://www.sciencedirect.com/science/article/pii/S016890021002098X>.
- 3798 [118] K Abe et al. "Improved constraints on neutrino mixing from the T2K experiment
3799 with 3.13×10^{21} protons on target". en. In: *Phys. Rev. D.* 103.11 (June 2021).
- 3800 [119] Tomislav Vladisljevic. *Predicting the T2K neutrino flux and measuring oscillation*
3801 *parameters*. 1st ed. Springer theses. Cham, Switzerland: Springer Nature, Sept.
3802 2020.
- 3803 [120] D Beavis, A Carroll, and I Chiang. "Long baseline neutrino oscillation
3804 experiment at the AGS. Physics design report". In: (Apr. 1995).
- 3805 [121] P.-A. Amaudruz et al. "The T2K fine-grained detectors". In: *Nuclear Instruments*
3806 and *Methods in Physics Research Section A: Accelerators, Spectrometers, Detectors and*
3807 *Associated Equipment* 696 (Dec. 2012), pp. 1–31. URL:
<https://doi.org/10.1016/j.nima.2012.08.020>.
- 3809 [122] N. Abgrall et al. "Time projection chambers for the T2K near detectors". In:
3810 *Nuclear Instruments and Methods in Physics Research Section A: Accelerators,*
3811 *Spectrometers, Detectors and Associated Equipment* 637.1 (May 2011), pp. 25–46. URL:
3812 <https://doi.org/10.1016/j.nima.2011.02.036>.
- 3813 [123] S. Assylbekov et al. "The T2K ND280 off-axis pi-zero detector". In: *Nuclear*
3814 *Instruments and Methods in Physics Research Section A: Accelerators, Spectrometers,*
3815 *Detectors and Associated Equipment* 686 (Sept. 2012), pp. 48–63. URL:
<https://doi.org/10.1016/j.nima.2012.05.028>.

- 3817 [124] D Allan et al. "The electromagnetic calorimeter for the T2K near detector
3818 ND280". In: *Journal of Instrumentation* 8.10 (2013), P10019–P10019. URL:
3819 <https://doi.org/10.1088%2F1748-0221%2F8%2F10%2Fp10019>.
- 3820 [125] F. Vannucci. "The NOMAD Experiment at CERN". In: *Advances in High Energy
3821 Physics* 2014 (2014), pp. 1–20. URL: <https://doi.org/10.1155/2014/129694>.
- 3822 [126] *UA1 magnet sets off for a second new life*. 2022. URL: <https://cerncourier.com/a/ua1-magnet-sets-off-for-a-second-new-life/>.
- 3824 [127] S. Aoki et al. "The T2K Side Muon Range Detector (SMRD)". In: *Nuclear
3825 Instruments and Methods in Physics Research Section A: Accelerators, Spectrometers,
3826 Detectors and Associated Equipment* 698 (Jan. 2013), pp. 135–146. URL:
3827 <https://doi.org/10.1016/j.nima.2012.10.001>.
- 3828 [128] K. Suzuki et al. "Measurement of the muon beam direction and muon flux for the
3829 T2K neutrino experiment". In: *Progress of Theoretical and Experimental Physics*
3830 2015.5 (2015), pp. 53C01–0. URL: <https://doi.org/10.1093%2Fptep%2Fptv054>.
- 3831 [129] S. Brooks et al. *Handbook of Markov Chain Monte Carlo*. CRC Press, 2011.
- 3832 [130] W. R. Gilks, S. Richardson, and D. J. Spiegelhalter. *Markov Chain Monte Carlo in
3833 Practice*. Chapman & Hall/CRC Interdisciplinary Statistics, 1995.
- 3834 [131] Clarence Wret. "Minimising systematic uncertainties in the T2K experiment using
3835 near-detector and external data". PhD thesis. Imperial College London, 2018.
- 3836 [132] Kirsty Elizabeth Duffy. "Measurement of the Neutrino Oscillation Parameters
3837 $\sin^2 \theta_{23}$, Δm_{32}^2 , $\sin^2 \theta_{13}$, and δ_{CP} in Neutrino and Antineutrino Oscillation at T2K".
3838 PhD thesis. Oriel College, University of Oxford, 2016.
- 3839 [133] Thomas Bayes Rev. "An essay toward solving a problem in the doctrine of
3840 chances". In: *Phil. Trans. Roy. Soc. Lond.* 53 (1764), pp. 370–418.
- 3841 [134] Artur Sztuc. "Standard and Non-Standard Neutrino-Antineutrino Oscillation
3842 Analyses and Event Reconstruction Studies using Markov Chain Monte Carlo
3843 Methods at T2K". PhD thesis. Imperial College London, 2021.
- 3844 [135] N. Metropolis et al. "Equation of State Calculations by Fast Computing
3845 Machines". In: *Journal of Chemical Physics* 21.6 (1970).
- 3846 [136] W. K. Hastings. "Monte Carlo Sampling Methods Using Markov Chains and
3847 Their Applications". In: *Biometrika* 57.1 (1970).
- 3848 [137] Joanna Dunkley et al. "Fast and reliable Markov chain Monte Carlo technique for
3849 cosmological parameter estimation". en. In: *Mon. Not. R. Astron. Soc.* 356.3 (Jan.
3850 2005), pp. 925–936.
- 3851 [138] Harold Jeffreys. *The Theory of Probability*. Oxford Classic Texts in the Physical
3852 Sciences. 1939.
- 3853 [139] Robert E Kass and Adrian E Raftery. "Bayes factors". en. In: *J. Am. Stat. Assoc.*
3854 90.430 (June 1995), pp. 773–795.
- 3855 [140] T.T. Böhlen et al. "The FLUKA Code: Developments and Challenges for High
3856 Energy and Medical Applications". In: *Nuclear Data Sheets* 120 (2014), pp. 211
3857 –214. eprint:
3858 <http://www.sciencedirect.com/science/article/pii/S0090375214005018>.

- 3859 [141] René Brun et al. *GEANT: Detector Description and Simulation Tool; Oct 1994*. CERN
3860 Program Library. Long Writeup W5013. Geneva: CERN, 1993. eprint:
3861 <http://cds.cern.ch/record/1082634>.
- 3862 [142] K. Abe et al. “T2K neutrino flux prediction”. In: *Phys. Rev. D* 87 (1 2013),
3863 p. 012001. URL: <https://link.aps.org/doi/10.1103/PhysRevD.87.012001>.
- 3864 [143] C. Zeitnitz and T.A. Gabriel. “The GEANT-CALOR interface and benchmark
3865 calculations of ZEUS test calorimeters”. In: *Nuclear Instruments and Methods in*
3866 *Physics Research Section A: Accelerators, Spectrometers, Detectors and Associated*
3867 *Equipment* 349.1 (1994), pp. 106–111. eprint:
3868 <http://www.sciencedirect.com/science/article/pii/0168900294906130>.
- 3869 [144] A. Fiorentini et al. “Flux Prediction and Uncertainty Updates with NA61 2009
3870 Thin Target Data and Negative Focussing Mode Predictions”. In: *T2K Technical*
3871 *Note* 217 (2017).
- 3872 [145] N. Abgrall et al. “Measurements of cross sections and charged pion spectra in
3873 proton-carbon interactions at 31 GeV/ c ”. In: *Physical Review C* 84.3 (2011). URL:
3874 <https://doi.org/10.1103/physrevc.84.034604>.
- 3875 [146] N. Abgrall et al. “Measurement of production properties of positively charged
3876 kaons in proton-carbon interactions at 31 GeV/ c ”. In: *Physical Review C* 85.3 (2012). URL:
3877 <https://doi.org/10.1103/physrevc.85.035210>.
- 3878 [147] N. Abgrall et al. “Pion emission from the T2K replica target: Method, results and
3879 application”. In: *Nuclear Instruments and Methods in Physics Research Section A:*
3880 *Accelerators, Spectrometers, Detectors and Associated Equipment* 701 (2013), pp. 99–114.
3881 eprint:
3882 <http://www.sciencedirect.com/science/article/pii/S016890021201234X>.
- 3883 [148] M. Apollonio et al. “Forward production of charged pions with incident protons
3884 on nuclear targets at the CERN Proton Synchrotron”. In: *Phys. Rev. C* 80 (3 2009),
3885 p. 035208. eprint: <https://link.aps.org/doi/10.1103/PhysRevC.80.035208>.
- 3886 [149] B. Blau et al. “The superconducting magnet of AMS-02”. In: *Nuclear Physics B -*
3887 *Proceedings Supplements* 113.1-3 (Dec. 2002), pp. 125–132. URL:
3888 [https://doi.org/10.1016/s0920-5632\(02\)01831-5](https://doi.org/10.1016/s0920-5632(02)01831-5).
- 3889 [150] S. Haino et al. “Measurements of primary and atmospheric cosmic-ray spectra
3890 with the BESS-TeV spectrometer”. In: *Physics Letters B* 594.1-2 (July 2004),
3891 pp. 35–46. URL: <https://doi.org/10.1016/j.physletb.2004.05.019>.
- 3892 [151] NASA. *U.S. Standard Atmosphere, 1976*. 1976.
- 3893 [152] S. Roesler, R. Engel, and J. Ranft. “The Monte Carlo Event Generator
3894 DPMJET-III”. In: *Advanced Monte Carlo for Radiation Physics, Particle Transport*
3895 *Simulation and Applications*. Springer Berlin Heidelberg, 2001, pp. 1033–1038. URL:
3896 https://doi.org/10.1007/978-3-642-18211-2_166.
- 3897 [153] Koji Niita et al. “PHITS—a particle and heavy ion transport code system”. In:
3898 *Radiation Measurements* 41.9-10 (Oct. 2006), pp. 1080–1090. URL:
3899 <https://doi.org/10.1016/j.radmeas.2006.07.013>.

- 3904 [154] T Sanuki et al. "Measurements of atmospheric muon spectra at mountain
3905 altitude". In: *Physics Letters B* 541.3-4 (2002), pp. 234–242. URL:
3906 [https://doi.org/10.1016/S0370-2693\(02\)02265-7](https://doi.org/10.1016/S0370-2693(02)02265-7).
- 3907 [155] P. Achard et al. "Measurement of the atmospheric muon spectrum from 20 to
3908 3000 GeV". In: *Physics Letters B* 598.1-2 (2004), pp. 15–32. URL:
3909 <https://doi.org/10.1016/j.physletb.2004.08.003>.
- 3910 [156] Kazufumi Sato. *Atmospheric Neutrino_Reviews on neutrino fluxes (low E atm nu)*.
3911 2022.
- 3912 [157] Yoshinari Hayato and Luke Pickering. "The NEUT neutrino interaction
3913 simulation program library". In: *The European Physical Journal Special Topics* 230.24
3914 (Oct. 2021), pp. 4469–4481. URL:
3915 <https://doi.org/10.1140/epjs/s11734-021-00287-7>.
- 3916 [158] Yoshinari Hayato. "A Neutrino Interaction Simulation Program Library NEUT".
3917 In: *Acta Physica Polonica B* 40.9 (2009).
- 3918 [159] C.H. Llewellyn Smith. "Neutrino reactions at accelerator energies". In: *Physics
3919 Reports* 3.5 (1972), pp. 261 –379. eprint:
3920 <http://www.sciencedirect.com/science/article/pii/0370157372900105>.
- 3921 [160] Omar Benhar, Adelchi Fabrocini, and Stefano Fantoni. "The nucleon spectral
3922 function in infinite nuclear matter". In: *Nuclear Physics A* 497 (June 1989),
3923 pp. 423–430. URL: [https://doi.org/10.1016/0375-9474\(89\)90484-3](https://doi.org/10.1016/0375-9474(89)90484-3).
- 3924 [161] R. Bradford et al. "A New Parameterization of the Nucleon Elastic Form Factors".
3925 In: *Nuclear Physics B - Proceedings Supplements* 159 (2006). Proceedings of the 4th
3926 International Workshop on Neutrino-Nucleus Interactions in the Few-GeV
3927 Region, pp. 127 –132. eprint:
3928 <http://www.sciencedirect.com/science/article/pii/S0920563206005184>.
- 3929 [162] A. A. Aguilar-Arevalo et al. "First measurement of the muon neutrino charged
3930 current quasielastic double differential cross section". In: *Physical Review D* 81.9
3931 (2010). URL: <https://doi.org/10.1103/PhysRevD.81.092005>.
- 3932 [163] R. Gran et al. "Neutrino-nucleus quasi-elastic and 2p2h interactions up to 10
3933 GeV". In: *Phys. Rev. D* 88 (11 2013), p. 113007. eprint:
3934 <https://link.aps.org/doi/10.1103/PhysRevD.88.113007>.
- 3935 [164] Ch. Berger and L. M. Sehgal. "Lepton mass effects in single pion production by
3936 neutrinos". In: *Phys. Rev. D* 76 (11 2007), p. 113004. URL:
3937 <https://link.aps.org/doi/10.1103/PhysRevD.76.113004>.
- 3938 [165] Ch. Berger and L. M. Sehgal. "Partially conserved axial vector current and
3939 coherent pion production by low energy neutrinos". In: *Phys. Rev. D* 79 (5 2009),
3940 p. 053003. eprint: <https://link.aps.org/doi/10.1103/PhysRevD.79.053003>.
- 3941 [166] Torbjörn Sjöstrand. "High-energy-physics event generation with PYTHIA 5.7 and
3942 JETSET 7.4". In: *Computer Physics Communications* 82.1 (Aug. 1994), pp. 74–89.
3943 URL: [https://doi.org/10.1016/0010-4655\(94\)90132-5](https://doi.org/10.1016/0010-4655(94)90132-5).

- 3944 [167] Christophe Bronner and Mark Hartz. "Tuning of the Charged Hadrons
3945 Multiplicities for Deep Inelastic Interactions in NEUT". In: *Proceedings of the 10th*
3946 *International Workshop on Neutrino-Nucleus Interactions in Few-GeV Region*
3947 (*NuInt15*). Journal of the Physical Society of Japan, Dec. 2016. URL:
3948 <https://doi.org/10.7566/jpsc.12.010041>.
- 3949 [168] M. Glück, E. Reya, and A. Vogt. "Dynamical parton distributions revisited". In:
3950 *The European Physical Journal C* 5.3 (1998), pp. 461–470. URL:
3951 <https://doi.org/10.1007%2Fs100529800978>.
- 3952 [169] Arie Bodek and Un-ki Yang. *Axial and Vector Structure Functions for Electron- and*
3953 *Neutrino- Nucleon Scattering Cross Sections at all Q^2 using Effective Leading order*
3954 *Parton Distribution Functions*. 2010. URL: <https://arxiv.org/abs/1011.6592>.
- 3955 [170] Arie Bodek and Un-Ki Yang. "Update to the Bodek-Yang Unified Model for
3956 Electron- and Neutrino- Nucleon Scattering Cross Sections". In: (2010). URL:
3957 <https://arxiv.org/abs/1012.0261>.
- 3958 [171] Sowjanya Gollapinni. "Neutrino Cross section Future". In: (2016). URL:
3959 <https://arxiv.org/abs/1602.05299>.
- 3960 [172] E. S. Pinzon Guerra et al. "Using world π^\pm -nucleus scattering data to constrain
3961 an intranuclear cascade model". In: *Phys. Rev. D* 99 (5 2019), p. 052007. URL:
3962 <https://link.aps.org/doi/10.1103/PhysRevD.99.052007>.
- 3963 [173] S. Agostinelli et al. "GEANT4: A Simulation toolkit". In: *Nucl. Instrum. Meth.*
3964 A506 (2003), pp. 250–303.
- 3965 [174] R. Brun et al. "GEANT3". In: (Sept. 1987).
- 3966 [175] K. Abe et al. "Search for <mml:math
3967 xmlns:mml="http://www.w3.org/1998/Math/MathML"
3968 display="inline"><mml:mi>C</mml:mi><mml:mi>P</mml:mi></mml:math>
3969 Violation in Neutrino and Antineutrino Oscillations by the T2K Experiment with
3970 <mml:math xmlns:mml="http://www.w3.org/1998/Math/MathML"
3971 display="inline"><mml:mn>2.2</mml:mn><mml:mo>x</mml:mo><mml:msup><mml:mn>
3972 Protons on Target". In: *Physical Review Letters* 121.17 (Oct. 2018). URL:
3973 <https://doi.org/10.1103/physrevlett.121.171802>.
- 3974 [176] K. Abe et al. "Measurements of neutrino oscillation in appearance and
3975 disappearance channels by the T2K experiment with<mml:math
3976 xmlns:mml="http://www.w3.org/1998/Math/MathML"
3977 display="inline"><mml:mn>6.6</mml:mn><mml:mo>x</mml:mo><mml:mn>1</mml:mn
3978 on target". In: *Physical Review D* 91.7 (Apr. 2015). URL:
3979 <https://doi.org/10.1103/physrevd.91.072010>.
- 3980 [177] R.B. Patterson et al. "The extended-track event reconstruction for MiniBooNE".
3981 In: *Nuclear Instruments and Methods in Physics Research Section A: Accelerators,*
3982 *Spectrometers, Detectors and Associated Equipment* 608.1 (2009), pp. 206–224. URL:
3983 <https://doi.org/10.1016\%2Fj.nima.2009.06.064>.
- 3984 [178] et al. S. Berkman. "fiTQun: A New Reconstruction Algorithm for Super-K". In:
3985 *T2K Technical Note* 146 (2013).
- 3986 [179] et al. A. Himmel. "Super-Kamiokande events and data quality studies for T2K
3987 Runs 5 and 6". In: *T2K Technical Note* 219 (2015).

- 3988 [180] F and James. "MINUIT: Function Minimization and Error Analysis Reference
3989 Manual". In: (1998). CERN Program Library Long Writeups. URL:
3990 <https://cds.cern.ch/record/2296388>.
- 3991 [181] Xiaoyue Li and Michael Wilking. "FiTQun Event Selection Optimization". In:
3992 *T2K Technical Note* 319 (2017).
- 3993 [182] Shimpei Tobayama. "An Analysis of the Oscillation of Atmospheric Neutrinos".
3994 PhD thesis. British Columbia U., 2016.
- 3995 [183] et al. D. Barrow. "Super-Kamiokande Data Quality, MC, and Systematics in Run
3996 10". In: *T2K Technical Note* 399 (2020).
- 3997 [184] A. Maghrabi, A. Aldosari, and M. Almutairi. "Correlation analyses between solar
3998 activity parameters and cosmic ray muons between 2002 and 2012 at high cutoff
3999 rigidity". In: *Advances in Space Research* 68.7 (Oct. 2021), pp. 2941–2952. URL:
4000 <https://doi.org/10.1016/j.asr.2021.05.016>.
- 4001 [185] K. Abe et al. "Atmospheric neutrino oscillation analysis with external constraints
4002 in Super-Kamiokande I-IV". In: *Phys. Rev. D* 97 (7 2018), p. 072001. eprint:
4003 <https://link.aps.org/doi/10.1103/PhysRevD.97.072001>.
- 4004 [186] J. Beringer et al. "Review of Particle Physics". In: *Phys. Rev. D* 86 (1 2012),
4005 p. 010001. URL: <https://link.aps.org/doi/10.1103/PhysRevD.86.010001>.
- 4006 [187] Yuuki Nakano and. "Radon background study in Super-Kamiokande". In: *Journal
4007 of Physics: Conference Series* 888 (2017), p. 012191. URL:
4008 <https://doi.org/10.1088/1742-6596/888/1/012191>.
- 4009 [188] S. Nakayama K. Iyogi and Y. Obayashi. "T2K data acquisition and FC event
4010 selection at Super-Kamiokande". In: *T2K Technical Note* 027 (2011).
- 4011 [189] LeeKaPik. "Study of the neutrino mass hierarchy with the atmospheric neutrino
4012 data observed in Super-Kamiokande". PhD thesis. Tokyo University, 2012.
- 4013 [190] R. Wendell et al. "Atmospheric neutrino oscillation analysis with subleading
4014 effects in Super-Kamiokande I, II, and III". In: *Phys. Rev. D* 81 (9 2010), p. 092004.
4015 URL: <https://link.aps.org/doi/10.1103/PhysRevD.81.092004>.
- 4016 [191] J. Hosaka et al. "Three flavor neutrino oscillation analysis of atmospheric
4017 neutrinos in Super-Kamiokande". In: *Phys. Rev. D* 74 (3 2006), p. 032002. URL:
4018 <https://link.aps.org/doi/10.1103/PhysRevD.74.032002>.
- 4019 [192] Laura Munteanu et al. "Constraining the Flux and Cross Section Models with
4020 Data from ND280 using FGD1 and FGD2 for the 2020 Oscillation Analysis". In:
4021 *T2K Technical Note* 395 (2020).
- 4022 [193] P. Bartet et al. " ν_μ CC event selections in the ND280 tracker using Run 2+3+4
4023 data". In: *T2K Technical Note* 212 (2015).
- 4024 [194] Will Parker. "Constraining Systematic Uncertainties at T2K using Near Detector
4025 Data". PhD thesis. Royal Holloway University of London, 2020.
- 4026 [195] V. Berardi et al. " $\bar{\nu}_\mu$ event selection in the ND280 tracker using Run 5c and Run 6
4027 anti-neutrino beam data". In: *T2K Technical Note* 246 (2015).
- 4028 [196] James Misset. "TN-318: Fit to Super-K Atmospheric Neutrino Data for
4029 Optimization of the fitQun Fiducial Volume Cuts and Estimation of Detector
4030 Uncertainties". In: *T2K Technical Note* 318 (2017).

- 4031 [197] et al. J. Chakrani. "NIWG model and uncertainties for 2021 oscillation analysis".
4032 In: *T2K Technical Note 414* (2022).
- 4033 [198] Morgan Wascko. "T2K Status, Results, and Plans". *Neutrino 2018*. 2018.
- 4034 [199] et al. Tomislav Vladisavljevic. "Flux Prediction and Uncertainty with
4035 NA61/SHINE 2009 Replica-Target Data (TN354 version 3.3)". In: *T2K Technical*
4036 *Note 354* (2020).
- 4037 [200] G Ambrosini et al. "K/ π production ratios from 450 GeV/c protons on
4038 beryllium". en. In: *Phys. Lett. B* 420.1-2 (Feb. 1998), pp. 225–232.
- 4039 [201] et al. Edward Atkin. "NIWG model and uncertainties for 2019-2020 oscillation
4040 analysis". In: *T2K Technical Note 344* (2019).
- 4041 [202] et al. D. Barrow. "Flux and interaction models for the initial T2K-SK atmospheric
4042 joint fit studies". In: *T2K Technical Note 422* (2022).
- 4043 [203] et al. D. Barrow. "SK atmospheric T2K beam joint fit technical note, MaCh3
4044 details". In: *T2K Technical Note 426* (2022).
- 4045 [204] A. A. Aguilar-Arevalo et al. "Measurement of ν_μ and $\bar{\nu}_\mu$ induced neutral current
4046 single π^0 production cross sections on mineral oil at $E_\nu \sim \mathcal{O}(1 \text{ GeV})$ ". In: *Phys.*
4047 *Rev. D* 81 (1 2010), p. 013005. eprint:
4048 <https://link.aps.org/doi/10.1103/PhysRevD.81.013005>.
- 4049 [205] Patrick de Perio and James Imber. "Super-K Systematic Uncertainties for RUN1-4
4050 Joint ν_e and ν_μ Analyses". In: *T2K Technical Note 186* (2014).
- 4051 [206] Patrick de Perio and James Imber. "Update of SK ν_e systematic error for 2012a
4052 oscillation analysis". In: *T2K Technical Note 107* (2012).
- 4053 [207] Cris Vilela Daniel Barrow. *T2K-SK Detector Matrix Uncertainties - MaCh3*
4054 *Integration*. <https://git.t2k.org/t2k-sk/t2ksk-detcovmat/-/tree/feature/MaCh3Integration>. Accessed: 22-06-2022.
- 4056 [208] Roger Wendell. "Three Flavor Oscillation Analysis of Atmospheric Neutrinos in
4057 Super-Kamiokande". PhD thesis. University of North Carolina, 2008.
- 4058 [209] Adam M Dziewonski and Don L Anderson. "Preliminary reference Earth model".
4059 en. In: *Phys. Earth Planet. Inter.* 25.4 (June 1981), pp. 297–356.
- 4060 [210] et al. D. Barrow. "Oscillation probability calculation for the T2K+SK atmospheric
4061 joint fit". In: *T2K Technical Note 425* (2022).
- 4062 [211] R G Calland, A C Kaboth, and D Payne. "Accelerated event-by-event neutrino
4063 oscillation reweighting with matter effects on a GPU". In: 9.04 (Apr. 2014),
4064 P04016–P04016. URL: <https://doi.org/10.1088/1748-0221/9/04/p04016>.
- 4065 [212] R. Wendell. <http://www.phy.duke.edu/~raw22/public/Prob3++/>.
- 4066 [213] Felix Kallenborn et al. "Massively parallel computation of atmospheric neutrino
4067 oscillations on CUDA-enabled accelerators". In: *Computer Physics Communications*
4068 234 (2019), pp. 235–244. URL: <https://www.sciencedirect.com/science/article/pii/S0010465518302790>.
- 4070 [214] Liban Warsame. *MaCh3 Analysis Progress*. URL: <https://indico.fnal.gov/event/50217/contributions/241232/attachments/155318/202209/MaCh3ProgressforDUNELBL\underscoreMay17%20%282%29.pdf>.

- 4073 [215] Simon Bourret, João A B Coelho, and Véronique Van Elewyck and. “Neutrino
4074 oscillation tomography of the Earth with KM3NeT-ORCA”. In: *Journal of Physics:*
4075 *Conference Series* 888 (2017), p. 012114. URL:
4076 <https://doi.org/10.1088%2F1742-6596%2F888%2F1%2F012114>.
- 4077 [216] C. Rott, A. Taketa, and D. Bose. “Spectrometry of the Earth using Neutrino
4078 Oscillations”. In: *Scientific Reports* 5.1 (Oct. 2015). URL:
4079 <https://doi.org/10.1038/srep15225>.
- 4080 [217] Kaoru Hagiwara, Naotoshi Okamura, and Ken ichi Senda. “The earth matter
4081 effects in neutrino oscillation experiments from Tokai to Kamioka and Korea”. In:
4082 *Journal of High Energy Physics* 2011.9 (Sept. 2011). URL:
4083 [https://doi.org/10.1007/jhep09\(2011\)082](https://doi.org/10.1007/jhep09(2011)082).
- 4084 [218] Dave Typinski. *Earth Gravity*.
4085 <http://www.typnet.net/Essays/EarthGravGraphics/EarthGrav.pdf>.
4086 Accessed: 24-06-2022.
- 4087 [219] Roger Barlow and Christine Beeston. “Fitting using finite Monte Carlo samples”.
4088 en. In: *Comput. Phys. Commun.* 77.2 (Oct. 1993), pp. 219–228.
- 4089 [220] J S Conway. *Incorporating nuisance parameters in likelihoods for multisource spectra*.
4090 2011.
- 4091 [221] D. Barrow. *T2K Beam + SK Atmospheric Joint Fit*. 2022.